

**Progress Report**  
**1994-1996**



PDC  
Center for Parallel Computers

# Progress Report 1994-1996



**Front Cover Picture:** A rendering of a geometric model of the SP-2 installed at the Center for Parallel Computers at KTH. The picture shows a few of the SP-2 frames and the screen of the Silicon Graphics Onyx RE2. The red tubes in the background represent the internal HiPPI network and the FDDI rings which connect PDC to SUNET and the world. The rendering model was developed by Johan Ihrén, using the ray tracing program *rayshade*.

On the screen there is a snapshot of a numerical simulation of an E-shaped waveguide transmitting electromagnetic waves. The calculations are performed by solving Maxwell's equations with finite differences in time domain. The antenna current is shown on the antenna, surface currents on the waveguide surface and energy density (log scale) in the field, projected on the three outer artificial surfaces. Calculations have been done by Gunnar Ledfelt, see Section 4.1 on page 35 for more details.

(Copyright © 1996 Center for Parallel Computers.)

PDC Paralleldatorcentrum  
Royal Institute of Technology  
S-100 44 Stockholm, SWEDEN  
Telephone: +46-8-790 78 00  
Telefax: +46-8-24 77 84  
Email: [info@pdc.kth.se](mailto:info@pdc.kth.se)  
WWW: <http://www.pdc.kth.se/>

Publisher: Paralleldatorcentrum, ©1996  
Editors: *Fredrik Hedman, Tomas Wilhelmsson, Ulf Andersson*  
Typesetting & layout: *Fredrik Hedman, Tomas Wilhelmsson*  
Printed by: *Ekblads, Västervik, November 1996*  
ISBN 91-7170-695-X

# Foreword

This progress report covers an intense period of transition and development at the Center for Parallel Computers (PDC). The progress occurred in different areas and most notably in the number of users and in the scope of their applications. There was also substantial development in the PDC organization, hardware and software.

The most important event during the period was the decision by the Swedish Council for High Performance Computing (HPDR) of choosing PDC for its major grant in the Summer of 1995. This followed an evaluation of different sites by a team of international experts. PDC was suggested as the leading Swedish high performance computing facility.

The contract with HPDR resulted in a strengthened organization and an improved level of service. Examples are doubling of the systems staff and extended help desk service. Another is the process for allocating computer time. Now the applications for resources are evaluated quarterly by a scientific evaluation committee which, whenever necessary, can request international refereeing.

The grant also resulted in a very substantial upgrade of hardware and software. For the first time in many years there is a high performance computer of international class in Sweden. This 96 node IBM SP-2 is the largest SP-2 outside the United States and it has already produced substantial scientific progress as can be seen from the projects described in this report. The improvements in networking and mass storage capability are also very important. See Chapter 1 in this progress report for details.

These changes have brought in new users and new applications to PDC. A relatively large number of application software systems have now been developed for the SP-2. This means, for example, that a typical Computational Chemist or Physicist can rely on the PDC resources. There has also been a shift from the data parallel programming paradigm to message passing and the user profile is now quite similar to that of the NSF centers in the United States. There is, furthermore, a smaller fraction of projects in the computer science of parallel processing and more dominance of chemistry, physics and other applications from the sciences. Many such examples are given in this progress report.

The industrial users have benefited from the creation of the Parallel and Scientific Computing Institute (PSCI) in 1995. PSCI is sponsored by Swedish industry, the Swedish National Board for Industrial and Technical development (NUTEK) and by the Royal Institute of Technology (KTH). Its mission is research and graduate education in industrial applications of scientific computing. The work is performed in close collabora-

tion with industry and a quick view of projects with industrial relevance can be seen in the color plates in Chapter 2, Figures 2.5 and 2.8–2.17. PDC and PSCI share some common resources and jointly participate in European projects.

PDC will continue to develop in the direction, which now has been established, but new programs will also be introduced in order to increase the use of high performance computing in emerging fields. These include advanced visualization and scientific data base techniques related to mass storage. One aspect of these efforts is the desire of reaching users outside the traditional fields of the computational sciences.

PDC is looking forward to the next few years with confidence. After these past years of a growing user base and improved infrastructure we strongly believe that high performance computing will continue to play an increasing role in science and engineering. We are also convinced that the level of service which PDC provides will continue at a high professional level and that increased resources will benefit both old and new user groups,

Björn Engquist  
Director

# Contents

<b>1</b>	<b>PDC – Paralleldatorcentrum</b>	<b>7</b>
1.1	Background and Highlights . . . . .	7
1.2	Organization of PDC . . . . .	7
1.3	Cost of Operation and Staff . . . . .	8
1.4	Hardware Resources . . . . .	9
1.5	Events and Educational Activities . . . . .	10
<b>2</b>	<b>Color Plates</b>	<b>11</b>
<b>3</b>	<b>Biology and Neural Modelling</b>	<b>27</b>
3.1	Large Neural Network Simulations on Multiple Hardware Platforms . . . . .	27
3.2	Neural Network Clustering and its Application in Remote Sensing . . . . .	29
3.3	Artificial Neural Networks for Modeling Airplane Pilot Dynamics . . . . .	30
3.4	A Neural Network Model of the Olfactory Cortex and Hippocampus . . . . .	32
3.5	Analysis of 3D Brain Data . . . . .	34
<b>4</b>	<b>Computational Electromagnetics</b>	<b>35</b>
4.1	2D Computational Electromagnetics on the CM200 . . . . .	35
<b>5</b>	<b>Computational Fluid Dynamics</b>	<b>37</b>
5.1	A Parallel CFD Project at C2M2 . . . . .	37
5.2	Homogeneous and Heterogeneous Distributed CFD Com- putations . . . . .	38
5.3	The NAS Parallel Benchmarks on a DEC Alpha Farm . . . . .	39
5.4	Parallel Programming Models for Multi-block Flow Com- putations . . . . .	40
5.5	Adapting a Regional Air Pollution Dispersion Model for MasPar and CM200 . . . . .	41
5.6	Numerical Simulation of Fully Developed Turbulent Plane Couette Flow . . . . .	45
5.7	Parallel Computing for Aircraft Design . . . . .	47
5.8	Solution of Compressible Flow Problems in Parallel with Static Load Balancing . . . . .	50
5.9	A Parallel Full Navier-Stokes Simulation of an Afterburner at Volvo Aero Corporation . . . . .	52
5.10	Parallel CFD on the IBM SP-2 . . . . .	54

5.11	Supersonic Inviscid Flow Computations on Adaptive Unstructured Grids . . . . .	57
5.12	Numerical Computation of Hydrodynamics in Fluidized Beds . . . . .	59
5.13	Consolidation of Concentrated Suspensions . . . . .	60
5.14	Flutter Analysis of Two Dimensional Viscous Flow in Turbomachines Using the Advection Upstream Splitting Method (AUSM) . . . . .	62
<b>6</b>	<b>Applications in Physics</b>	<b>67</b>
6.1	An Universal Scaling Law for Atomic Diffusion in Condensed Matter . . . . .	67
6.2	Atomic Kinetics and Dynamical Phason Disorder in a Quasicrystal . . . . .	70
6.3	Electric and Magnetic Non-Linear Properties Obtained with Response Theory . . . . .	73
6.4	Finite Element Modeling of Acoustic Emission . . . . .	78
6.5	An Exact Absorbing Boundary Condition for 3D Thin Structures . . . . .	79
6.6	The Continuation of Transient Data for a Hyperbolic Equation in a 3D Inhomogeneous Half-Space . . . . .	80
6.7	Hypercycles versus Parasites in Spatial Models of the Origin of Life . . . . .	81
6.8	A Coupled Map Lattice Model of Self-Propelling Particles	82
6.9	Monte Carlo Studies of the Dynamics of Re-Entrant Ising Spin Glasses . . . . .	83
6.10	Code Porting and Cluster-Finding Experiences on the IBM SP-2 and the CM200 . . . . .	88
6.11	Electronic Structure Calculations for the Physics and Chemistry of Surfaces . . . . .	91
6.12	Quantum Wavepacket Studies of Dynamical Processes at Surfaces . . . . .	94
6.13	First-Principles Modeling Defects in Semiconductors: Oxygen in Silicon . . . . .	96
6.14	Fluctuations in Atomic Collision Cascades . . . . .	101
6.15	Transport Simulation of Electrons Reflected Elastically from Solids . . . . .	103
6.16	One-Group Radiation Transport Benchmarks for Anisotropically Scattering Medium . . . . .	105
6.17	Modified Artificial Viscosity in Smooth Particle Hydrodynamics on the CM200 . . . . .	106
6.18	Reduction of Impurity Scattering from Correlation of Donors . . . . .	107
6.19	A Monte Carlo Model for Radionuclide Transport in Fractured Media . . . . .	108

<b>7</b>	<b>Applications in Geophysics</b>	<b>111</b>
7.1	Numerical Experiments on Gravitational Instability of Geostructures . . . . .	111
7.2	Molecular Dynamic Study of Melting of Earth’s Materials	113
7.3	Finite Difference Modeling of Seismic Wave Propagation in Heterogeneous Media . . . . .	115
<b>8</b>	<b>Applications in Chemistry</b>	<b>119</b>
8.1	A Conformational Free Energy Landscape of ApApA from Molecular Dynamics Simulations . . . . .	119
8.2	Dynamics of Hydrogen Atoms in Strong External Fields .	120
8.3	Parallel Molecular Dynamics Simulations of DNA Systems	121
8.4	Molecular Dynamics Simulation of a Poly(Ethylene Ox- ide) Surface . . . . .	126
8.5	Molecular Dynamics Simulation of Ion Mobility in the Crystalline Poly(Ethylene Oxide) Surface . . . . .	127
8.6	An Integral Direct, Distributed-Data, Parallel MP2 Algo- rithm . . . . .	127
8.7	The Structure of the Blue Copper Proteins . . . . .	133
8.8	Ab Initio and DFT Investigations of Solution Tautomerism of DNA Bases . . . . .	135
8.9	Basis Set and Correlation Effects on Geometry of Octa- hedral Second-Row Transition-Metal Complexes . . . . .	136
8.10	A First Principles Study of the Dehydroxylation of 2M <sub>1</sub> -Muscovite . . . . .	138
<b>9</b>	<b>Miscellaneous Projects</b>	<b>141</b>
9.1	Multi-Disciplinary Parallel Optimization . . . . .	141
9.2	Simulation and Prediction of Real and Artificial Financial Systems . . . . .	143
9.3	Burgers’ Equation with Noisy Initial Data . . . . .	144
9.4	PDC++ and Parade — C++ Class Library and Visualizer for Data Parallel Programming . . . . .	145
	<b>Bibliography</b>	<b>147</b>
	<b>Index</b>	<b>161</b>



# 1 PDC – Paralleldatorcentrum

This fourth progress report of the Center for Parallel Computers (PDC) at the Royal Institute of Technology (KTH) covers the activities of the center from 1994 up until the end of June 1996. A brief overview of the most important activities at the center during this period follows in this section. User projects are described in Chapters 3 through 9.

## 1.1 Background and Highlights

The Center was formed in January 1990 to act as a focal point and national forum for research on and use of parallel computers. Our goal is to stimulate research and spread information on the use of parallel computers.

This is achieved by providing high-performance parallel computers and expertise on their use to the technical and scientific computing community in Sweden.

The two years covered in this Progress Report has been a period of great change and rapid development. During 1994 we upgraded our Connection Machine to a 16K CM200 and also installed our first IBM SP-2. We also moved both people and all hardware to new and renovated facilities at KTH.

In 1995, the most important event was the HPDR decision to select PDC for its major grant and the subsequent contract between HPDR and KTH/PDC, signed on June 28 1995. The decision and contract followed after the evaluation, of PDC and other sites, by a committee of international experts. The increased funding allowed us to substantially upgrade the SP-2 to 96 nodes and also acquire a mass storage system. To balance the expanded hardware base and increased responsibilities PDC has also hired more people.

So far, 1996 has been a period of consolidation and further expansion in hardware, resources and staff. Most notably, PDC has taken on the systems support of the CRAY J932 owned by the KTH KALLSUP consortium. This arrangement is set up as a win-win arrangement which equally benefits both KALLSUP and PDC users.

## 1.2 Organization of PDC

PDC has a board, a scientific council and a director. P. G. Hedström, Corporate Technical Director of Electrolux AB is chairman of the PDC board, Professor S. Lennart Johnsson is chairman of the PDC scientific council and Professor Björn Engquist is the PDC director. Furthermore,

there are 3 associate directors, 4 System Managers, 1 system engineer, 2 program and application developers, 1 information officer and 2 secretaries. Affiliated with PDC there are also 3 affiliated researchers.

---

Corp. Tech. Dir., P. G. Hedström	Chairman, PDC Board
Prof. S. Lennart Johnsson	Chairman, Scientific Council
Prof. Björn Engquist	Director
Fredrik Hedman	Associate Director
Gert Svensson	Associate Director
Dr. Per Öster	Associate Director
Harald Barth	System Manager
Jonas Engström	System Manager
Johan Ihrén	System Manager
Lars Malinowsky	System Manager
Johan Danielsson	System Engineer
Peter Carlsson	Information Officer
Nils Jönsson	Application Specialist
Anders Ålund	Application Specialist (part time)
Dr. Per Hammarlund	Application Scientist
Dr. Erik Aurell	Scientist
Dr. Mikhail Dzugotov	Scientist
Berith Bodelsson	Secretary
Britta Svensson	Secretary

---

The associate directors each have a field of responsibility: Systems & Operations, Science & Customer Relations and Administration. The system managers have specific primary and secondary systems assigned to them where they act as respectively responsible or back-up. They report to the head for Systems & Operations. The program and application developers and information officer also have specific tasks and allocated to them. They report to the head of Science & Customer Relations.

### 1.3 Cost of Operation and Staff

The operational cost, including staff and investments, has been covered by the Swedish Council for High Performance Computing, HPDR, the Royal Institute of Technology and the Swedish National Board for Industrial and Technical Development, NUTEK. A grant of 8 MSEK for the budget year 93/94 and 7 MSEK for 94/95 was given by FRN to purchase a scalable MIMD-system. This grant was used to make the initial investment in SP-2 technology.

Operational costs			
	94/95 (12 months)	95/96 (18 months)	
NUTEK	400 kSEK	HPDR	8 081 kSEK
KTH	3 594 kSEK	KTH	380 kSEK
		Other	1 659 kSEK
Total	3 994 kSEK		10 120 kSEK

Investments			
	94/95 (12 months)	95/96 (18 months)	
FRN	15 879 kSEK	HPDR	33 607 kSEK
KTH	3 239 kSEK		
Total	19 118 kSEK		33 607 kSEK

## 1.4 Hardware Resources

### *Networking*

PDC is connected directly to SUNET via a dedicated FDDI connection. Internally, PDC has implemented a high-speed network infrastructure to support large-scale I/O and enable computational clusters of PDC systems. A Netstar Gigarouter is the heart of the network, with a HiPPI connection to large systems and FDDI connections to various networks. All large systems are connected to a HiPPI network (800 Mbit/s) via Netstar HiPPI ClusterSwitch. Other systems, such as AFS file servers, are connected to a number of FDDI (100 Mbit/s) rings separated by a Digital Equipment FDDI GigaSwitch.

### *Current Hardware*

- 96 node IBM SP-2, 80 T2 nodes, 16 wide nodes and 380 Gbyte user available disk. The peak performance is 267 Mflop/s per node giving a peak performance for the machine of 25.6 Gflop/s. Total of 18.5 Gbyte memory.
- A CRAY J932 managed by PDC for the KALLSUP consortium at KTH. Peak 6.4 Gflop/s, total memory 8 Gbyte, total disk 150 Gbyte.
- Connection Machine CM200 with 16 384 processors, 2 Gbyte memory and a 10 Gbyte DataVault. Scalable massively parallel SIMD-computer with data-parallel programming environment.
- High-end equipment for visualization. One SGI Onyx RE2 with two R4400 CPUs and 640 Mbyte memory and three SGI Indigo R4000.

### *Mass storage*

IBM 3494 Tape Library Dataserver with four IBM 3590 Magstar tape drives. Can store up to 12 Tbyte of data. The current HSM system runs on a the CRAY J932. HSM functionality is provided by Data Migration Facility (DMF) from CRAY Research.

### **1.5 Events and Educational Activities**

Throughout these two years PDC has arranged conferences, workshops and events as well as several seminars on the use of parallel computers. The SP-2 and the Connection Machine has been used for courses in the M.Sc. programs at KTH, CTH and Högskolan Gävle/Sandviken. See Tables below.

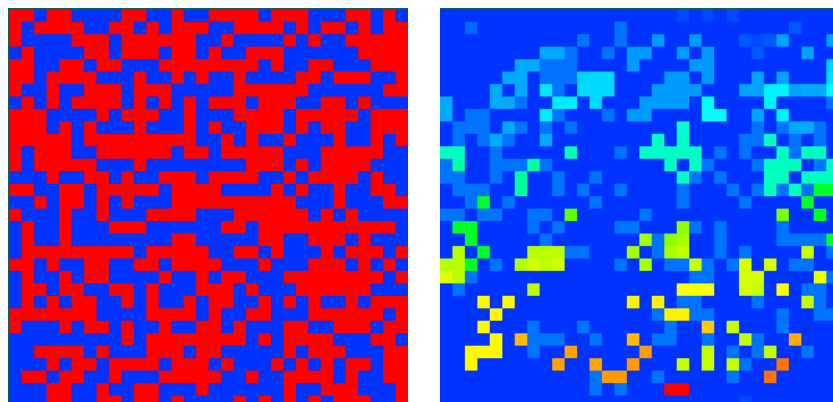
Event	Date
Conference on “Parallel Computing in Science and Industry” and Inauguration of 54 node SP-2 “Strindberg”	941215-16
SP-2 Administrator Workshop	951218-19
Nordic EUROPORT Conference	960229
Inauguration of 96 node SP-2 “Strindberg”	960301
Swisc96, Swedish Industrial Scientific Simulations	960530-31

Course	Date	Students
New Comp. Arch. for Numerical Calculations <sup>a</sup>	Jan. 94	16
Programming of MPP Computers	Mar. 94	23
Parallel Computer Systems	Spring 94	47
Problem Solving Using Massively Parallel Computers	Nov. 94	14
Numerical Solution of Large Sparse Systems <sup>a</sup>	Nov. 94	11
Introduction to Parallel Computing on the SP-2	Dec 94	23
Introduction to Parallel Computing on the SP-2	May 95	17
Introduction to Parallel Computing on the SP-2	May 95	21
Parallel Computer Systems	Spring 95	27
Problem Solving Using Massively Parallel Computers	Oct. 95	16
Introduction to Parallel Computing on the SP-2	Oct. 95	15
Introduction to Parallel Computing on the SP-2	Nov. 95	18
Introduction to Parallel Computing on the SP-2	Nov. 95	18
Introduction to Parallel Computing on the SP-2	Mar. 96	15
Introduction to Parallel Computing on the SP-2	Apr. 96	6
Introduction to Parallel Computing on the SP-2	May 96	15
Parallel programming in MPI <sup>b</sup>	May 96	40
Parallel Computer Systems	Spring 96	34
MPI Techniques for MD and MC	Jun 96	19

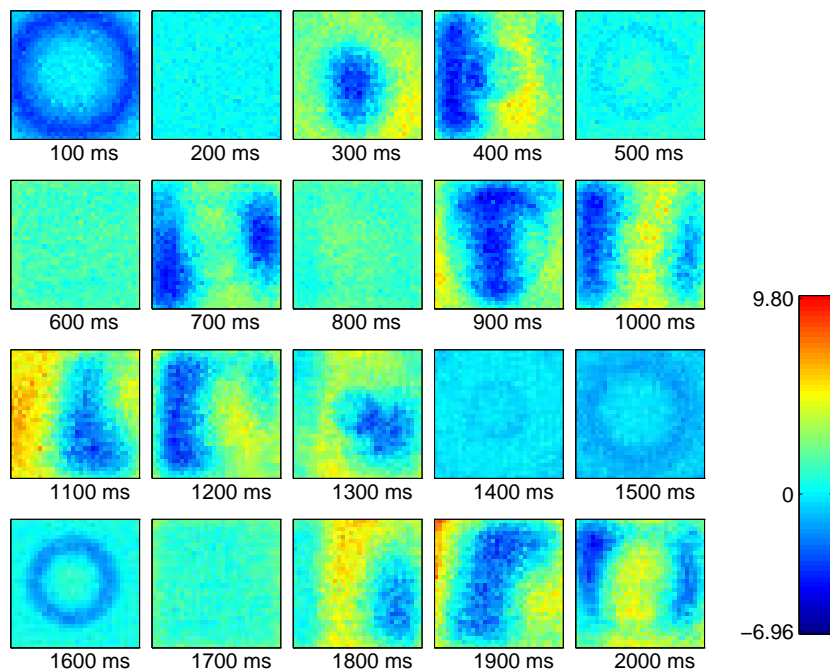
<sup>a</sup>At CTH.

<sup>b</sup>At Högskolan Gävle/Sandviken.

## 2 Color Plates

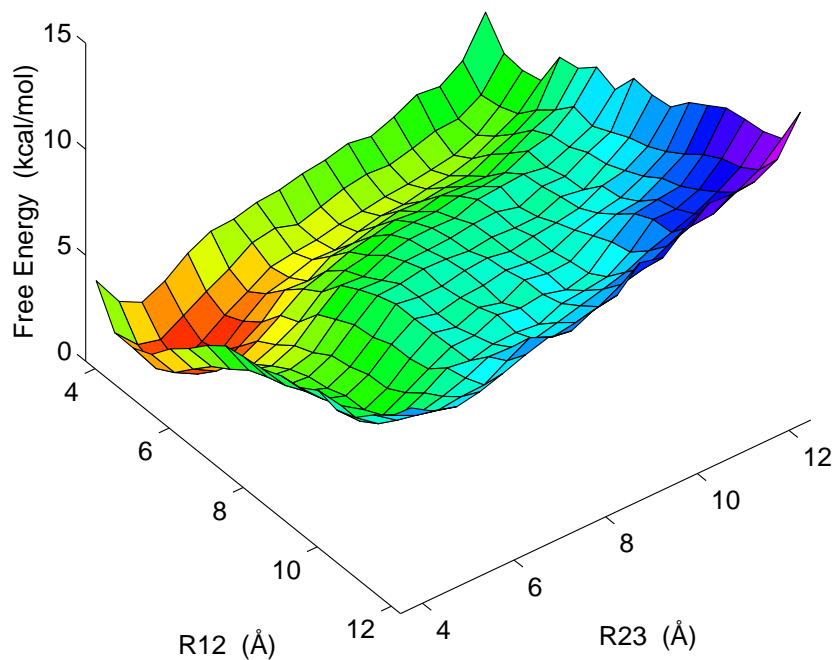


**Figure 2.1.** Lattices before (left) and after (right) cluster-finding. This system is what is typically generated and analyzed by the Coffeepot program. (See Section 6.10 on page 88.)

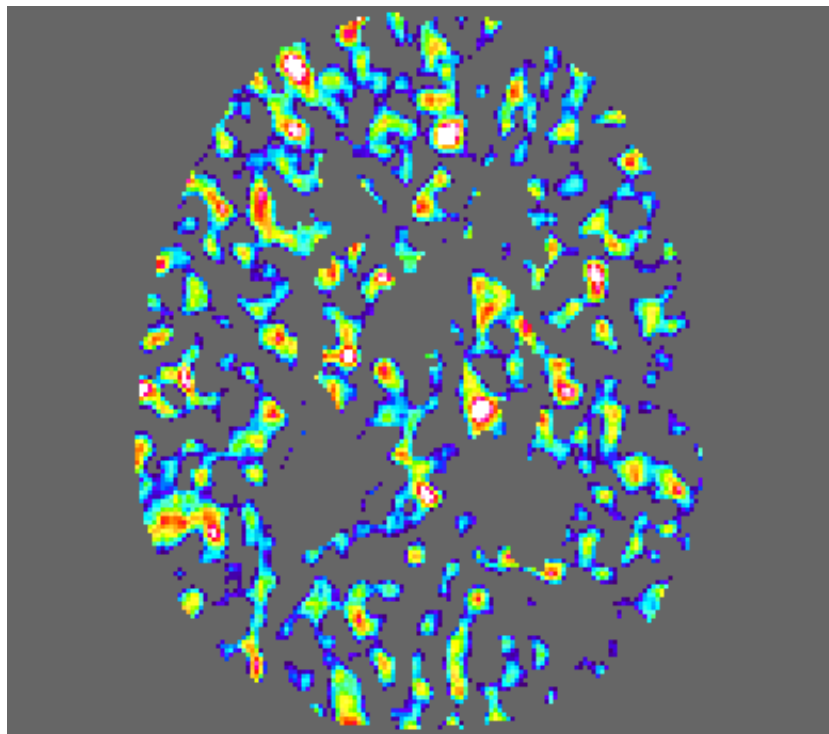


**Figure 2.2.** Global oscillatory behavior induced in the excitatory network layer by noise in a single (feedforward) inhibitory unit. Simulations are run on the CM200 with  $32 \times 32$  network units in each of the three layers. Here the activity color coded for all units in the excitatory layer is displayed. This shows that spontaneous disinhibition (possibly caused by inhibitory neuronal random generators) can result in synchronized oscillatory activity in the excitatory layer. (See Section 3.4 on page 32.)

**Figure 2.3.** A contour map of the conformational free energy of the ApApA trimer by using the reaction coordinates  $R_{12}$  and  $R_{23}$ . (See Section 8.1 on page 119.)



**Figure 2.4.** This is an example of a Positron Emission Tomography (PET) image of a human brain. PET-images normally contains brain activation calculated as regional cerebral metabolism or regional cerebral blood flow. (See Section 3.5 on page 34.)



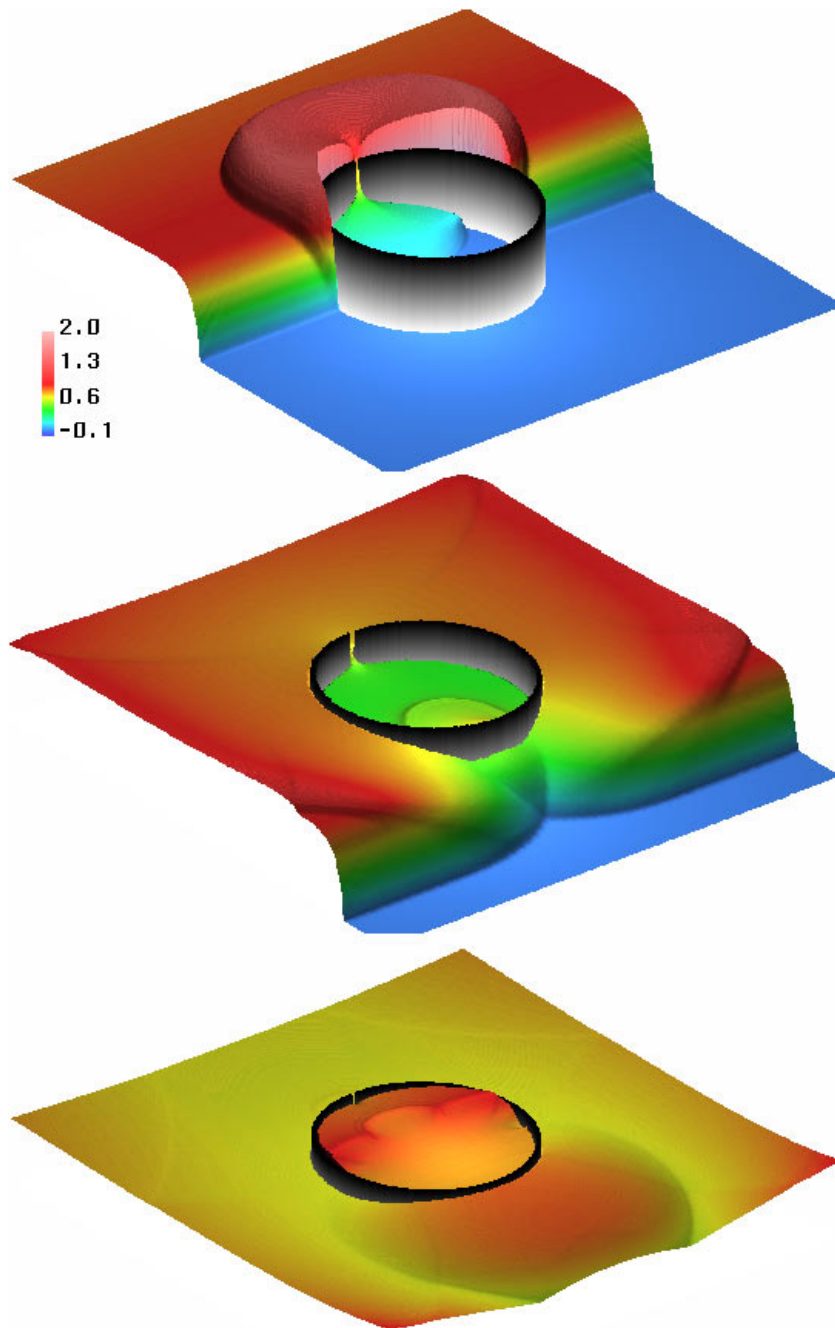
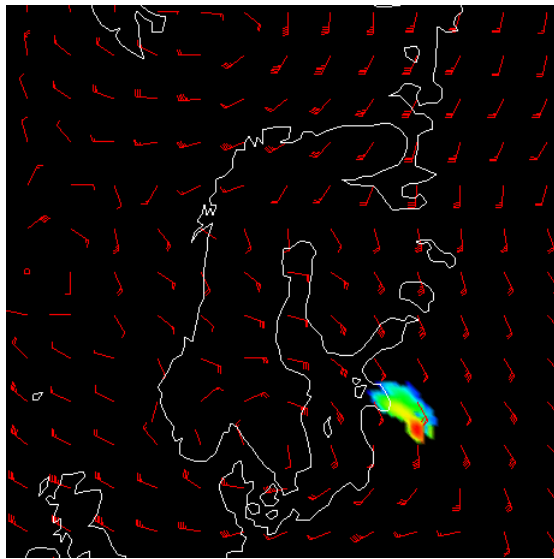
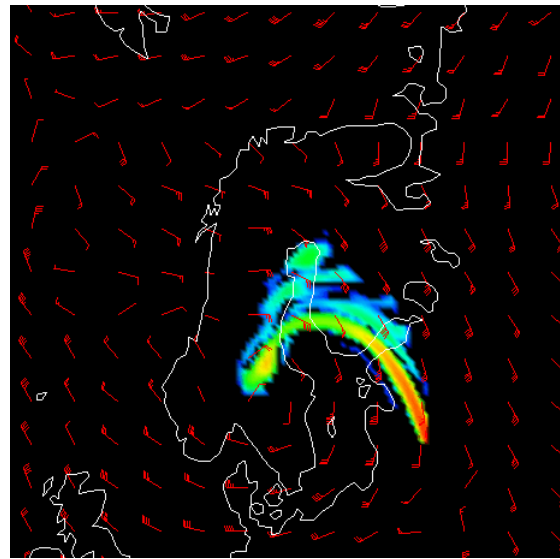


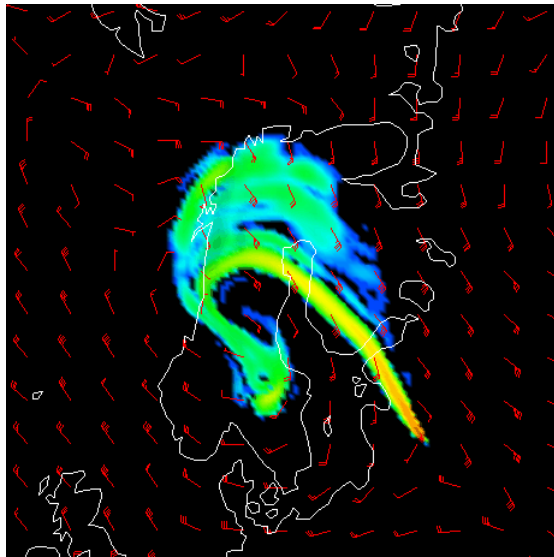
**Figure 2.5.** An electromagnetic pulse strikes a metallic cavity with a narrow opening of  $1/40$  of the diameter. Even though the opening is small a substantial amount of the electromagnetic pulse sneaks inside. The pictures show the amplitude of the magnetic field at three different times. In the top picture the pulse has propagated along half the cavity. We can see how the field leaks into the cavity and how the field outside the cavity is scattered by the metal. In the middle picture the front of the pulse has just passed the cavity and we can see some surface waves inside the cavity. Notice how the scattered field in the picture above passes the outer boundary giving rise only to small reflections. The bottom picture shows that the field inside the cavity is of almost the same amplitude as the original pulse. The possibility to simulate these phenomena is crucial to understand principles important to constructing electronic equipment immune to external fields. (See Section 4.1 on page 35.)



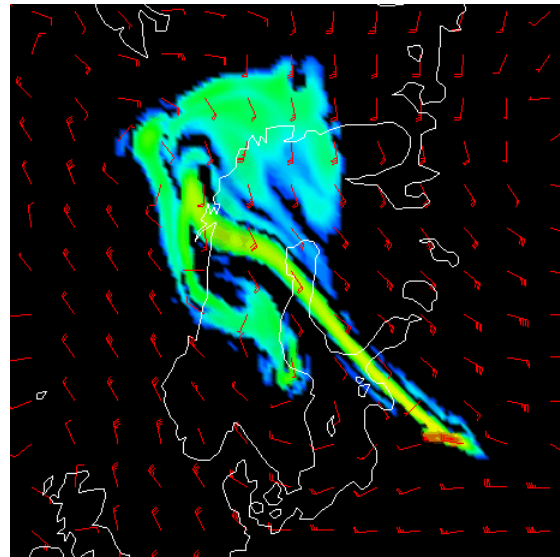
6 h



18 h

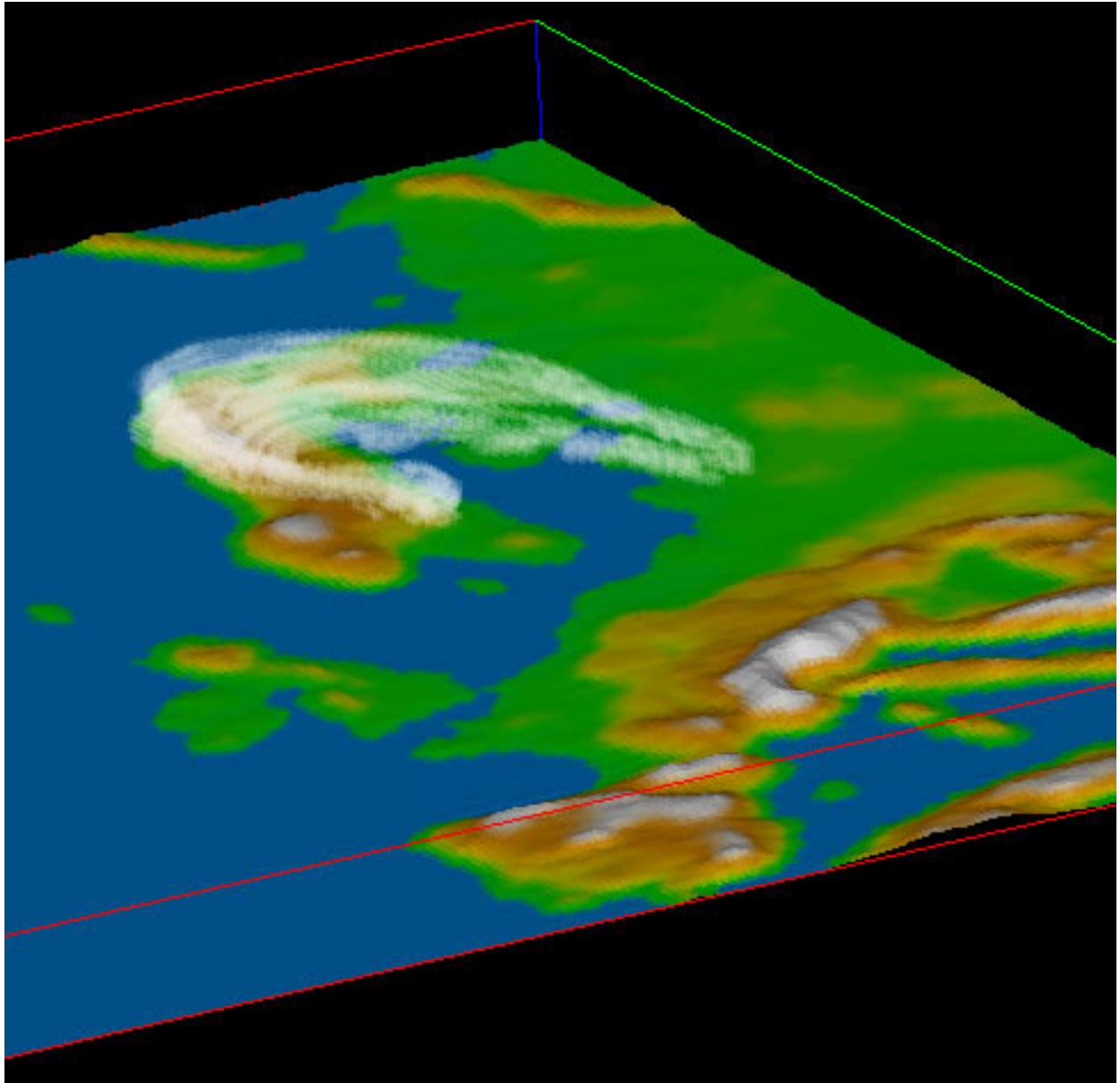


30 h



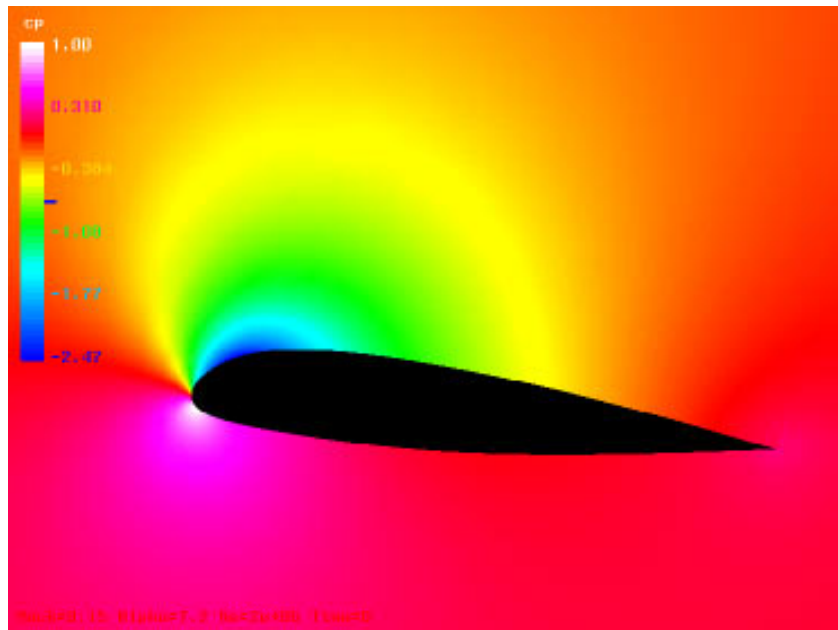
42 h

**Figure 2.6.** This sequence shows a *fictive* radioactive release from the nuclear power plant Ignalina in Lithuania. The release starts at 6 am on November 12, 1992 and continues with constant intensity for the entire 51 hour simulation. During this time a low pressure system over southern Scandinavia moves towards north, while decreasing in intensity. The four frames show a section of the full simulation domain with 12 hours separation starting 6 hours after the beginning of the release. Radioactivity is color coded with red for high air concentration and blue for low. The red arrows indicate wind direction with more “feathers” for higher wind speeds. (See Section 5.5 on page 41.)

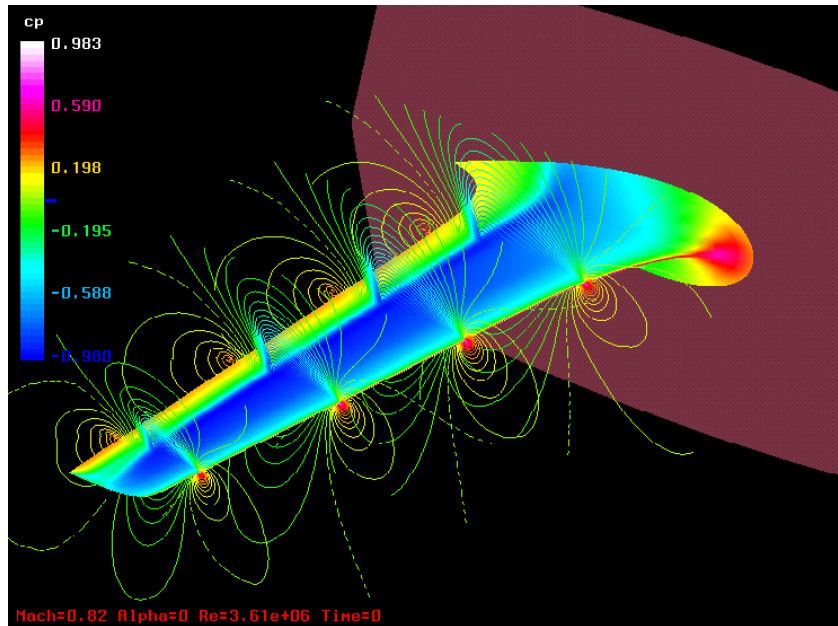


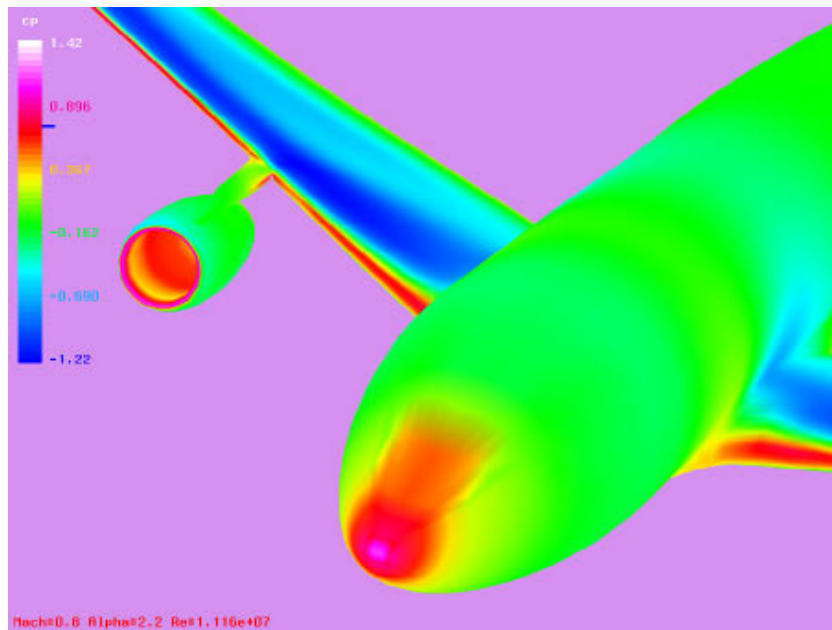
**Figure 2.7.** A 3D view of a radioactive cloud from a *fictive* release at the Ignalina nuclear power plant in Lithuania. This shows the cloud at 6 am on November 13, 1992, which is 24 hours after the start of the release. The modeling domain is 241 by 241 gridpoints at 22 km horizontal resolution and has 16 layers between the surface and about 25 km. (See Section 5.5 on page 41.)

**Figure 2.8.** Pressure distribution around an A-airfoil at  $7.2^\circ$  angle of attack, Mach number = 0.15 and Reynolds number per meter,  $Re/m = 2\,000\,000$ . Calculation made on 16 IBM SP-2 processors, with a  $512 \times 128$  mesh, using Baldwin-Lomax turbulence model. (See Section 5.7 on page 47.)

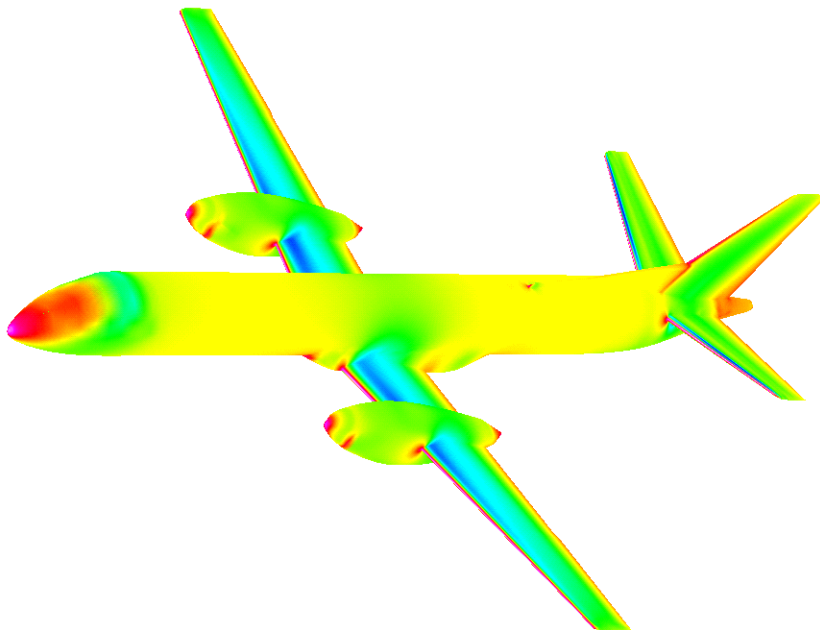


**Figure 2.9.** Pressure distribution on the surface and isobars for a F5-wing at  $0^\circ$  angle of attack,  $M = 0.82$  and  $Re/m = 3\,610\,000$ . Calculation made on 32 IBM SP-2 processors, with a  $192 \times 40 \times 48$  mesh, using Baldwin-Lomax turbulence model. (See Section 5.7 on page 47.)



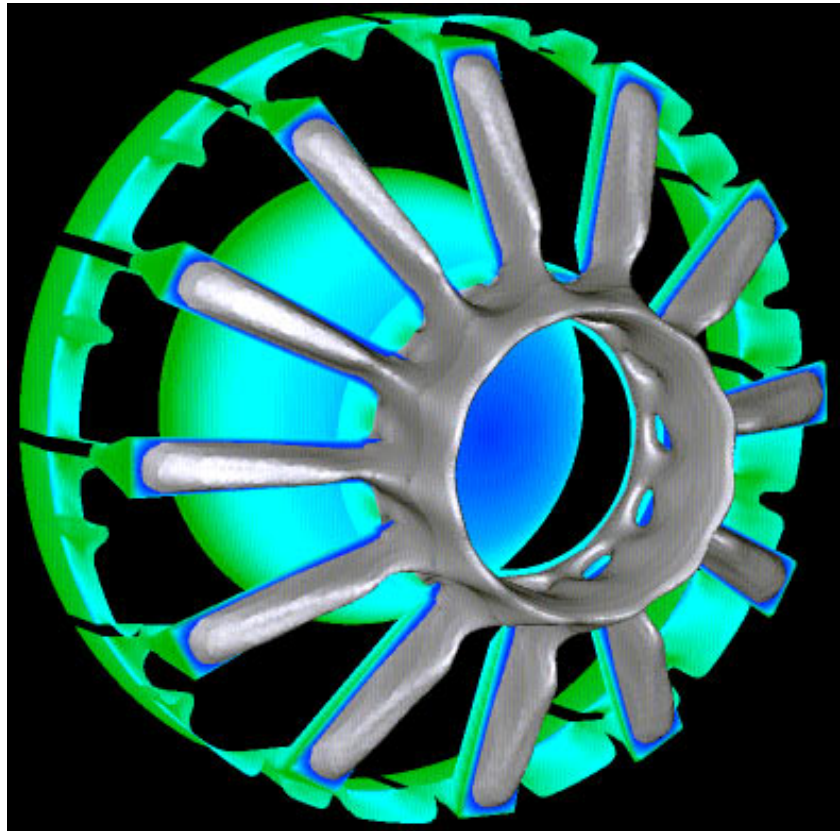


**Figure 2.10.** Pressure on the surface for an aircraft, with pylons, nacelle, etc. at  $2.2^\circ$  angle of attack,  $M = 0.8$  and  $Re/m = 11\,160\,000$ . The computational mesh consists of 3.5 million grid points in 62 blocks and the computation was made on 32 IBM SP-2 processors. The Granville turbulence model was used for this case, which gives around 4500 floating point operations per timestep and grid cell, or approximately  $2 \cdot 10^{14}$  floating point operations to get a converged solution. (See Section 5.7 on page 47.)

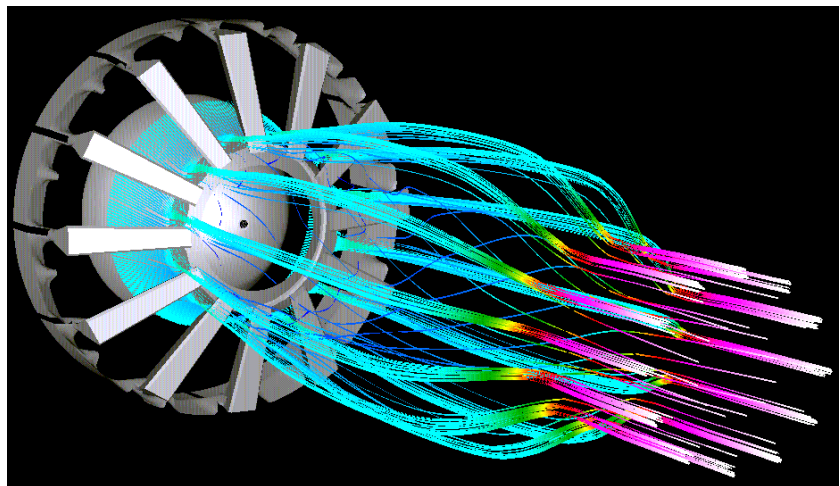


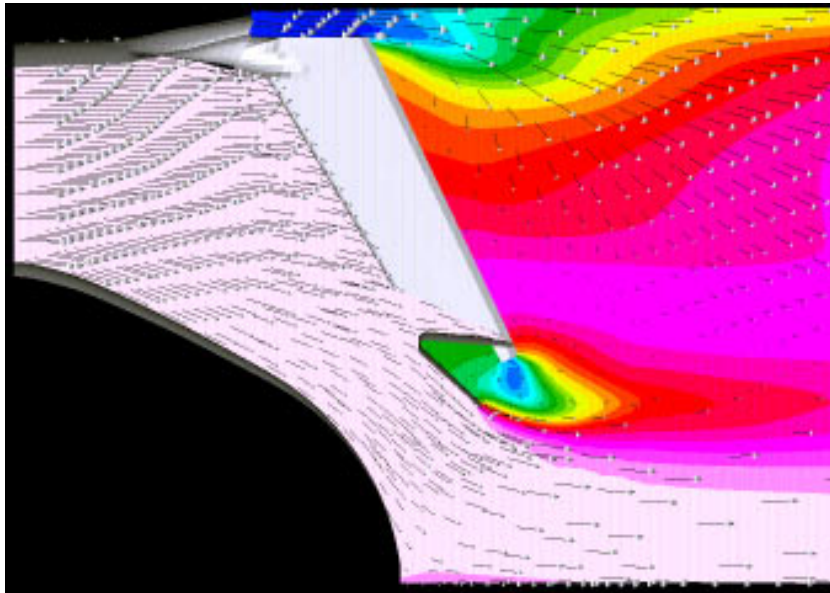
**Figure 2.11.** The colors represent the pressure coefficient  $c_p$ , proportional to the static pressure  $p$ , on the surface of a Saab 2000 (blue=low  $p$ , red=high  $p$ ). (See Section 5.8 on page 50.)

**Figure 2.12.** The gray surface is an iso-surface where the absolute velocity is zero and defines the recirculation zone of the afterburner where the flame is expected to stabilize. The structures are color coded using axial velocity. (See Section 5.9 on page 52.)

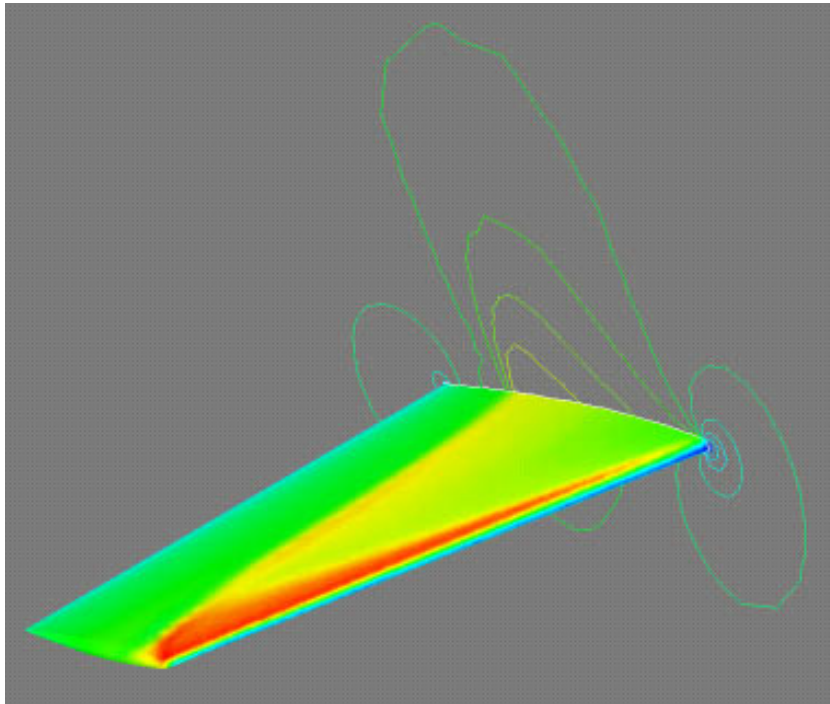


**Figure 2.13.** This figure depicts the flowfield downstream the afterburner. The streamlines are injected at a thought fuel injection radius and are colored with Mach numbers. (See Section 5.9 on page 52.)



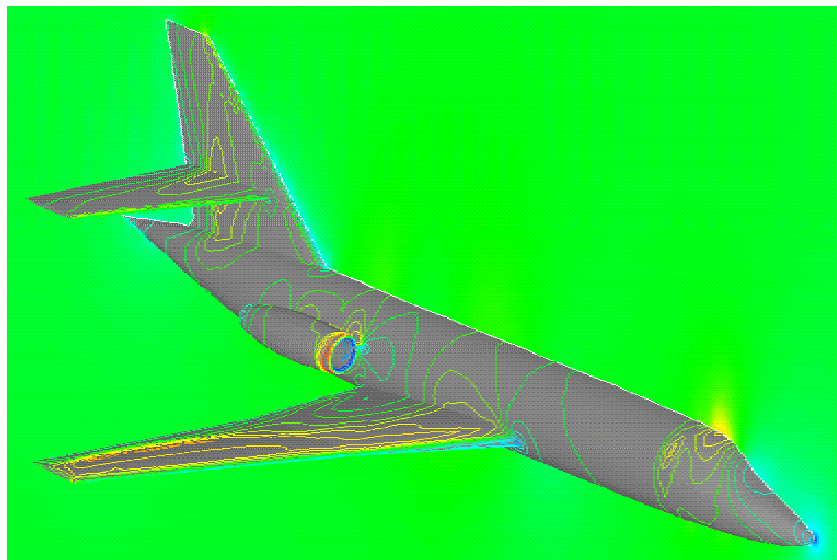
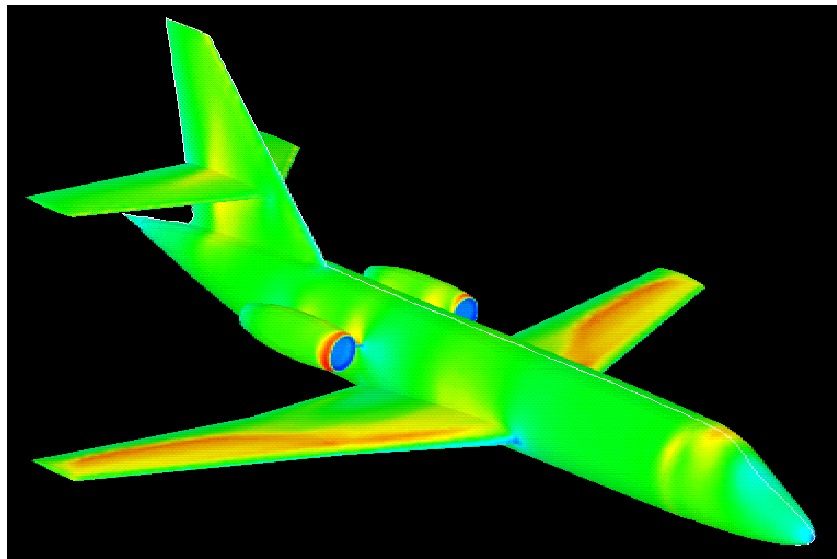


**Figure 2.14.** This figure gives a detailed picture of the flow around the flame holder of the afterburner. The colors represent static temperature and the arrows indicate the local velocity of the fluid. (See Section 5.9 on page 52.)



**Figure 2.15.** The picture shows the computed negative  $C_p$  on the ONERA M6 wing. This Euler solution was obtained using a free stream Mach number of 0.84 and the angle of attack was set to 3.06 degrees. On the symmetry plane, pressure contours are plotted. The computation was performed on the IBM SP-2 using AVBP. (See Section 5.10 on page 54.)

**Figure 2.16.** As an illustration of the inherent capability of the AVBP program to treat realistic aerodynamical problems, a transonic flow about a twin engined Dassault Falcon jet plane has been computed. For the simulation a free stream Mach number of 0.85 is assumed and the angle of attack is taken to be two degrees. Flow through conditions are imposed at the engines. Due to the symmetry of the flow, the numerical computations were performed using only one half of the aircraft geometry. The Euler solution show leeward side wing shocks and a shock at the top of the aircraft, both phenomena typical for these flight conditions. The top picture shows the surface pressure and the bottom picture shows pressure contours on the aircraft surface with a shaded pressure field on the symmetry plane. (See Section 5.10 on page 54.)



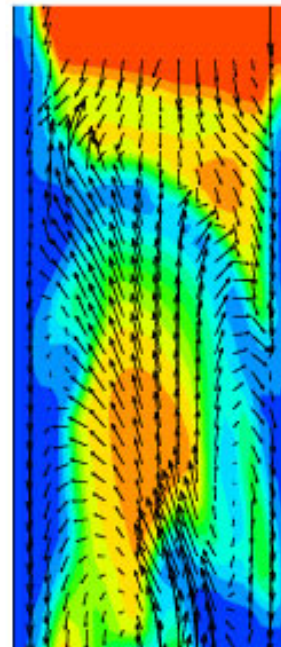
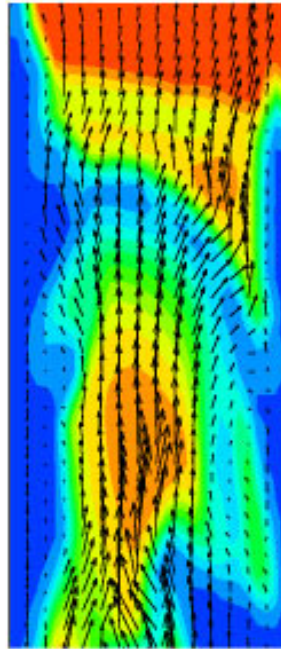
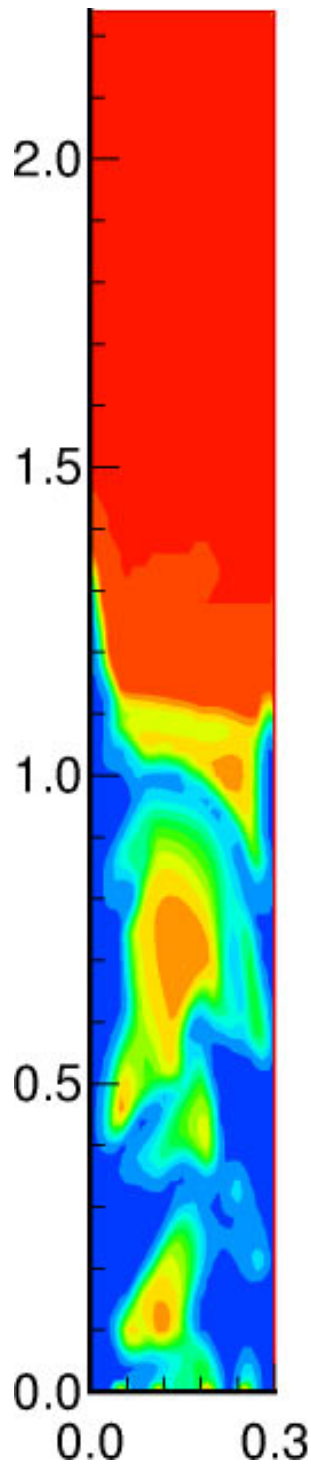


**Figure 2.17.** A bubbling fluidized bed can technically be described as a container in which the solid phase in the form of closely packed particles (in this case silica sand with a mean diameter of 0.7 mm) is brought into motion by an air flow inserted at the bottom of the container through an air distributor. The air tends to form bubbles which rise through the bed, but can also flow through the dense regions and shortcut between the bubbles. The word fluidization comes from the fact that, at a gas flow rate within a certain range, the mixture becomes fluid-like. Fluidized beds have been in industrial use for several decades mainly as chemical reactors, solid fuel combustors and dryers. These pictures show how gas bubbles, defined as the regions where the gas concentration is larger than approximately 70%, rise up through the bed chaotically but with a regularity in a statistical sense. (See Section 5.12 on page 59.)

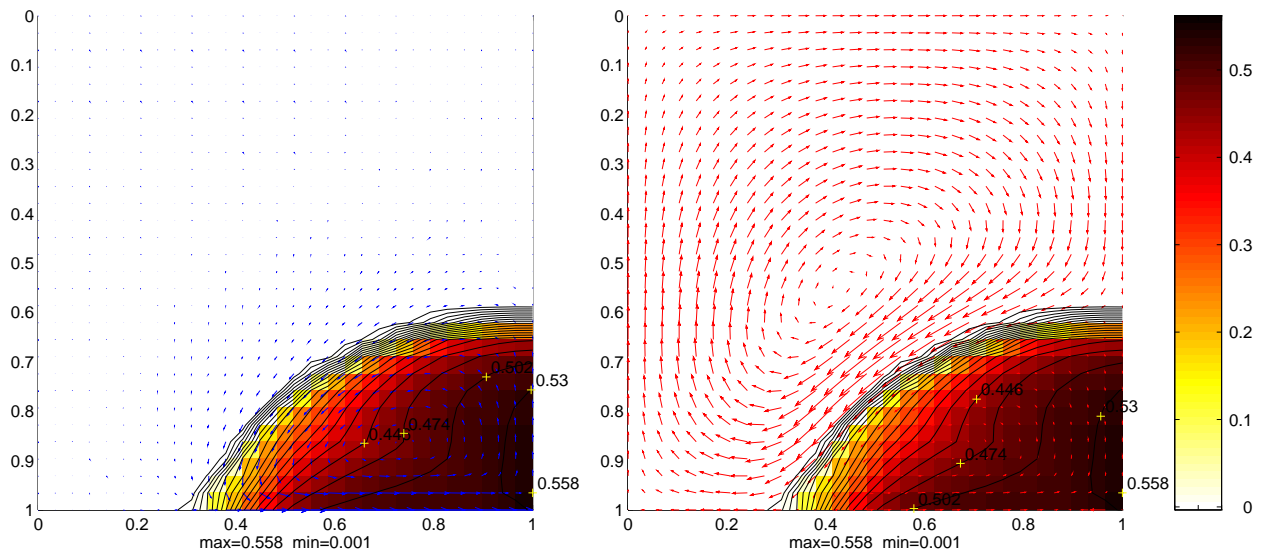
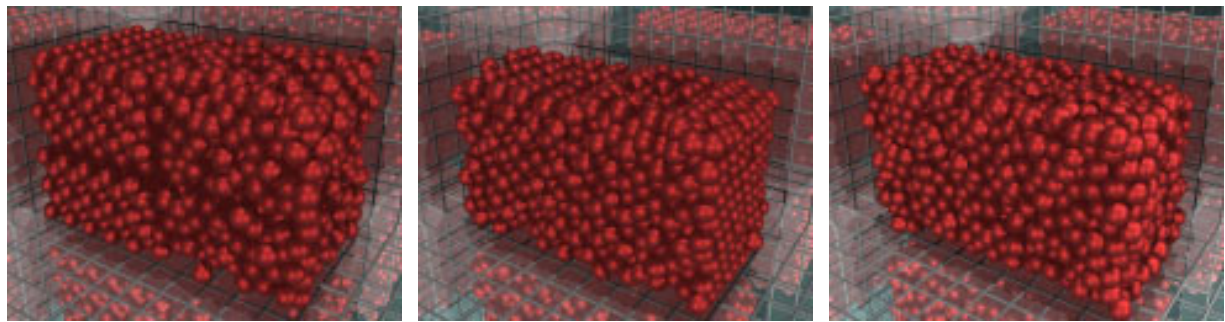


**Figure 2.18.** The pictures shows a numerically computed solution of a test problem in a closed quadratic container. The solution is almost stationary. The bottom wall is moving to the right. The color contours represent the volume fraction of solid particles. The blue arrows show particle velocity scaled with the volume fraction of particles. The red arrows show fluid velocity scaled with the volume fraction of fluid. (See Section 5.13 on page 60.)

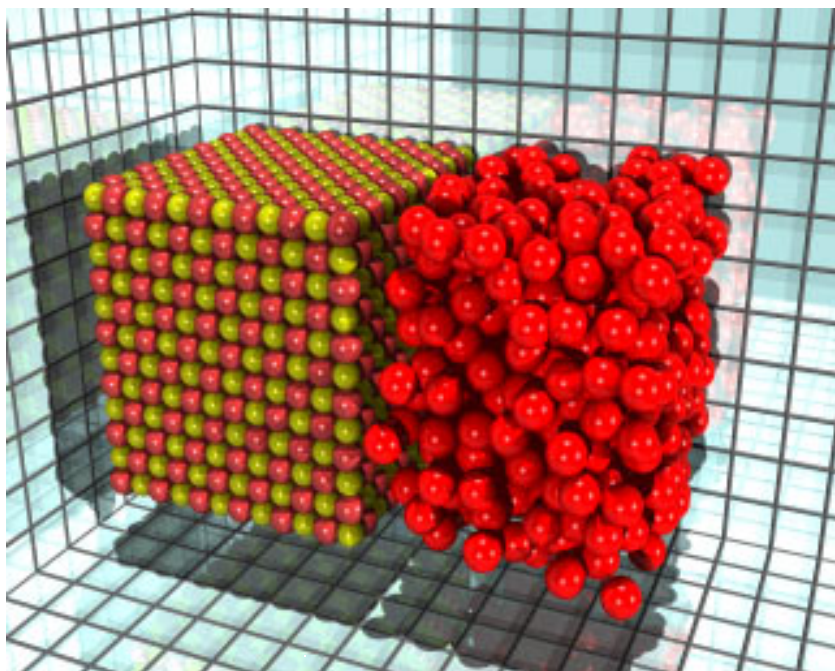


(a) Initial two-phase setup

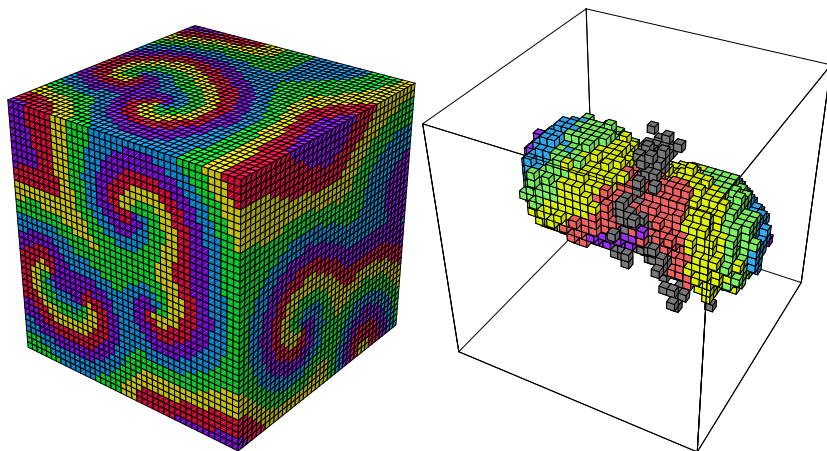
(b) Solid iron crystal

(c) Calculated molten configuration

**Figure 2.19.** 3D view of MD computational cell containing 2048 atoms of iron (shown as spheres). Mirror reflections emphasize the 3D periodic boundary conditions. The melting temperature of iron according to the embedded-atom method is about 7500 K at a pressure of 3.3 million atmospheres at the boundary between the inner and outer Earth's core. (See Section 7.2 on page 113.)

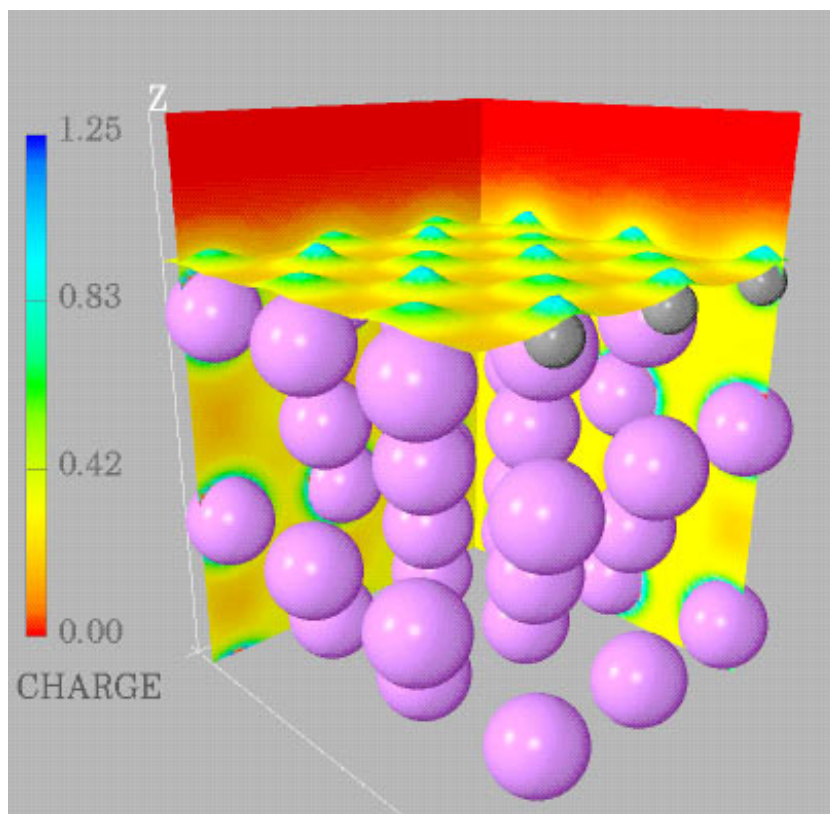


**Figure 2.20.** 3D view of a perfect MgO crystal (smaller spheres) presuritized by argon (large red spheres). This setup was used to study recrystallization in the diamond anvil cell. Pressures in the directions parallel and perpendicular to the interface between Ar and MgO are different. (See Section 7.2 on page 113.)

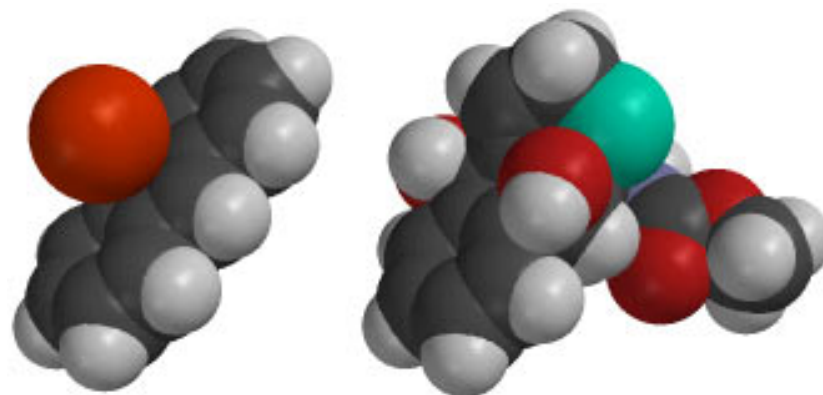


**Figure 2.21. Left:** A system of scroll rings in a three dimensional partial differential equations model on a  $40 \times 40 \times 40$  lattice. The different colors, which correspond to different molecular species, indicate which molecular species is present at the highest concentration on each lattice point. **Right:** A simplified picture of a parasite infecting a writhed, sausage-shaped scroll wave cluster in a five-component hypercycle cellular automata on a  $128 \times 128 \times 128$  lattice. The cluster has a spiral cross section. Each colored cube corresponds to  $8 \times 8 \times 8$  lattice points. The cubes are colored according to the dominant species on the corresponding lattice points, but they are only displayed if less than half of the lattice points are empty. All cubes where the parasite dominates are displayed in grey regardless of the number of empty lattice points. The parasite, which here advances into the core region at the central part of the cluster, will kill the cluster. (See Section 6.7 on page 81.)

**Figure 2.22.** Electron charge distribution for H chemisorbed on a (100) face of a slab of Ni atoms. The large and small spheres represent the ioncores of the Ni and H atoms, respectively. (See Section 6.11 on page 91.)



**Figure 2.23.** Examples of molecular systems that are currently studied at PDC, employing the newly developed integral direct, distributed-data parallel MP2 implementation. **Left:** The van der Waals complex anthracene-Ar in its supposed minimum-energy configuration is displayed, i.e. with the Ar atom “adsorbed” on the inner ring of the catacondensed aromatic ring system. **Right:** A subunit of the anti-cancer drug calicheamicin in its configuration after the trigger reaction and ring closure. (See Section 8.6 on page 127.)



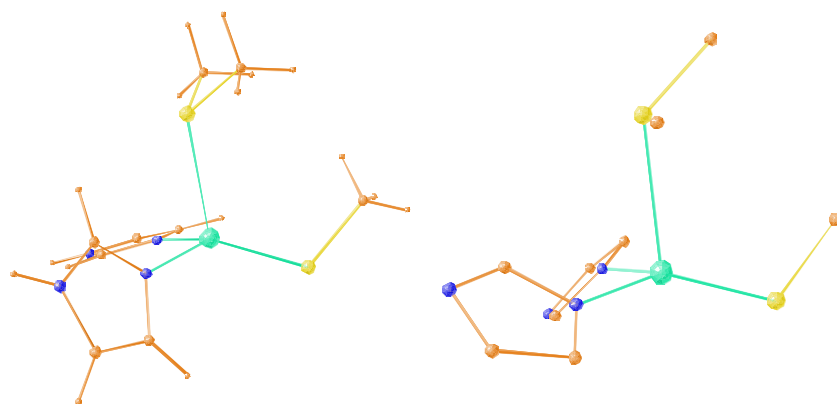


**Figure 2.24.** The optimized structure of  $[\text{Cu}(\text{imidazole})_2\text{SCH}_3\text{S}(\text{CH}_3)_2]^+$  (left) compared to the crystal structure of plastocyanin (right) [Guss *et al.*, 1992]. The theoretical structure has been optimized with the density functional B3LYP method. This close similarity between the two structures show that the trigonal geometry of the copper ion is not enforced by the protein [Malmström, 1994, Williams, 1995], but is an effect of the intrinsic chemical properties of the copper ion and its ligands. (See Section 8.7 on page 133.)

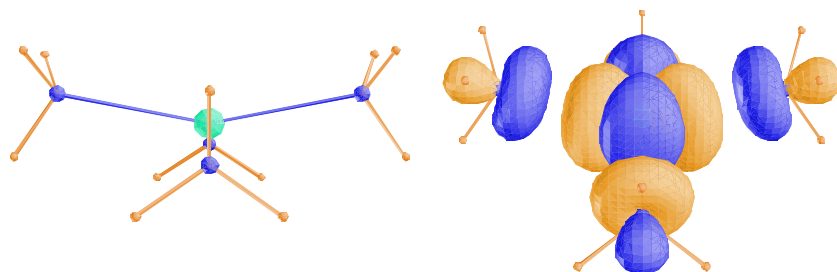


**Figure 2.25.** The optimized structure (left) and the singly occupied orbital (right) of  $[\text{Cu}(\text{NH}_3)_4]^{2+}$  in accordance with the ligand-field theory, the structure is slightly distorted square planar and all the four ligands from  $\sigma$ -bonds to the copper. (See Section 8.7 on page 133.)

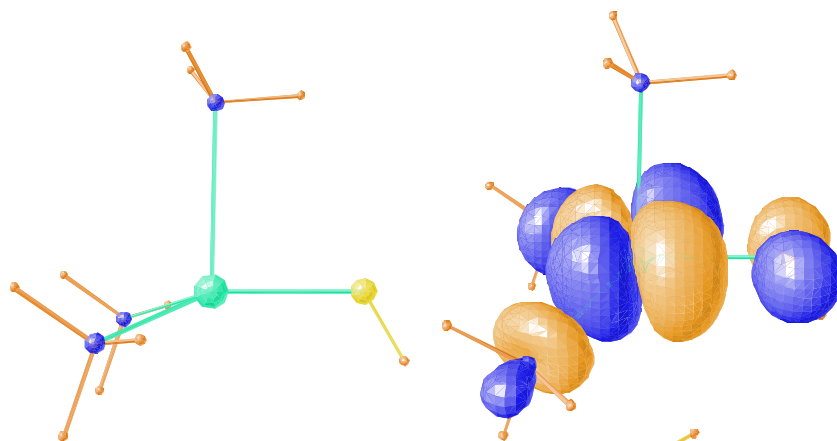


**Figure 2.26.** The optimized trigonal structure (left) and the singly-occupied orbital (right) of  $[\text{Cu}(\text{NH}_3)_3\text{SH}]^+$ . Two of the ammonia ligands form  $\sigma$ -bonds to the copper ion while the  $\text{SH}^-$  ligand forms a  $\pi$ -bond to the copper ion, which overlaps with two of the lobes of the Cu  $3d$  orbital, thereby occupying *two* ligand positions in a square coordination. (See Section 8.7 on page 133.)

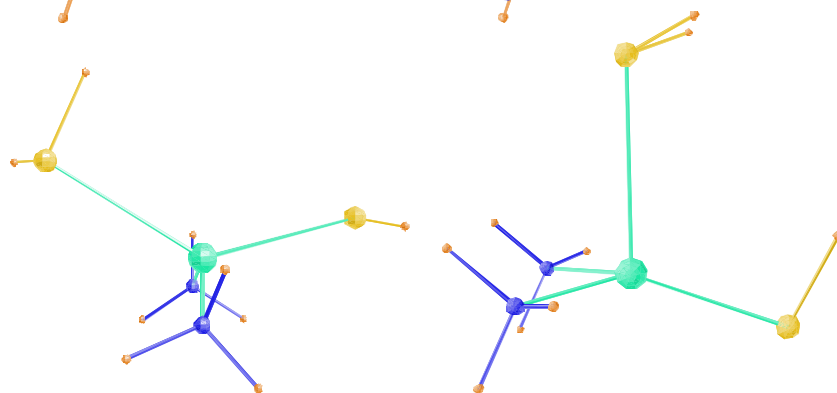


**Figure 2.27.** Two optimized structures of  $[\text{Cu}(\text{NH}_3)_2(\text{SH})(\text{SH}_2)]^+$ . The structure on the left is distorted tetragonal and the structure on the right is the trigonal. For this complex, the trigonal structure is the most stable in accordance with the structures found in the crystals of the blue copper proteins. The energy difference between the two structures is so low, however, that both structures may be occupied at ambient temperatures. (See Section 8.7 on page 133.)

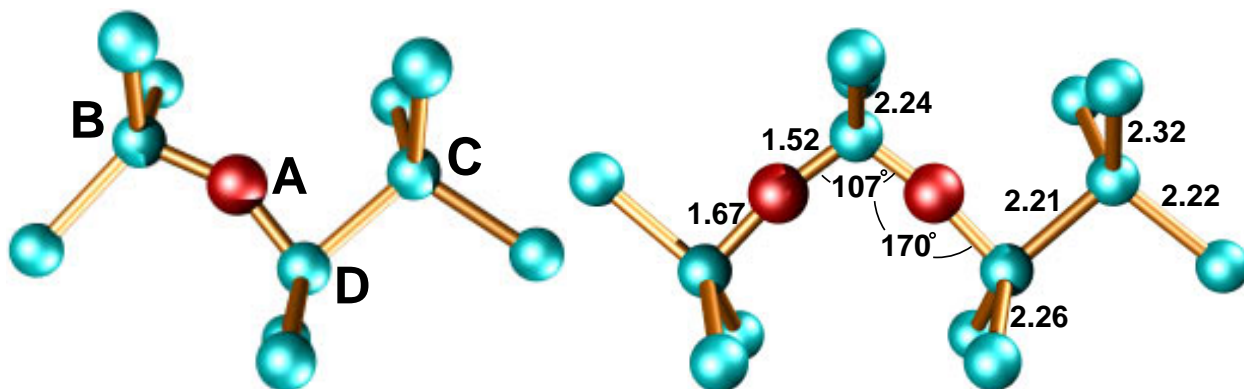


**Figure 2.28.** Interstitial oxygen,  $O_i$ , is shown on the left and the oxygen dimer,  $O_{2i}$  on the right, both in silicon. Symmetry axis lies along  $[100]$  and the O atoms are aligned along  $[011]$ . All lengths in Å. (See Section 6.13 on page 96.)

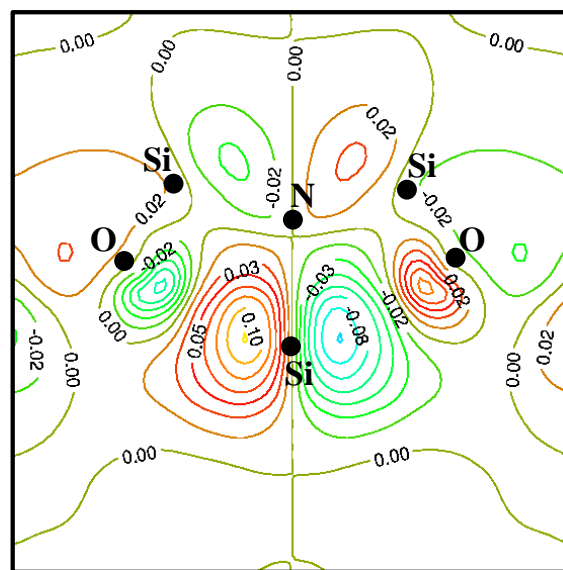
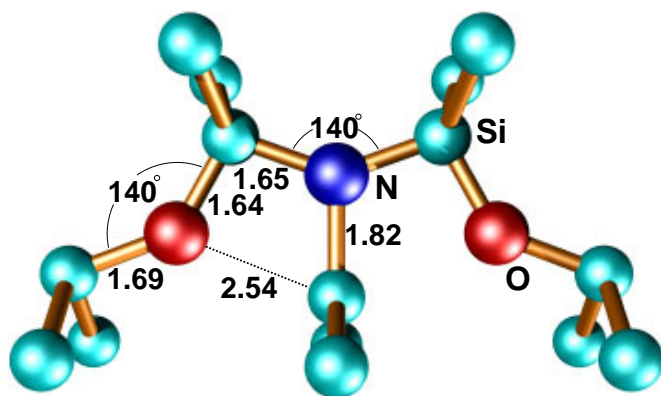


**Figure 2.29. Left:** The core structure of the neutral  $N_i-O_{2i}$  shallow thermal donor defect. The symmetry axis lies along  $[100]$  and the O atoms are aligned along  $[011]$ . All bond lengths are in Å. **Right:** The pseudo-wavefunction ( $\times 100$  a.u.) of the highest occupied orbital of  $N_i-O_{2i}$ . Note that it has little amplitude on N and is localized on the Si radical. There are nodal surfaces lying between this atom and the O atoms demonstrating anti-bonding behavior. (See Section 6.13 on page 96.)

## 3 Biology and Neural Modelling

### 3.1 Large Neural Network Simulations on Multiple Hardware Platforms

*Per Hammarlund, Tomas Wilhelmsson*

Department of Numerical Analysis and Computing Science, KTH

This section describes the SPLIT neural network simulation library; it highlights the techniques for implementing simulators for large biologically realistic neural networks on multiple hardware platforms [Hammarlund and Ekeberg, 1996]. SPLIT is a general purpose simulation library that takes as input a specification of the system to be simulated. The novel contributions of this work are general techniques for efficient simulation on a wide range of computer architectures.

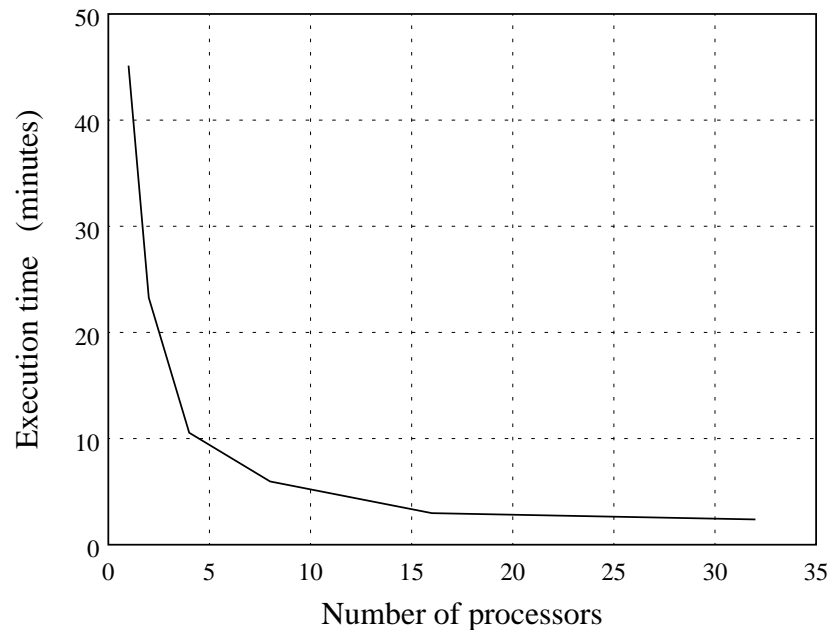
The performance of the SPLIT library is high on the supported architectures: CRAY PVP, clusters with MPI or PVM, shared memory machines with threads, and the IBM SP-2. For example, SPLIT for clustered systems parallelizes well and the speedup is quite good. Figure 3.1 shows the execution times using an IBM SP-2 for the simulation of a network with 2500 neurons and 127 000 synapses. To date, the largest simulations performed on the IBM SP-2 at PDC include a system of 58 000 neurons and over 4 million synapses. Simulating this system for 100 ms with a time step of  $50 \mu\text{s}$  on 8 processors took about 100 minutes while initialization took another 100 minutes.

The biologically realistic neural networks are sparse and unstructured at many levels. At the level of nodes in a network, different neurons have different shapes and different numbers of ion channels and other mechanisms. At the system level the neurons are, in unpredictable patterns, connected sparsely through synapses. To gain performance the structure of the networks should be exploited at all levels and at the same time no unnecessary restrictions on the different possible networks that can be simulated should be imposed. Here specification and representation techniques are used that allow the simulator to exploit network structure for groups of “similar” neurons and synapses. At the same time the user is allowed to create multiple groups with different structures. Apart from plain performance optimizations, the groups also allow implementation of techniques for limiting the memory requirements of large simulations.

Systematically, for optimizations and hardware particularities, the general is separated from the specific. Using object oriented programming and conditional compilation, the interfaces to data structures have been created such that the general parts of the SPLIT library can be programmed without consideration for the specific. The specific parts of the data structure representations and the computational optimizations

*To date, the largest simulations performed on the IBM SP-2 at PDC include a system of 58 000 neurons and over 4 million synapses*

**Figure 3.1.** Performance of SPLIT on IBM SP-2 when simulating a 2500 neuron and 127 000 synapses network.



*The implementation of the SPLIT library finds a balance between the convenience of object oriented programming at a high level and the necessity of performance oriented coding at the low level.*

are completely hidden. The implementation of the SPLIT library finds a balance between the convenience of object oriented programming at a high level and the necessity of performance oriented coding at the low level.

Using the techniques for separation of the general and specific, the library executes on multiple hardware platforms. The library has the same software interface on all platforms and a user is almost completely unaware of the target architecture specifics. The internal organization of SPLIT for shared and distributed memory systems is shown in Figure 3.2. Supporting multiple platforms protects the user's investment in the specification of a large and complicated simulation network. The supported hardware platforms have different performance characteristics and the simulation experiments have different requirements; a particular simulation experiment can use the most suitable available computer architecture.

The shared memory parallel version achieves high utilization of the available processors by limiting the overhead from using locks to synchronize the execution and the distributed memory parallel version achieves scalability by minimizing the communication time through the use of buffers in the communication routines, and by exploiting the structure, synaptic connectivity and delays, of typical simulation neural networks. Three different communication algorithms have been developed for distributed memory parallel machines. These communication algorithms have different characteristics and efficiently support a wide range of simulated systems and parallel systems.

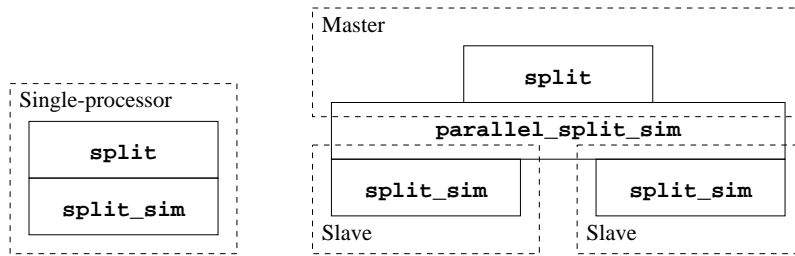


**Figure 3.2.** The internal organization of SPLIT for shared memory and distributed memory systems (clusters). The `parallel_split_sim` object takes care of the parallelism on distributed memory systems.

### 3.2 Neural Network Clustering and its Application in Remote Sensing

*Björn Levin*

SANS, Numerical Analysis and Computing Science, KTH

It has previously been observed (see, e.g. [Lansner, 1991]) that a recurrent Bayesian neural network [Lansner and Ekeberg, 1989] of the kind developed within the SANS project is capable of showing a clustering behavior. This is manifested in that training patterns sufficiently similar to each other create a common fix-point for the relaxation. In other words, when the relaxation is started in the trained network, with a pattern relatively close to either of the two training patterns, the result will in both cases be the very same output pattern. For this property to be practically useful, however, a method is needed of controlling the degree of similarity required for the clustering to occur. During the spring, summer and early autumn of 1994, the CM200 at KTH was used to perform a series of experiments evaluating ten different schemes of exercising such control. The basis of the implementation of the neural network algorithm came from the investigations into SIMD-parallelization reported in earlier PDC annual reports. The approach used in the new clustering experiments was to assign a virtual processor to each combination of starting pattern and value of the clustering parameter governing the similarity required for forming the clusters. When higher resolution than the number of processors was desired for the clustering parameter an automatically activated interval bisection scheme was implemented. Regarding the results, a strong advantage of three of the methods was observed. With the added motivation of being developed from an intuitive assumption of disturbances during learning, one of the schemes stood out as a clear winner. The underlying idea in this scheme is that, during training, the patterns occasionally get displayed simultaneously and then activate the union of units that would have been activated by each of the patterns taken by itself. The resulting clustering is by necessity somewhat noisy but with clear collection of the strong clusters.

Using the improved clustering, the investigations into the interpretation of satellite images were resumed during the autumn of 1994. A

new set of images was acquired, including a verified ground-truth and reference interpretation using a more conventional automated method. The two methods compared evenly regarding the reliability of the resulting classifications. However, it should then be noted that the more conventional method requires the manual selection of training areas and that the neural network method shows distinctly more promising results when part of the data of a measuring point is missing.

The results of both the above investigations are reported in the doctoral thesis by Levin [Levin, 1995].

### 3.3 Artificial Neural Networks for Modeling Airplane Pilot Dynamics

*Magnus Rosenlund*

SANS, Numerical Analysis and Computing Science, KTH

Artificial neural networks (ANN) seem to be more flexible and extendible than classical PID-regulators as models of airplane pilot dynamics. The purpose of modeling is multiple. At present the models are used, among other things, to estimate the flying abilities of different aircrafts. In the future the goal would be more automatic and better flying. Initially the interest is in simulating the dynamics of an airplane pilot in a landing situation and this task is accomplished by training an ANN with real flight data from several landings with a well known Swedish fighter aircraft. The problem that arises can be put as follows: Given a certain flight situation at times  $t-1$ ,  $t-2$ , ... how will the pilot react at time  $t$ ? The object would then be to use the ANN to predict the pilots behavior i.e. commands, from a time history of events that may have influenced him. The methods applied have mainly been developed at SANS under the guidance of Dr Anders Lansner and uses a Bayesian (probabilistic type) neural network with data represented using localized RBF-type functions. During these simulations it is common to partition the data into two sets called the training-data and the test-data. The ANN is then trained with the training-data, an operation making use of massive computer power since the amount of both data and processing becomes extensive by necessity. Now the ANN is used in purely feedforward style (no relaxation) to predict new values from training-data and test-data. The reason for this working scheme is manifold, but enables checking of the principal feature of interest, namely the ANN's ability to predict well from previously unseen data. Figures 3.3 and 3.4 show an example of simulation results (aileron angle) from a session using as training-data a set consisting of 21 landings and test-data consisting of one. Each graph regard either training-data or test-data, and represent one landing (randomly chosen in the case of training-data) in unchanged condition and the ANN's prediction of the same.

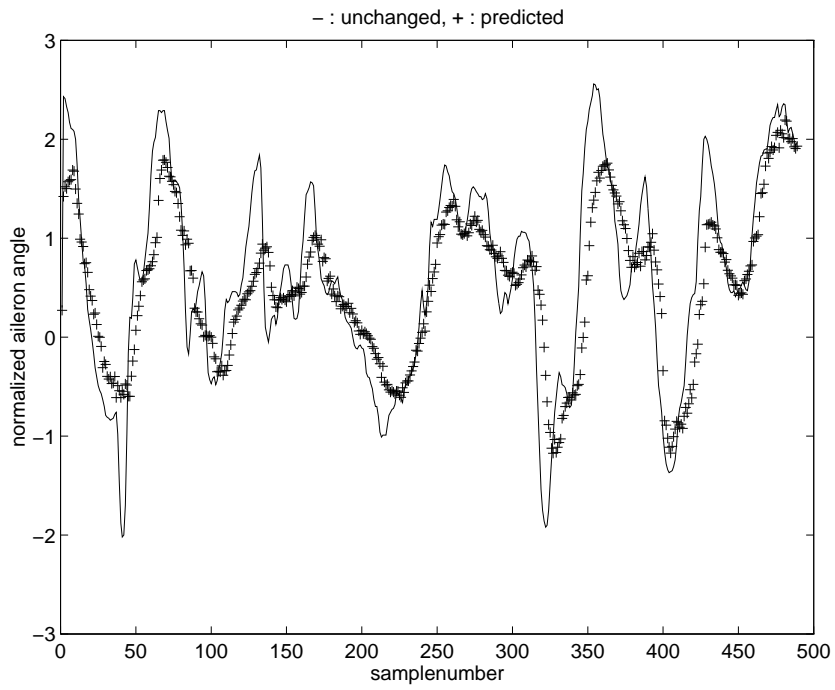


Figure 3.3. Training data.

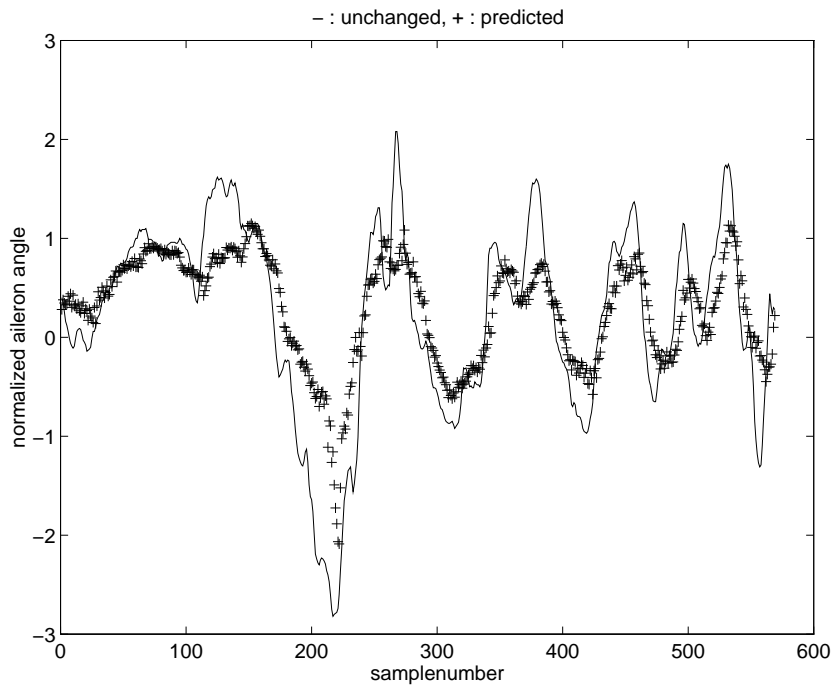
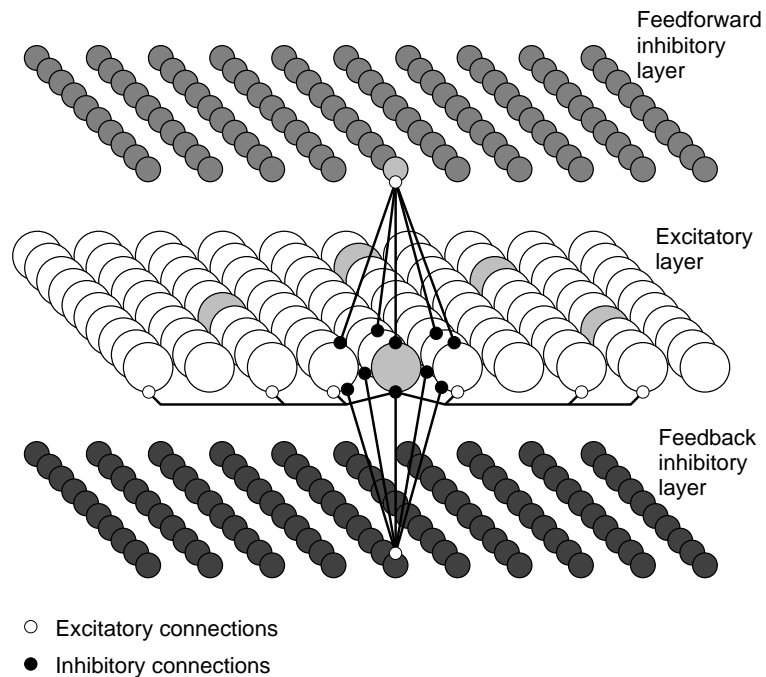


Figure 3.4. Test data.

**Figure 3.5.** The three layered network model used, mimicking the structure of the hippocampus or the olfactory cortex. The top layer consists of inhibitory “feedforward interneurons”, the middle layer of excitatory “pyramidal cells”, and the bottom layer consists of inhibitory “feedback interneurons”. Connections within the network are shown for the center front most unit of each layer. Excitatory (associative) connections are long range and sparse while inhibitory connections are local. Spontaneously active units are indicated. The model area corresponds to a  $10 \times 10$  mm square of the hippocampus of a rat.



### 3.4 A Neural Network Model of the Olfactory Cortex and Hippocampus

*Tomas Wilhelmsson, Hans Liljenström*

SANS, Numerical Analysis and Computing Science, KTH

We have implemented a model of the olfactory cortex, the “odor brain”, for large-scale simulations on the CM200 [Wilhelmsson, 1995]. This model is now being modified to fit data for the hippocampus, a brain structure associated with learning and memory. The objective is to investigate the biological significance of the complex neurodynamics of a cortical structure, in particular with respect to perception, learning and associative memory [Liljenström, 1995].

The model complexity lies between that of abstract Hopfield nets and more biologically detailed simulations with spiking, compartmentized network units. Network units correspond to populations of cells (neurons) with a continuous (sigmoid) input–output relation, describing pulse density characteristics. The organization and connectivity of the model is illustrated in Figure 3.5. Connection weights are adaptive and under neuromodulatory control to allow for learning and associative memory to be studied. In the current simulations, we simulate a  $10 \times 10$  mm square area of the hippocampus of a rat.

Previous simulations, using workstations, have shown that this model is capable of reproducing the essential characteristics of experimentally

*We simulate a  $10 \times 10$  mm square area of the hippocampus of a rat*

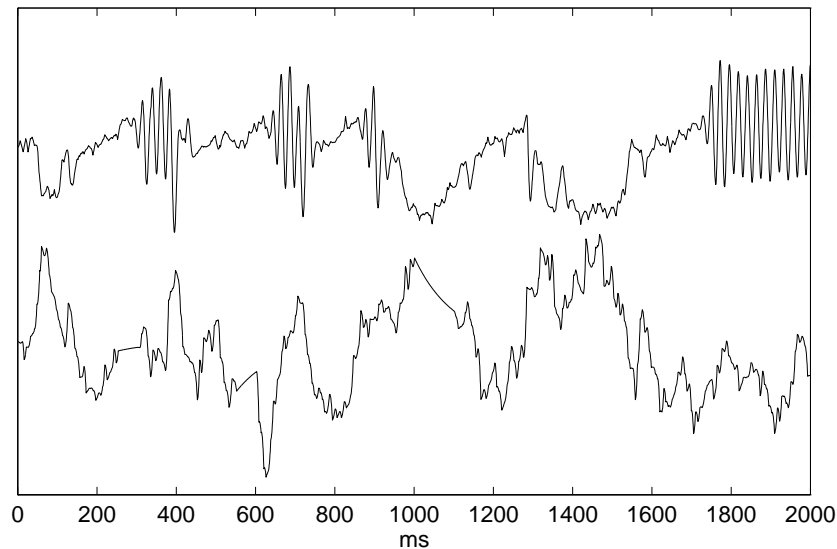


**Figure 3.6.** Global oscillatory behavior induced in the excitatory network layer by noise in a single (feedforward) inhibitory unit. Simulations are run on the CM200 with  $32 \times 32$  network units in each of the three layers. Here the activity of an excitatory network unit (top) and of the noisy inhibitory unit (bottom). This shows that spontaneous disinhibition (possibly caused by inhibitory neuronal random generators) can result in synchronized oscillatory activity in the excitatory layer.

observed and previously simulated dynamic behavior of the olfactory cortex [Liljenström, 1991]. These earlier simulations were made with  $10 \times 10$  network units in each layer. Using the 16K CM200 with 2 Gbyte main memory, we are able to simulate systems with up to  $128 \times 128 \times 3$  units and more than 100 million connections. Networks with  $64 \times 64 \times 3$  units are conveniently simulated in less than one second per integration step. The much higher processing speed of the parallel implementation makes it possible to run large simulations in minutes instead of hours, which is crucial when tuning model parameters.

With the current parallel implementation we get a better spatial resolution, reaching the limit for a population representation with each network unit corresponding to the order of a hundred neurons. The larger number of network units and connections also reduces unwanted boundary effects. Further, we can more effectively study local effects and the balance of excitation and inhibition due to network circuitry. Effects of local noise generators or oscillators with various intrinsic frequencies can now be studied in a large system of active and oscillating units. For example, it can be shown that a few noisy elements are capable of inducing global oscillatory behavior in the entire network, see Figure 3.6 and Figure 2.2 on page 11. Based on experimental evidence, we have shown that spontaneous disinhibition of single inhibitory elements can result in synchronous oscillations in thousands of excitatory network units. In the future, we also intend to study how external driving forces interfere with the intrinsic system oscillations. Finally, we will investigate the memory efficiency of this model network, where the much larger systems that now can be simulated allow for many more sparse or dense patterns to be stored in the network connections.

*49 000 units and more than  
100 million connections*

### 3.5 Analysis of 3D Brain Data

*Sebastian Åkerman*

Department of Neuroscience, Karolinska Institutet

Functional brain-imaging methods, such as Positron Emission Tomography (PET) used for measurements of the regional cerebral metabolism or the regional cerebral blood flow, sample data from more than 125 000 parts of the brain, see Figure 2.4 on page 12. The PET-technique suffers from low signal to noise ratio (SNR) in investigations of human subjects. The abundant noise in PET images calls for thorough investigations on noise behavior. Performing noise simulations on images from PET require computations for a massive amount of data that can only be accomplished by high performance computers, like the CM200.

*Computations for a massive amount of data that can only be accomplished by high performance computers*

We have performed a series of simulations to study the effects of noise on different detection schemes to be used in the analysis of PET images. By simulating 1000 re-runs of the same experiment using distribution data from a group of human subjects in the control state, i.e. a state in which the brain is not engaged in a particular task, it was possible to generate empirical distributions of false positive activation events.

The simulations have been repeated for different image subtractions to investigate the effect of physiological noise. Comparing the result of the original simulation of the physical noise, i.e. noise caused by the imaging technique, with the simulation of physiological noise and normal test situations provide hints on how to set thresholds in our normal test images as to achieve a certain probability for false positive activations.

The simulations were done in several steps. First the CM200 was used to investigate the spatial 3D autocorrelation function in a sample of regional cerebral blood flow images. This function was then used to generate a 3D filter that imposes the found autocorrelation in subsequent simulated images. Finally, to get the desired accuracy in the estimations, tens of thousands of randomly generated images having the correct statistical properties were analyzed and false positive events were recorded. In each such generated image around 1 000 000 values mimicking measurements of biochemical and physiological variables in the brain are generated simultaneously, making the task very well suited for analysis by data-parallel computing.

FFT-techniques were used to calculate autocorrelations and filters for the sample generation phase. For the wide autocorrelation functions of the physiological noise and tested activation FFT-based filtering proved essential for efficient generation of the numerous samples needed in the simulations.

Future simulation include another simulation run for a new PET-camera with higher resolution as well as simulation of overlapping activation clusters from different test groups. Overlapping clusters are defined as groups of clustered activations from different images that have one or more points of activation at corresponding positions.

# 4 Computational Electromagnetics

## 4.1 2D Computational Electromagnetics on the CM200

*Ulf Andersson, Gunnar Ledfelt*

Center for Computational Mathematics and Mechanics, KTH

Computational Electromagnetics (CEM) has recently become a field of significant interest. The reason for this is that the understanding of electromagnetic phenomena becomes crucial as electronic devices become more complicated and integrated and hence more vulnerable to external fields. A striking example of this are the restrictions on the use of cellular phones in airplanes.

As even our daily life becomes more dependent on electronics the issue of electromagnetic compatibility, i.e. how to avoid undesired interferences, is ever more important. Who will buy a car if it is known to lose control close to radio transmitters?

Today most of the data in electromagnetic compatibility comes from measurements and experiments but it is desirable to use numerical methods to supplement or replace these costly experiments. The computational burden of simulating the electromagnetic phenomena important to these issues is very heavy. Only computers with Gbytes of memory and Gflop/s performance are capable of solving realistic problems.

The analysis of wave propagation can be carried out in the *time domain* or in the *frequency domain*. In the area of electromagnetic compatibility there is a great potential for time domain methods such as the method presented here. If the frequency response is still desired the results of a transient calculation can be postprocessed by a Fourier transform giving results for multiple frequencies.

Time integration with explicit methods is well suited to massively data-parallel computers since the PDE is a model for local interaction. When discretized by a structured (finite difference or finite volume) grid, the data can be mapped to the CM architecture and requires communication only between nearest neighbors. Indeed one of the code variants runs at almost 50% peak speed of the CM200.

Another benefit of time-domain techniques in CEM is that they can take advantage of the software technology developed for Computational Fluid Dynamics (CFD). The Maxwell equations (see below) are a hyperbolic system of equations just like the Euler equations of fluid dynamics. It is therefore possible to take algorithms developed for the Euler equations and use them to solve (4.1).

*Only computers with Gbytes of memory and Gflop/s performance are capable of solving realistic problems*

For a transverse electric field in an isotropic, conducting medium in 2D the Maxwell equations can be written as

$$\begin{cases} \frac{\partial}{\partial t} E_x = \frac{1}{\epsilon} \frac{\partial}{\partial y} H_z - \frac{\sigma}{\epsilon} E_x \\ \frac{\partial}{\partial t} E_y = -\frac{1}{\epsilon} \frac{\partial}{\partial x} H_z - \frac{\sigma}{\epsilon} E_y \\ \frac{\partial}{\partial t} H_z = -\frac{1}{\mu} \frac{\partial}{\partial x} E_y + \frac{1}{\mu} \frac{\partial}{\partial y} E_x \end{cases} \quad (4.1)$$

where  $\bar{E} = (E_x, E_y, 0)^T$  is the electric field,  $\bar{H} = (0, 0, H_z)^T$  is the magnetic field,  $\sigma$  is the conductivity,  $\epsilon$  is the permittivity and  $\mu$  is the permeability.

We have developed a Finite Volume method based on central differences and time discretization with a three stage Runge-Kutta method. This is second order accurate in both space and time for regular grids. The code has been tested on a series of cases and compared with other approaches in a European CEM project [Andersson and Ledfelt, 1995].

With outer boundary conditions simulating conducting walls, modeling e.g. the field inside a metal container, the code runs at an astonishing speed of 2.5 Gflop/s. But in exterior problems where there is no physical outer boundary the computational domain must be truncated. The infinite exterior of the computational domain is simulated by an Absorbing Boundary Condition (ABC) which must be transparent for waves propagating towards the boundary from within. At the same time the ABC must allow waves to enter the computational domain. This is achieved by modifying the Maxwell equations near the outer boundary and is described in detail in [Gradin and Ledfelt, 1995]. Using an ABC reduces the performance of the code by a factor five mainly due to the implementation of the source term. We estimate that this could be substantially improved by a more careful implementation of the ABC.

The FLOP/s-rates are taken from calculations with  $4096 \times 2048$  cells in single precision which is the maximum problem size that fits into the 2 Gbyte primary memory of the CM200. For every test case so far single precision has proven to be sufficient.

Figure 2.5 on page 13 shows an electromagnetic pulse that strikes a cavity with a thin slit. The main question is how strong the field will be inside the cavity. The opening in the cavity must be sufficiently resolved in order to capture the physics and guarantee that the numerical method predicts a correct solution.

*The code runs at an astonishing speed of 2.5 Gflop/s*

# 5 Computational Fluid Dynamics

## 5.1 A Parallel CFD Project at C2M2

*Magnus Bergman*

Center for Computational Mathematics and Mechanics, KTH

The C2M2 project on Parallel CFD was supported from its start in 1990-91 by the NUTEK Super- and Parallel Computing Program. During the two first years the work was mainly directed to the efficient data-parallel implementations of multi-block flow solvers using the PDC Connection Machine CM200 as main target architecture. This work [Sawley and Bergman, 1994] has been widely published and still continues at EPFL as described in Section 5.4.

During 1993-94 work has been focused on the use of workstation farms with fast network switches for industrial multi-block CFD computations. The work has been supported by FOA and DEC who contributed with a workstation farm consisting of three 133MHz DEC Alpha with FDDI interface and a 3.6 Gbit/s DEC GIGAswitch. The CMB code has been rewritten using the PVM message passing library to parallelize on farms of workstations and tightly coupled MIMD machines [Bergman and Sawley, 1993]. A software layer, CCL, has been developed [Fristedt and Bergman, 1994] that gives portability between different machines and efficiency using native communication libraries. An efficient scheduler for load balancing of these multi-block meshes for MIMD machines has also been developed [Özen, 1993, Ljungquist *et al.*, 1993]. The work continues as two different projects, one ESPRIT funded project extending the software to handle 3D multi-block meshes, and one project in collaboration with Uppsala University to develop a dynamic load-balancing procedure for MIMD machines. Furthermore many different tools for the usage of workstation farms has been installed and tested. For example the LSF software that can distribute UNIX commands to idling resources on the farm.

The usage of workstation farms has been followed with interest from Swedish industry. In particular from ABB Corporate Research, Volvo Data and Saab Aerospace for which we have presented several benchmarks together with some measurements of the throughput of the GIGAswitch. In particular of interest is the maximum channel bandwidth, the network latency and the total throughput of the system. A large effort has been made in reducing the latency since it was found to be the most important factor in reducing performance. This work was quite successful and the low latency routines are now being implemented into the CCL library.

**Table 5.1.** A farm of Sun 10 workstations with Ethernet connection running a test case of a mesh around the mid section of a car with 16 equally sized blocks. The number of workstations ranged from 1 to 16 and grids ranging from one thousand to one million points. High efficiencies was obtained except for the smaller grid systems. Performances above 100 Mflop/s using 16 Sun 10 workstations was also obtained.

N	log <sub>2</sub> (N)	1	2	4	8	16
1024	10	1.27	2.05	3.75	6.1	9.69
2048	11	2.18	3.68	7.33	13.0	21.6
4096	12	3.55	6.70	12.9	24.3	42.6
16384	13	5.13	10.2	20.2	39.6	72.4
65536	14	6.3	12.6	25.0	49.2	95.4
262144	15	4.55	13.7	27.6	56.0	100.1
1048576	16		14.5	56.4	101.8	

## 5.2 Homogeneous and Heterogeneous Distributed CFD Computations

*Magnus Bergman, Erland Fristedt*

Center for Computational Mathematics and Mechanics, KTH

*Mark Sawley*

IMHEF, EPFL, Switzerland

The interest of the work here is to use networked computers to solve large CFD problems. The study includes both the usage of identical workstations (homogeneous farm) and a mixture of different computer architectures (heterogeneous farm). The former work, described in detail in [Bergman and Sawley, 1993], concerns the usage of Sun 10 workstations with Ethernet connection. As a test case a mesh around the mid section of a car with 16 equally sized blocks was used. A large number of runs was made in order to get the full behavior of the workstation farm as a computational resource. The number of workstations ranged from 1 to 16 and grids ranging from one thousand to one million points. This large number of test cases gives the possibility to study effects like Amdahl's and Gustafsson's laws and so called super-linear speed-ups. High efficiencies was obtained except for the smaller grid systems. Performances above 100 Mflop/s using 16 Sun 10 workstations was also obtained. See Table 5.1.

Furthermore a series of heterogeneous CFD computations was done using of different workstations (SGI, DEC Alpha, HP 700 series) together with a vector computer, a single processor CRAY Y-MP. As a test case a mesh around a wing profile with an extended flap was used. The mesh comprised of 16 blocks of different sizes ranging from some hundred points to 8000 points. Load balancing was done by means of a simple algorithm that sorts the machines in order of processing power (performance was tested by running a test problem with 4000 grid points). The blocks are then assigned to processing nodes starting with the largest block until each machine exceeds its relative performance. Several test runs during different times of the day showed that the computational time could be reduced by a factor of 2 compared to a single processor CRAY Y-MP. An extensive description of the work can be found in [Bergman and Sawley, 1993].

Kernel	Total time Alpha farm	Communication time	Total time CRAY Y-MP
The EP Kernel	414	NA	126
A 3D Multigrid Solver	212	20	22
Conjugate Gradient	69	15	12
Integer Sort	89	45	11
3D FFT	238	NA	29

**Table 5.2.** Timings of a PVM version of the NAS benchmarks running on a cluster consisting of four DEC Alpha model 500 (200 MHz) and a GIGAswitch.

### 5.3 The NAS Parallel Benchmarks on a DEC Alpha Farm

*Erland Fristedt, Magnus Bergman*

Center for Computational Mathematics and Mechanics, KTH

*Magnus Persson*

Digital Equipment, Sweden

The NAS parallel benchmarks are a set of applications that emulates real CFD-codes. The NAS benchmarks includes both data-movement and computational characteristics and has therefore been widely used for benchmarking of parallel machines. The work below is an effort in order to test workstation farms for a wider range of CFD applications. The work was started by Anders Ålund at ITM who ported the NAS benchmarks from the serial and Intel versions [Ålund and Sunderam, 1993] to PVM (Parallel Virtual Machine) message-passing library. This version was tested using four DEC Alpha model 500 (200 MHz) farm and a GIGAswitch.

The NAS benchmarks was implemented with a modified PVM, which have better performance then the original version. Both latency and bandwidth has improved, latency has decreased from 1.5 to less than 1 millisecond and the bandwidth has increased from 15 Mbit/s to about 70 Mbit/s on DEC Alpha model 500. The observed timings on Alpha's are compared with other workstation farms and a CRAY Y-MP using an identical program. See Table 5.2.

The performance of this applications are rather disappointing. This is described in [Fristedt and Bergman, 1994]. The communication time is too large compared with total time which will reduce the scalability of the codes. This is mainly due to the fact that communication in this benchmark is frequent and relatively low-volume meaning that the network latency is determining the achieved performance and scalability. It is important observations that this version of the NAS benchmark was developed for the CRAY computer leading to bad performance on the workstation also on the nonparallel parts. We have tried the KAP preprocessing tools on the DEC Alpha in order to adapt the code to the size of the cache, etc. This did not improve the performance and we will continue to investigate this in order to find an appropriate tools for code rearrangement and optimization.

One critical point is that PVM uses standard network protocol (i.e. TCP/UDP/IP); these are unsuitable for scalable parallel computing. We have tested latency and bandwidth using standard network protocols giving latencies of 256 microseconds and maximum bandwidth of 96 Mbit/s. Further optimization of the PVM software is therefore necessary to reach high performances of the NAS benchmarks on workstation farms. A more complete report on the testing will be given at the end of the DEC/FOA/KTH project [Fristedt and Bergman, 1994].

#### 5.4 Parallel Programming Models for Multi-block Flow Computations

*Mark Sawley, Jon Tegnér*  
IMHEF, EPFL, Switzerland

Block structured computational meshes exhibit both a coarse-grain parallelism at the block level, and a fine-grain parallelism at the mesh point level. For efficient parallel computation, the granularity of the problem needs to be matched to that of the parallel computer employed.

In the present work, the time-dependent Euler equations for inviscid, compressible flow in 2D geometries are resolved. The equations are discretized in space using a finite volume formulation, using central differencing with added artificial dissipation. An explicit five-stage Runge-Kutta scheme is used to perform the time integration. To enhance convergence to the required steady state, a local time stepping technique is employed.

Initial studies using the parallel computer systems at PDC employed fine grain parallelism, which is appropriate for both the CM200 and MP-1 systems. It was found that the data parallel programming model provides a convenient means to resolve the flow equations. In addition, high performance levels and good scalability with the number of processing elements (PEs) employed can be achieved. Multi-block flow computations have been undertaken using a serial data-parallel multi-block method, whereby individual blocks are treated in a sequential manner, the solution in each block being computed using a data parallel approach [Sawley and Tegnér, 1994].

For the IBM SP-2 system, which has a much smaller number of processors, coarse-grain parallelism is more appropriate. For multi-block computations, this is implemented in a straightforward manner using what is sometimes termed a “control parallel” method. Here, the flow in different blocks is computed in an independent manner on different processors. The necessary exchange of data between the neighbouring blocks (block connectivity) is undertaken using message passing. Both the PVM and MPI libraries have been implemented in the code for computation on the SP-2.

Apart from the level of granularity, there is a number of other differences in the above two approaches [Sawley and Tegnér, 1995]. Firstly, while Fortran 90 based languages were necessary to run the data parallel code on the CM200 and MP-1 systems, Fortran 77 was employed for the control parallel code on the SP-2. Adhering to these language standards has shown to provide good code portability: the data parallel code has been run with only minor modifications on CM5 and CRAY T3D systems, while the control parallel code has been used on an Intel Paragon, CRAY T3D, NEC Cenju-3 and workstation clusters. Secondly, load balancing issues differ for the two approaches. For the data parallel method it is desirable to have the number of mesh cells (plus “ghost cells”) in each block a multiple of the number of PEs. Since the blocks are treated in a sequential manner, an equal number of mesh cells in each block is not required. For the control parallel method, for which the blocks are computed in parallel, the number of cells in each block should be equal. This may in some cases impose considerable constraints on mesh generation. Finally, the communication is implicit for the data parallel method. While the explicit message passing used for the control parallel method provides more programmer control, this is generally not required for multi-block flow computations, and leads in a greater probability of coding errors.

Timing results have shown that high performance levels can be obtained on the SP-2 using the control parallel method. This is a consequence of both a high single processor performance and the relatively low level of communication required for block connectivity. Due to this low level of communication, the performance of the flow solver has been found to scale linearly with the number of processors used on the SP-2 system at PDC.

## 5.5 Adapting a Regional Air Pollution Dispersion Model for MasPar and CM200

*Tomas Wilhelmsson*

Department of Numerical Analysis and Computing Science, KTH

*Joakim Langner, Lennart Robertson*

Swedish Meteorological and Hydrological Institute, Norrköping

A large part of the services generated at the Swedish Meteorological and Hydrological Institute (SMHI) is based on the output from numerical models. The single most important model is the numerical weather prediction (NWP) model HIRLAM (High Resolution Limited Area Model) [Källberg, 1989] which generates routine forecasts over Europe of up to 48 hours. Several other numerical models are closely linked to HIRLAM. One of these is the MATCH model (Mesoscale Atmospheric Transport and Chemistry) [Persson and Robertson, 1990]. MATCH can generate distributions and depositions of various pollutants based on meteorological data from e.g. HIRLAM. Computing resources put a limit on

the amount of complexity that can be included in these types of models. It is therefore of great interest for SMHI to explore the possibilities of parallel computer architectures which are now becoming available in order to make increasing computing resources accessible in the future.

MATCH is an Eulerian atmospheric dispersion model. The basic model treats the physical processes (horizontal and vertical advection and diffusion) governing the atmospheric transport of an arbitrary number of chemical components. Depending on the application, different modules describing emissions, chemical interactions, and removal can be added to the basic model. MATCH is an off-line model meaning that it reads the meteorological data necessary to drive the transport and other modules from external archives. The model is coded to be very flexible with respect to the geometry of the input data and caters for the most commonly used horizontal and vertical grid structures. A typical grid used in an operational emergency response application of the model is shown in Figure 5.1.

At present the horizontal advection is calculated using a fourth order integrated flux scheme [Bott, 1989a, Bott, 1989b]. This scheme utilizes polynomial fitting between neighboring gridpoints of a discrete integrated concentration field in order to simulate the advective fluxes through the boundaries of adjacent grid boxes. It is a positive definite mass conserving scheme with low numerical diffusion which is necessary in air pollution applications. For the vertical advection a second order version of the scheme is used.

#### *Adapting MATCH for parallel processing*

The MATCH model code available at the beginning of the project was written in Fortran 77 and used a linear memory model. It was first recoded (still in Fortran 77) following conventions for scalable programming [Thi, 1993]. This made the code more portable to other kinds of computer architectures as well.

Since the parallel computers readily available for the project were of SIMD type (Connection Machine CM200 and MasPar MP-1 and MP-2) the adaption of the code was done using the data parallel programming model. The strategy chosen was to use the MasPar supplied VAST translator which vectorizes Fortran 77 DO-loops to Fortran 90 array syntax. Major parts of the translated code ran efficiently from the beginning. However, in some cases compiler directives and restructuring of the Fortran 77 code was necessary in order to generate efficient Fortran 77 code. The MasPar VAST translator gave much better code than TMC's CMAX translator so it was used also for generating code for CM200.

The horizontal dimensions of the model is mapped to the processors organized in a two-dimensional grid thereby keeping the vertical dimension locally in each processor. Both parallel platforms showed some peculiar behavior with regard to the mapping of arrays onto the pro-

*Used in an operational  
emergency response application*

*Major parts of the translated  
code ran efficiently from the  
beginning*

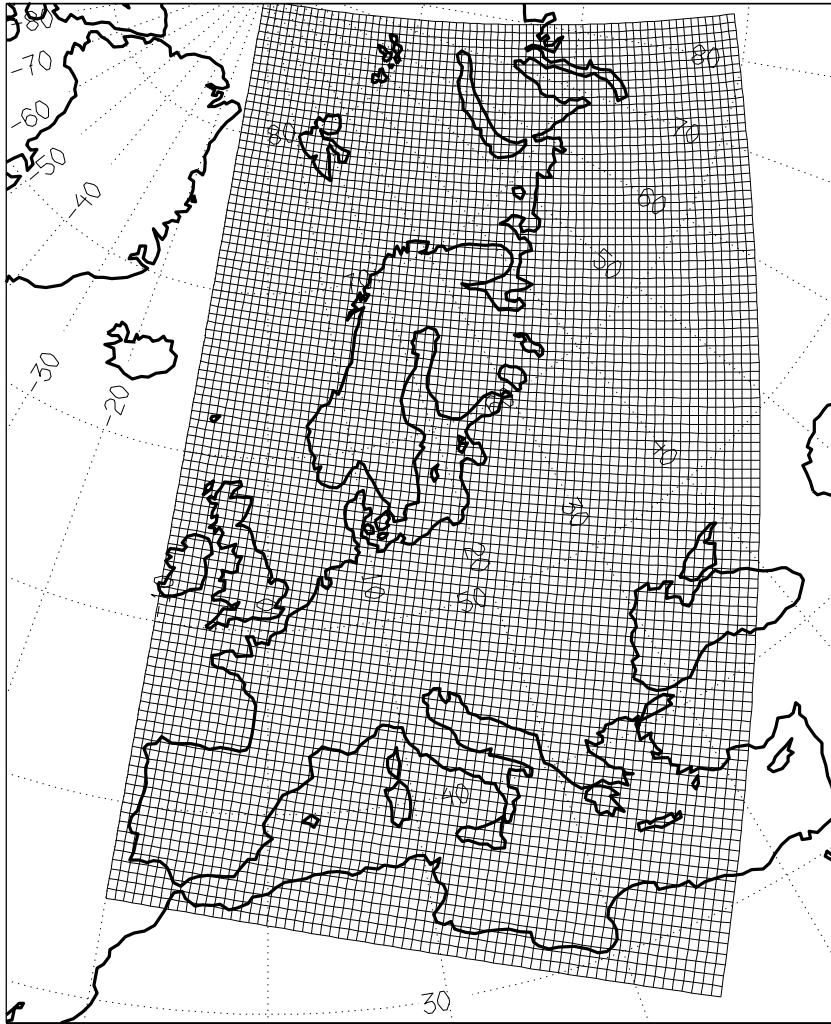


**Figure 5.1.** Modeling domain used in an operational emergency response application. The grid is 68 by 108 gridpoints at 55 km horizontal resolution and is a part of the operational HIRLAM grid at SMHI.

processors. The CM200 compiler required that the dimension kept locally in each processor should come first in the array declaration in order to generate efficient code. A set of `awk` scripts was used to rotate all array indices when compiling for the CM200. The MasPar compiler on the other hand, generated a code that was twice as fast if all array dimensions were fixed at compile time. This problem was solved by including a file with parameter statements for all array dimensions when compiling for MP-1 and MP-2. This of course had the disadvantage that recompiling was necessary when changing the size of the model domain. The CM200 on the other hand ran efficiently with array bounds dynamically set at runtime.

### *Adaption of the GRIB I/O library*

Input meteorological data and output fields are stored in a binary packed format called GRIB (Gridded Binary). This format contains, besides the data field, packing parameters and information about the geometry of the data (projection, resolution etc. ). GRIB is a standard used in meteorological applications and a full implementation of the model therefore requires an efficient implementation of GRIB-based I/O. The simplest thing to do is just to run the GRIB I/O routines serially on the front end and communicate the unpacked data to the parallel processors. This means however, that the time spent on I/O becomes a dominating fraction of the total execution time. In order to improve efficiency the following strategy was used: 1) read the GRIB record from disk on the front end. 2) unpack the parts of the GRIB record containing the descriptive information and packing parameters on the front end. 3) communicate the packed data field to the processor array. 4) unpack the data locally on each processor. Storing works the other way around. This strategy gives less communication since data is sent in packed format and enables the unpacking to be performed in parallel.

### *Timing and profiling*

A number of test runs have been carried out on different platforms using the recoded Fortran 77 version on workstations and the Fortran 90 version on the parallel machines. All test runs were performed using meteorological data from HIRLAM to drive the transport.

The table below summarizes the results for a horizontal grid covering about the same area as the operational HIRLAM model run at SMHI but with twice the horizontal resolution. Times are in minutes for a 51 hour forecast using a 5 minute timestep. The modeling domain is 241 by 241 gridpoints at 22 km horizontal resolution and has 16 layers between the surface and about 25 km. The simulation requires 265 Mbytes of memory. Input data is read every 3 hours and output is stored every 1 hour. Figures 2.6 and 2.7 on pages 14 and 15 illustrate the simulation output.

Machine	Configuration	Time (min)	Advection (%)	I/O (%)
MasPar MP-2	16K processors	35.7	61.5	26.8
MasPar MP-1	16K processors	46.4	73.2	12.7
MasPar MP-1	8K processors	82.9	77.2	7.8
TMC CM200	512 processors	29.8	55.7	36.0
TMC CM200	256 processors	52.5	43.6	17.5
DEC Alpha	1 proc., 175 MHz	378.0	76.0	2.0

The 512 processor CM200 is fastest and computes a 51 hour simulation in 30 minutes while the simulation on MP-2 takes 36 minutes. The parallel platforms are about 12 times faster than the DEC Alpha workstation for this particular problem. Most of the execution time is spent in the advection part of the model on all platforms. On the parallel machines I/O is second in importance and constitutes a significant fraction of the total execution time. The fraction of time spent on I/O is much smaller on the workstation, but is similar in absolute numbers.

For MP-1 and CM200 the simulation has been run on different number of processors in order to investigate scalability of the code. The parallel efficiency (defined as the achieved speedup divided by the theoretical speedup) is very similar on the two platforms. It is 88% when going from 256 to 512 processors on CM200 and 89% when going from 8K to 16K on MP-1. On both CM200 machine sizes, 14% of the execution time is spent on communication.

### *Conclusions*

The MATCH dispersion model has been successfully implemented on two different parallel platforms using the data parallel programming model. The implementation required a major recoding of the original model to replace the linear memory model with a memory model suitable for distributed memory systems. Once recoded the porting of the code to run on the parallel platforms was relatively straight forward using the VAST translator to translate from Fortran 77 to Fortran 90. All changes to the code were done in the Fortran 77 version of the code in order to maintain a portable code.

The parallel platforms were about 12 times faster than the DEC Alpha workstation presently used in operational applications on the test case. So far however, no efforts have been made to optimize the cache usage on the workstation. Although a major increase in I/O performance was achieved by parallelizing the unpacking of binary GRIB records, I/O represented a significant fraction of the execution time on the parallel platforms (8% to 36%) while only 2% of the execution time was spent on I/O on the workstation. The available timings for executing the test runs on different number of processors indicate a good efficiency for both MasPar and CM200 when increasing the number of processors.

*The MATCH dispersion model has been successfully implemented on two different parallel platforms*

## **5.6 Numerical Simulation of Fully Developed Turbulent Plane Couette Flow**

*Jukka Komminaho, Anders Lundbladh, Arne Johansson*  
Department of Mechanics, KTH

Fully developed turbulence in plane Couette flow is studied by means of direct numerical simulation. Experience has shown that this is a particularly difficult case to study because of a tendency to develop extremely

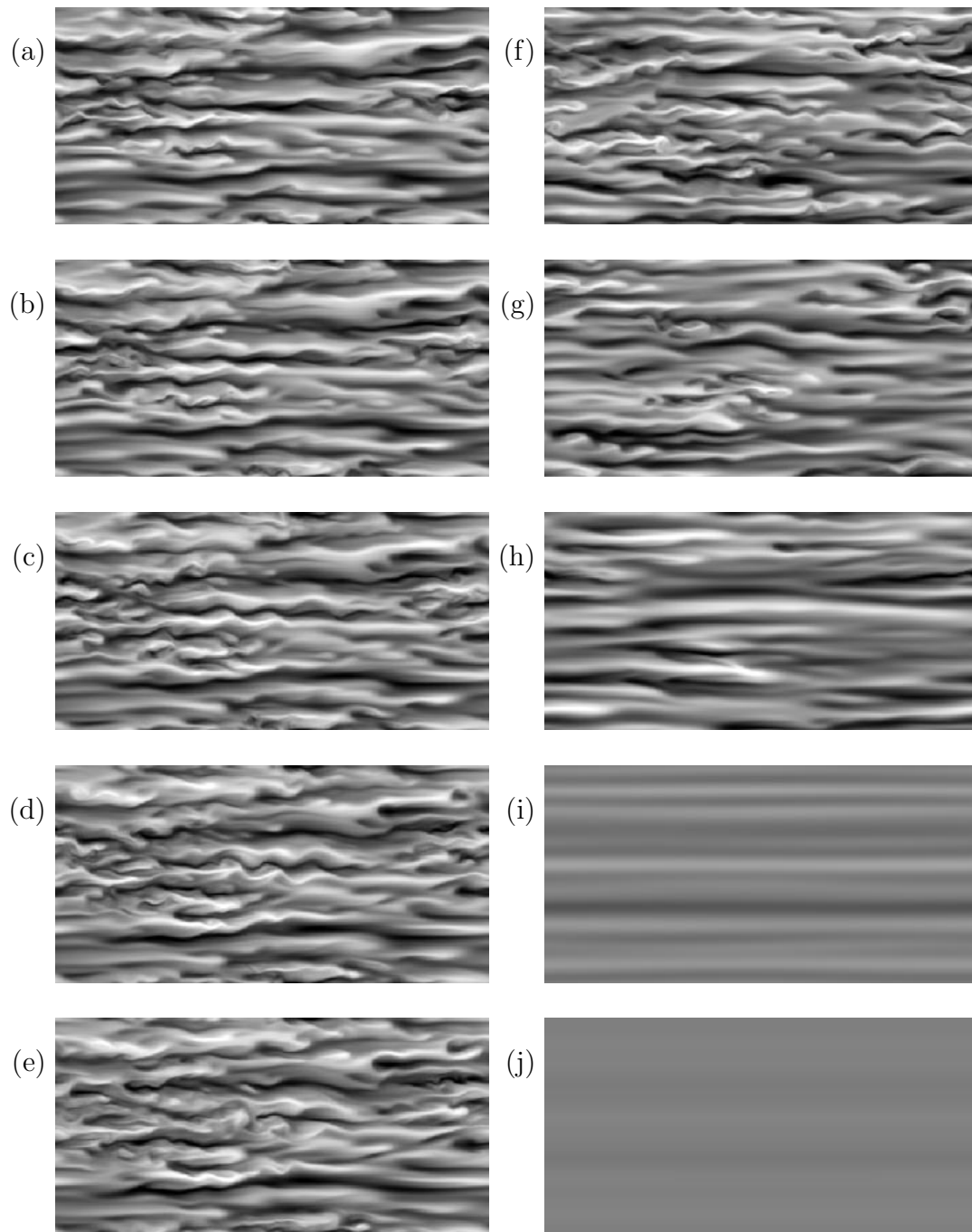


**Figure 5.2.** A grey scale coding of the streamwise velocity component in the midplane between the two walls moving in opposite directions. The relaminarization process at  $Re = 350$  is here depicted at a number of consecutive times (here marked by a-j).

long vertical structures aligned in the streamwise direction. For a numerical simulation study an extremely long (and also rather wide) box is needed, almost 90 half-heights long in the present case.

The computations were carried out on the massively parallel CM200 at PDC where the calculations amounted to a total of about one CPU month. Accurate statistics have been acquired and the long structures have been studied in detail. It was also shown that a weak (spanwise) rotation has a drastic effect on the long structures. Comparisons with experimental results show excellent agreement [Bech *et al.*, 1995].

Also the relaminarization of plane Couette flow turbulence was studied by a step-wise lowering of the Reynolds number, see Figure 5.2. This was achieved by increasing the viscosity, thereby avoiding the instabilities that would occur if the velocity suddenly was decreased. The transition Reynolds number could hereby be determined to about 360 thereby substantiating the previous numerical/experimental findings of Lundbladh & Johansson and Tillmark & Alfredsson. Also the turbulence regeneration mechanisms could be elucidated at low Reynolds numbers. Strong similarities were found with the streak instability mechanisms observed in typical bypass transition scenarios in various flows.

The code has recently also been ported to the IBM SP-2 machine and some preliminary results look promising for the performance on that machine. A study of two dimensional turbulence has recently been initiated where the aim is to perform simulations with up to  $4196 \times 4196$  spectral modes. Furthermore a study of turbulent pipe flow by use of a novel technique of utilizing an efficient spectral method has recently been initiated.

In addition to the publications [Komminaho, 1995, Komminaho *et al.*, 1995a, Komminaho *et al.*, 1995b], results from this project have been presented at The 47:th annual meeting of the Fluid Dynamics Division of the American Physical Society, Atlanta, November 1994 and at EU-ROMECH Colloquium 236 in Trondheim, June 1995.

## 5.7 Parallel Computing for Aircraft Design

*Anders Ytterström, Arthur Rizzi*

Department of Aeronautical Engineering, KTH

*Thierry Poinsot, Vincent van Kemenade*

CERFACS, France

*Jan Vos*

IMHEF, EPFL, Switzerland

Developing and improving simulation tools to study the aerodynamics around complete vehicles or in complex internal geometries is a key priority in the aerodynamic offices of many aeronautical engineering companies. Major European aerospace companies such as Saab and Aerospaiale want to turn the Navier Stokes simulation method into a practical tool that design engineers can use on a routine basis. Today this method

*The calculations amounted to a total of about one CPU month*

applied to a full configuration is still at a research stage because long run times with millions of grid points on expensive supercomputers prohibit the widespread use of the method and therefore refinement of the tool goes slowly. Aerospatiale and Saab believe that running these large-scale 3D viscous simulations on massively parallel (MPP) platforms can bring down the cost of these advanced simulations by a factor of ten which will lead to a more rapid development of the method, and ultimately put it in the hands of the designer so that Airbus for example can remain competitive in the international aerospace market.

#### *European aerospace code*

The PAR-AERO project was an ESPRIT-EUROPORT1 project started in January 1994 and ended in December 1995. The Swedish part of the project was financed by NUTEK.

In the PAR-AERO project, nine European partners (CERFACS, KTH Stockholm, Aerospatiale, EPF Lausanne, Saab, PSS, ENSEEIHT, RU Stuttgart, CIRA) have collaborated to implement parallel versions of the Navier-Stokes solver called NSMB (Navier Stokes Multi Block) [Leyland *et al.*, 1995, Vos *et al.*, 1995] developed and used by EPFL, KTH, CERFACS, Saab and Aerospatiale. The entire code has been parallelized with PARMACS and PVM and ported to most existing parallel platforms: IBM SP-1 and SP-2, CRAY J916, SGI clusters, IBM clusters, Meiko CS2, Meiko CS 2HA, CRAY T3D, Intel Paragon, Convex MPP. A specific tool to split meshes into multiple blocks (MB Split) has been developed and coupled to NSMB.

#### *Benchmarks*

Test cases included a two dimensional airfoil (A-airfoil with 65 000 cells, see Figure 2.8 on page 16), a three dimensional wing (F5 wing with 370 000 cells, see Figure 2.9 on page 16) and a full aircraft configuration (AS28G with 3.5 million points, see Figure 2.10 on page 17). The fuselage-wing-pylon-nacelle computation has never been done before on vector machines because the memory required exceeds the usual vector machine capacity. The execution speed on a CRAY Y-MP vector computer for the first two benchmark cases was around 170 Mflop/s. The parallel performance has been about 90%, and scalability was shown to be excellent. Relative speed-ups compared to the CRAY Y-MP ranged from 0.8 to 10 depending on the configurations. Figure 5.3 present speedup obtained for the A airfoil on the SP-2.

The difference in speedup for the 2 curves in Figure 5.3, is due to the increased amount of work when the computational grid is split into more domains, or blocks. This difference is much larger for a 3D case, because the number of extra ghost cells outside the computational domain is much larger in a 3D case, compared to a 2D case.

*The parallel performance has been about 90%, and scalability was shown to be excellent*

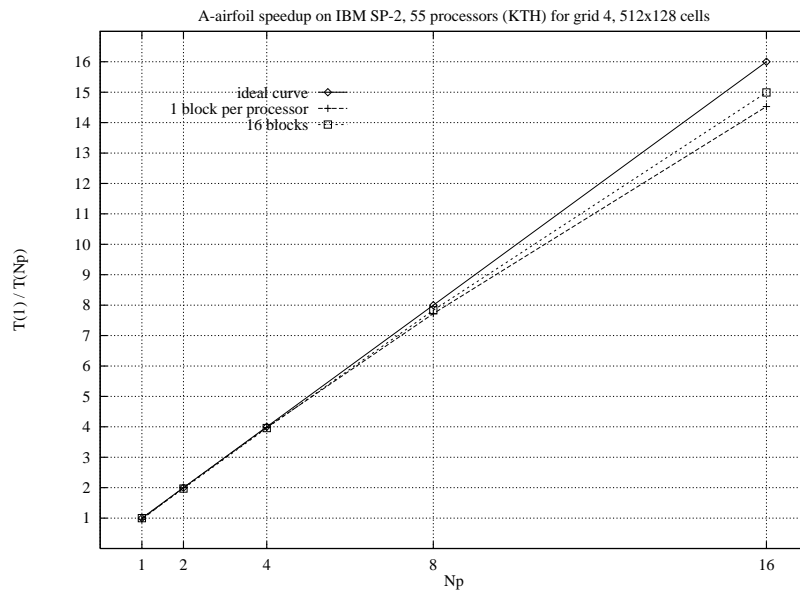


**Figure 5.3.** Speedup for the A-airfoil on the IBM SP-2. The difference between the two curves is the extra work performed on a computational grid with many blocks, compared to a single block grid. The 16 blocks curve gives the same amount of work on all cases, but the 1 block-per-processor curve gives an increased amount of work on cases with more processors.

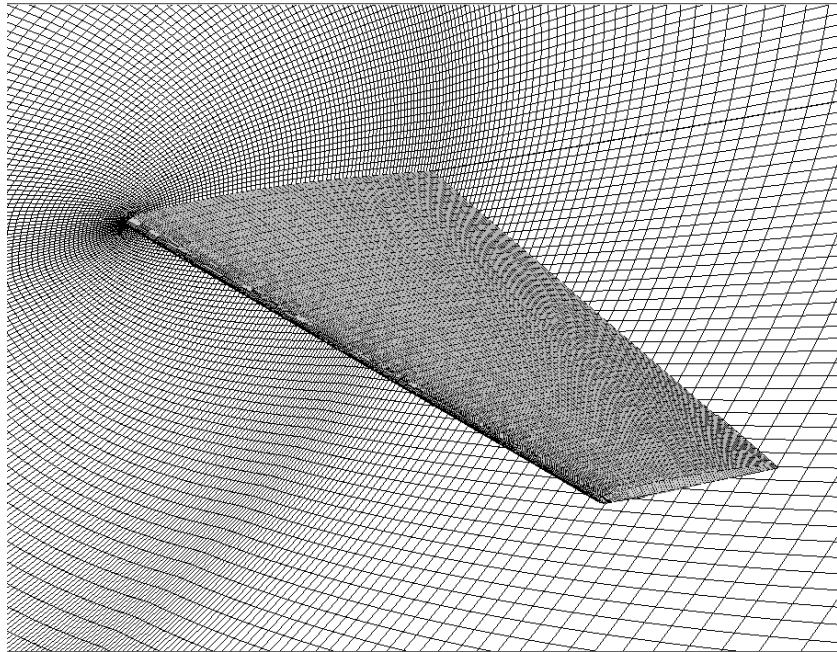
### *Vision for aerospace*

The very competitive aerospace market forces European industry to work with the most technically advanced tools in the most cost-effective ways. The design teams must be able to make air flow simulations over the complete aircraft, and not just the components separately as done before, in order to assess the interactions and interferences between the components. The precision of the simulation must also be very high, and this leads to a computational problem of very large magnitude and high cost. Multiprocessor parallel machines are relieving the bottlenecks of high cost and limited computational capacity and allowing these computational tools to get into the hands of the design engineer. But more research needs to be done in refining the algorithmic methods, in optimizing the parallel performance of the software and in integrating the software into the industrial workplace.

In the EUROPORT newsletter INSIGHTS (11 2/96), Saab claims that “Parallel NSMB has convinced us that cost-efficient industrial application of aerodynamic analysis and design tools for 3D viscous flows requires parallel processing.”

In the same newsletter, Aerospatiale Aircraft Business says: “We are now convinced that even complex numerical simulation packages can be efficiently parallelized in a portable way. The high scalability of NSMB makes us confident that the performance we need to remain competitive with the US Aerospace industry can be reached on larger MPP machines (more than 128 processors, say).”

**Figure 5.4.** The grid around the M6 wing.



## 5.8 Solution of Compressible Flow Problems in Parallel with Static Load Balancing

*Anders Ålund*

Swedish Institute of Applied Mathematics, Göteborg

*Per Lötstedt, Mattias Sillén*

Saab Military Aircraft, Linköping

Computational fluid dynamics (CFD) for aerospace applications require computers with large storage capacity and high speed floating point capability. Parallel computers with large primary memories and powerful processors connected by a high speed network are suitable for CFD problems. The performance of a parallel version of an industrial production code is here evaluated on the IBM SP-2 machine at PDC. In the open environment at PDC it is possible to work with research oriented projects. For the large group of calculations at Saab dealing with classified geometries a higher security level is required, which means that they have to be run on a machine installed in a more controlled environment.

MultNaS is a program developed at Saab for solution of the Euler and Navier-Stokes equations of compressible flow [Lötstedt and Sillén, 1993]. The grid is partitioned into a number of blocks. Each block has a structured grid. The system of partial differential equations is discretized according to Jameson. Steady state solutions are calculated by Runge-Kutta time-stepping and multigrid acceleration. Originally the code was designed to run on one processor of a CRAY vector computer. The serial

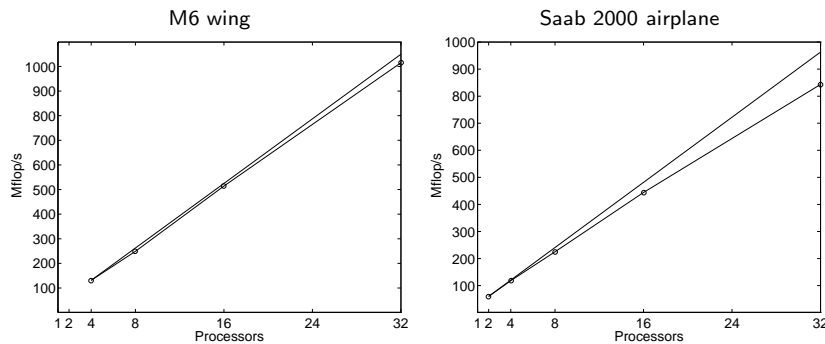


**Figure 5.5.** The Mflop/s rate for the M6 wing and Saab 2000 airplane using from 2 up to 32 ( $\circ$ ) processors compared to the ideal speedup.

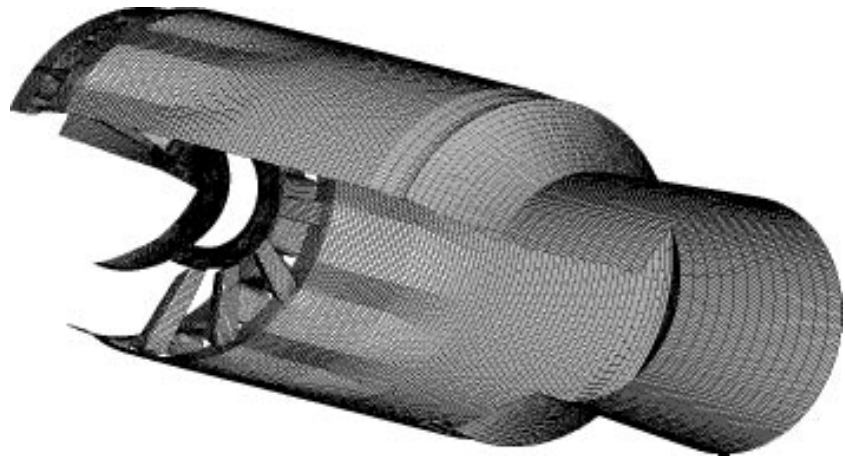
version of MultNaS was modified in [Lötstedt and Ålund, 1994] to fit the message-passing programming model supported by PVM. The message-passing paradigm is the standard choice when transforming validated CFD production codes to parallel processing. A master process initializes and controls the execution of the slaves. Each slave process calculates the solution in one or more blocks. The data at the block boundaries must be sent to the processors holding the adjacent blocks. The parallel version of the program and the performance on a cluster of workstations is described in [Lötstedt and Ålund, 1994] and [Ålund *et al.*, 1994].

The performance of the code on IBM SP-2 with *thin* nodes is tested in two examples, where the Euler equations are solved. The first example is the standard wing ONERA M6. The freestream Mach number  $M_\infty$  is 0.84 and the angle of attack  $\alpha$  is  $3.06^\circ$ . The grid around the wing consists of  $1.96 \cdot 10^6$  cells partitioned into 32 blocks of equal size. The grid on the wing and the symmetry plane is shown in Figure 5.4. Using a static load balancing algorithm, which takes the communication time into account, the steady state solution is calculated on 4, 8, 16 and 32 processors. The Mflop/s rate for the iteration is plotted in Figure 5.5. On 32 processors the computational speed is 1.015 Gflop/s.

Saab 2000 is a propeller driven airplane for 54 to 58 passengers. A computational grid with 48 blocks and more than  $0.8 \cdot 10^6$  cells surrounds the port side. The cruise speed  $M_\infty$  is 0.62 and  $\alpha$  is  $0^\circ$ . A plot of the solution on the port side and its image on the starboard side is found in Figure 2.11 on page 17. The colors represent a coefficient proportional to the static pressure on the surface of the airplane. The efficiency for 16 and 32 processors in Figure 5.5 is lower than it is for the M6 wing. The reason is the heterogeneous sizes of the blocks in this more realistic configuration. One block is much larger than the others and must be split to obtain a good load balance.

A detailed report with a description of the static load balancing algorithm, results for the Navier-Stokes equations with the  $k-\varepsilon$  turbulence model and comparisons with workstation clusters and CRAY Y-MP are found in [Ålund *et al.*, 1995].

**Figure 5.6.** Mesh consisting of 80 blocks and 480 000 nodes.



The work described here is part of a project in NUTEK's program for super and parallel computing. Project partners are ABB Corporate Research, Saab Military Aircraft, Volvo Aero Corporation, and the Swedish Institute of Applied Mathematics.

### **5.9 A Parallel Full Navier-Stokes Simulation of an Afterburner at Volvo Aero Corporation**

*Roland Rydén*

Volvo Aero Corporation, Trollhättan

*Anders Ålund*

Swedish Institute of Applied Mathematics, Göteborg

*The multiblock grid was created using NURBS surfaces retrieved from the concurrent CAD work*

Since the autumn 1994 Volvo Aero Corporation (VAC) has been involved in a design process, aiming to increase the life of the flame holders in the RM12 afterburner. The CFD activities were initiated at an early stage and present a very challenging task, modeling the complex geometry of the afterburner. The multiblock grid was created using NURBS surfaces retrieved from the concurrent CAD work and imported into G3DMESH<sup>1</sup> [Lindblad, 1995] via IGES format. The final mesh consists of 80 blocks and 460 000 nodes, see Figure 5.6.

The solver used in this simulation VolSol V2<sup>2</sup> [Rydén, 1995] was parallelized using PVM in February 1994 [Ålund *et al.*, 1994, Ålund and Rydén, 1994], and has been used in production runs since then, using available workstation clusters at VAC. The solver consists of one host process holding the complete problem, distributing the problem to the slaves using static load balancing algorithm, and then makes the synchronization at each time step. The slave processes exchange data at

---

<sup>1</sup>VAC in-house developed multi-block structured mesh generator.

<sup>2</sup>VAC in-house developed solver for 3D compressible Navier-Stokes with reacting flow.

interface boundaries once in every time step. Because the time integration is done using a three stage Runge-Kutta algorithm, the interface fluxes in the first step are also sent between interfacing processes and then kept constant for the next two steps in order to keep the conservation.

When the IBM SP-2 at PDC, became available, during the afterburner design process, this was a great opportunity to test the code on a full-scale problem. The full compressible Navier-Stokes equations including  $k-\varepsilon$  turbulence model, species transport and droplet tracking and evaporation presents a very complex engineering problem. The computational effort on grid cell basis is very high and thus very feasible for parallelization using the message passing paradigm since the communication is on surface basis and small compared to the computational effort which is on volume basis. The degrees of freedom within each cell is nine consisting of

- Continuity equation (1)
- Momentum equations (2–4)
- Total energy equation (5)
- Turbulence kinetic energy transport (6)
- Dissipation of turbulence kinetic energy transport (7)
- Species transport equations (8–9)

This gives the problem as a whole 4 140 000 degrees of freedom. The block sizes holds 0.12% to 2.25% of the complete problem. This gives a fairly well balanced problem for 10, 20 or 40 nodes. The runs performed on Strindberg used 1, 20 and 40 *thin* nodes with speed-up figures given in the table below. The “possible speedup” is defined as the inverse of the largest node percentage, i.e. taking the load balancing into account.

# nodes	Smallest node size (%)	Largest node size (%)	CPU time for one time step (seconds)	Possible speed-up	Achieved speed-up
1	100.00	100.00	109.04	1.00	1.00
20	4.85	5.15	5.65	19.42	19.28
40	2.30	3.00	3.28	33.30	33.24

The speed-up is embarrassingly good for this problem, reducing the time for one solution from 1200 CPU hours (50 days) to 36 CPU hours when using 40 nodes on Strindberg. It opens completely new possibilities for the CFD modeling to be used as a powerful engineering tool. Visualization of some output from this simulation can be seen in the color figures where Figure 2.12 on page 18 shows the recirculation zone where the flame is stabilized, Figure 2.13 on page 18 shows streamlines

*The computational effort on grid cell basis is very high and thus very feasible for parallelization using the message passing paradigm*

*It opens completely new possibilities for the CFD modeling to be used as a powerful engineering tool*

from a thought fuel injector radius, and Figure 2.14 on page 19 gives a detailed picture of the flow around the flame holder.

The essential part of the work described in this report is part of a project in NUTEK's program for super and parallel computing. Project partners are ABB Corporate Research, Saab Military Aircraft, Volvo Aero Corporation and the Swedish Institute of Applied Mathematics.

## 5.10 Parallel CFD on the IBM SP-2

*Ingemar Persson*

Center for Computational Mathematics and Mechanics, KTH

Computational fluid dynamics (CFD) encompasses the computation of fluid flow around bodies for all speed regimes. The aim is to use CFD as a design tool to increase performance and effectiveness on the actual object of interest. The fundamental equations of fluid flow, the Navier-Stokes equations, are considered to be exact and to apply to even the smallest observable eddies of turbulence as long as we assume that the fluid is a continuous medium. However, the Navier-Stokes equations are very difficult to solve. Not only because of the need of enormous computing power but also due to the grid quality requirements. Thus it is common to eliminate the viscous stress terms in the Navier-Stokes equations which yields the so called Euler equations. These equations relaxes both the computing power needed and the requirements on the grid. Within the EU Human Capital and Mobility project we have examined a modular cell-vertex finite volume code designed to solve realistic compressible fluid flow problems. The code, called AVBP, is able to handle structured and unstructured meshes in both 2D and 3D. The AVBP code developed at CERFACS has been used to solve the Euler equations for three dimensional inviscid, compressible flows in the transonic speed region. As test cases we have used geometries known as the ONERA M6, a simple wing geometry and the Dassault Falcon aircraft, a full aircraft geometry. Both grids are unstructured tetrahedral grids suitable for Euler flow calculations and were generated using J. Peraire and J. Peiró's unstructured grid generator. Such flows are described by the Euler equations,

$$\frac{\partial \bar{w}}{\partial t} + \sum_{i=1}^3 \frac{\partial \bar{F}_i}{\partial x_i} = \bar{0}$$

where

$$\bar{w} = \begin{pmatrix} \rho \\ \rho u_1 \\ \rho u_2 \\ \rho u_3 \\ \rho E \end{pmatrix}, \quad \bar{F}_i = \begin{pmatrix} \rho u_i \\ \rho u_i u_1 + p \delta_{i1} \\ \rho u_i u_2 + p \delta_{i2} \\ \rho u_i u_3 + p \delta_{i3} \\ u_i (p + \rho E) \end{pmatrix}$$

and  $\delta_{ij}$  is the Kronecker delta function.

AVBP uses a cell-vertex finite volume method. The semi-discrete scheme formulation for node  $k$  becomes,

$$\frac{d\bar{w}_k}{dt} = -\frac{1}{V_k} \sum_{j|k \in \Omega_j} D_{\Omega_j}^k V_{\Omega_j} R_{\Omega_j}$$

where  $D_{\Omega_j}^k$  are the cell-vertex distribution coefficients,  $V_k$  is a control volume associated with node  $k$ ,  $R_{\Omega_j}$  defines the cell residual of cell  $\Omega_j$  and  $V_{\Omega_j}$  defines the volume of cell  $\Omega_j$ .

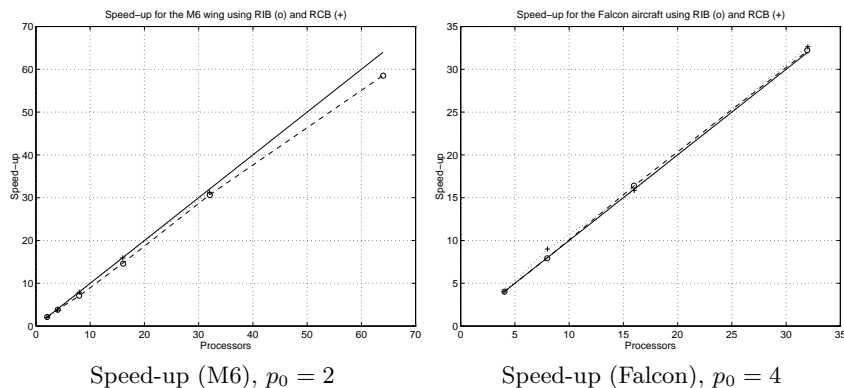
AVBP has been implemented in Fortran77, with non-standard extensions to allow dynamic memory allocation. The coarse grained block data structure in the sequential algorithm made it natural to parallelize the code in a master/slave fashion by using PVMe or Parmacs as message passing library. This in turn necessitates a decomposition of the computational mesh that assigns equal amounts of data to each processor and minimizes the communication cost of the interfaces. In AVBP, two rather simple decomposition methods have been implemented. As a preprocessing step to the parallel execution of the code, the mesh can be decomposed by either the RCB (Recursive Coordinate Bisection) or the RIB (Recursive Inertia Bisection) partitioning algorithms. They try to balance the number of generalized elements between the generated partitions. The decomposition is done on the master node and thereafter each partition is mapped onto a slave node. Each partition is made up of blocks and a block has a group as a substructure. The group is a set of elements on which operations are performed and it work as a cache blocking strategy. This grouping strategy shows to be a useful tool to tune the code to perform efficiently on a specific machine architecture without the need of hand-tuning critical parts of the code. Details on partitions, blocks and groupings can be found in [Rudgyard *et al.*, 1994].

### *Performance results*

In order to evaluate the parallel performance of the computer code, tests with different parameter settings have been made. Altered parameters are the number of used processing nodes, the partition technique employed, and the element grouping within each subdomain. The ONERA M6 wing (57041 nodes, 306843 tetrahedral elements) can be considered as a relatively small test case, whereas the twin engined Dassault Falcon aircraft configuration (155932 nodes, 847361 tetrahedral elements) can be classified as a relevant industrial test case, see Figures 2.15 and 2.16 on pages 19 and 2.16. For both cases, explicit 4-stage Runge-Kutta time-stepping has been used to advance the solution to reach the prescribed residual. The performance of the IBM SP-2 on a wide node was 41 Mflop/s and 27 Mflop/s for a thin node. All tests were performed in a 'semi-dedicated' mode, i.e. having a dedicated switch but a non-

*This grouping strategy shows to be a useful tool to tune the code to perform efficiently on a specific machine architecture without the need of hand-tuning critical parts of the code*

**Figure 5.7.** Speed-up graphs for the M6 wing and the Falcon aircraft using RIB (o) and RCB (+)



dedicated CPU. We define speed-up,  $S_{p_0}^{opt}(p)$ , of base  $p_0$  as,

$$S_{p_0}^{opt}(p) = \frac{T^{opt}(p_0) p_0}{T^{opt}(p)},$$

where  $T^{opt}(p)$  denotes the "optimal" CPU time for  $p$  processors. With "optimal" we mean picking out the run times from the groupings that has given the best performance, i.e. used least CPU time. From the data we can conclude that AVBP parallelizes with excellent performance, see Figure 5.7. In the case of the M6 wing, we get linear speed-up and for the Falcon aircraft we receive super-linear speed-up. The performed parameter studies [Persson, 1995] have given us a good knowledge about what can be chosen as a nearly optimal grouping of the elements on the IBM SP-2 system.

### Conclusions

*The AVBP compressible fluid flow solver program can be used to solve realistic CFD problems in a scalable and efficient way on the IBM SP-2 system*

The present study has shown that the AVBP compressible fluid flow solver program can be used to solve realistic CFD problems in a scalable and efficient way on the IBM SP-2 system. Certainly, several routines could be further optimized for speed but then the design of a single code running efficiently on several platforms would be compromised. As demonstrated in [Persson, 1995], care has to be taken when choosing the 'grouping number'. A non-appropriate chosen 'grouping number' may induce up to 50 % longer computation time. The choice of decomposition algorithm has shown to be of less importance. The different decomposition techniques usually give within 10 % the same run times. This small difference comes as no surprise since the two methods compared are relatively similar.

## 5.11 Supersonic Inviscid Flow Computations on Adaptive Unstructured Grids

*Ingemar Persson*

Center for Computational Mathematics and Mechanics, KTH

The following results treats the computation of the axial symmetric flow around a shell. Shells used in the Swedish army need to have at least two independent security systems to avoid unintentional detonations. One common system is based upon the rotation of the shell. However, the shell used in these calculations is stabilized by small wings and thus do not rotate. Instead, the approach used in this case is based on the difference in pressure over a membrane, when the shell reaches a specific speed. The problem is to find suitable places for the two channel-entrances to the membrane. Pressure is the only variable of interest here, and with a Reynolds number of several millions and no danger for separations, we decided to perform inviscid calculations, i.e. solving the Euler equations. Another thing of interest was the possible impact of detonation knob-length and the pressure difference at different speeds.

*Shells used in the Swedish army need to have at least two independent security systems to avoid unintentional detonations*

### *The numerical treatment of the flow problem*

The NSC2KE code [Mohammadi, 1994] has been used to solve the axial symmetric Euler equations for inviscid, compressible flows in the supersonic speed region. Our assumption that the flow is axisymmetric means that all of the  $\theta$  derivatives are zero. We also assume that the swirl or the  $\theta$  component of the velocity is zero.

The Euler equations are discretized in space on unstructured meshes using a Finite Volume-Galerkin technique with a kinetic Riemann solver for the convective part.

If we suppose that the flux  $F$  varies linearly on each triangle, the weak formulation is given by: Find  $W_h \in (V_h)^4$  such that  $\forall \phi_h \in V_h := \{v \in C^0(\Omega), v|_T \text{ is linear } \forall T \in \mathcal{T}\}$

$$\int_{\Omega} \frac{\partial W_h}{\partial t} \phi_h - \int_{\Omega} F_h(W_h) \nabla(\phi_h) + \int_{\partial\Omega} F_h \cdot n \phi_h = 0$$

$$\Leftrightarrow$$

$$|C_i| \frac{W^{n+1} - W^n}{\Delta t} + \int_{\partial C_i} F_d(W^n) \cdot n = 0$$

where  $C_i$  is denoting a cell and

$$F_d(W_h) = \begin{cases} F(W_{\partial\Omega}) & \text{on } \partial C_i \cap \partial\Omega \\ \text{piecewise constant approximation of } F(W) & \text{otherwise} \end{cases}$$

The approximation of  $F(W)$  fulfills

$$\int_{\partial C_i} F_d \cdot n = \sum_{j \neq i} \Phi(W'|_{C_i}, W'|_{C_j}) \int_{\partial C_i \cap C_j} n$$

where  $\Phi(u, v) = \frac{1}{2}(F(u) + F(v)) - d(u, v)$  and a kinetic proposition for the numerical diffusion,  $d$ , is used. In order to get second order spatial accuracy a MUSCL like extension involving combinations of upwind and centered gradients is applied.

Rather than using the explicit time integration scheme given above, NSC2KE make use of a four stage Runge-Kutta scheme. This also enables us to treat time dependent flows if wanted. In our case, we have used a local time stepping procedure where  $\Delta t(s_i) = \frac{\Delta x}{|u|+c}$  and  $\Delta x$  is a minimum height of the triangles having node  $s_i$  in common.

#### *Vectorization and Parallelization*

In order to achieve high performance, NSC2KE was first vectorized on the CRAY J90 and later also parallelized using CRAY microtasking. As the code only had an inherent parallelism of 13%, a graph coloring scheme had to be implemented enabling parallelization of the most time consuming parts of the code. This edge and element coloring made the code almost 85% parallel. On 4 processors a speed-up of 2.4 was measured which can be considered good keeping in mind that Amdahl's law predict a maximal theoretical speed-up of 2.76. The performance on a single processor was 50 Mflop/s.

#### *Computational results*

In order to investigate the pressure ratio over the membrane and any possible knob-length dependence, several runs for different parameter settings have been made. The altered key parameters here are the free stream speed and the knob-length. All grids, generated using a Delaunay mesh generator, are unstructured triangular grids suitable for Euler flow calculations, see Figure 5.8. To enhance the resolution, e.g. shock capturing, the grids were adapted using NSCADAP [Persson and Ytterström, 1996]. The refinement can be done with respect to flow quantities such as density or pressure. Refinement can also be done with consideration taken to a fixed wall.

*The computations resulted in the knowledge that the suggested knob-length variation was not significant*

The computations resulted in the knowledge that the suggested knob-length variation (1 mm difference) was not significant and that the pressure ratio over the membrane was a factor three or more.

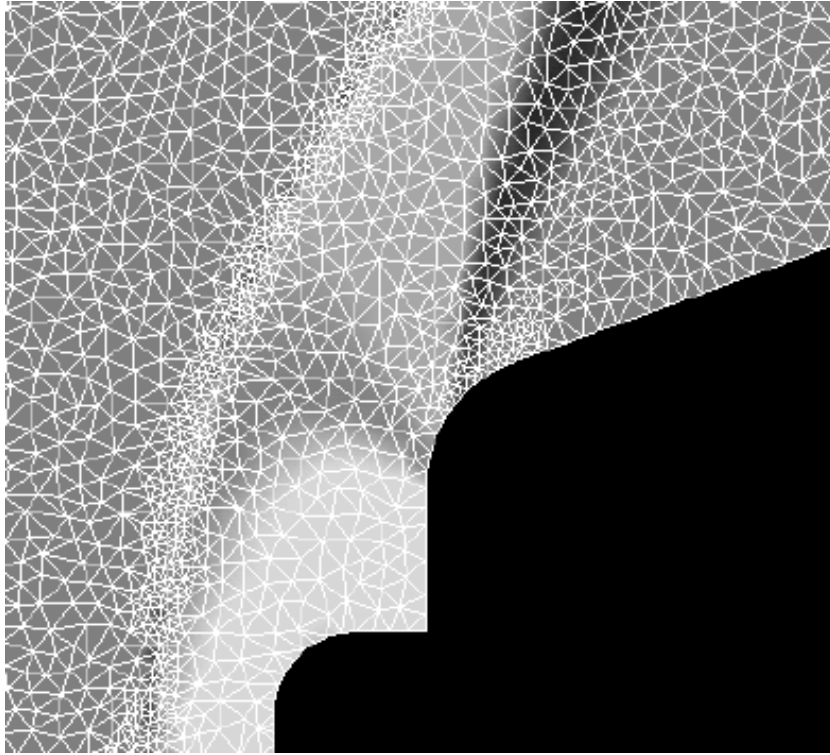


**Figure 5.8.** Density field at Mach=2.06 on a coarse adapted grid.

## 5.12 Numerical Computation of Hydrodynamics in Fluidized Beds

*Hans L fstrand*

Department of Thermo and Fluid Dynamics, CTH

*Eric Peirano*

Department of Energy Conversion, CTH

The main objective of this work is to develop a method to evaluate a two-fluid model of the gas and particle flow fields in a fluidized bed. A bubbling fluidized bed can technically be described as a container in which the solid phase in the form of closely packed particles (in this case silica sand with a mean diameter of 0.7 mm) is brought into motion by an air flow inserted at the bottom of the container through an air distributor. The air tends to form bubbles which rise through the bed, but can also flow through the dense regions and shortcut between the bubbles. The word fluidization comes from the fact that, at a gas flow rate within a certain range, the mixture becomes fluid-like. Fluidized beds have been in industrial use for several decades mainly as chemical reactors, solid fuel combustors and dryers.

The two-fluid model is an averaged form of the Navier-Stokes equations for each phase, cf. [Drew, 1983], and is represented by one continu-

*Fluidized beds have been in industrial use for several decades*

ity equation for each phase and one momentum equation in each direction and for each phase. In the averaging process, interfacial momentum transfer terms enter the momentum equations. These terms as well as the particle pressure term are modeled using empirical correlations.

The numerical algorithm is based on a well-known finite difference method for two-fluid models, the IMF method by Harlow and Amsden [Harlow and Amsden, 1975]. A first order scheme, the upwind scheme, is used for the convective terms. The equations are discretized semi-implicitly in time, treating the space derivatives of unknown variables explicitly, so that a one-point scheme is obtained.

The solution of the equations show how gas bubbles, defined as the regions where the gas concentration is larger than approximately 70%, rise up through the bed chaotically but with a regularity in a statistical sense. A typical instantaneous flow field is shown in Figure 2.17 on page 21. The above mentioned regularity has also been observed in experiments, where these statistical quantities have been evaluated from capacitance probe signals, cf. [Olowson and Almstedt, 1990]. In order to get relevant statistical quantities from the computations, simulations of at least 30 seconds real time are necessary. The large amount of computer time required to solve this kind of transient two-phase flow problems using powerful workstations renders such a project impossible. To remedy this, a multiblock-version of the code has been adapted, with the aid of MPI, for use on parallel computers such as IBM SP-2.

Presently, work is going on to guarantee that the mean values of the microscales (velocity, pressure, density profiles) and the macroscales (bubble frequency, mean bubble length, mean bubble rise velocity, etc. ) are independent of the block structure used. The future goal is to validate different submodels for the interfacial momentum transfer term, different boundary conditions, and to investigate effects of three-dimensionality.

### 5.13 Consolidation of Concentrated Suspensions

*Jacob Yström*

Center for Computational Mathematics and Mechanics, KTH

*Heinz-Otto Kreiss*

University of California, Los Angeles, USA

#### *Condensed research description*

*It is for many applications unrealistic to use models that take into account each separate particle in a suspending fluid, therefore, a continuum modeling is desirable*

A concentrated suspension is a two constituent mixture, consisting of a fluid and solid particles, and where the interaction between particles is not negligible. The particles are observable on an experimental scale but it is for many applications unrealistic to use models that take into account each separate particle in a suspending fluid, therefore, a continuum modeling is desirable. We consider a continuum formulation for suspensions, where the fluid is incompressible Newtonian and where there is

one type of incompressible solid particles. The density of the particles is assumed different from the fluid density, which makes the gravity field an important forcing function. The separation of the two constituents due to gravitational effects is called consolidation. Examples of concentrated suspensions are sludge, paste and paint.

The main contributions are:

- We formulate a continuum model for the consolidation of concentrated suspensions in several space dimensions. This model is based on classical equations for mixture theory and a series of assumptions consistent with the standard model in one space dimension and by rather general assumptions regarding the constitutive relations specific to the multidimensional case.
- The linearized system of equations of the suspension model is for the periodic Cauchy problem proved to be well-posed.
- A general continuum formulation of irreversible compression, used to model compression rheology for flocculated suspensions in Eulerian coordinates is developed.
- A numerical solver for a genuinely two dimensional test problem for concentrated suspensions is developed. This test problem is a driven cavity type of problem where the cavity is a closed box and with constant gravity perpendicular to the direction of a tangentially moving wall. Numerically computed solutions in one and two space dimensions are demonstrated to be well-behaved. The one dimensional computations are consistent with other computations which in turn have been validated to experiments.

#### *The use of the IBM SP-2*

The numerical solver and the computed solutions can be seen as a validation process of the theoretical results. In this process a fast computer has been necessary. The equations behave as ODE's coupled to a system of elliptic equations. The solver is implemented in C++, using a finite difference class library D++, that takes care of space discretization. The elliptic separate problems are therefore solved with a direct band-solver. The numerical algorithm is robust but not very effective, it is furthermore implemented as a single processor code. Plans for future work include a more effective 2D solver that can be used in an experimental verification process. For numerical example see Figure 2.18 on page 22. For further details see [Yström, 1993] and [Yström, 1996].

## 5.14 Flutter Analysis of Two Dimensional Viscous Flow in Turbomachines Using the Advection Upstream Splitting Method (AUSM)

Wolfgang Höhn, Torsten Fransson

Department of Energy Technology, KTH

### *Introduction*

The design of more efficient turbomachines leads to higher loaded blades with increased flow temperatures and velocities.

Moreover, improved lighter blade materials for turbo-engines are introduced as well as more slender blades in order to increase the performance and decrease the weight. This is of important interest, especially for aircraft engines.

Long blades in compressors or in the last stage of turbines therefore become more sensitive to flow induced vibrations. Consequently, aeroelasticity is an important discipline as the combination of the aerodynamic and the structural dynamics of the blade in turbomachines.

Different kinds of aeroelastic phenomena are defined in the literature (see [Försching, 1974]). One can divide them in static and dynamic appearances. The last one can be divided in forced vibrations and self excited vibrations, usually called flutter.

For realistic modern flow configurations nonlinear and viscous effects are far from negligible, especially in the vicinity of shocks as well as for shock boundary layer interaction. Due to that the aerodynamic work of the fluid on the structure can be strongly influenced by separated flow situations in compressors and by shocks occurring in turbine cascades.

Therefore, the presented numerical method accounts for unsteady, viscous, fully turbulent flow around cascaded blades towards a better understanding of the above mentioned flow situations.

### *Computational Method*

An unsteady, compressible, two dimensional Navier Stokes solver is used to predict the flow around cascaded vibrating blades. The presented method applies the “Advection Upstream Splitting Method” (AUSM) for the discretization of the convective terms [Wada and Liou, 1994] and central differences for the diffusive terms. The AUSM scheme is based on the idea of the van Leer’s flux vector splitting method. Turbulence is modeled by using the Baldwin-Lomax turbulence model. The time accurate integration of the governing equations is performed by applying an explicit four stage Runge-Kutta scheme.

Advantages of the method are its simple implementation in comparison to for instance flux difference splitting methods and that there is no need to specify numerical dissipation parameters as for example for “central schemes”.

The blade flutter phenomena is simulated by imposing a motion on the

*Aeroelasticity is an important discipline as the combination of the aerodynamic and the structural dynamics of the blade in turbomachines.*

*The presented method applies the “Advection Upstream Splitting Method”*

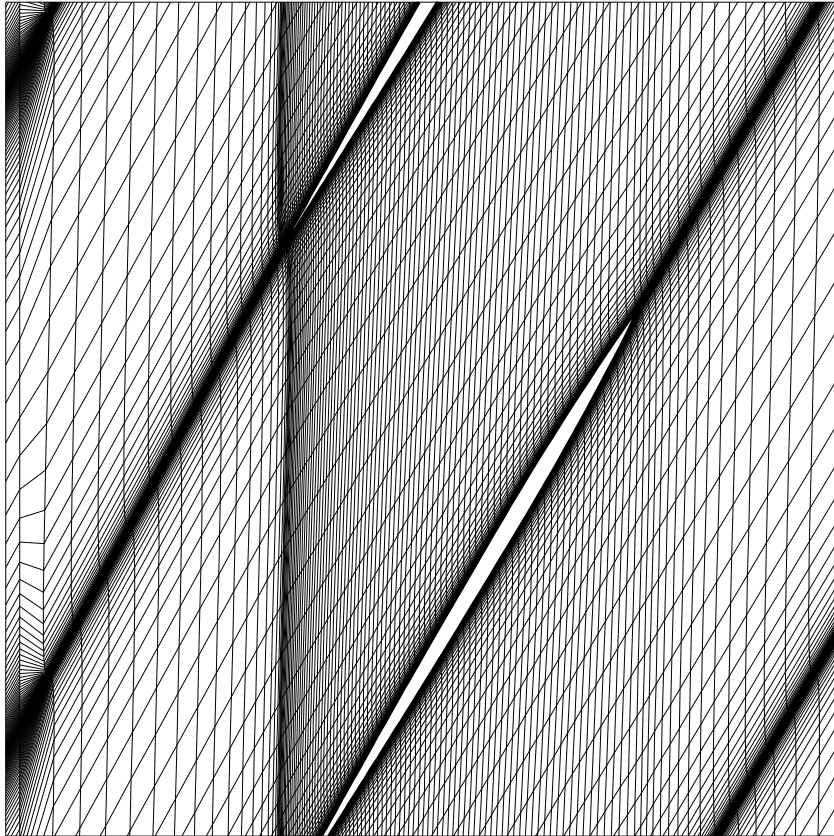


**Figure 5.9.** Mesh used for standard configuration 5,  $120 \times 100$  meshpoints.

blade, which consists of harmonic body translation in two directions and rotation, allowing an interblade phase angle between two neighboring blades. The studied test cases apply either a bending or a torsional motion. No combined motion, i.e. bending and torsional motion, has been investigated.

In the first step the solution for the steady state flow is calculated, which is then used as initial condition for the unsteady analysis, in which the Navier-Stokes equations are solved in a time accurate manner. In order to simulate the blade motion the computational mesh has to be deformed. To account for this mesh motion extra terms arise in the governing equations. The simulation of non-zero interblade phase angles is handled by storing the computed flow variables at the periodic boundary nodes and applying the stored quantities at a later time on the opposite periodic boundary [Erdős *et al.*, 1977]. In this way the computational domain only has to include one blade passage.

The code was validated by flat plate cases for laminar and turbulent flow at different Reynolds numbers, laminar flow around a 2D cylinder, different turbine and a compressor cascade test cases.

**Table 5.3.** Steady state flow parameters, international standard configuration 5.

	Experiments	INSTHPT
$Ma_{inlet}$	0.5	0.51
Inlet flow angle	63.3	63.3
$Ma_{outlet}$		0.47
Outlet flow angle		60.7
Angle of incidence	4.0	4.0

*Emphasis is made on the investigation of the unsteady inviscid and viscous flow situations in cascaded flow*

Emphasis is made on the investigation of the unsteady inviscid and viscous flow situations in cascaded flow for three standard configurations (see [Bölcs and Fransson, 1986]), i.e. a turbine and a compressor test case, and is performed on the parallel computer IBM SP-2 at KTH, using MPI as message passing system.

### Results

As an example, the results for a compressor cascade (standard configuration 5 [Bölcs and Fransson, 1986] are shown.

This two-dimensional subsonic cascade configuration has been tested in a rectilinear cascade air tunnel at the Office National d'Etudes et de Recherches Aéropetiale (ONERA).

Figure 5.9 shows the cascade geometry and the mesh used for the calculations of the program INSTHPT with 80 points on the blade on the upper and the lower side, respectively and  $120 \times 100$  meshpoints in total.

Table 5.3 shows the flow parameters of the calculations and the experimental data. The Reynolds number based on the inlet velocity and the chord length is 1 400 000 for this flow case [Fransson, 1993].  $Y^+$  is about 1.5 close to the leading edge for the calculations conducted with INSTHPT.

The cascade is forced into a pure torsional vibration mode of a frequency of 550 Hz and a amplitude of  $0.1^\circ$  with an interblade phase angle of  $180^\circ$ . The used steady state initial solution is characterized by an incidence angle of  $4^\circ$  and an inlet Mach number of 0.5. As the Figures 5.10 and 5.11 show the results for the unsteady amplitude and phase based on the frequency of the blade motion of the of the surface pressure distribution are in reasonable agreement with experiments done by [Bölcs and Fransson, 1986]. The results are shown for the pressure side (LS) and the suction side (US) of the blade.

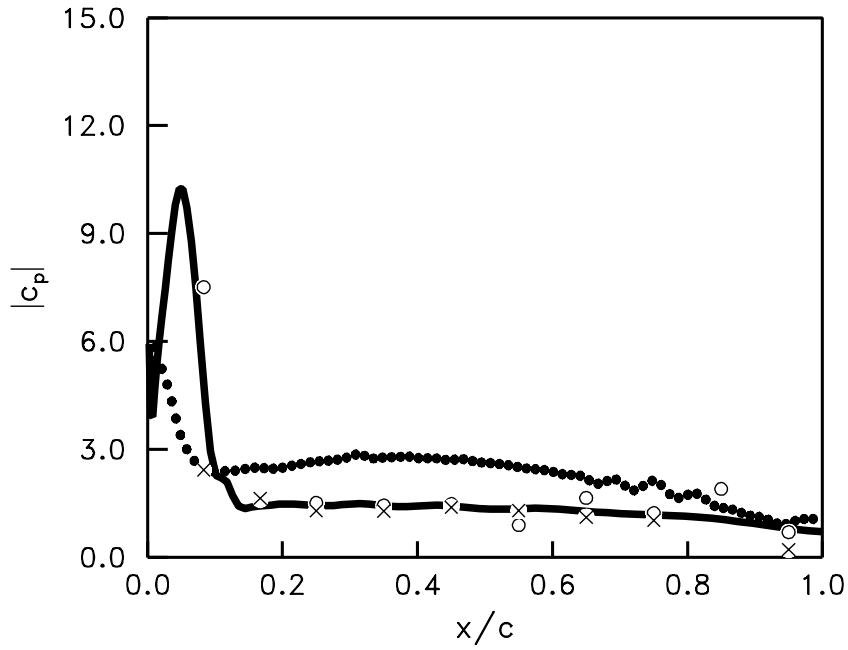


**Figure 5.10.** Amplitude of the unsteady pressure over chord for standard configuration 5, interblade phase angle of  $180^\circ$ : comparison AUSM - experiments.

- INSTHPT AUSM: US
- INSTHPT AUSM: LS
- Experiment: US
- × Experiment: LS

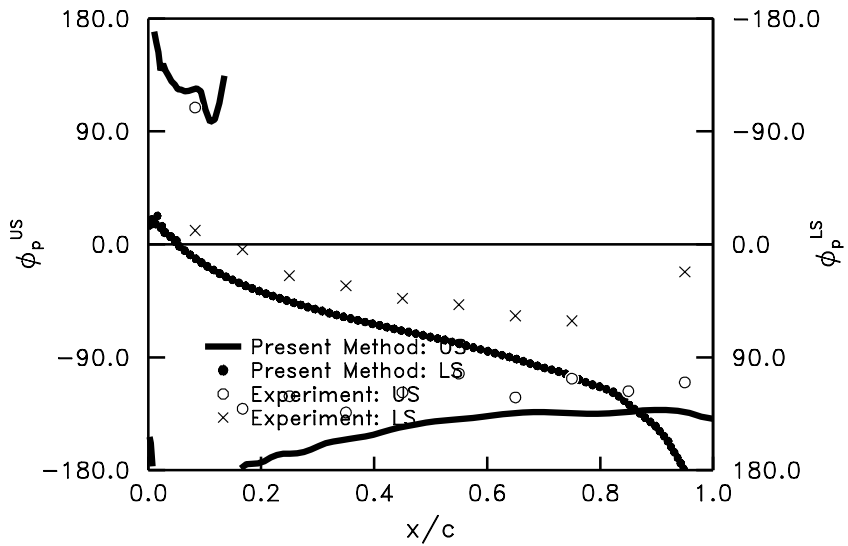


**Figure 5.11.** Phase of the unsteady pressure over chord for standard configuration 5, interblade phase angle of  $180^\circ$ : comparison AUSM - experiments.



# 6 Applications in Physics

## 6.1 An Universal Scaling Law for Atomic Diffusion in Condensed Matter

*Mikhail Dzugutov*

Center for Parallel Computers, KTH

Atomic diffusion in condensed matter has so far eluded a unifying quantitative description. Although explicit expressions have been obtained for the transport coefficients of the dense fluid of hard spheres, their consistent generalization to the rich variety of atomic structures arising at high densities remains a formidable challenge for kinetic theory. Atomic dynamics in condensed phases is dominated by the so-called cage effect whereby the diffusive atomic motions are coupled to the structural relaxations. Due to the pronounced structural correlations, each atom finds itself in a cage formed by the immediate neighbors, and its diffusive motion is effected by local density fluctuations transforming the surrounding atomic configuration. The kinetic theory description of this diffusion mechanism represent a generalization of the Enskog theory for the dense hard-sphere fluid; to apply this description to a real system, a hard-sphere model is required. However, the structural diversity of condensed atomic phases, and the dependence of this diversity on the details of interatomic interactions, impose a fundamental limitation on the range over which the hard spheres can adequately describe real systems.

In this study, molecular dynamics (MD) simulation was employed to test a new approach which is based on the following two arguments.

(i) The time-scale of atomic dynamics at high densities is defined by the Enskog frequency of binary collisions:

$$\Gamma_E = 4\sigma^2 g(\sigma) \rho \sqrt{\pi k_B T / m} \quad (6.1)$$

where  $m$  and  $\sigma$  are the atomic mass and the hard sphere diameter, respectively;  $g(\sigma)$ , the value of the radial distribution function at the contact distance, represents the density of the immediate neighbors ( $\sigma$  is defined as the position of the first maximum of  $g(r)$ ). Using  $\sigma$  and  $\Gamma_E^{-1}$ , respectively, as natural units of length and time, the diffusion coefficient  $D$  can be expressed in a dimensionless form as  $D^* = D\Gamma_E^{-1}\sigma^{-2}$ .

(ii) The frequency of the local structural relaxations, which defines the rate of the cage diffusion, is obviously proportional to the number of accessible configurations (per atom). In an equilibrium system, this scales as  $e^S$ , where  $S$  is the excess entropy; hence,  $e^S$  and  $D^*$  must be connected by a universal linear relationship.

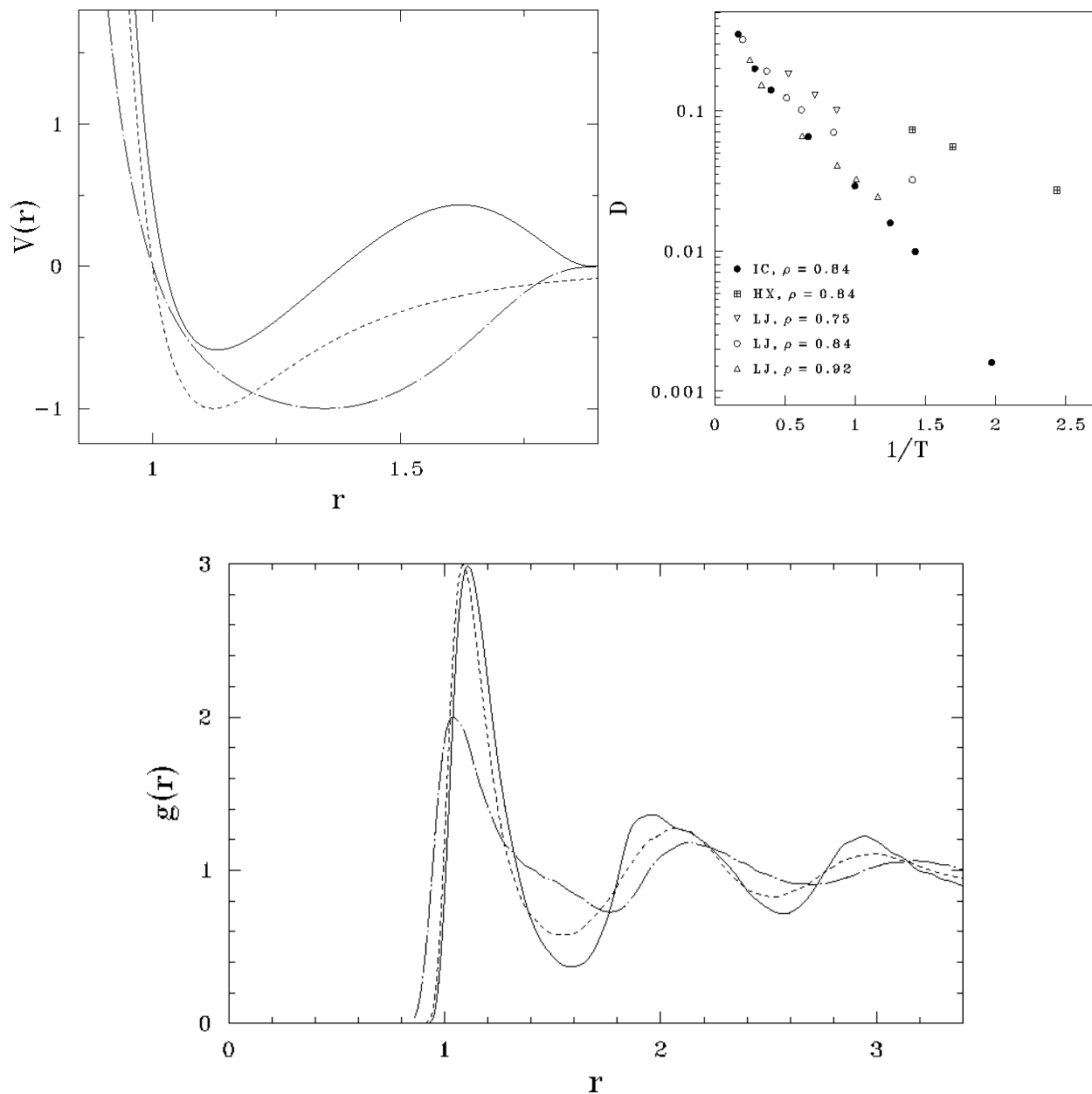


**Figure 6.1.** Three liquid models examined in the Molecular Dynamics simulation. (Top left) The pair potentials. (Top right) Arrhenius plot for constant-density diffusion variations in IC, HX and LJ liquids. (Bottom) radial distribution functions, as calculated at the reduced density  $\rho = 0.84$  and the temperature  $T = 0.7$ . Dashed line, the Lennard-Jones system (LJ). Solid line, IC liquid, possessing a predominantly icosahedral local order. Chain-dotted line, HX liquid, where local order is topologically related to the primitive hexagonal lattice.

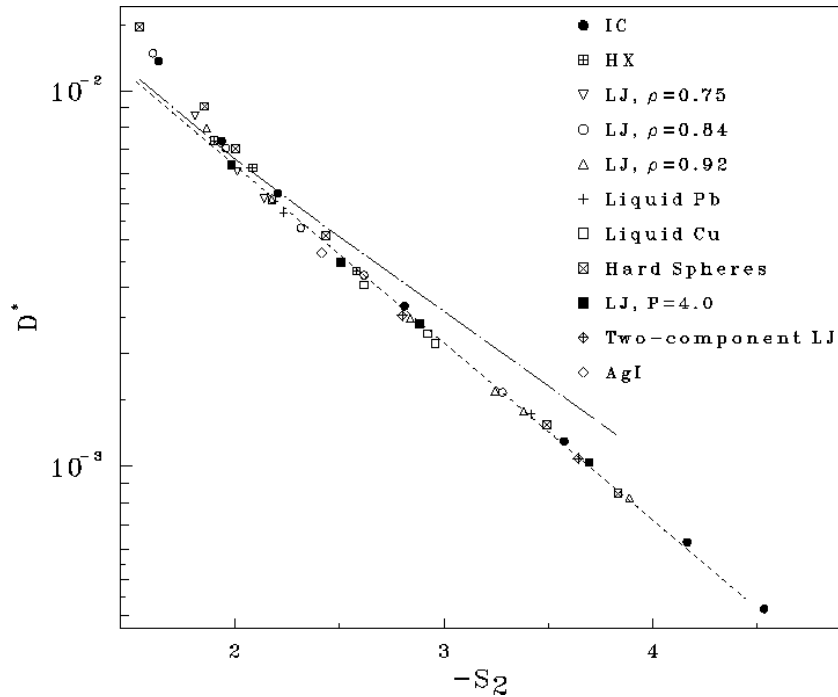


**Figure 6.2.** The scaled diffusion coefficient  $D^* = \Gamma_E^{-1} \sigma^{-2}$ , for various models, as a function of the excess entropy, in the pair approximation, Equation 6.2 where  $\Gamma_E$  is the Enskog collision frequency, Equation 6.1), and  $\sigma$  is the effective hard-sphere diameter. Dashed line, Equation 6.3; chain-dotted line, Enskog result for hard spheres.

We also assume here that  $S$  can be restricted to the two-particle approximation:

$$S_2 = -2\pi\rho \int_0^\infty \{g(r)\ln[g(r)] - [g(r) - 1]\}r^2 dr \quad (6.2)$$

We tested three systems which represent distinct prototypes of liquid structure and exhibit dramatic variations in the atomic diffusivities (Figure 6.1). Other systems examined were two liquid metals, Cu and Pb, as well as the hard-sphere fluid. Figure 6.2, shows that for all these liquids diffusivity can be described by a simple scaling law:

$$D^* = 0.049 e^{S_2} \quad (6.3)$$

This scaling law was also found to be valid for a two-component LJ liquid, as well as for the diffusivity of  $Ag^+$  in solid ionic conductor  $\alpha - AgI$ .

We conclude that the relationship between  $D$  and  $g(r)$ , as expressed by Equations (6.1) to (6.3), is universal for equilibrium condensed atomic systems, both liquid and solid, regardless of the structures, interatomic interaction potentials or the microscopic dynamical mechanisms involved.  $D$  can thus be calculated from the diffraction data in those cases where its direct measurement is not possible, or inferred from a structural model. A more general conclusion is that the rate of exploration of the con-

figurational space is controlled by the excess entropy. For details see [Dzugutov, 1996c] and [Dzugutov, 1996b].

This study was supported by the Swedish Natural Science Research Council (NFR).

## 6.2 Atomic Kinetics and Dynamical Phason Disorder in a Quasicrystal

*Mikhail Dzugutov*

Center for Parallel Computers, KTH

Quasicrystals possess a generic form of structural relaxation dynamics associated with incommensurate or phason degrees of freedom. A spatially uniform shift along a phason coordinate results in a set of configurations which belong to the same local isomorphism class as the original configuration. Therefore, such shift represents a continuous macroscopic symmetry, and its breaking by introducing a non-uniform variation in the phase space generates associated dynamical modes (phasons). But the microscopic mechanisms of the phason dynamics are still unclear. If one postulates that a quasicrystal relaxes the phason strain by the virtue of energy minimization, a virtually infinite range of interatomic interactions has to be assumed. Alternatively, the phason dynamics can arise in the entropic scenario as postulated by random tiling model. It assumes that phason flips connect energetically degenerate structural units, thus producing a large configurational entropy with the maximum at zero phason strain. This process can stabilize the quasicrystal long-range order as long as the rate of phason dynamics is high enough.

An important aspect of phason dynamics is that the local atomic motions involved give rise to a novel form of diffusion, which, due to small activation energy of a phason flip, is expected to be much faster than the conventional vacancy driven diffusion in crystals and glasses. An intellectual appeal of this phenomenon is in that the transparent geometry of phason fluctuations provides a clear interpretation of the relevant modes in terms of local atomic motion. In this study, phason mediated structural relaxations as well as the related atomic diffusion were observed in a realistic 3D model of a dodecagonal quasicrystal simulated by Molecular Dynamics (MD). The model is based on a short-range pair potential, conceived to favor icosahedral local order in the first coordination shell. The quasicrystal has been formed by this model from the liquid state as it was undercooled at constant density  $\rho = 0.84$  below its apparent melting point at  $T = 0.5$  (the Lennard-Jones reduced units are adopted in this simulation). It represents a uniaxial stacked layered structure with 12-fold symmetry. Figure 6.3 depicts the projected configuration of a structural layer; It is composed of CN14 blocks (hexagonal antiprisms) which are seen at the projection as dodecagonal rings. By connecting the adjacent centers of these rings, a characteristic tiling with 12-fold sym-

metry is produced. Besides squares and triangles, characteristic of the related Frank-Kasper phases, it includes  $30^\circ$  rhombi and 3-fold hexagons (shields). The structure observed demonstrates a close consistency with the real dodecagonal phases formed by Ni-Cr and V-Ni-Si alloys.

Figure 6.3 presents the dynamics which the model displays at reduced temperature  $T = 0.48$ , while remaining in apparent thermodynamical equilibrium. The principal observation is a considerable rate of spontaneous local structural rearrangements resulting in tile flips, which can be seen as mutual transformations of the rhombi and the shields. Although changing the tiling dramatically, this dynamics does not violate its global 12-fold symmetry. These flips can be analyzed by comparing with the perfect 12-fold tiling patterns as produced by projection method. This analysis associates the rhombus-shield flip with a fluctuation in the boundary of the acceptance region, defined in the phason space. Thus, the transformations observed may be interpreted as phason dynamics. Figure 6.4 demonstrates that the two structures shown in Figure 6.3 are entirely coherent and possess the same long-range order.

We also observe that the phason dynamics is coupled with the dynamics of vacancies the presence of which one can see in Figure 6.3. The prohibitively high energy cost of the vacancy creation implies that the phason dynamics must preserve their number. Note that both of the two structural blocks connected by the phason flip contain an octahedral configuration. In the transformation observed, this element, which may be regarded as a defect in otherwise tetrahedrally packed structure, is topologically moved from its location in the center of the rhombus to the center of the shield. Thus, the flip, preserving both vacancies and octahedra, is energetically degenerate.

The phason flips described recurrently involve each atom in an uncorrelated hopping, which gives rise to the unbounded diffusion. For sufficiently large times, the atomic motion is a random walk with asymptotically linear mean square displacement. The temperature variation of the estimated diffusion coefficient demonstrates Arrhenius behavior in the temperature domain that corresponds to the stable quasicrystal phase. This can be regarded as an indication that the activation energy for the diffusion mechanism involved does not change with temperature.

This result is the first observation of phason dynamics in a 3D quasicrystal. It provides important insight into the microscopic mechanism of this phenomenon. The energetically degenerate phason dynamics observed indicates that quasicrystals represent a special phase of condensed matter where the long-range order is stabilized by the entropy. For details see [Dzugutov, 1996a], [Dzugutov and Phillips, 1995] and [Dzugutov, 1995].

*This result is the first observation of phason dynamics in a 3D quasicrystal*

**Figure 6.3.** Two configurations of a structural layer separated by  $10^6$  timesteps. Tiling is produced by connecting the adjacent centers of apparent dodecagonal rings.

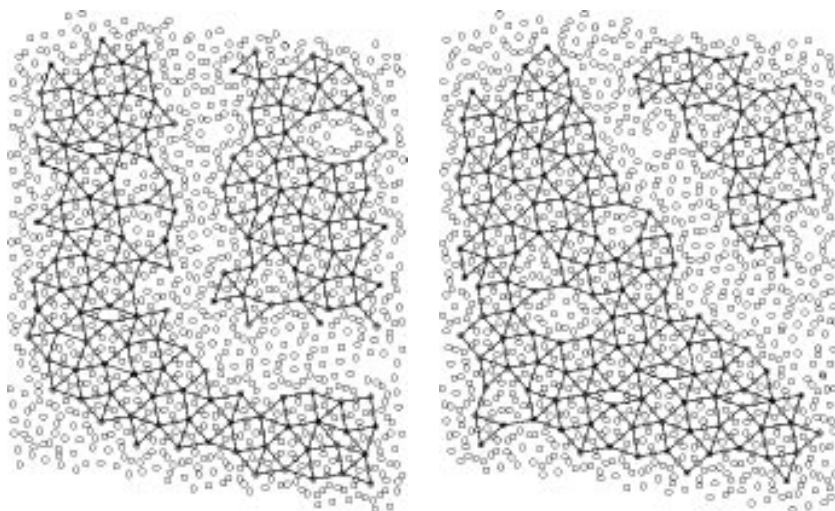
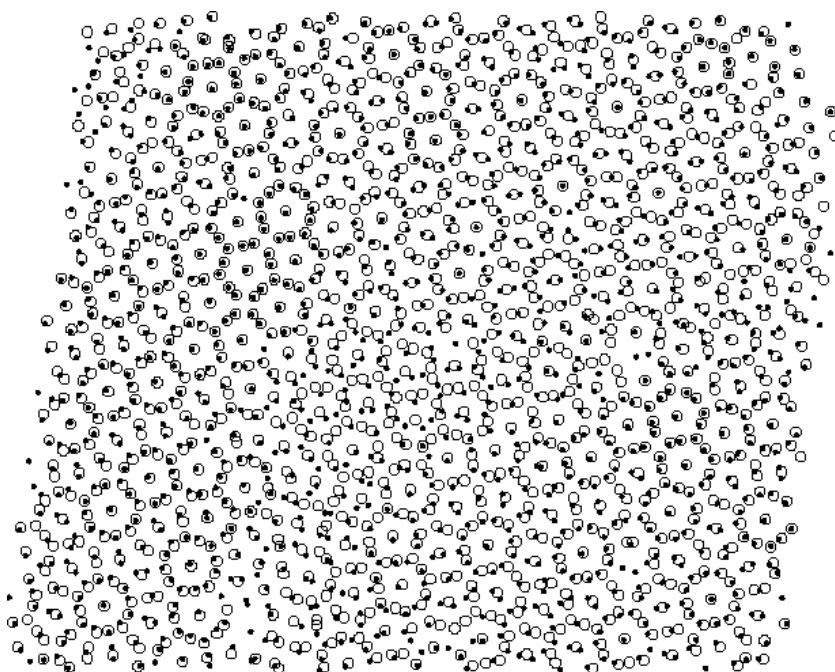


**Figure 6.4.** Two sets of symbols represent superposition of the two configurations of a layer depicted in Figure 6.3



### 6.3 Electric and Magnetic Non-Linear Properties Obtained with Response Theory

*Patrick Norman, Dan Jonsson, Olav Vahtras, Hans Ågren*  
Department of Physics, Linköping University

The basic goal of our current research is to relate the appearance of the strong non-linearity with both electronic and geometric structures of materials, with the ultimate goal in mind to design optically active and conducting devices through the use of molecular modeling and computations. We focus on quantum first-principle methods, since their inherent fulfillments of rigorous computational criteria are very useful for pinpointing specific properties and functions of particular chemical groups and substituents. The response theory methods have been developed in a broad Scandinavian collaboration and is now routinely applied to a number of non-linear properties, be it magnetic and electric, internal and external, time-dependent and time-independent, etc. Some of these are exotic, others have a very strong potential for technical applications and material science. Our efforts are collected into the DALTON [Helgaker *et al.*, 199X] quantum chemistry program, which has been used for all the presented calculations. In Linköping we have, so far, focused our applications on the following three non-linear effects.

- Materials with strong second and third harmonic generations, SHG and THG. Such materials can be used for doubling, respectively, tripling of laser frequencies, introducing laser technology into the blue and near-UV wavelength regions. The SHG and THG capabilities are directly connected with hyperpolarizability tensors that we now can compute for polymeric compounds, metal-polymer interfaces, bucky molecules and solid charge transfer complexes, all with exceptional properties in this area. The industrial impact of UV lasers in the electronic industry is obvious, only to mention the possibility to manufacture extremely compact storage disks (CDs). We use here the double direct random-phase approximation (RPA) and also the quadratic and cubic response extensions of RPA.
- Electro-optic and magneto-optic Kerr effects. These effects, connected to the electric, respectively magnetic, hyperpolarizabilities and susceptibilities, describe the action of external fields (electric or magnetic) on the polarization directions of light. A switch (or not) of the polarization plane gives an efficient representation of binary 0:s or 1:s, and Kerr compounds, like, probably, some first row transition metal alloys, therefore hold great promises as materials in future optical computers.
- Strong charge transfer complexes with potential use as optical switches. Simulations of 1-dimensional charge transfer complex for which a strong in-plane longitudinal excitation dominates the hyperpolarizability, are now being extended to 2- and 3-dimensional charge-transfer

compounds with several donors and/or acceptors connected to the ring systems (so-called quadrupolar and octopolar molecules). Due to competing in-plane orthogonal excitations and "phase-matching" these are suitable non-linear materials. With reaction field response model calculations the critical role of the surrounding solvent can be monitored. The calculations of non-linear electric properties have mostly focussed on hyperpolarizabilities that connect directly to measured non-linear susceptibilities. These quantities play a key role in the understanding of non-linear optical response of molecules. The molecular systems that we have accessed fall largely into three categories; small systems, such as neon isoelectronic hydrides, for which extensive computational tests on electron correlation, basis sets, role of frequency dependence and vibrational dependence have been accomplished; oligomer sequences, in particular polyenes and polyenes for which the length dependence and convergence to the polymer value of the hyperpolarizability is of interest, and; special donor-acceptor compounds, in particular disubstituted benzenes, for which the charge transfer character of the HOMO-LUMO (highest occupied to lowest unoccupied molecular orbital) excitations implies large polarizabilities and hyperpolarizabilities.

#### *Why do we need parallel computing?*

The development of *ab initio* methods is driven by on one hand the theoretical improvements and on the other hand the development of more powerful computing resources and is aiming at an improved description of large scale systems. Solving the Schrödinger equation for a molecule at the *ab initio* level forces us to compute a vast number of integrals for the two-electron Coulomb operator. Traditionally a quantum chemistry calculation is preceded by computing all the needed integrals and storing them on disk. However, since the number of integrals grows as the number of basis functions to the fourth power we soon end up with a problem of storage. As the speed of computers has drastically increased we have been lead to a different (*direct*) strategy, namely to recompute the integrals whenever needed, for which the efficiency is determined by the ratio of I/O and computing speed. The former method is at present faster but as mentioned it suffers from the disk space deficiency. Thus by combining *direct* methods with parallel computing, we not only avoid the bottleneck of disk space but also drastically improve the speed of large-scale calculations. Furthermore, the CPU demanding tasks are strongly localized to a few subroutines so that our parallel implementation is relatively easy to perform and, in addition, will be very effective, cf Table 6.1. Recently, we have presented this technique by calculating the polarizability and second hyperpolarizability at the RPA (Random Phase Approximation) level for a number of  $\pi$ -conjugated compounds.

*By combining direct methods with parallel computing, we not only avoid the bottleneck of disk space but also drastically improve the speed of large-scale calculations*

# rings	# nodes	Slave efficiency	Total efficiency	Theoretical
1	9	98.5	85.2	88.9
2	8	99.1	86.8	87.5
3	9	99.0	87.5	88.9
4	8	99.1	86.5	87.5
5	8	99.2	86.6	87.5
6	10	98.9	88.8	90.0

**Table 6.1.** Parallel efficiency for the polyacene calculation described below. The number of nodes is the total number of nodes (including the master), and the number of slaves is this number minus one.

As a selection of recent publications we would like to refer to [Ågren *et al.*, 1993, Norman *et al.*, 1996b, Norman *et al.*, 1996a, Jonsson *et al.*, 1996]. More information can be found at our web site:

<http://www.ifm.liu.se/Compphys/html/publicat.html>

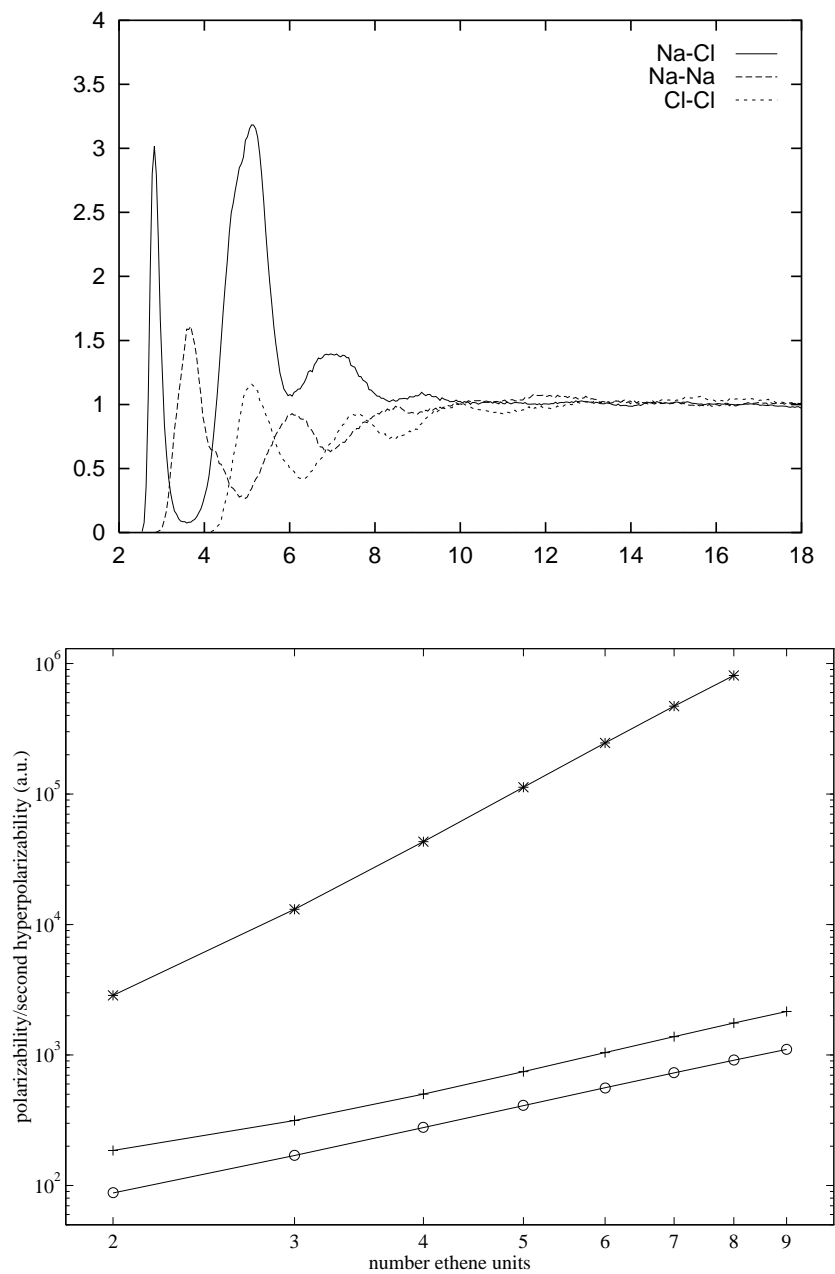
### *Recent results with parallel computations*

#### *Trans-polyenes*

Polarizability and hyperpolarizability calculations of the first excited  $B_u$  state are carried out as a first choice for polyenes, since the  $1B_u$  state, determining the energy gap, presents the main feature of the absorption spectrum and plays a key role in understanding the mechanism of the optical linearity and nonlinearity. A good description of the  $1A_g \rightarrow 1B_u$  transition is a requirement for reliable polarizability calculations and it is therefore important to compare calculated excitation energies with experiment. It has been shown that the excitation energies of the  $1B_u$  states for the short polyenes (from  $C_2H_2$  to  $C_8H_{10}$ ) can be accurately determined at the RPA level using optimized geometries. But we see from Figure 6.5 that also polymeric geometries predict excitation energies in excellent agreement with the experimental data (included as crosses) for those molecules as well as for  $C_{10}H_{12}$  and  $C_{12}H_{14}$ . We observe that the length dependence of the energy gap is well described by a power law, here with  $E_g \propto N^{-0.4}$ , cf. Figure 6.5.

A power dependence with  $\alpha_{xx}^{1B_u} \propto N^{1.8}$  is found for the excited state polarizability. Compared to the ground state polarizability,  $\alpha_{xx}^{1A_g}$ , an enhancement of approximately a factor of 2 is found for all members of the polyenes. This appears as an additive shift in the logarithmic plot, see Figure 6.5. It is known that for polyenes  $\alpha_{xx}^{1A_g}$  is dominated by the virtual transition from the ground state to the excited  $1B_u$  state. Although such a transition is still of importance for the excited state polarizability,  $\alpha_{xx}^{1B_u}$ , it would only provide a negative contribution to the final value of  $\alpha_{xx}^{1B_u}$  due to the negative transition energy, cf. Equation (6.5). The large positive values for  $\alpha_{xx}^{1B_u}$  thus indicate that the transition moments between the reference  $1B_u$  state and excited  $nA_g$  states are of the same order as that between  $1A_g$  and  $1B_u$ . A major contributor to the ground

**Figure 6.5.** Gap energy (upper) and polarizabilities (lower) versus number of ethene units.



state hyperpolarizability is the transition route



All the transition channels contributing to  $\alpha_{xx}^{1B_u}$  are included here and since the RPA method already has provided ground state polarizability and hyperpolarizability values for polyenes that are in excellent agreement with experimental gas phase data we believe that the excited state polarizability,  $\alpha_{xx}^{1B_u}$ , also should be well described at this level.

$$\alpha_{r_0, r_1}(\omega_0; \omega_1) = P(0, 1) \sum_{f \neq 0} \frac{\mu_{0f}^{r_0} \mu_{f0}^{r_1}}{\omega_{f0} - \omega_1} \quad (6.5)$$

Also the ground state hyperpolarizability is shown in Figure 6.5 displaying a power form dependence of  $\gamma_{xxxx}^{1A_g} \propto N^{4.2}$ .

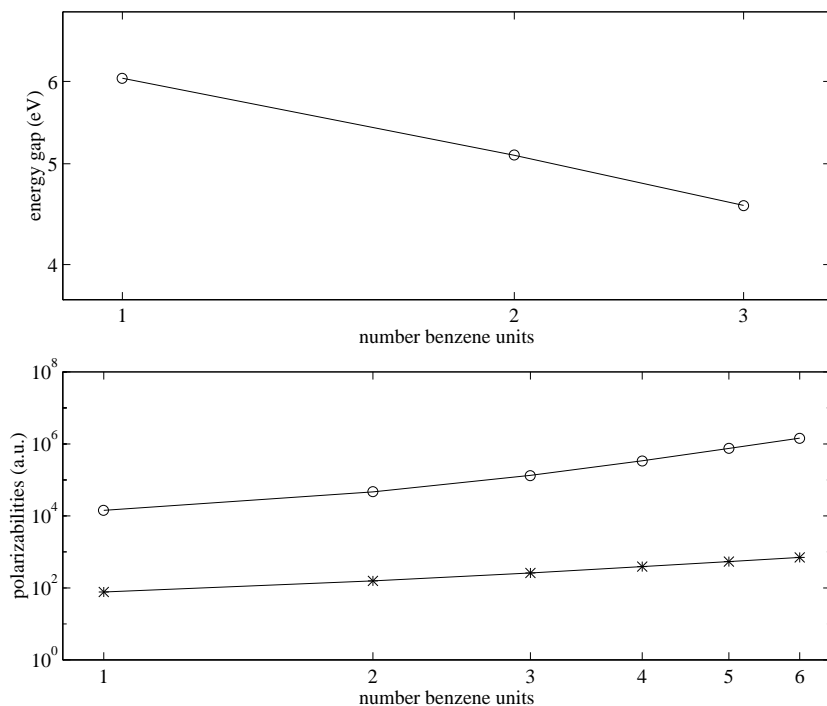
### *Polyacenes*

Much theoretical work have been devoted to linear conjugated systems for which the size dependence of non-linear response and the relationship between the optical properties and electronic and geometrical structure parameters have been of special interest. Although the gap in size between systems that are manageable for theoretical investigations and those of technical interest has been narrowing, the applicability of *ab initio* calculations of non-linear optical responses is still restricted by the rather large basis sets needed. Because of the size of the constituting units, the polyacenes belong to the category of interesting systems, which, except for the first three members, has been out of reach for *ab initio* calculations of its non-linear properties. This is unfortunate from the point of view that many promising optically active materials contain benzene rings as building blocks, often connected by special bridge units and terminated by groups of donor/acceptor character. It is therefore desirable to investigate further the polyacenes as model compounds and compare, for example, with the linear polyenes for which a great deal already has been learned.

We here demonstrate that with an effective parallel implementation of non-linear response theory at the random phase approximation level, calculations of polarizabilities and hyperpolarizabilities can be applied to systems that are sufficiently large to be of technical interest. Apart from directly predicting properties, these calculations make it possible to calibrate trends from already established semi-empirical techniques. The polarizability and the second hyperpolarizability of the molecules in the polyacene series, chosen here for illustration, were found to scale as  $N^{1.4}$  and  $N^{3.5}$ , respectively, where  $N$  is the number of benzene units, see Figure 6.6. These scalings are weaker than those predicted for the linear polyenes in terms of ethylene units.

*Calculations of polarizabilities and hyperpolarizabilities can be applied to systems that are sufficiently large to be of technical interest*

**Figure 6.6.** Gap energy (upper) and polarizabilities (lower) versus number of benzene units.



## 6.4 Finite Element Modeling of Acoustic Emission

*Anna Sundström*

Department of Solid Mechanics, KTH

As a part of an ongoing research project directed into analysis of Acoustic Emission as a method for quantitative measurements of damage evolution in structural materials, a Masters Thesis project [Sundström, 1996] was carried out on finite element modeling of wave propagation in composite laminates.

Acoustic emission is the term used to describe the spontaneous release of transient elastic waves in solids caused by sudden localized changes in stress. In order to determine the wave propagation characteristics that result from micro crack initiation in composite laminates, accurate numerical models must be developed. In the present work two different models for transverse micro crack initiation in composite laminates have been investigated, one with a crack through the middle layers of the composite and the other one with an edge crack. The calculations have been carried out by the Finite Element program Spectrum on the IBM SP-2. The numerical results have been analyzed in terms of wave propagation modes and frequency content.

Spectrum is a commercial finite element solver designed for the analysis of multiple and interacting physical phenomena. It supports static and transient solutions, linear and nonlinear structures, a comprehensive set of material models, compressible and incompressible flows, turbulence models and ALE fluid mesh movement.

One of the most important objectives of the Spectrum program is to develop a capability for large-scale engineering simulations. In addition to the multiphysics capabilities, the Spectrum Solver is designed to make maximal use of high-performance parallel computer systems. The same architecture that supports multiple physics simulation naturally and cleanly supports independent and parallel computation.

To enable higher levels of parallelism and to achieve better load balancing of the parallel computation, Spectrum also incorporates an automatic domain decomposition feature. Individual regions can be subdivided into subdomains to any user specified level. Spectrum employs a spatial decomposition algorithm called Recursive Spectral Bisection (RSB). Simply stated, each physical region (or subdomain thereof) can be run in parallel on separate processors. Therefore, the entire work loads of each subdomain are run in parallel, not just part of the computations (i.e. not just the linear equation solver).

*The entire work loads of each subdomain are run in parallel*

## **6.5 An Exact Absorbing Boundary Condition for 3D Thin Structures**

*Jiasu Cao, Sailing He*

Department of Electromagnetic Theory, KTH

In many scattering computations (in particular, for time-domain three-dimensional scattering), it is essential to use a mesh of limited size and apply proper boundary conditions on the boundaries of the mesh. All the widely used absorbing boundary conditions are approximate conditions. They may give perfect absorption at a certain angle of incidence, but they are far from perfect for many other angles, in particular, near the grazing angle. In some scattering situations, such as a point source closely above a thin structure, the accuracy of the absorbing boundary conditions is crucial, and a local approximation of the absorbing boundary condition may not give a reliable numerical result. Thus, an exact absorbing boundary condition is desirable in these situations. This has been demonstrated by numerical examples.

The exact absorbing boundary condition is in fact a by-product of the three-dimensional wave-splitting formalism for time-domain scattering problems. Wave-splitting is the decomposition of the total field into two components which propagate in opposite directions in a homogeneous region. The two opposite propagating waves obey down-going and up-going wave conditions respectively, which are exact absorbing boundary

conditions, because so called down-going, or up-going, means propagating without any reflection. By formal Taylor expansion, different orders of local approximations can be obtained from the exact absorbing boundary condition.

We have implemented the exact absorbing boundary condition on the Connection Machine CM200 and conducted several numerical simulations for both non-dispersive and dispersive thin structures. The results show that using the exact conditions can bring remarkable improvement, comparing using the conventional second order local approximation, though it's more time consuming to use the exact conditions. For further details see [Cao and He, 1996].

## 6.6 The Continuation of Transient Data for a Hyperbolic Equation in a 3D Inhomogeneous Half-Space

*Jiasu Cao, Sailing He*

Department of Electromagnetic Theory, KTH

For any time-domain layer-stripping approach to an inverse problem, one has to propagate the transient wave field (the Dirichlet data) and its normal derivative (the Neumann data) to the next layer below (layer by layer) starting from the surface data which can be obtained from experimental measurements. In the present project we treat such a data continuation problem for the second order hyperbolic equation.

We have considered the ill-posed problem of the time-domain data continuation for a second order hyperbolic equation in a 3D inhomogeneous half-space. Two different approaches, namely the local continuation approach and the wave-splitting approach, have been used to propagate the surface data (the fields and their normal derivatives) to the data at deeper planes. A local continuation theorem has been given, and its finite-difference form has been used for the data continuation. To obtain a stable continuation result, a regularization process at each time at each plane is necessary in the local continuation approach. The wave-splitting approach uses larger transverse spatial domain of dependence, and gives reasonably stable results even without any additional smoothing process. Both methods have been implemented on the Connection Machine CM200. Also comparison has been made between the local continuation approach, the wave-splitting approach, and the finite difference time domain method by several numerical simulations of acoustic wave propagation. For further details see [Cao and He, 199X].

## 6.7 Hypercycles versus Parasites in Spatial Models of the Origin of Life

*Mikael Cronhjort*

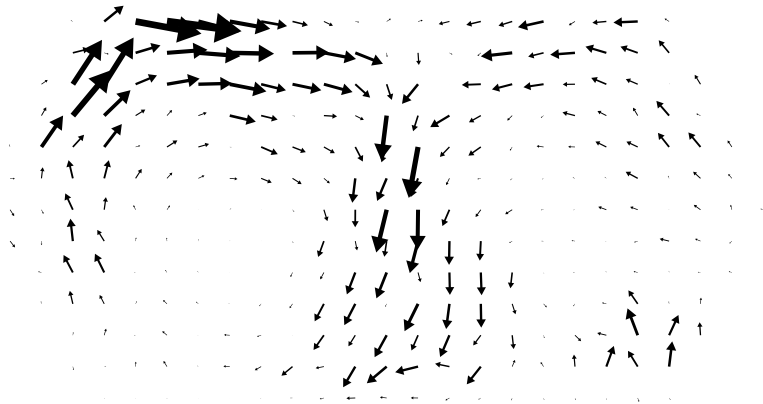
Department of Theoretical Physics, KTH

Reaction-diffusion systems often lead to spatial patterns which appear for a large number of different applications. Three dimensional scroll waves, for instance, are known from the Belousov-Zhabotinsky in chemistry and the Ginzburg-Landau equation in superconductivity. They also appear in the three dimensional hypercycle system, which has been proposed as a model for accumulation of information at an early stage in the origin of life [Eigen *et al.*, 1981]. The hypercycle is a molecular system in which a number of RNA-like “species” catalyse the replication of one another: Species 1 catalyses the replication of species 2, which catalyses species 3, and so on. The last species,  $n$ , closes the cycle by catalysing the replication of species 1. A parasite is a molecule which has lost the ability to catalyse any replication, but it still receives catalytic support from the hypercycle for its replication. Such parasites may be fatal for the system.

Spatial models of this system can be of two different types: partial differential models, or cellular automata models. In both models replication, decay, and diffusion of the molecular species considered. The differential equations are approximated with finite difference equations for the concentrations of the molecular species. In the cellular automata, which are highly discrete models, each lattice point can be either empty or may contain a single molecule, which may interact with its neighbors according to certain rules including random events. On the Connection Machine a three dimensional cellular automaton simulation, which is suitable for parallel computing, takes about a day. On other machines, it would require a month of CPU time.

The spatial organization that arises is essential for obtaining resistance to parasites in these systems: Without it, parasites are likely to kill the hypercycle. In two dimensions spiral patterns arise [Boerlijst and Hogeweg, 1991, Cronhjort and Blomberg, 1994]. The spirals are resistant to parasites in cellular automata models, but not in partial differential equation models. As mentioned above, scroll waves arise in three dimensions [Cronhjort and Nyberg, 1995]. These have a spiral cross section but are extended along a singular filament (the spiral axis). If the filament is a closed circle, the scroll wave is called a scroll ring (see left part of Figure 2.21 on page 23). The three dimensional scroll waves do not seem to offer any resistance to parasites [Cronhjort, 1995]. In two and three dimensions many different types of clusters can be formed (see right part of Figure 2.21 on page 23) [Cronhjort, 1995]. Work is in progress on understanding these clusters better.

**Figure 6.7.** In the figure, the system spontaneously forms a two cell convection. The lattice size is actually  $128 \times 64$  sites, and the length of each arrow is proportional to the linear momentum averaged over several sites.



## 6.8 A Coupled Map Lattice Model of Self-Propelling Particles

*Jan Hemmingsson*

Department of Physics, Linköping University

Inspired by the spatial patterns formed by organisms in nature, we have tried to design a toy model that would be able to reproduce some of these effects. Examples of such collective behavior where the patterns are much larger than the participating particles range from birds flying in formation to swimming microorganisms [Childress, 1981].

Our starting point is systems of granular media on air table, where the energy is actually dissipated in the collisions. Our numerical model is a coupled map lattice and resembles the popular lattice gas models that have been widely used the last few years [Frisch *et al.*, 1986, Frisch *et al.*, 1987]. Instead of simulating discrete particles, the model treats densities of mass. It has three parameters; viscosity, acceleration and dispersion. Since energy is really dissipated in the collisions, energy has to be reintroduced by acceleration. The acceleration of each particle is taken to be in the direction of its velocity, and can be motivated by the disordered energy input by shaking or stirring of granular media. However, our approach is purely phenomenological, and we do not intend to simulate any specific system. For details of the model, please see [Hemmingsson, 1995].

The simulations were performed on a triangular lattice, and to make the reflecting boundaries as symmetric as possible, they were given a hexagonal shape. What happens after the system has been randomly initiated, is that convection can be found, see Figure 6.7. Above some energy input, the convection seems to be instable, just as one would expect.

This project was supported by the Swedish Institute and the Swedish Natural Research Council (NFR).

## 6.9 Monte Carlo Studies of the Dynamics of Re-Entrant Ising Spin Glasses

*Jan-Olov Andersson*

Nordita, Denmark

*Tomas Jonsson, Johan Mattsson*

Solid State Physics, Centre of Technology, Uppsala University

### *Background*

Spin glasses are magnetic system with two fundamental properties: randomness and frustration. Randomness in the sense that the interactions between the magnetic moments (the 'spins') of the magnetic atoms, i.e. can be either ferromagnetic or antiferromagnetic in a random fashion. Frustration can be illustrated by the fact that for three spins with an antiferromagnetic coupling there is no way to satisfy all bonds at the same time. This leads to a nontrivial energy landscape. For a spin glass the energy landscape gets extremely complicated which leads to very slow dynamics. The slow dynamics is seen by the fact that the magnetization is different when cooling in an external magnetic field, the field cooled (fc) procedure, from cooling in a zero field and then apply the field, the zero field cooled (zfc) procedure.

Spin glass behavior has been found experimentally for a number of materials, but basically there are two major types of spin glasses. Metallic spin glasses consists of a small concentration of magnetic atoms (like Fe, Cr or Mn) in a nonmagnetic host (like Cu, Ag or Au). The randomness is due to the random positions of the spins and the RKKY interaction between the spins. The RKKY interaction oscillates with distance  $R$  between the spins and the magnitude of the oscillation decays as  $R^{-3}$ . In insulating spin glasses the magnetic moments are positioned regularly but by using a mixture of magnetic atoms, e.g. Fe and Mn, the interactions are different for Fe-Fe, Fe-Mn and Mn-Mn, which can lead to spin glass behavior.

The standard model for a spin glass, the Edwards-Anderson (EA) model [Edwards and Anderson, 1975] leaves out the microscopic details, but still captures the essential points of the physics in question. The Hamiltonian considered is

$$\mathcal{H} = -\frac{1}{2} \sum_{i,j} J_{ij} S_i S_j + H \sum_i S_i, \quad (6.6)$$

where  $J_{ij}$  is the interaction between spin  $i$  and spin  $j$ . The simplification in the model is (a) to put the spins onto the sites of a regular lattice and (b) to introduce the disorder by choosing a suitable distribution  $P(J_{ij})$  of exchange interactions. EA's choice is a Gaussian bond distribution  $P(J_{ij}) = (1/\sqrt{2\pi J}) \exp(-J_{ij}^2/J^2)$  with zero mean and variance  $J^2$ . Normally, for practical reasons, the variance is set equal to 1. The interactions can be either long or short ranged. In the latter case, only

nearest-neighbor interactions are considered. For insulating spin glasses the ' $\pm J$ ' probability distribution, i.e. the bonds are  $+J$  with a probability  $p$  (normally  $p = 0.5$ ) or  $-J$  with the probability  $1 - p$ , is slightly more realistic.

The mean field (MF) solution, based on the EA model, turned out to be very far from trivial and was solved around 1980. Since MF is only correct for high spatial dimensions (above 8 in the spin glass case) some qualitative understanding can be gained from it. In order to study the behavior at physical dimensions numerical methods have to be used.

Less is known about the behavior in low dimensions. No exact solution exists in two or three dimensions, but renormalization group arguments [McMillan, 1984, Bray and Moore, 1985] supported by numerical results are the basis for the droplet model [Fisher and Huse, 1988, Koper and Hilhorst, 1988] which in contrast to the mean field solution has only two thermodynamical states, related by a global spin reversal and as a consequence there exists no spin glass phase in non-zero magnetic field according to this model.

When considering competition between spin glass and ferromagnetic or antiferromagnetic order even less is known. In the SK model, for Ising spins with a Gaussian bond distribution with  $J_0/J < 1$  one has a spin glass state without spontaneous magnetization  $M_s$ . For  $J_0/J_1$ , the system goes with decreasing temperature first into ferromagnetic state and then into a spin glass state with replica symmetry breaking. Since this state has a non-zero spontaneous magnetization it is sometimes called a 'mixed' state or a 'magnetized spin glass'

Whether the 'mixed' phase exists for low-dimensional samples is not entirely clear. Neutron-scattering results on several re-entrant ferromagnets have shown that, within experimental resolution, the ferromagnetic Bragg scattering, present in the ferromagnetic phase, disappears at low temperatures [Maletta *et al.*, 1982]. It can from this be concluded that true reentrance may occur in low-dimensional magnets. Recently it was shown for a re-entrant ferromagnet that there exists a linear response region at low temperatures and a dynamic scaling analysis in that region indicate a transition to a spin glass phase [Jonason *et al.*, 1996, Jonason *et al.*, 199X]. However, neutron depolarization experiments on reentrant ferromagnets suggest a randomly canted ferromagnet rather than a pure spin glass at low temperatures [Mirebeau *et al.*, 1990].

Several experimental observations of re-entrance have been obtained during the last years, but the results have in some cases been attributed to long range interactions or from transverse spin components [Reger and Young, 1989]. Our purpose has therefore been to show that the qualitative features found in the experiments are evident also as the results of numerical simulations on the CM200 of a nearest-neighbor interaction Ising model.

### *Ac field dependence of the Ac susceptibility*

We first studied the ac- and dc-field dependence ( $H_a = H_{dc} + H_{ac} \sin(\omega t)$ ) of the ac susceptibility. In the case of  $H_{dc} = 0$ , the results were found to be in agreement with corresponding zfc simulations and in qualitative agreement with experimental results. Although similar results have been obtained in earlier simulations this shows that the results are reasonable and that therefore the new results are also reliable. At high temperatures  $\chi(T)$  follows a Curie law behavior, with  $\chi'(T) = 1/T$  and  $\chi''(T) = 0$  and  $\chi$  being independent of frequency, indications of equilibrium. As the temperature is lowered,  $\chi'$  departs from Curie behavior and  $\chi''$  starts to grow. The temperature at which  $1/\omega = t_{eq}$ , where  $t_{eq}$  is the equilibration time, defines a freezing temperature  $T_f(\omega)$  and can be identified from either the peak in  $\chi'(T)$  or the inflection point in  $\chi''(T)$ .  $T_f$  decreases with decreasing  $\omega$ , just as can be expected from critical slowing down,  $t \propto (T - T_g)^{-z\nu}$ . Using our data, we find  $T_g \approx 1.0$  and  $z\nu \approx 9.1$ , which is in reasonable agreement with earlier determinations of transition temperature and exponents using other numerical methods considering our relatively limited frequency range.

The equilibrium susceptibility is never strictly linear, but is always nonlinear to some extent. However, the non-linearity depends on the temperature, which implies that for any field there will be an intermediate field region where the non-linearity is relatively strong and a high-temperature region where the non-linearity is negligible within the statistical accuracy. However, for any temperature above the phase transition or rather any temperature above the freezing temperature corresponding to the longest time scale reachable in a simulation or experiment, there is a low-field regime for which linear response almost applies. On the other hand, at low temperatures, equilibrium is never reached and in this case the magnetic response is limited by the dynamics which leads to a time scale dependent linear response regime. In the inset we can observe the dynamics-limited linear-response regime at low temperatures and we can also observe that although the susceptibility is never exactly field independent its field dependence is within the statistical resolution of our results. The strongest field dependence can be found near the freezing temperature, where there is a transition between the different regions. It is interesting to observe the  $H_{ac}$ -dependence seen for  $H_{ac} = 0.4$ , where we clearly observe the effect of the nonlinearity. Since the equilibrium susceptibility decreases with field it is not surprising that the observed susceptibility is lower than the low-field susceptibility at high temperatures. However, for low temperatures, the behavior is the opposite: the susceptibility is higher than the low-field susceptibility. Although at first surprising, this can be understood from the fact that the dynamics-limited susceptibility after its linear regime increases with field. Only when  $N_{mc}$  is larger than the equilibration time  $t_{eq}$ , equilibrium is reached in the simulation and the result is the equilib-

rium ac susceptibility. However,  $\chi(\omega, T)$  is close to its quasi equilibrium dynamics value when  $N_{mc} \gg P$ .

#### *Dc field dependence of the ac susceptibility*

The results in the nonzero  $H_{dc}$  case show a remarkable qualitative agreement with experimental results [Mattsson *et al.*, 1993a]. The reason for the interest in using a non-zero  $H_{dc}$  is that in this way it is possible to study the quasi equilibrium behavior within a linear response regime at a non-zero field by using a small  $H_{ac}$  to probe the system. At high temperatures, the susceptibility is independent of frequency but a relatively strong  $H_{dc}$ -dependence is seen. The differential field cooled (fc) susceptibility  $\chi_{FC} = dM_{FC}/dH$  can be found to coincide with the ac susceptibility in this region. Not too surprisingly, it can be observed that the susceptibility seems to become independent also of  $H_{dc}$  within the experimental resolution for very large temperatures. More interesting is the crossover from the frequency-independent susceptibility region to a frequency-dependent and  $H_{dc}$ -independent region.

The results can be understood in the following way. At high temperatures  $1/\omega \gg t_{eq}$  and the system has sufficient time find the equilibrium susceptibility. On the other hand, at low temperatures,  $1/\omega \ll t_{eq}$  and the system is unaware of any dc-field which results in a  $\omega$ -dependent but  $H_{dc}$ -independent susceptibility. As  $1/\omega = t_{eq}$  defines the freezing temperature  $T_f$  both components of  $\chi$  obey  $\chi(H_{dc}, T, \omega) = \chi(H_{dc} = 0, T, \omega)$  for  $T < T_f(H_{dc}, \omega)$  and  $\chi(H_{dc}, T, \omega) = \chi(H_{dc}, T, \omega \rightarrow 0)$  for  $T > T_f(H_{dc}, \omega)$ . In the figures the crossover is seen as a crossover rounding in the vicinity of  $T_f(H_{dc}, \omega)$ . However, a much better way is to obtain  $T_f(H_{dc}, \omega)$  as the crossing between  $\chi(H_{dc} = 0, \omega)$  and  $\chi_{FC}(H_{dc})$ .

#### *Aging behavior in a non-zero $H_{dc}$*

The results of this kind of simulations for  $H_{dc} = 0$  were presented in earlier papers [Andersson *et al.*, 1992, Andersson *et al.*, 1994]: an inflection point in  $m(t, t_w)$  and a corresponding maximum in  $\partial m / \partial \log(t)$  is found at a time  $t \approx t_w$ . We also show that the applicability of the fluctuation-dissipation theorem (see e.g. [Binder and Young, 1986]) only to short times  $t < t_w$  gives evidence for aging behavior being a transition from quasiequilibrium to nonequilibrium behavior. Since the auto correlation function can only be related to the equilibrium susceptibility in the symmetric bond, zero field case, we do not present the auto correlation function at all in this paper.

Clearly the aging behavior can still be observed for non-zero  $H_{dc}$  and the aging behavior is not very much influenced by the field. The observed weak  $H_{dc}$ -dependence agrees well with the fact that the ac susceptibility is nearly  $H_{dc}$ -independent at low temperatures, although the  $H_{dc}$ -dependence is somewhat stronger in the aging behavior than in the ac susceptibility.

### *Competition between spin-glass and ferromagnetic order*

As was already mentioned, there is a strong non-linearity of the magnetic response on the applied field (due to the ferromagnetic ordering), even though there exists a low-field region at low temperatures where  $\chi$  does not depend on the probing field. Thus ac-susceptibility or zero field cooled magnetization measurements can reveal inherent zero-field dynamics of re-entrant ferromagnets at low temperatures, provided that the probing field is chosen to be sufficiently small. It also implies that care had to be taken in our simulations to ensure that a small enough  $H_{ac}$  was used. A cusp in  $\chi'(T)$  at relatively high temperatures signals the ferromagnetic phase. Well below the maxima in  $\chi'(T)$  and  $\chi''(T)$ , both components of  $\chi(T)$  are independent of  $H_{ac}$  just as is found in experiments [Jonason *et al.*, 1996, Jonason *et al.*, 199X]. In other words, for a specific temperature  $T$ , there exists a linear response regime such that  $\chi$  is independent of  $H_{ac}$  for  $H_{ac} < H_{max}$  (within the simulation accuracy of  $\chi$ ). Interestingly enough, the curves for  $H_{ac} < 0.10$  show a second maximum in  $\chi''(T)$ . This is clear evidence of glassy dynamics at low temperatures but whether these features are evidence of a true spin glass phase cannot be determined from these dynamical data.

Clearly, the maximum is even more evident for lower frequencies, but the range of time scales available is too small for us to be able to say anything about the existence of an equilibrium transition. What can be said is that the qualitative features of the simulation results are rather similar to the experimental results. There is a very strong  $H_{dc}$ -dependence near the peaks corresponding to the ferromagnetic transition while the  $H_{dc}$ -dependence at low temperatures looks more like the corresponding dependence in the pure spin glass case. Again, this is not a proof for a true spin glass transition, but it is yet another qualitative agreement with the behavior of experimental spin glasses.

Another typical feature of ordinary spin-glass dynamics is the aging behavior. The susceptibility is found to have a clear  $t_w$ -dependence, but in contrast to the ordinary aging behavior there is no inflection point and no corresponding maximum in the relaxation rate at  $t \approx t_w$ .

### *Competition between spin-glass and antiferromagnetic order*

In the antiferromagnetic case, a maximum in the in-phase component  $\chi'$  can be identified just as easily as in the  $J_0 = 0$  case and in contrast to the ferromagnetic case, this maximum is not plagued by a very strong non-linear field dependence. The peak is found at a temperature of the order 40% ( $J_0/J = -0.7$ ) and 60% ( $J_0/J = -0.8$ ) higher than the peak temperature found for  $J_0 = 0$ . The anti-ferromagnetic transition can also be identified in a small peak in the out-of-phase component  $\chi''$  at a temperature slightly lower than the in-phase peak temperature). The peak is clearly visible in the case  $J_0/J = -0.7$  while it for  $J_0/J = -0.8$  is only barely visible due to the rather small signal-to-noise ratio.

More interesting is the fact that a second peak in  $\chi''$  appears at lower temperatures, much lower than the in-phase peaks. This can be seen in both cases, a clear signature of the antiferromagnetic to spin-glass re-entrant transition. Just as in the ferromagnetic case, this is of course not evidence for an equilibrium transition. In contrast to the results in the ferromagnetic case, the normal aging results with a maximum in  $S(t, t_w)$  at  $t \approx t_w$  are found.

## 6.10 Code Porting and Cluster-Finding Experiences on the IBM SP-2 and the CM200

Lawrence V. Thomas<sup>1</sup>

Department of Numerical Analysis and Computing Science, KTH

### *Introduction*

We describe the initial experiences in porting a code designed mainly for statistical mechanics problems from the CM200 machine to the IBM SP-2. We also present some early results gleaned from the cluster-finding process embedded within that code.

It is seldom that a program is so simple that it contains only one type of parallel computation. The more complex the task of the program, the more likely it contains *data*, *functional* (or task) and/or *master/slave* parallel computation [Koelbel *et al.*, 1994] in some combined form. Thus, it may be useful to know how a given machine runs programs which contain several types of parallel computations.

Another goal of the project is to get code which was originally written in CMFortran for the CM200 converted to High Performance Fortran (HPF) to be used on the IBM SP-2 machine. To do so will give some insights into the probable difficulties which potential users of the IBM SP-2 machine may face when porting their code or writing code for the machine.

The CM200 and the IBM SP-2 may perform quite differently concerning processor-to-processor communications. Therefore, this aspect of the study will focus on how an interpretation of the multigrid algorithm [Brower *et al.*, 1994] performs on the respective machines.

### *Software*

The CoffeePot program is a statistical mechanics program which has been used to perform simulations for supersymmetry in CHC theory [Klein and Batrouni, 1990]. Its main objective is to simulate many body systems, such as Ising or Heisenberg magnets, and analyze their properties [Thomas, 199X]. Such systems can also be evolved over time

---

<sup>1</sup>I would like to thank Jesper Ooppelstrup of NADA for all the input and help he has and continues to provide to this project. Also, a thanks must go out to Helena Strümpel for all her help and input.

via Metropolis algorithms [Gould and Tobochnik, 1985, Metropolis and *et al.*, 1953] and exposed to various conditions after their creation, such as chemical potentials or magnetic fields. These systems are then analyzed for insights into their properties. The CoffeePot program is used in this study [Thomas, 199X] because of its ability to scale lattices and loops, independently and simultaneously.

A major part of the CoffeePot code is the cluster finding routine. Figure 2.1 on page 11 shows lattices before and after cluster-finding. It depicts a system which is typically generated and analyzed by the CoffeePot program. The program must first find all the clusters of isolated “material”. Then the clusters must be labeled so that they are distinctive. Finally the sites within the system can be analyzed for information pertaining to their various properties.

### *Results and Analysis*

The porting of the code from the CM200 to the IBM SP-2 was successfully completed. The code was translated to HPF with a minimal amount of changes. Thus, nearly identical codes now run on both machines with no apparent problems. The main task involved in the port was to rid the CM code of all machine dependent calls (especially libraries) so that it consisted only of standard Fortran90 code. Besides the “purification” of the code, the typical CM Fortran declarations had to be modified to fit the HPF syntax.

The results generated by the cluster-finder revealed that the costs of communications on smaller Ising model lattices can be said to be minimal-to-negligible (see Figures 6.8 and 6.9). If the communications caused by the cluster-finding were more expensive, a greater fall off in the speedup times presented in Figure 6.8 would be expected.

### *Conclusions*

Programs in standard Fortran90 can be easily ported from the CM200 machine to the IBM SP-2. The task becomes more difficult when the translation of libraries are involved. The SP-2 performed better than expected for the CoffeePot code which contains a complex mix of different data structures and operations. When the timing results from the cluster-finding routine were examined, the predicted communication cost [Koelbel *et al.*, 1994, TMC, 1994, Brower *et al.*, 1994] were not found to be too expensive. This bodes well for HPF programs running on the IBM SP-2 architecture.

**Figure 6.8.** The speedup in the cluster-finding operations on the IBM SP-2 and CM200. The speedup is defined as the ratio of the time to perform operations on the least amount of processors (sequencers) by the times it takes to perform the same process on increasing amounts of processors (sequencers). Note that, although the CM200 actually performed better in terms of overall time to complete a simulation, it seemed to have no speedup when going from one sequencer to two. Also, the speedup graph suggests that the performance of the algorithm does not particularly suffer despite the fact that it is communication intensive on the IBM SP-2 (as was expected).

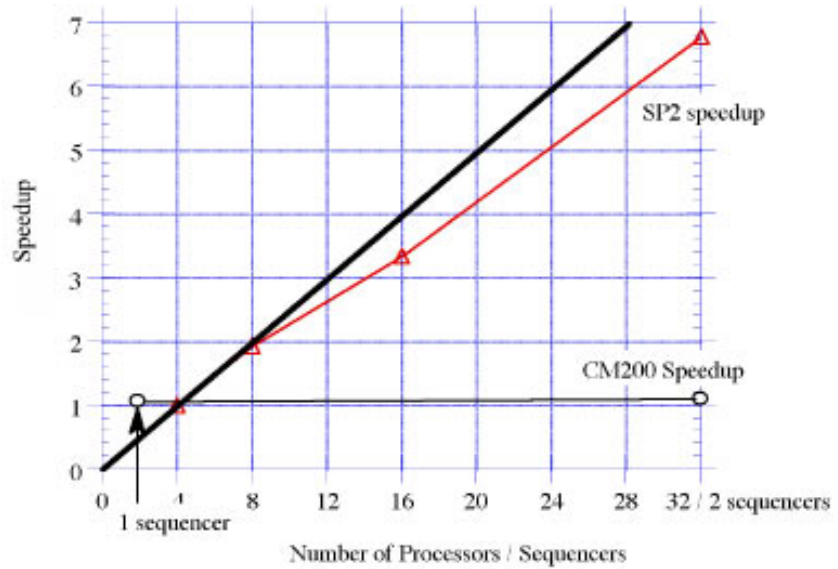
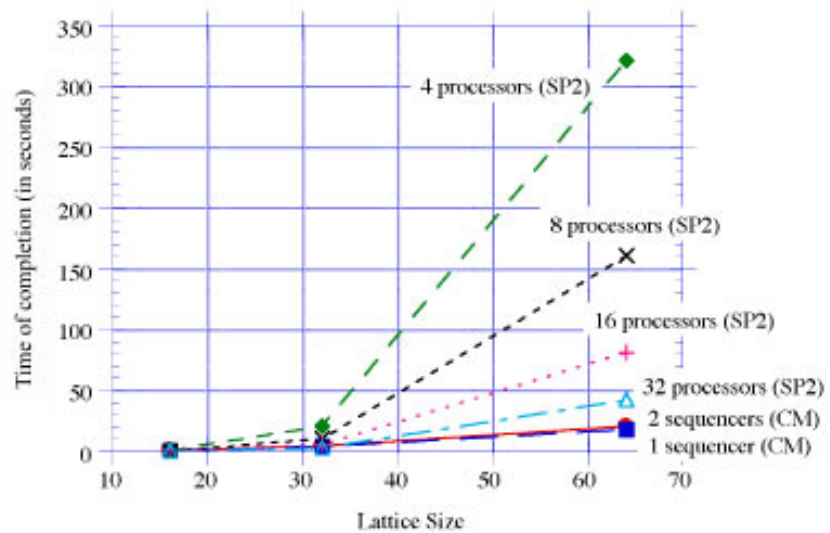


**Figure 6.9.** Timings for the CoffeePot code for different lattice sizes. It can be seen that for this particular code and implementation we need approximately 64 nodes of the IBM SP-2 to reach the performance of the CM200.



## 6.11 Electronic Structure Calculations for the Physics and Chemistry of Surfaces

*Lennart Bengtsson, Thomas Mattsson, Johan Strömqvist,  
Mats Persson, Göran Wahnström*  
Department of Applied Physics, CTH

Over the recent years considerable progress has been made in the developments of techniques for the *ab initio* calculations of the total energy of solids, surfaces and molecules. Plane-wave, pseudopotential methods, based on density functional theory, have now progressed to the point where accurate and reliable calculations can be performed on systems containing tens to hundreds of atoms. These methods will have an increasing impact on our understanding of the physics and chemistry of surfaces. For instance, this expectation has already been confirmed in the field of surface reaction dynamics by groups in Denmark and United Kingdom. They have demonstrated that it is possible to calculate potential energy surfaces (PES) for the dissociation of hydrogen molecules on metal surfaces [Hammer *et al.*, 1994, White *et al.*, 1994]. In particular, this work has provided an answer to the question: “Why Gold is the noblest metal ?” [Hammer and Nørskov, 1995]. We are presently applying these electronic structure methods to the calculation of PESs for atom- and molecule-surface interactions on the IBM SP-2 machine at PDC. This work is done in close contact and collaboration with the group headed by Nørskov at DTU in Denmark.

Before discussing our current projects concerning surface reaction dynamics and quantum diffusion on surfaces, we will first present some details behind the plane-wave pseudopotential method and its implementation. This method calculates the total energy of a many-atom system in a super cell geometry by solving iteratively the one-electron Kohn-Sham equations in density functional theory using the conjugate gradient method in a plane wave basis [Payne *et al.*, 1992]. The ion-core interactions are represented by a pseudopotential and the exchange-correlation energy is treated within the local density approximation. Our serial version of the code, obtained from Hammer at DTU in Denmark, originates from an effective implementation of the plane-wave pseudopotential method that has been developed by Payne and collaborators in Cambridge. Based on this serial version of the code, we have developed a coarse-grained parallel version over  $k$ -points in the Brillouin zone using the parallel virtual machine (PVM) software. PVM enables us to make most of the developments of the code on a local cluster of SPARCstations while the production runs are done on SP-2. The CPU and primary memory requirements of the calculation are determined essentially by three factors; number of valence electrons, the high-energy cut-off and the number of  $k$ -points in the Brillouin zone. Specific examples will be given below.

## *Surface Reactions: Eley-Rideal Dynamics*

*Lennart Bengtsson, Johan Strömqvist, Mats Persson*

For more than 70 years gas-surface reactions have generally been classified in terms of two idealized mechanisms. This classification has been based on the speculation that an impinging atom or molecule can react directly upon striking an adsorbed species in a process that is referred to as an Eley-Rideal (ER) mechanism or in a process that is referred to as a Langmuir-Hinshelwood (LH) mechanism in which the reaction occur between species that have become fully accommodated to the surface. Already in 1922, Irwin Langmuir stated that “With our increasing knowledge of the structure of solid bodies and of the atoms and molecules which they are built we should now ... gradually begin to gain a clear insight into mechanisms of surface reactions.” But only most recently have we begun to gain the expected insight into mechanisms of surface reactions. This progress has been made possible both by the developments of dynamical measurements that goes beyond structural and kinetic measurements and by the aforementioned development of calculational schemes of accurate and reliable PESs that can be used in dynamics calculations.

The Eley-Rideal mechanism for the recombinative reaction between hydrogen atoms on a Cu surface provides an interesting model case suitable for a fruitful interplay between experimental and theoretical studies. In collaboration with Bret Jackson, University of Massachusetts, Amherst, Persson have studied the dynamics of this reaction by propagating wavepackets in a realistic model where PDC has been crucial for the success of these calculations, see Section 6.12 on page 94. These calculations have so far been based on empirical PESs and electronic structure calculations are in progress to construct more convincing and reliable models of the PES. For instance, in order to answer a question like: Is the exothermicity in the PES in the entrance channel as the empirical PESs suggest? This project will include an interesting extension of these methods to include spin-polarization in order to treat the formation of the bond between the incoming open shell hydrogen atom with the adsorbed hydrogen atom.

At this stage, we have calculated the total energy for a  $(1 \times 1)$  overlayer of H-atoms adsorbed on a  $(111)$  face of a Cu slab with 5 atoms. This calculation takes about 6 minutes per iteration on 10 processors including the master with one  $k$ -points on each slave and is converged after about 40 iterations. Some parts of the program have not yet been parallelized and the speed-up is so far about a factor 2 below the theoretical value. However, this preliminary calculations makes us confident that we will be able to handle a larger slab with 12 Cu atoms that is necessary for the interactions between the periodic images of the H atoms to be small.

## Quantum Tunneling

Thomas Mattsson, Göran Wahnström

Hydrogen diffusion on metal surfaces has been subject of great theoretical effort over the years with a renewed interest due to recent experiments on hydrogen diffusion on nickel surfaces in the low-temperature regime [Lin and Gomer, 1991, Zhu *et al.*, 1992]. Mainly two different techniques have been used and some very recent experimental results by Cao, Wong and Zhu [Cao *et al.*, 1996] for H on Ni(111) seem to contradict the earlier experimental data. The need for highly accurate calculations is therefore even more important than before.

From a basic physical point of view possible quantum effects are in focus but an improved understanding of metal-hydrogen systems is also important in more applied oriented areas; as for instance in materials science (hydrogen embrittlement and nickel-hydride batteries) and in chemical physics (the behavior of hydrogen in different catalysts).

Our recent work [Mattsson *et al.*, 1993b, Mattsson and Wahnström, 1995] has successfully shown that it is possible to gain qualitative understanding of the quantum behavior of hydrogen diffusion on metal surfaces, especially concerning the transition from semi-classical diffusion to quantum tunneling when lowering the temperature. However, fundamental questions still remain unsolved, in particular the experimentally observed absence of a pronounced isotope effect. Both the transition temperature between semi-classical and quantum behavior as well as the magnitude for the diffusion constant in the quantum regime are found to be similar for both hydrogen and deuterium, but from simplified theoretical arguments a large difference is expected due to the difference in mass between the two isotopes.

The path-centroid formulation for quantum tunneling appears very promising and presently the main shortcoming is the lack of detailed information about the PES. Tunneling behavior is very sensitive to the PES, which makes it crucial to have good knowledge of the potential also in regions where experimentally derived information is often both limited and indirect. The natural way to proceed is first-principles electron structure calculations. Our calculations [Mattsson *et al.*, 1996] have been performed on a dense ( $1 \times 1$ ) overlayer on a 5 layer slab with one Ni atom in each layer (see Figure 2.22 on page 24). The calculations for the hollow site have been performed on a single processor using the serial version while the larger number of  $k$ -point for the bridge site makes it more beneficial to use the parallel version. This latter calculation is running on 14 processors including the master with 2  $k$ -points on each slave. The description of Ni metal involves half-filled  $d$ -bands which makes the calculation more demanding than for instance Cu.

The quantum diffusion calculations performed using the new potential agrees excellently with experimental results at high temperatures. The

transition to tunneling diffusion occurs at a diffusion rate of  $D \approx 10^{-15}$  cm<sup>2</sup>/s [NAT, 1996], which should be compared with the experimental value  $D \approx 10^{-12}$  cm<sup>2</sup>/s [Lin and Gomer, 1991]. Tunneling, as mentioned before, is very sensitive to details both in theory and experiments and the agreement is therefore quite reasonable. The quantum diffusion calculations are made in parallel over 32 nodes which makes it possible to compute the data for four different temperatures simultaneously.

These projects are supported by NFR and by NUTEK/NFR interdisciplinary materials consortium: Theoretical and Computational Materials Physics and are gratefully acknowledged.

## 6.12 Quantum Wavepacket Studies of Dynamical Processes at Surfaces

*Mats Persson*

Department of Applied Physics, CTH

The detailed mechanisms behind a wide variety of important surface phenomena like surface chemical reactions in heterogeneous catalysis, are most convincingly revealed by dynamical studies of elementary processes on an atomistic scale. The rapid advances and developments in experimental methods for the study of such processes like, for instance, state-to-state molecular beam scattering makes this field into a timely subject for theoretical studies.

In many cases a quantum mechanical description is needed and the associated complexity makes it often necessary to perform computer simulations of simplified models. We have an ongoing project where we study elementary dynamical processes at surfaces using pseudospectral methods for *time-dependent propagation of multi-dimensional wavepackets* on the Connection Machine. In these methods the multi-dimensional wavefunction is represented on a grid and in each timestep the action of the kinetic part of the Hamiltonian on the wavefunction is handled by discrete Fourier transform of the wave-function [Rev, 1991]. The limiting factors in the computations are then determined by the primary memory needed to represent the wave function and the speed of the fast Fourier transform subroutines. A parallel machine like CM200 is found to be very well suited to handle these factors.

In collaboration with Bret Jackson at Department of Chemistry, University of Massachusetts, I am studying a prototype catalytic surface reaction which proceeds via an Eley-Rideal pathway; the formation of hydrogen molecules by the direct reaction of an incoming hydrogen atom with an adsorbed hydrogen atom on a copper surface. This theoretical study is motivated by recent dynamic measurements of this reaction [Rettner, 1992, Rettner and Auerbach, 1995] and its dynamics is of interest, for instance, in understanding the formation of hydrogen molecules in interstellar space and also for plasma-wall interactions in fusion reactors.

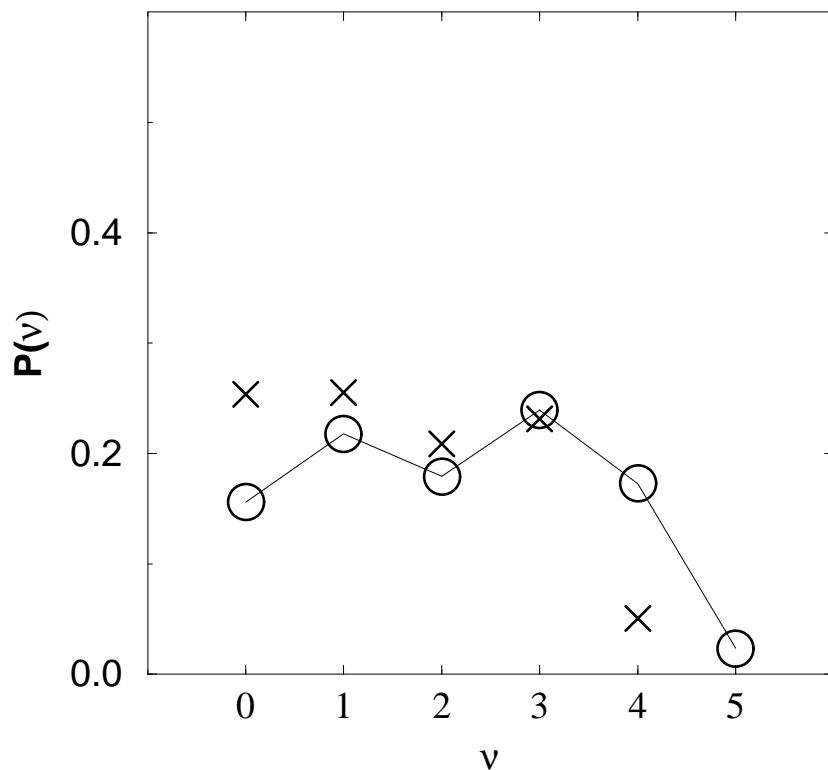


**Figure 6.10.** Experimental and theoretical vibrational distributions of the HD product.  $P(\nu)$  is the probability to find the HD molecule in a vibrationally excited state  $\nu$  as the result of the reaction of an incident D atom with an adsorbed H atom on the (111) face of Cu. The experimental data, crosses, are taken from [Rettner and Auerbach, 1995] and the circles are the result from our theory.

We have developed a flat-surface quantum mechanical model of the Eley-Rideal reaction that gives full rovibrational product distributions and reactive cross-sections [Persson and Jackson, 1995a]. The model is based on a flat surface approximation for our model potential energy surface which reduces all six degrees of freedom for the two atoms to a tractable three-dimensional problem in curvilinear coordinates by introducing three conserved quantities. Our extensive computational studies include the different isotopic combinations of hydrogen and consider the dependence of the reactive cross-section and the product distributions on the shape of the model potential energy surface, on the state of the incident atom and on the vibrational state of the adsorbed atom. These results have, for instance, demonstrated the importance of the zero-point motion of the adsorbed reactant on the product rovibrational distributions. In particular, our predictions for the isotope effects on the rovibrational distribution of the HD product [Persson and Jackson, 1995b, Jackson and Persson, 1995] have recently been confirmed by a state-to-state molecular beam study by Rettner and Auerbach. This confirmation is demonstrated in Figure 6.10.

The code is written in CMFortran and we use a CMSSL subroutine for the time-consuming discrete fast Fourier transform (FFT). For the

isotopic studies, the grid size of  $128 \times 128 \times 256$  being used for the H atoms is not sufficient and we are forced to use a grid size of  $256 \times 256 \times 256$ . The calculations using this larger grid size requires a bigger machine than the 16K CM200 available at PDC. Thanks to the assistance by Dianne Lynch at Thinking Machines Inc. in Cambridge, USA, these calculations could be performed on a 64-node CM5 machine with 128 Mbyte on each node whereas the final state analysis were readily done at PDC. A typical run for the isotopes involves 6000 time steps, takes about 9 1/2 hours with about half the time spent in the fast Fourier transforms subroutines and requires about 5 Gbyte of primary memory.

In summary, computational studies of dynamical processes at surfaces using multi-dimensional quantum wave packets are well-suited for a data parallel machine like CM200 and CM5 and are computationally very demanding, in particular, with respect to primary memory. The availability of a 64-node CM5 machine, through contacts arranged via PDC, have made it possible for us to study isotope effects using a realistic model for an Eley-Rideal surface reaction involving hydrogen atoms. In fact, this model is the first realistic quantum mechanical model of a full surface reaction. Our predictions about the isotope effects on the product rovibrational distributions have recently been confirmed by state-to-state molecular beam experiments.

### 6.13 First-Principles Modeling Defects in Semiconductors: Oxygen in Silicon

*Sven Öberg*

Department of Mathematics, Luleå University

Oxygen is the primary impurity in commercially grown silicon, and is able to form a great many electrically active defect complexes, both alone and in combination with other light element impurities. The most important of these are electrically active *thermal donors*, a family of defects which despite intensive study for over forty years, still leave us with elementary questions such as the nature of their atomic structure. Point defects such as these have been identified as one of the primary restrictions on Si chip speed in the near future. However many light element dopants such as oxygen, hydrogen and nitrogen are deliberately added to silicon to strengthen the wafers and improve other bulk properties. Therefore there is a greater need now than ever to fully understand the way in which oxygen precipitates in silicon, so that careful processing can maximize the benefits from point defects and minimize the damage that they cause. Crucial to an understanding of point defect interactions in silicon is the role of *silicon self-interstitials*, silicon atoms which have been forced out of their normal lattice sites and have to share a lattice site with a second silicon atom. They are able to diffuse extremely rapidly and it has been suggested that they mediate many of the de-

fect formation processes in silicon, and may even lie in the core of the thermal donors. Our recent work casts into doubt many of the common assumptions in this field.

We have been studying light element defects in silicon using a local density functional scheme, applied to atomic clusters. The program has been used and developed in collaboration with others [Jones, 1992], in many successful applications to a wide variety of molecular and semiconductor problems. The code models clusters of atoms in real space. It can therefore be directly applied to molecules, and for the simulation of defects in bulk, large hydrogen terminated clusters. It determines many physical properties, including total energies, structure and symmetry, energy surfaces and vibrational frequencies on an *ab initio* level. Since there is no experimental input this maximizes the predictive capability of the code.

Much work has been put into efficiently parallelizing the code, and incorporation of the block algorithm SCALAPACK routines. These routines take full advantage of massively parallel architectures. The code can run with comparable efficiency across a variety of platforms including parallel machines (such as the IBM SP-2 and CRAY T3D), workstation clusters, and single workstations (e.g. SGI, IBM, DEC and HP machines). The code effectively load balances and routinely achieves very high scale-up efficiency with increasing number of nodes. Efficiency for the calculations reported here using 16 nodes is about 90% (speedup of about 14). Most of the oxygen defect work described here was performed using the SP-2 at PDC.

Cluster methods employing localized basis sets are important for studying impurities such as O and N in Si. The localized nature of the basis allows an increase in basis size around atoms such as O or H which have rapidly varying charge density. Moreover clusters are easily constructed around aggregates, making this method ideal for their study. One of the problems with oxygen is that many of its associated defects cause long range relaxation in the Si lattice, so large clusters are required to accurately model their structure. This is particularly important when modeling diffusion processes where long range relaxations can significantly alter the energy barrier to diffusion. Thus most of the clusters used for these calculations contain between 100–150 atoms with many basis functions required to accurately model the point defect; such large calculations can only be realistically tackled with powerful machines such as the SP-2.

*Such large calculations can only be realistically tackled with powerful machines such as the SP-2*

### *Oxygen-vacancy complexes*

We initially tackled the problem of oxygen–vacancy (OV) complexes. Normally oxygen sits in a bond centred (BC) site, forming interstitial oxygen,  $O_i$ . However irradiating Si creates many vacancies, which can trap  $O_i$ , initially forming the so-called off-site substitutional oxygen,  $O_s$ .

However the subsequent annealing behavior is complex. A-centres break down at around 300°C and a transient, intermediate defect is created before the formation of a stable defect characterized by a local vibrational mode (LVM) at 889 cm<sup>-1</sup> [Corbett *et al.*, 1964]. At higher temperatures this too breaks down and a variety of other LVMs are formed.

From our calculations, we have determined that the transient centre arises from O<sub>i</sub>O<sub>s</sub>, where a normal bond centred oxygen atom sits next to an A centre. This is then able to reconstruct into V(O<sub>s</sub>)<sub>2</sub> (a ‘di-oxygen vacancy’ complex, where two oxygen atoms share the same vacancy site), with a calculated O stretch mode close to 889 cm<sup>-1</sup>. Although a V(O<sub>s</sub>)<sub>2</sub> model has been proposed before, there was no explanation of the apparent lack of coupling between the oxygen atoms, or of the formation mechanisms involved. Our calculated LVMs are in excellent agreement with experiment [Ewels *et al.*, 1995], and our predictions of the symmetry have since been experimentally verified [Nielsen *et al.*, 1996]. We have also examined the way in which further oxygen atoms add to this defect, performing calculations for various VO<sub>3</sub> models. J. L. Lindström and T. Hallberg at Linköping University are currently performing further experimental work [Hallberg and Lindström, 1992] to determine the LVMs of large vacancy–oxygen clusters. We are working closely with them to compare the theoretical models with the new experimental results, and this work is leading to a comprehensive understanding of the dynamic process of oxygen aggregation at vacancy sites in irradiated Si.

### *Oxygen diffusion in silicon*

We are currently examining oxygen diffusion and complexing in silicon, one of the longest running and hardest problems in defect physics. Diffusion is an extremely important process in solids, affecting both their atomic structure and stability. However it is a difficult problem to handle theoretically for several reasons. Firstly there are many possible channels for diffusion, including simple atomic exchange, interstitial or vacancy controlled diffusion, and diffusion catalysed by other impurities. Secondly, diffusion involves non-equilibrium structures, and requires the accurate determination of *saddle point structures*. These are the structures possessing the highest energy along a particular diffusion path. The energy difference between this and the equilibrium structure is the energy barrier that must be overcome for diffusion to occur along that path.

Isolated interstitial oxygen can hop from site to site at temperatures above 380°C (from bond centre D-B to bond centre D-C, see the left part of Figure 2.28 on page 26), and the barrier will occur at some intermediate point as bonds A-B and C-D are broken, and new bonds form between A-C and B-D. Our calculations, when unconstrained, lead to equilibrium ground state stable structures. Therefore to obtain saddle point energies it is necessary to constrain the problem in some way. The

energy of the diffusion barrier is crucially dependant on which bonds are required to break / form, and so we constrain the problem by fixing important bond lengths to a given length. For  $O_i$  diffusion these are the O-Si lengths, shown in the left part of Figure 2.28 on page 26 as A-B and A-C. The rest of the structure is allowed to relax to equilibrium subject to these constraints. The saddle point occurs when  $A-B = A-C$ . In practise it is also necessary to constrain the bonds D-B and D-C, since there is also a Si-Si bond between D-C which has to break and a bond between D-B which forms during one diffusion hop. By varying these two constraints we obtain an ‘energy surface’, from which the saddle point energy can be directly found through interpolation.

The experimental barrier for  $O_i$  diffusion is 2.54 eV [Stavola *et al.*, 1983], and using the method described above we obtain a calculated value of 2.6 eV, in excellent agreement. However, this means interstitial oxygen diffuses too slowly to explain the formation kinetics of thermal donors. It has therefore been proposed that there may be an alternative faster diffusion mechanism for oxygen. One possible solution is oxygen migrating in interstitial pairs, and with this in mind we modeled a centre consisting of two  $O_i$  in adjacent bond centres,  $(O_i)_2$  (see the right part of Figure 2.28 on page 26). This is more stable than two isolated  $O_i$  atoms by  $\approx 0.7$  eV. We then examined possible  $(O_i)_2$  diffusion mechanisms, and found that it can diffuse more easily than isolated  $O_i$  via concerted motion [Ewels *et al.*, 1996a]. As  $O_i$  moves from one bond centre to the next it passes through a central point where it has two very dilated Si-O bonds (A-B and C-B). However the presence of an adjacent  $O_i$  compresses these dilated bonds and lowers their energy, lowering the overall energy barrier to diffusion by  $\approx 1$  eV. This means that oxygen pairs should diffuse much more rapidly than isolated  $O_i$ , and is close to the observed thermal donor formation energies.

### *Nitrogen – Oxygen defects*

We have previously shown that N in Si primarily exists in the form of  $(N_i)_2$  pairs [Jones *et al.*, 1994a]. More recently we showed the primary N—O defect to be  $(NN)O$ , consisting of  $O_i$  neighboring a  $(N_i)_2$  pair [Jones *et al.*, 1994b]. Many experimental groups have observed a family of *shallow thermal donors* (STDs) in Si that contains both O and N. Our calculations predict that a defect consisting of a single  $N_i$  surrounded by two  $O_i$  acts as a STD [Ewels *et al.*, 1996b] (see the left part of Figure 2.29 on page 26). Isolated  $N_i$  possesses a deep donor state localized on a neighboring Si. However in  $N_i(O_i)_2$  this donor level is electrostatically ‘squeezed’ by the  $O_i$ , which pushes it towards the conduction band to form the observed shallow level (see the right part of Figure 2.29 on page 26). The mechanism is not restricted to  $N_i$  based defects and can also be produced from a defect core of  $(C-H)_i-O_{2i}$ .

One of the fascinating aspects of this model is that this is a new mechanism for the formation of shallow donor levels, and only initially requires a defect with a deep level state. There are many implications of this work beyond the direct attempt to determine the structure of STDs. This mechanism could explain the source of shallow donor levels in a wide range of materials, including commercially important shallow donors in diamond [Prins, 1995]. Ultimately it may even be possible to attempt ‘defect level engineering’, treating a material in such a way as to produce defects with energetically ‘squeezed’ levels lying at precisely the energies required for device design.

### *Carbon – Oxygen defects and the Thermal Donors*

We are currently investigating the role of carbon in silicon, and its interactions with other point defects such as oxygen. Carbon can exist in either a substitutional ( $C_s$ ) or interstitial ( $C_i$ ) form and is able to interact with many other impurities (indeed, these two can even complex together, leading to defects such as the ‘T-line’ defect,  $C_sC_iH$  [Safonov *et al.*, 1996]) Carbon behavior is particularly relevant to the study of oxygen since carbon is known to suppress thermal donor formation. The mechanism has, until now, been explained in terms of silicon self-interstitials. Substitutional carbon can trap these through a ‘kick-out’ mechanism, where the carbon swaps places with the silicon interstitial to become  $C_i$ . This soaks up the silicon interstitials and since carbon suppresses thermal donor formation this has been used as evidence to suggest that silicon interstitials exist in the thermal donors.

However, our latest results suggest that this may not be the case, and carbon could suppress thermal donors through a much simpler mechanism. Many defects have been assigned to  $C_i-O_n$ ,  $0 < n < 4$  complexes due to their high vibrational modes ( $C_i$  is more compressed than  $C_s$  and so vibrates at higher frequencies). However we find that the presence of neighboring oxygen compresses  $C_s$  until it gives vibrational modes of a similar frequency. Therefore the defect complexes supposed to be  $C_i-O_n$  could, in fact, be due to  $C_s-O_n$ , and carbon is then simply suppressing thermal donors by ‘mopping up’ the oxygen so there is insufficient left to form thermal donors. Current experimental work by Lindström and Hallberg to provide data on the isotopic shifts of these modes, coupled with theoretical modeling currently underway should help to confirm or deny this idea.

Alongside this work we have started examining larger oxygen aggregates, in order to find out how this clustering occurs and ultimately determine the structures of the thermal donors (TDs). Over 40 years of research has led to a bewildering wealth of experimental data on the thermal donors, much of it conflicting, and together painting a picture of very complicated kinetics and thermodynamics. Thermal donors are a family of double donor defects (there are 17 reported TDs) that form

in silicon during low temperature anneals (450°C). The later TDs are known to have  $C_{2v}$  symmetry (a reflection plane and a 2-fold rotation axis) and they all have oxygen present in the defect core. In addition, the first two TDs are *bistable*, sharing a common electrically inactive form as well as their respective donor structures.

We have examined structures consisting of three  $O_i$  atoms and found that they can form either electrically inactive ‘linear chains’ or more complex structures which do indeed exhibit donor activity. In addition we are currently examining structures of four  $O_i$  atoms which demonstrate many of the required properties of the later thermal donors. Further modeling is required to test whether these are indeed the correct structures for thermal donors. These structures can adopt many possible configurations and it is essential to ensure that our models are the most stable. In addition they must be carefully correlated with the available experimental data [Lindström and Hallberg, 1995]. Again, the latest work by Lindström and Hallberg on the isotopic shifts of thermal donor vibration will be essential in this respect.

#### 6.14 Fluctuations in Atomic Collision Cascades

*Roumiana Chakarova, Imre Pázsit*

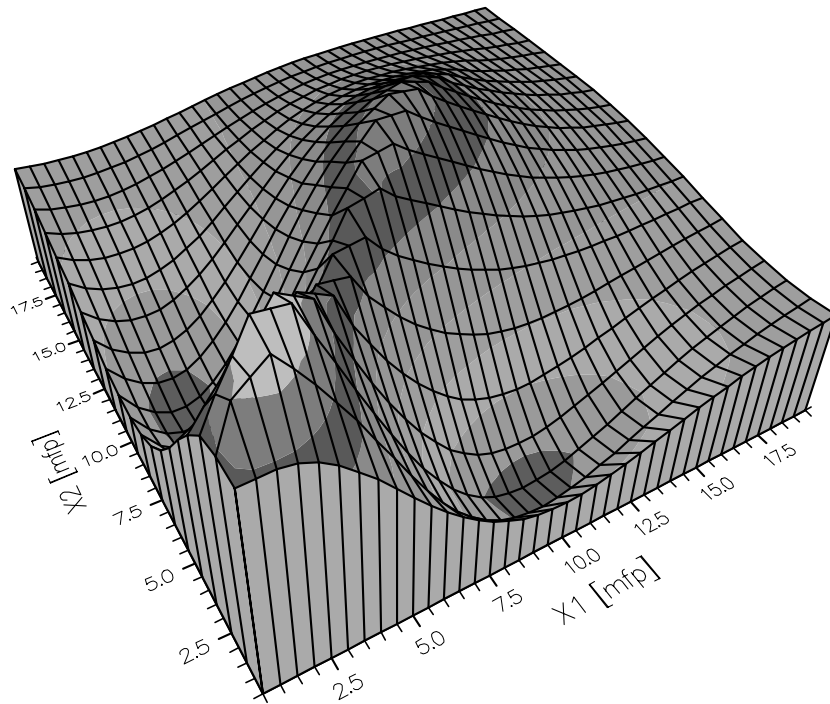
Department of Reactor Physics, CTH

Particle cascade processes are described most often by mean values. However a thorough understanding of the fluctuations in collision processes can give more insight into the physics of the particle transport and the properties of the material in which the transport takes place. The relative variance of the sputtering yield is a monotonically increasing (i.e. diverging) function of the energy of the bombarding particle with both constant cross sections and hard sphere potential as well as Lindhard and power law cross section. Some other collision processes, such as ion pair production or total number of defects in an infinite medium, on the other hand, have relative variances that are asymptotically constant with the bombarding energy and much less than unity (i.e. deeply sub-Poisson).

To understand the reason of such a difference an extensive study of the energy and spatial correlations has been performed using Monte Carlo method. The algorithm employs constant cross sections and the model of Khinchin and Pease for the defect creation mechanism. It was found that in half-spaces, unlike in infinite media, the relative variance of defects becomes over-Poisson and increasing with increasing bombarding energy. The structure of the correlation functions was indeed helpful in understanding the behavior of the variance in various cases, see Figure 6.11 from [Pázsit and Chakarova, 1996].

Most of the quantities calculated (energy and depth distributions of the origin of sputtered particles, depth distributions of vacancies and

**Figure 6.11.** Depth correlation function of vacancies created in a semi-infinite medium. Particles with energy  $E_0$  are injected at  $X_1 = X_2 = 0$  mfp.  $X_1$  and  $X_2$  are depth variables.  $U = \ln(E_0/E_d) = 8$ , where  $E_d$  is the atomic displacement energy.



interstitials, energy and depth correlations), are of the density type. Obtaining results with a satisfactory accuracy required long CPU time on the Sun SPARCstation at the Department. This was especially true for the correlations. The complete mapping of a correlation function over the two dimensional domain of interest turned out to be a very demanding task. Therefore the Monte Carlo program was parallelized on the basis of the MPI library and implemented on the IBM SP-2 machine. The CPU speedup was estimated by running a test problem on the Sun station and IBM SP-2 when using different number of processors. Figure 6.12 shows the advantage and applicability of the SP-2 parallel architecture to Monte Carlo particle transport problems.

Test calculations with the parallel code were performed as well as using the MPICH portable version of the MPI library installed on the “Sun network” of the Department. It includes three workstations. The efficiency of the MPICH utilization was restricted by the limited number of stations available, the differences in their characteristics and particular occupation. The MPICH was considered to be most useful when developing a parallel algorithm.

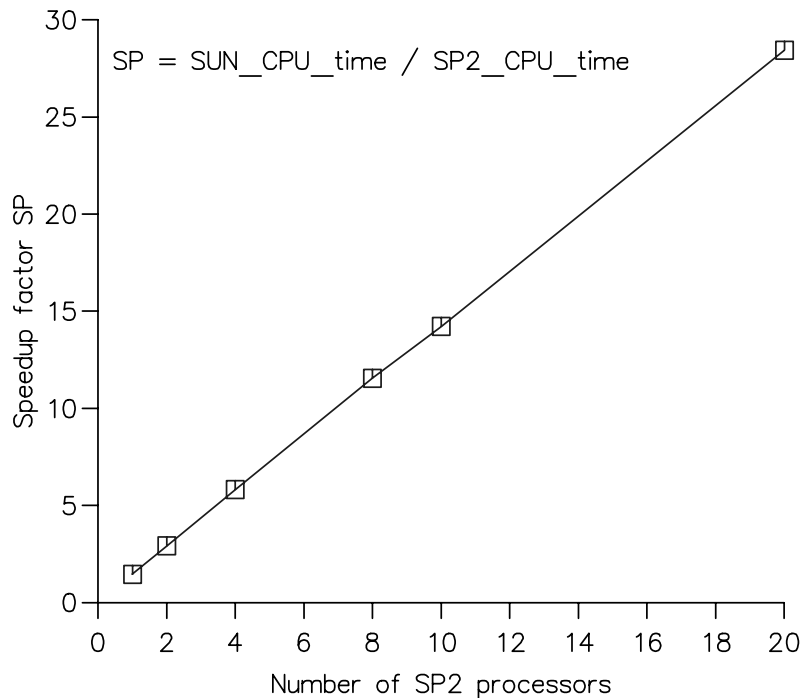


**Figure 6.12.** Scaled CPU speedup of the parallel Monte Carlo code based on the CPU time for a single Sun SPARCstation.

### 6.15 Transport Simulation of Electrons Reflected Elastically from Solids

*Imre Pázsit, Roumiana Chakarova*

Department of Reactor Physics, CTH

*Fredrik Hedman*

Center for Parallel Computers, KTH

The energy spectrum of reflected electrons is an information carrier of the material properties. Theoretical investigations of the spectrum in the vicinity of the elastic peak involve decoupling of the spatial and angular transport from the energy degradation process. This is achieved by considering all scattering events as being elastic and determining the path-length distribution of the reflected particles. The latter is then convoluted with the energy loss function in order to obtain the energy spectrum.

The path length distribution can be determined from an energy independent, angle-, depth- and time-dependent transport equation, since the path length of the electrons is proportional to their flight time in the medium. However, standard transport theory solution methods, such as the  $P_1$  or  $DP_1$  methods, fail to give correct results, due to the free surface, a singular source term and the complicated angular dependence of the scattering kernel. Therefore an analog Monte Carlo model has been applied to simulate electron elastic scattering. Path-length and

**Figure 6.13.** Number of 1 keV electrons vs path-length and depth they penetrate before being reflected elastically from aluminum. The distributions are non monotonic. Zero mfp corresponds to aluminum surface.

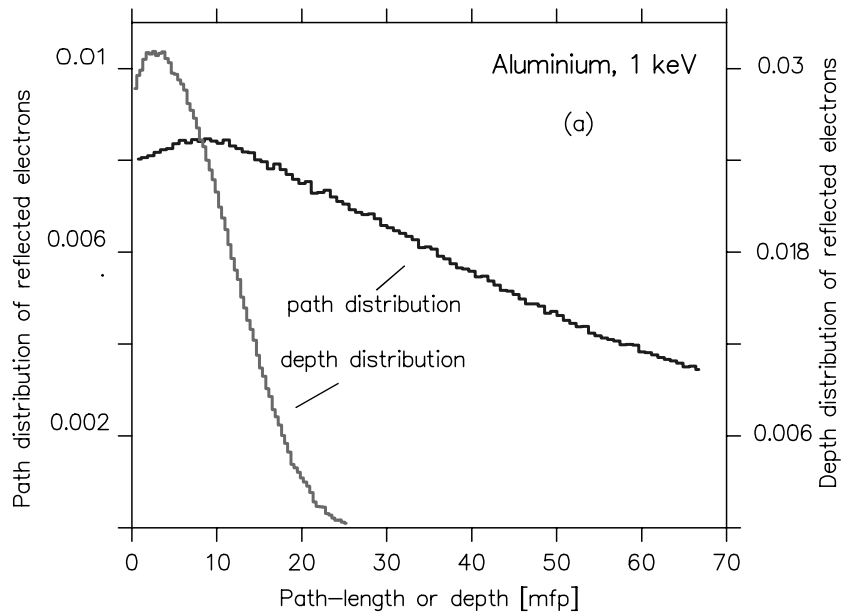
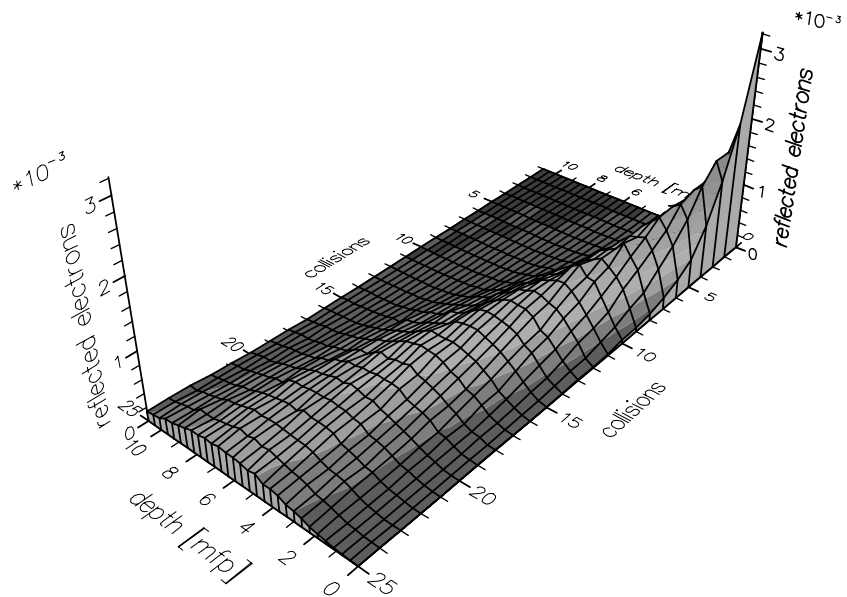


**Figure 6.14.** Depth distribution of 1 keV electrons reflected from aluminum after a fixed number of collisions. Electrons suffering one and two interactions have monotonic distribution. A maximum appears for those with three collisions. It moves to larger depth values with increasing the collision number (the electrons penetrate deeper into the medium).



depth distributions as well as angular distributions of reflected electrons have been calculated for several elements and energies in the range 0.4–20 keV. It was found that the path-length and depth distributions are not monotonous for selected elements (e.g. aluminum, carbon and copper), for certain energies, see Figures 6.13 and 6.14. This behavior was related to the structure of the differential elastic scattering cross section [Pázsit and Chakarova, 1994].

Statistical analysis of the Monte Carlo results was based on the number of particles scored in each depth or angular bin. A large number of electron histories needed to be simulated in order to achieve good statistical accuracy which led to long running times of the serial code. The problem was solved by implementing the model on the Connection Machine CM200. A parallel code was written that allows simultaneous simulation of the penetration of up to 200 000 particles. The number of the source electrons was not limited by the number of the processors attached because of the virtual processor capability of CM200.

Test comparison between the sequential and parallel algorithms was carried out on a Sun SPARCstation and 8K CM200 respectively. It was found that the CM200 outperforms the workstation by a factor of 17. The parallel algorithm can be optimized to achieve higher CPU speedup.

### **6.16 One-Group Radiation Transport Benchmarks for Anisotropically Scattering Medium**

*Roumiana Chakarova, Imre Pázsit*  
Department of Reactor Physics, CTH

Radiation transport calculations are performed by user developed codes or by standard packages linked to user written routines. It is essential to test the codes against high quality data in order to establish their accuracy and proper work. Selection of benchmarks is preferable which are valid for situations closely related to that of the particular problem. Therefore the generation of a wide variety of benchmarks remains an actual task. Analytical, numerical or experimental results may serve as a test as well as calculations by Monte Carlo method. Advantage of the Monte Carlo method is the capability to handle complex configurations and scattering kernels. However the requirement of high accuracy may lead to long running times. One way of reducing CPU times is to apply parallel computing techniques.

We have calculated neutron flux and current distributions in an anisotropically scattering subcritical medium with a parallel Monte Carlo code on the Connection Machine CM200. Both monodirectional and isotropic sources were considered at the surface of a semi-infinite, slab or cylindrical medium. The code is based on a detailed Monte Carlo simulation with variance reduction technique. An exponential transform is included to enhance the efficiency for the deep penetration cases. The particle is

represented by its position coordinates and direction of motion. Its trajectory in the medium is constructed as a series of successive interaction events. The parallel procedure is described briefly below.

Each particle characteristic is an element of a certain array whose dimensions are not restricted by the number of processors because of the virtual processor capability of CM200. Operations simulating particle histories are performed here on 500 000 dimensional arrays. The current state of  $i$ -th particle is determined by the  $i$ -th element of each characteristic array. A flux or current scoring array for a certain interface contains the particle contributions to the score. The update of the  $i$ -th elements of the characteristic and scoring arrays comprises the  $i$ -th history. Array elements belonging to particles absorbed or escaped from the medium are marked and ignored by the scoring procedure. The computation continues until all element positions are marked. The total flux or current value for a certain interface is obtained by summing the elements of the corresponding array. This completes the simulation of the particles of one statistical batch.

The code is written in CMFortran. The CPU time for a run (500 000 histories) on 8K CM200 varied from 10 to 180 seconds depending on the absorption probability parameter. Because of the short running time, it was possible to simulate the transport of hundred millions source neutrons for each case and to keep the statistical error between 0.1 and 2.5%. More details can be found in [Chakarova and Pázsit, 1995].

### **6.17 Modified Artificial Viscosity in Smooth Particle Hydrodynamics on the CM200**

*Magnus Selhammar*

Uppsala Astronomical Observatory, Uppsala University

Smooth Particle Hydrodynamics (SPH) is a gridless Lagrangian hydrodynamic method, and instead of a grid to discretize the fluid one uses particles. The method is often efficient in astrophysical applications, and the particle representation makes SPH suitable to implement in three dimensions and to include gravitation. The method is first described by Lucy 1977, and independently by Gingold and Monaghan also in 1977.

The particles represent the model's density distribution, where a specific particle has a finite extension in space by a radius of two smoothing lengths,  $2h$ , which is specific for each particle. This makes hydrodynamic interaction with other particles, called neighbors, possible within this radius. To maintain similar resolution throughout the model despite density variations over time,  $h$  is updated every iteration to keep the number of neighbors constant.

Artificial viscosity forms shocks and broadens them to a few smoothing lengths, which is the resolution of the model. It also damps the post shock oscillations and to prevent that particles penetrate each other. The

artificial viscosity consists of two terms. The bulk viscosity that scales as the particle velocity times the sound speed, and the von Neumann-Richtmeyer viscosity that scales as the quadrate of the particle velocity. In the supersonic region the von Neumann-Richtmeyer viscosity dominates to form shocks, but with subsonic particle velocities the bulk viscosity becomes important to damp the post shock oscillations. Both terms prevent particle penetration in their velocity regions respectively.

The artificial viscosity gives erroneous results because it damps desirable velocity differences among the particles and heats the model, mainly due to the poor spatial resolution. The effect is particularly prominent in gravitational collapses, which are common in astrophysical SPH models.

To delimit these problems the von Neumann-Richtmeyer viscosity is restricted to supersonic velocities only. The bulk viscosity is modified to interact, not with each neighbor separately, but a weighted mean of the particles. Comparisons with standard tests show comparable or better results than with standard artificial viscosity. The results are submitted to Astronomy and Astrophysics.

## 6.18 Reduction of Impurity Scattering from Correlation of Donors

*Thomas Palm*

Department of Electronics, KTH

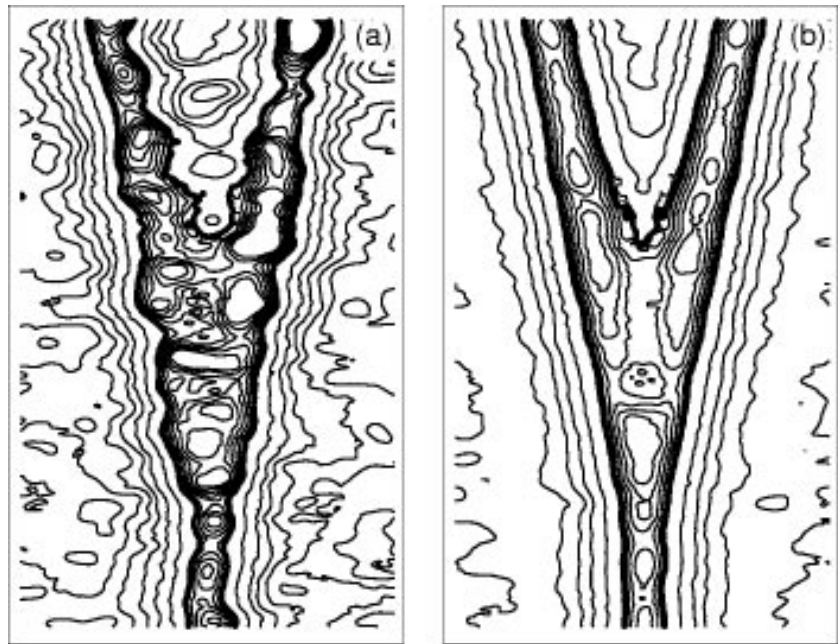
Scattering from donors is a serious problem for devices based on ballistic electron transport. Using modulation doping where an undoped spacer layer is placed between the donors and the electrons reduce this problem, but for a random donor distribution the remaining remote impurity scattering still ruins the performance of studied devices.

It has been suggested that since usually only a fraction (around 70%) of the donors are ionized in a realistic structure, the ionized donors would form a more regular pattern to minimize electrostatic energy. This would reduce scattering.

To find this distribution, a random donor distribution was created. A fraction of these were initially selected to be ionized and the resulting potential was calculated. In the next step the donors located at points with lowest potential were selected to be ionized and the potential was recalculated. This was iterated until no further change was seen. In addition, a Fermi-distribution was added to model a finite temperature in the distribution of ionization.

For the chosen parameters the change of ionization at one point made a large difference in potential at neighboring donors. In initial attempts the solution therefore tended to oscillate wildly rather than converge. A form of under-relaxation where only a small (10%) of the donors were allowed to change ionization state at each iteration was therefore introduced. This improved stability, but several hundred iterations were

**Figure 6.15.** Contour lines of the potential of a Y-branch under symmetric bias. The thick line shows the Fermi-level. Above this level each contour represents 50 mV potential difference. Below the Fermi-level screening reduces the fluctuations and the contour lines have been drawn at 2 mV distance. The left device is without donor correlations, the right include these.



*Made possible by the large capacity of the Connection Machine*

needed to reach an equilibrium, which was made possible by the large capacity of the Connection Machine CM200 at PDC.

This crude algorithm was not able to reach a true thermal equilibrium for temperatures below approximately 500 K, and the resulting potential was therefore an upper limit to the amount of scattering expected in real devices (assuming the underlying model is correct). Nevertheless, scattering was reduced to a point where ballistic transport appears possible, see Figure 6.15 [Palm, 1995].

### 6.19 A Monte Carlo Model for Radionuclide Transport in Fractured Media

*Marlene Andersson, Bruno Mendes, Antonio Pereira<sup>2</sup>*  
Department of Physics, Stockholm University

Geological deposition is, in many countries with nuclear power production, the main alternative to handle long-term risks associated with stocks of high-level nuclear waste. Underground repositories can be embedded in different geological environments such as clay, salt domes and granitic rocks.

<sup>2</sup>Since this project is related to parallel computing developments in the field of high-level nuclear waste two of the authors (B. Mendes and A. Pereira) thank the European Commission for financial support in the frame of the GESAMAC project.

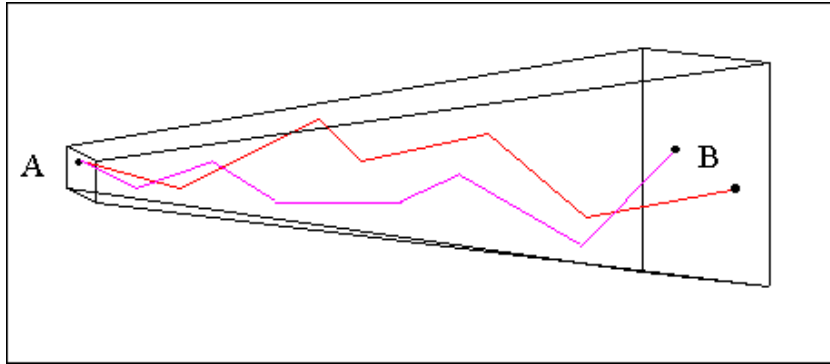


**Figure 6.16.** In the CRYSTAL3D model the pathways are formed by series of connected fractures.

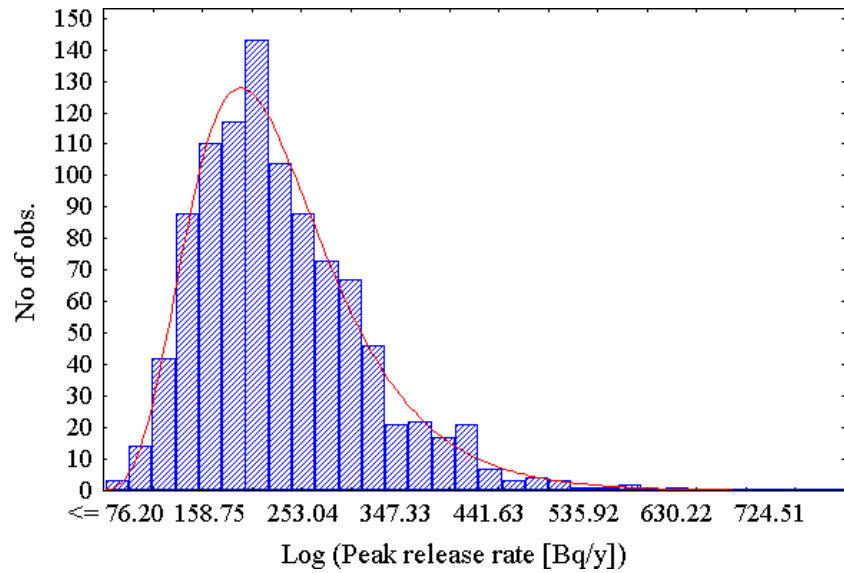
The application of Monte Carlo methods is very useful in the estimation of long-term radiological risks. This project is a feasibility study of geosphere transport modeling in fractured media, to be used in uncertainty and sensitivity analysis of Monte Carlo simulations.

Granitic rock environment is typically a fractured media exhibiting strong heterogeneity. Transport codes actually in used in Monte Carlo assessments of high-level nuclear waste do not included heterogeneity, probably to keep the total number of needed simulations manageable. In the CRYSTAL3D model, now under development, the heterogeneity of fractured media has been introduced, which magnifies the computational burden with two orders of magnitude. Therefore, our model, first developed in a serial environment had to be ported to a parallel computer. The code has been implemented recently on the IBM SP-2 at PDC, using the Message Passing Interface, MPI.

CRYSTAL3D is an extension of the CRYSTAL model [Worgan and Robinson, 1992] to three dimensions. Our conceptual model is show schematically in Figure 6.16: in CRYSTAL3D, the transport pathways that connect the source of radionuclides (at inlet area A) to the biosphere is model-LED by a series of connected fractures ending at the outlet area B, which can be a fracture zone in direct contact with the biosphere. Physical, chemical and geological properties can vary from fracture to fracture reflecting the heterogeneity of the media. The input parameters describing these properties can be sampled from several PDFs. The fractures are generated stochastically within the volume defined by the inlet and outlet areas.

In our first tests we have simulated the transport of one nuclide with no decays chains. Although the number of simulations was limited, some very interesting results have been obtained. In fact, the mean value of release rates to biosphere decrease by one order of magnitude if compared with results from the option in which heterogeneity is not taken into account (in manuscript). The variance of the output distribution has also decreased. Figure 6.17 shows an output distribution obtained using circa 100 000 transport simulations [Worgan and Robinson, 1992].

**Figure 6.17.** This figure shows the output distribution of peak release rate of  $^{243}\text{Am}$ .



*Future work*

Model development will continue. Also the performance of the code will be studied to optimize it. A detailed study of the impact of heterogeneity on release rates to biosphere will be done, which implies the need of varying other input parameters that were kept constant during the first tests and also of monitoring a significantly higher number of Monte Carlo realizations.

## 7 Applications in Geophysics

### 7.1 Numerical Experiments on Gravitational Instability of Geostructures

*Ali T. Ismail-Zadeh, Boris M. Naimark*

IIEPTMG, Russian Academy of Sciences, Moscow, Russia

The problems of gravitational instability involving distinct chemical layers are challenging in geophysical fluid dynamics. Motions of material interfaces separating geomaterials of differing material properties are essential to subduction of lithospheric slabs, ascending of mantle plumes, sinking of heavy bodies in the asthenosphere, salt diapirism, and many others. We have examined the models of salt diapir evolution with laterally homogeneous and inhomogeneous overburdens of sediments and also models of descending slab in attempt to explain the observed distributions of intermediate-depth earthquakes. To compute these models, we solved the 2D Stokes equation, represented in terms of the stream function, and the transfer equations for density and viscosity. The numerical method used in this study combines a Galerkin-spline technique with a method of interface tracking to represent discontinuous variations of material parameters. We analyze models where a viscous incompressible fluid filling a square box is divided into layers by advected boundaries, across which density and viscosity change discontinuously. Free slip conditions are assumed at the model sides. The numerical approach, being Eulerian, avoids the difficulties due to material discontinuities at intermediate boundaries, like Moho or the earth's surface, and is also free from the deficiencies of the Lagrangian approach always resulting in mesh distortion. Special algorithms and codes were developed for these aims. The 2D models were solved numerically on IBM SP-2 by using one of its nodes. Here we present a model of salt motions in the presence of laterally asymmetrical loading and show the evolution of the resultant salt structure, see Figures 7.1(a)–(f). The nappe of sediments was imposed on the overburden with the growing symmetrical diapir (a). The velocity of nappe sinking in the overburden is greater than the rate of the diapiric growth. This is clearly seen from velocities presented in (a) and (b). Figure (b) demonstrates also how the shape of the diapir becomes slightly asymmetrical. When the nappe attains its equilibrium, the rate of diapiric penetration increases (c). Subsequent phases of diapiric evolution are shown in (d) and (e). It is seen that the diapir remains asymmetric only slightly. However, even this minor asymmetry leads to a quite asymmetric shape of the diapir in its subsequent evolution (f).

For further details see [Naimark and Ismail-Zadeh, 1995] and [Naimark *et al.*, 1996].

*Attempt to explain the observed distributions of intermediate-depth earthquakes*

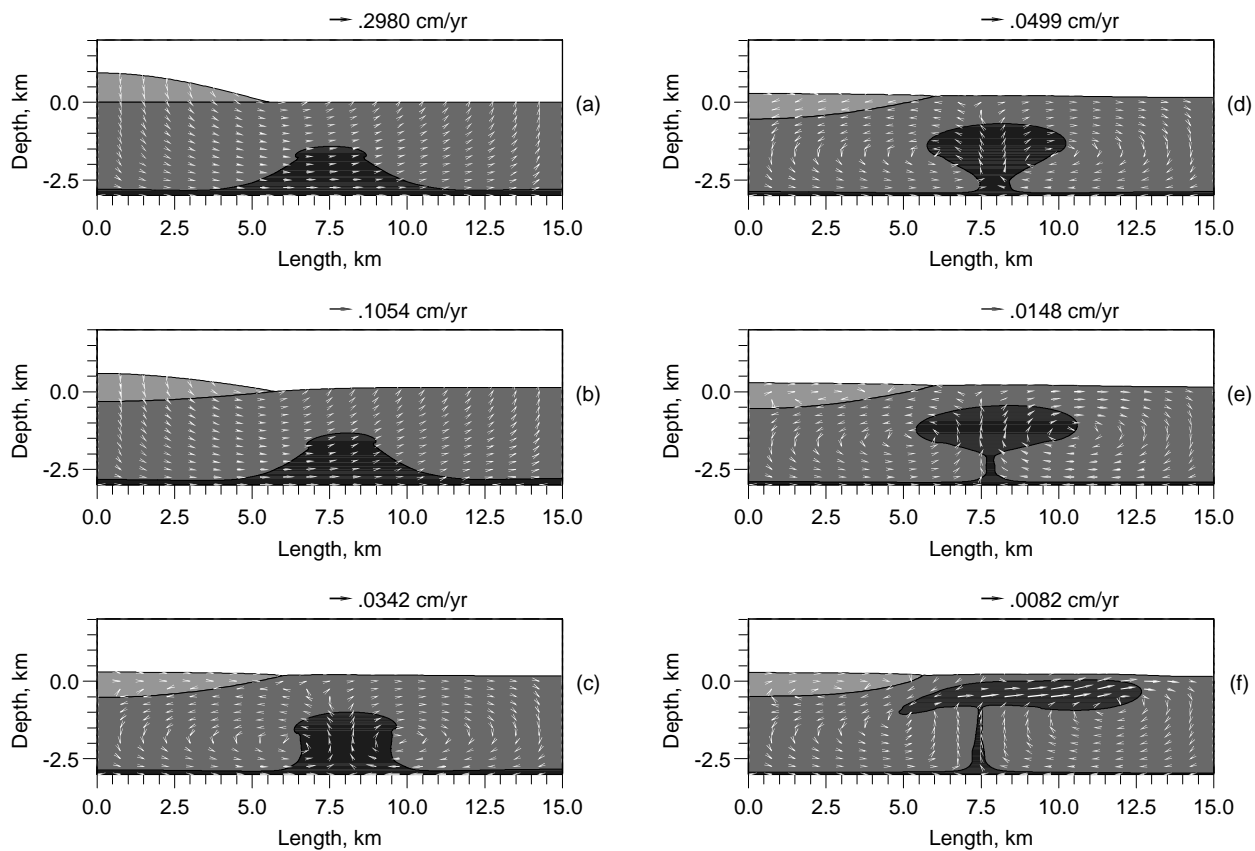


**Figure 7.1.** Evolution of salt diapirs under the effect of laterally inhomogeneous sedimentary loads. Viscosities and densities are the following:  $10^{18}$  Pa s and  $2.2 \times 10^3$  kg m $^{-3}$  (salt, heavy shading);  $10^{20}$  Pa s and  $2.3 \times 10^3$  kg m $^{-3}$  (overburden, grey);  $10^{20}$  Pa s and  $1.9 \times 10^3$  kg m $^{-3}$  (nappe of sediments, light grey). Flow velocities are shown by arrows. Velocity scale is given at the top of each figure. (a)  $t = 0$ , (b)  $t = 0.3$  Myr; (c)  $t = 3.3$  Myr; (d)  $t = 6.4$  Myr; (e)  $t = 10.2$  Myr; (f)  $t = 30.5$  Myr.

## 7.2 Molecular Dynamic Study of Melting of Earth's Materials

Anatoly B. Belonoshko

Institute of Earth Sciences, Uppsala University

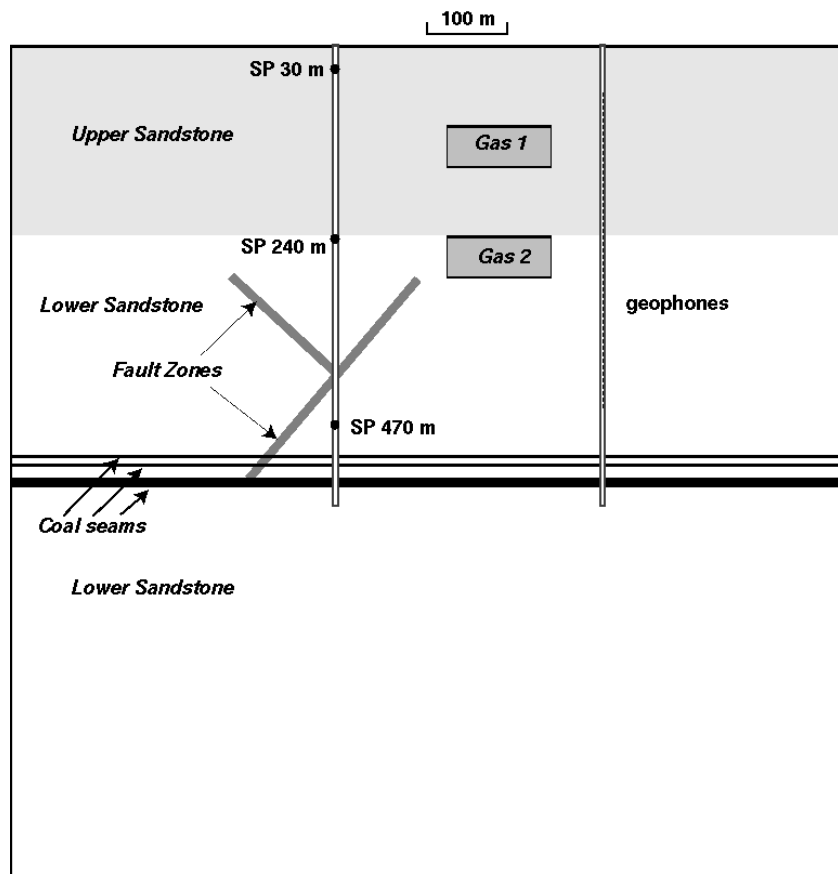
Our knowledge of the Earth's composition comes mainly from the cosmic abundances of the elements. Based on these data in combination with phase equilibria in such materials and seismic data the Earth is viewed as being composed mostly of silica and a  $\text{MgSiO}_3$ -perovskite mantle, and an iron liquid outer and solid inner core. The range of pressures relevant to studies of the Earth materials is from 1 to more than 3.5 million atmospheres. Naturally, experimental studies are extremely difficult at such a high pressure, especially in combination with high temperature. The problem of melting is of particular importance for the Earth science, because there are a number of factors which critically dependent on melting temperatures. Theoretical studies allow us to get insight into the mechanism of melting at very high pressures and provide very reasonable estimates of melting temperatures.

We have studied the melting of  $\text{SiO}_2$  (stishovite and quartz),  $\text{MgSiO}_3$  (perovskite),  $\text{NaCl}$  (B1 and B2 phases - as a test),  $\text{MgOFe}$  (bcc, fcc, and hcp phases) using the molecular dynamic method and the IBM SP-2 computer, [Belonoshko and Dubrovinsky, 1995], [Belonoshko and Dubrovinsky, 1996], [Belonoshko and Ahuja, 199X] and [Belonoshko, 1994]. Apart from the problem of description of interatomic interaction, the simulation of melting requires adequate choice of simulation technique because of the well known phenomenon of overheating in MD simulation of melting. To avoid overheating, the so called two-phase simulation have been carried out. An initial computational cell was composed of a solid and a liquid portion put together as shown in Figure 2.19(a) on page 22. Starting from such an initial configuration simulations have been performed at a given temperature and pressure. If the sample became a crystal (Figure 2.19(b) on page 22) then in the next run temperature was increased and simulations were repeated raising temperature until the sample became molten (Figure 2.19(c) on page 22). In such a way it was possible to determine an exact position of the melting temperature at a given pressure. The use of parallel computers are crucial in such simulation, because the choice of temperature in the next run depends on the results of the previous one. Therefore, the runs can not be performed independently and require a fast computer. The use of the two-phase simulation method was demonstrated to be equivalent to the method of free energy calculations and allows us to calculate melting temperatures of modeled systems very precisely.

Because of significant experimental problems of ultra-high pressure-temperature experiments, computer simulation becomes equal copartner of experimental studies. For example, MD computer simulations of experiments employing diamond anvil cell technique with laser heating have allowed to reveal the importance of thermal stress. A typical com-

*The use of parallel computers are crucial in such simulation, because the choice of temperature in the next run depends on the results of the previous one*

**Figure 7.2.** Geological model used in producing the synthetic seismograms in Figure 7.3. See Table 7.1 for the elastic parameters used in the finite difference modeling.



putational cell in those studies is shown in Figure 2.20 on page 23. A perfect MgO crystal was pressurized by Argon. However, different pressures were applied to different faces of the MgO crystal. When the difference in pressure reaches a critical value, recrystallization is observed. This has allowed to solve the experimental problem of systematically too low melting temperatures when the diamond anvil cell technique with laser heating is employed.

The size and time scale of simulation is out of reach of serial computers. Without distributed calculations these studies will hardly be feasible.

### 7.3 Finite Difference Modeling of Seismic Wave Propagation in Heterogeneous Media

*Christopher Juhlin, Lena Frenje*

Solid Earth Physics, Department of Geophysics, Uppsala University

Our research over the last years has focused on modeling seismic wave propagation in three types of media. These are (1) 2D elastic anisotropic media [Juhlin, 1995], (2) 2D acoustic seismic modeling of geological structures associated with oil exploration and (3) 2D and 3D randomly varying media.

#### *Elastic wave propagation in 2D anisotropic media*

The original code written in 1992 for the CM200 is still being used extensively for modeling geological structures where anisotropy is important. An example is the use of modeling in understanding borehole seismic data from coal fields in Australia. The coal seams are located at about 500 m depth and it is crucial that they be imaged properly using the seismic method prior to mining. A possible geological model developed at Uppsala University which explains the events observed on the borehole seismic records from a typical area is shown in Figure 7.2. The elastic properties of the rocks are given in Table 7.1 and use the nomenclature of Thomsen [Thomsen, 1986] to define the anisotropy.

From several modeling runs it was found necessary to include the two gas pockets in the model and the two fault zones where the elastic properties differ markedly from the surrounding rock. Three crosshole synthetic seismic shot gathers were generated for the model (Figure 7.3) using the approach of Juhlin [Juhlin, 1995]. The algorithm uses the stress-velocity formulation of the elastic equations on a staggered grid for hexagonal anisotropic heterogeneous media. Modeling parameters were,  $D_x$  and  $D_z = 1$  m,  $D_t = 0.15$  ms, a Ricker wavelet source with 90% of its energy below 150 Hz and absorbing boundary conditions on all sides. The shot gathers were generated at source depths of 30, 240 and 470 m, corresponding to the depths for the real data shown in Figure 7.4. The synthetic data in Figure 7.3 have many of the characteristics of the real data in Figure 7.4. Generation of synthetic data which did not include the gas pockets and the fault zones do not show many of these characteristics.

#### *Seismic modeling of geological structures*

In cooperation with the Institute of Earth Sciences at Uppsala University, geological models relevant to petroleum exploration and tectonic interpretation are being modeled seismically using 2D acoustic methods (an example is shown in the PDC Progress Report 1993). Since realistic situations are being modeled, the models tend to be large and a great deal of core memory is required. Therefore, we have been limited to 2D

*The coal seams are located at about 500 m depth and it is crucial that they be imaged properly using the seismic method prior to mining*

**Figure 7.3.** Synthetic vertical component seismograms from the model shown in Figure 7.2 with shots located at (a) 30 m, (b) 240 m and (c) 470 m depth. The receiver spacing is 6 m.

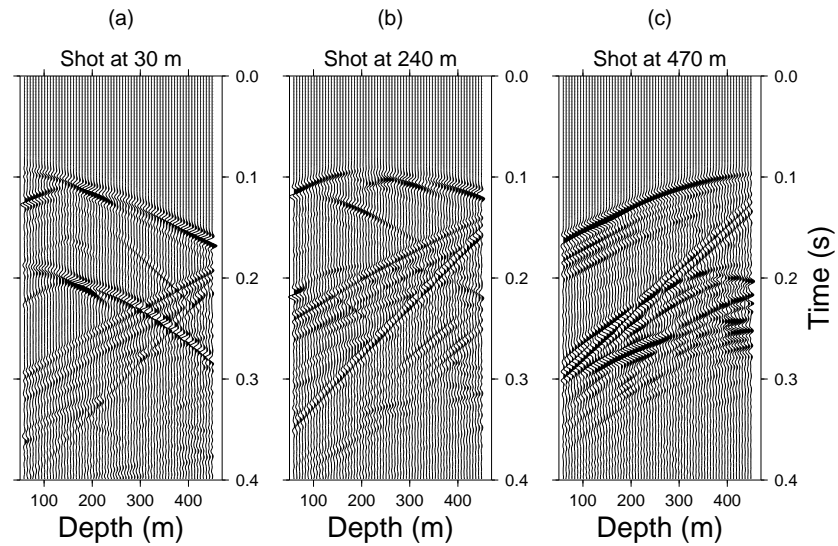


**Table 7.1.** Elastic parameters used in the finite difference modeling. The nomenclature of Thomsen [Thomsen, 1986] is used to define the anisotropy.

Media	$V_p$ (m/s)	$V_s$ (m/s)	$e$	$d^*$	$g$	$\rho$ (g/cc)
Upper						
Sandstone	3346	1907	0.25	0.056	0.0	2.5
Lower						
Sandstone	3464	1925	0.133	0.032	0.0	2.5
Coal	2400	1200	1.4	0.0	0.0	1.4
Gas 1	2645	1907	0.137	0.55	0.0	2.5
Gas 2	3033	1925	0.152	0.05	0.0	2.5
Fault Zones	3464	1000	0.133	0.032	0.0	2.4

acoustic modeling, rather than 3D acoustic or elastic modeling. However, the 2D acoustic results have been useful in interpreting real seismic data and in relating these data to geological structures.

#### *Seismic modeling of 2D and 3D random media*

Research has shown that there is often a random or stochastic component in geological structures, but that this component can be quantified by fractal parameters. We are currently using sonic velocities measured in boreholes to generate 2D and 3D models which have the same stochastic properties as the sonic logs that have been acquired in the boreholes. Figure 7.5 shows an example of 2D random media generated in this manner. Future work will involve propagating seismic waves through models such as this and comparing the results with observed data. Through this we hope to be able to extract the stochastic properties of the rock that the seismic waves have propagated through.

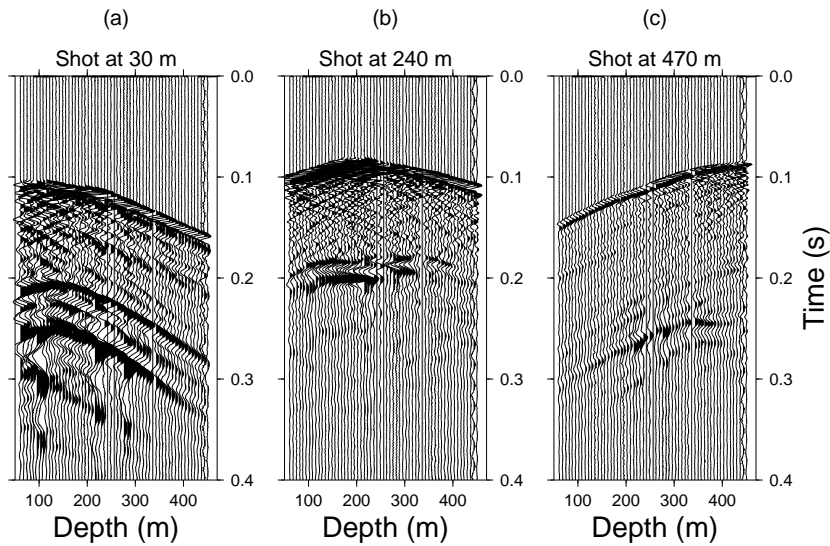


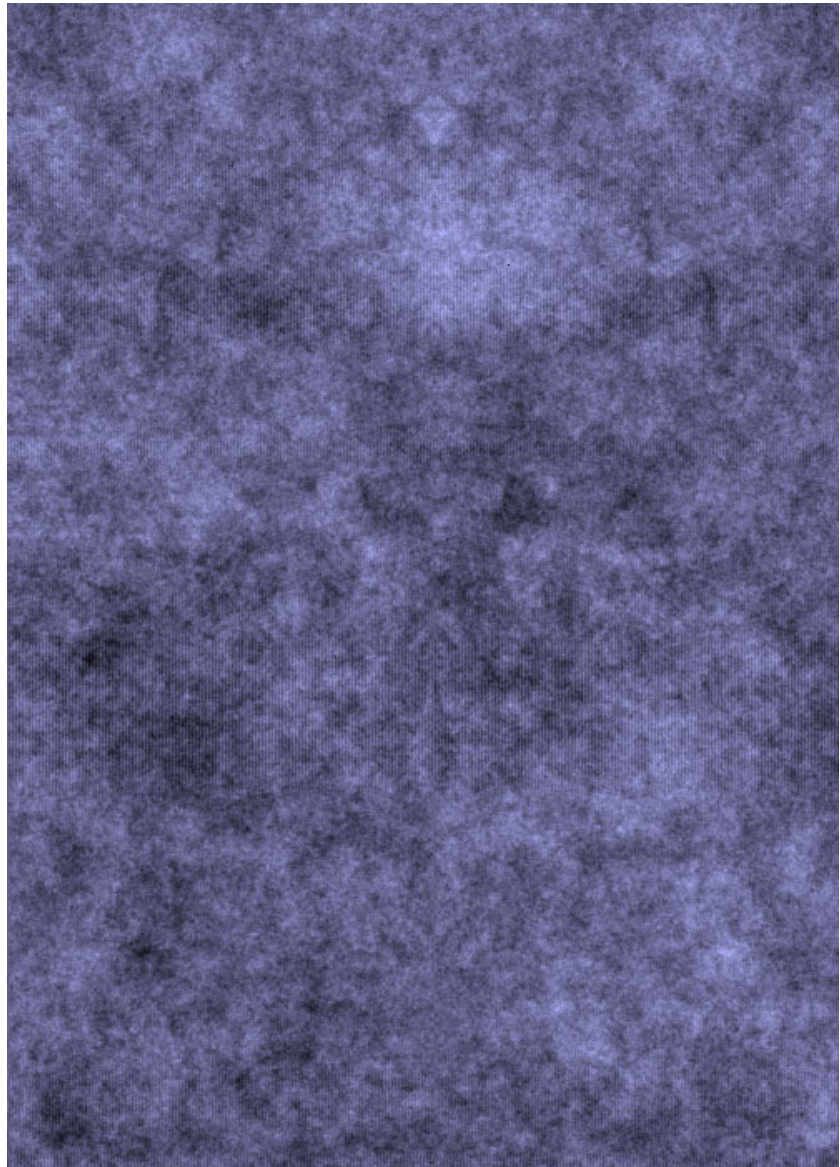
**Figure 7.4.** Typical real raw shot gathers from the crosshole survey with shots located at (a) 30 m, (b) 240 m and (c) 470 m depth. The receiver spacing is 6.7 m.

*Summary*

The speed of the CM200 allows us to seismically model realistic geologic structures much faster than on our Sun SPARCstations. Modeling which would require overnight runs on the Sun are completed in 15 minutes on the CM200. In addition, the large core memory allows us to model geological structures which we are not able to model on a workstation. However, to model realistic 3D structures, we require access to even larger amounts of core memory.

*Modeling which would require overnight runs on the Sun are completed in 15 minutes on the CM200*

**Figure 7.5.** A self-similar random 2D velocity model based on sonic velocity data from the deep Gravberg-1 borehole in the Siljan Ring area of Sweden.



## 8 Applications in Chemistry

### 8.1 A Conformational Free Energy Landscape of ApApA from Molecular Dynamics Simulations

*Jan Norberg, Lennart Nilsson*

Center for Structural Biochemistry, Karolinska Institutet

Investigations of molecular conformational states and substates are essential for understanding the relationship between structure and function. Nucleic acids are highly flexible molecules and one of the main forces stabilizing their three dimensional structure is stacking of the planar bases [Saenger, 1988]. Solvents are known to influence the conformational stability of nucleic acids, with stacked structures being favored in aqueous solution, but the stacking mechanism is not yet completely understood.

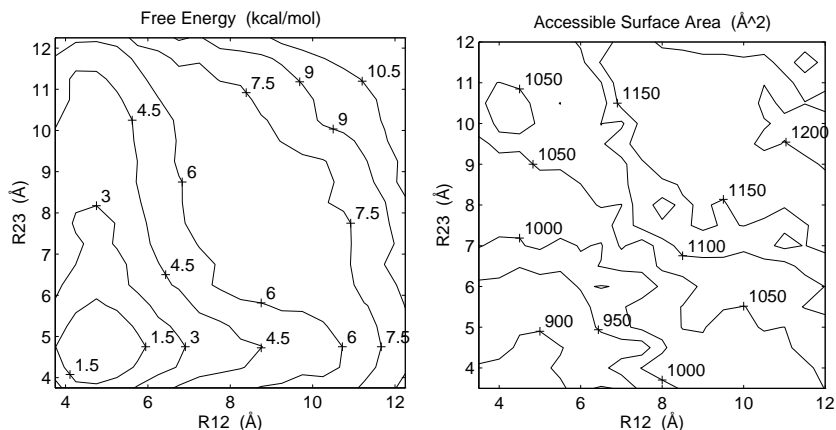
We have determined a conformational free energy landscape of the single stranded ribotrinucleoside diphosphate adenylyl-3',5'-adenylyl-3',5'-adenosine (ApApA) [Norberg and Nilsson, 1995a]. This free energy landscape was constructed from potential of mean force calculations, which were based on umbrella sampling in 324 molecular dynamics simulations of the ApApA trimer in aqueous solution, using the distances between the glycosidic base nitrogen atoms of neighboring bases as reaction coordinates. The total simulation time was 7.168 ns including the equilibration periods. All calculations were carried out using a parallel version of the program CHARMM [Brooks *et al.*, 1983].

A large number of very different conformations was obtained, ranging from a compact conformation with all three bases stacked to more extended conformations with all three bases unstacked, but also intermediates between these categories were observed.

The conformational free energy landscape of the ApApA trimer is presented in Figure 2.3 on page 12. The global minimum corresponds to a structure, which has the three bases stacked on top of each other. Local minima were obtained for structures having two bases stacked and one unstacked.

A contour map of the conformational free energy is presented in the left part of Figure 8.1. This is used to visualize the height of the transition barriers for the stacking-unstacking process of the three bases in the trimer. As a measure of the solvent influence on the conformational stability of the ApApA trimer we determined its solvent accessible surface area as shown in a contour map in the right part of Figure 8.1. The solvent accessible surface area of the global minimum structure was about 900 Å<sup>2</sup>, and this increased by 300-400 Å<sup>2</sup> when all bases were unstacked.

**Figure 8.1.** These contour maps show the conformational free energy and the accessible surface area of the ApApA trimer by using the reaction coordinates  $R_{12}$  and  $R_{23}$ .



In summary, we have by comparing the calculated 2D PMF surface of ApApA stacking with previous calculations of ApA stacking [Norberg and Nilsson, 1995b] found indications that stacking of the terminal base depends both on the length of the oligonucleotide on which it stacks, and also that the stack is somewhat more stable on the 5' side of the trimer.

## 8.2 Dynamics of Hydrogen Atoms in Strong External Fields

*Hans O Karlsson, Osvaldo Goscinski*

Department of Quantum Chemistry, Uppsala University

Research on hydrogenic atoms in strong external electric and magnetic fields has attracted much attention recently. The presence of an magnetic field, the Zeeman effect, allows for a comparison between an quantum (highly excited) state and a classical system with chaotic behavior, and the addition of an electric field, the Stark effect, give rise to interesting resonance features in, e.g. photo ionization cross sections.

With the use of an efficient parallel implementation of a direct recursive residue generation method (D-RRGM) on the CM200 [Karlsson and Goscinski, 1994, Karlsson and Goscinski, 1993] we have studied the photo ionization cross section  $\sigma$  for an hydrogen atom in different combinations of crossed electric and magnetic fields. The matrix sizes needed varied from  $\mathcal{N} = 20000$  to  $\mathcal{N} = 45000$ . The purpose was to test whether the auto-correlation function

$$C(\epsilon) = \frac{1}{\bar{\sigma}^2} \int_{E_1}^{E_2} [\sigma(E + \epsilon) - \bar{\sigma}][\sigma(E) - \bar{\sigma}] dE \quad (8.1)$$

( $\bar{\sigma}$  is the average cross section) could be used as a measure when comparing the quantum system with classical chaotic systems. It was found that such a comparison is non-trivial and that supplementary methods

are needed [Karlsson and Goscinski, 1994, Karlsson and Goscinski, 1993, Karlsson and Goscinski, 1995].

The D-RRGM approach was also used to study the time-evolution of a hydrogenic wave packet in the presence of crossed electric and magnetic fields. Highly excited hydrogenic wave packets mimic closely classical particles and are thus an excellent prototype for comparison between classical and quantum physics. We calculated the density-of-states from which the survival probability

$$P(t) = | \langle \Psi(0) | \Psi(t) \rangle |^2 \quad (8.2)$$

is given via a Fourier transform. By changing the magnitude and direction of the external fields, the shape and lifetime of the wave packet can be studied. We found that an increase in electric field strength might lead to a wave packet with longer lifetime. The survival probability was found to be an insufficient measure in comparing with classical chaotic systems [Karlsson, 1994].

*Highly excited hydrogenic wave packets mimic closely classical particles and are thus an excellent prototype for comparison between classical and quantum physics*

### 8.3 Parallel Molecular Dynamics Simulations of DNA Systems

*Aatto Laaksonen, Alexander P. Lyubartsev*

Department of Physical Chemistry, Arrhenius Laboratory,  
Stockholm University

Computer simulation methods, such as, Molecular Dynamics (MD) and Monte Carlo (MC) have now become important techniques to study fluids and solids. These methods provide a link between theory and experiment and they are also the only way to study complex many-body systems when both experimental techniques and analytical theories are unavailable.

The MD method provides a numerical solution of classical (Newton's) equations of motion:

$$m_i(d^2r_i/dt^2) = F_i(r_1, \dots, r_N) \quad (8.3)$$

The most time-consuming part (sometimes up to 99% of CPU time) of the MD simulations is the calculations of the forces  $F_i(r_1, \dots, r_N)$ . In a typical case of pair interactions the CPU time may scale with number of particles  $N$  between  $O(N^2)$  and  $O(N)$  depending on the algorithm and the type of interaction potential (note, that scaling as  $O(N)$  may be reached only at a very large  $N$  and for systems with short-range interactions).

Now it is a standard routine procedure to simulate molecular systems consisting of 100–1000 particles, which in some cases (e.g. simple liquids) is sufficient to obtain a good description of corresponding macrosystem. For other systems, a larger number of particles is needed in order to describe them in a realistic way. Complex bio- and organic molecules (e.g.

*Computer simulations of many-particle systems are very well suited for parallel computer systems*

proteins, nucleic acids, membranes, carbohydrates, etc. ) immersed into a solvent increase the number of atoms to be involved into a simulation one to two or more orders. Also, the larger the molecular systems grow, the longer simulations are needed to follow low-amplitude motions and slow conformational transitions. It is clear that the rate of the progress towards more complex molecular models is set, to a large extent, by advances in microprocessor technology and computer architecture.

Computer simulations of many-particle systems are very well suited for parallel computer systems. The basic reason for this is that the forces acting on each particle can be calculated independently in different processors. However, the most optimal parallel scheme for a particular problem depends both on the hardware in hand and on the system under investigation (size, type of interaction, etc. ). Electrostatic interactions, fast intramolecular motions due to explicit modeling of hydrogens, angle and torsional angle forces of macromolecules - all these kinds of forces require a special treatment to create an effective parallel code. The present project has the aim to develop a software to simulate systems of complex molecules (including DNA solutions) with number of atoms in the order of  $10^3$ – $10^4$  during a possibly longer time (up to several nanoseconds) using several or several dozens connected processors.

### ***The Molecular Dynamics Algorithm***

#### *General organization*

Complex molecular systems are often described by force fields like AMBER [Weiner *et al.*, 1986] or Gromos [van Gunsteren and Berendsen, 199X]. These force fields contain terms for following interactions:

1. atom-atom short-range interactions (Lennard-Jones potential)
2. atom-atom electrostatic interactions
3. intramolecular interactions: covalent bonds, covalent angles and torsional angles.

In principle, calculations of atom-atom interactions require a double sum over all the atom pairs. The application of a cut-off radius for the non-bonded interactions allows to considerably reduce the CPU time for calculation of atom-atom interactions, by effectively setting the interactions between particles separated by distances larger than the cut-off to zero.

Two problems, however, emerge here. First, the electrostatic interactions are long-ranged, and strictly, no cut-off without a special treatment can be applied. Second, in order to decide whether to calculate the forces between a given atom pair or not, one still should know the distances between all atomic pairs, or at least to have a list of atom pairs with distances less than the cut-off (list of neighbors).

One of the most effective and popular methods of treatment of electrostatic interactions is the Ewald summation method [Ewald, 1921]. The Ewald method splits up the total force into a long-range and short range component. The long-range part is calculated in the reciprocal space while the short-range part is treated alongside with the Lennard-Jones forces. The convergence of the two parts of the Ewald sum is regulated by a parameter. The optimal choice of the convergence parameter leads to scaling of the CPU time as  $O(N^{3/2})$ .

Creation of the neighbor lists is another problem. In liquids this list should be updated periodically. In the linked-cell method the search of neighboring pairs can be limited only by the current and the touching cells; this leads to an  $O(N)$  algorithm. However the true  $O(N)$  algorithm is achieved only at very large  $N$ ; for the “average size” systems of  $10^3$ – $10^4$  particles periodical (e.g. each 10 MD steps) update of neighbors list by looking through all the atom pairs occurs effective enough. Though CPU time of this block is scaled as  $O(N^2)$ , the coefficient is small, and for example in a test run with 2000 H<sub>2</sub>O molecules (6000 atoms) this part of the program consumes about 6% of the CPU time.

Calculations of intramolecular forces due to covalent bonds, angles and torsional angles are straightforward, although the the resulting expressions may be complicated.

Irrespectively to the parallelization, an essential saving of CPU time may be achieved by applying the multiple time scale algorithm. Different kinds of forces in the system fluctuate at different, characteristic time scales. In systems with explicit treatment of hydrogens, covalent bond forces, Lennard-Jones and electrostatic interactions at short distances between atoms require an updated force calculation after 0.2–0.4 fs, whereas long range parts of Lennard-Jones and electrostatic interactions, which consume most of the CPU time, may be calculated after 2–4 fs. In the present program the two time scale algorithm is applied [Tukerman *et al.*, 1992]. The covalent forces and atom-atom forces for atoms closer than 5 Å are calculated at every short time step. Forces between atoms with distance from 5 Å to cut-off and reciprocal part of the Ewald sum are calculated at every long time step. Correspondingly, two lists of neighbors are calculated in the program—for fast and for slow forces.

In the present project a SIMD scheme (Single Instruction Multiple Data) is applied. All nodes have the same program code, but it is executed on different data. The “core” of the MD algorithm: preparation of the initial state, moving of particles, average collection, output—that takes only a minor CPU time—is executed on one (master) node. After each MD step new coordinates and velocities of particles are transferred to the other nodes for force calculations.

*An essential saving of CPU time may be achieved by applying the multiple time scale algorithm*

### *Parallelization of specific parts of the program*

For an effective parallelization the whole list of atom pairs ( $I, J = 1, \dots, N, I < J$ ) should be uniformly divided between the available number of nodes. The condition  $I < J$  is set to avoid a double count, but it makes it difficult to divide equally the atom pairs between the nodes. To avoid this, the following scheme was applied. All particles are divided equally between processors (loop do  $I = \text{TASKID}, N, \text{NUMTASK}$ , where  $\text{TASKID}$  is the node number,  $\text{NUMTASK}$  is the total number of available nodes). For each  $I$  we have an inner loop over  $J$  with the following condition:  $I - J$  is even for  $I > J$  and  $J - I$  is odd for  $I < J$ . So the atom pairs occur uniformly distributed between nodes and each one is treated only once. Then for each node lists of close ( $r < 5\text{\AA}$ ) and far ( $5 < r < R_{cut}$ ) neighbors are calculated. These lists are local for each node and are recalculated after about 10 long time steps. They are used for Lennard-Jones and electrostatic (real space part) force calculations.

Parallelization of the reciprocal part of the Ewald sum is more or less straightforward. This contribution is expressed as a sum over reciprocal space vectors. Each node calculates force contributions due to a certain (fixed for this node) group of reciprocal vectors.

Calculations of forces due to covalent bonds, angles and torsions can be done independently for each bond, angle, or dihedral angle. They are easily distributed among available nodes for parallel calculations.

Forces acting on each particle from other particles are summed up on each node separately. After completing the calculation they are transferred to the “master” node, which executes moving of the particles according to a chosen integration scheme (in the present project three versions of MD are implemented: constant energy (NVE), constant temperature (NVT) and constant pressure and temperature (NPT) molecular dynamics). The new positions and velocities of particles are then transferred back to the other nodes.

### *Program timing*

In the presented algorithm the CPU time for force calculations scaled as  $1/n$  with the number of processors  $n$ , while the time for the data transfer between processors is proportional to  $n$ . As a result of this the speedup is not linear as the number of processors is increased. The increasing overhead due to the growing data transfer slows down the speed of the calculations as the number of processors is increased.

The test calculations showed that a maximum speed is achieved for 12–18 nodes, giving a factor about 6–9 in time gain comparatively to the run on a single processor (these values are slightly dependent on number of particles and some parameters of the MD algorithm). For 8–10 nodes the gain may be of factor 5–6, that can be considered as an optimal number of nodes in our applications.

### *Next step*

At present the work is focusing on an alternative parallelization algorithm which should reduce greatly the data transfer between nodes and make the program suitable for parallel computations with a much larger number of processors. The basic idea is to split the whole simulation cell into subcells, each corresponds to separate processor. In this case most of interactions (first of all “fast” forces recalculated at each small time step) act between particles in the same subcell, and can be calculated on the same processor. Data transfer would be needed only to calculate inter-cell interactions and in cases when a particle leaves one subcell for another. The dependence of data transfer on the number of processor would still be mainly linear, but with a much smaller coefficient.

### *Simulation results*

During the first half of 1995 the parallel algorithm was under development and testing. Simultaneously a MD simulation of a real molecular system have been carried out: aqueous ionic (NaCl) solution. The simulations was carried out on the IBM SP-2 computer at PDC.

Studies of electrolyte solutions have a great practical interest both in technological and biological applications. Simulation of ionic solution are complicated by the fact that the long-range electrostatic interactions are essential and often have a decisive role in the behavior of such systems. In this connection is important to make simulation in sufficiently large simulation cell to check size effects. On the other hand, there exists very slow processes in this system (e.g. creation and dissociation of ionic pairs) with characteristic time scale of about 100 ps. That is why simulations on a long time scale are needed.

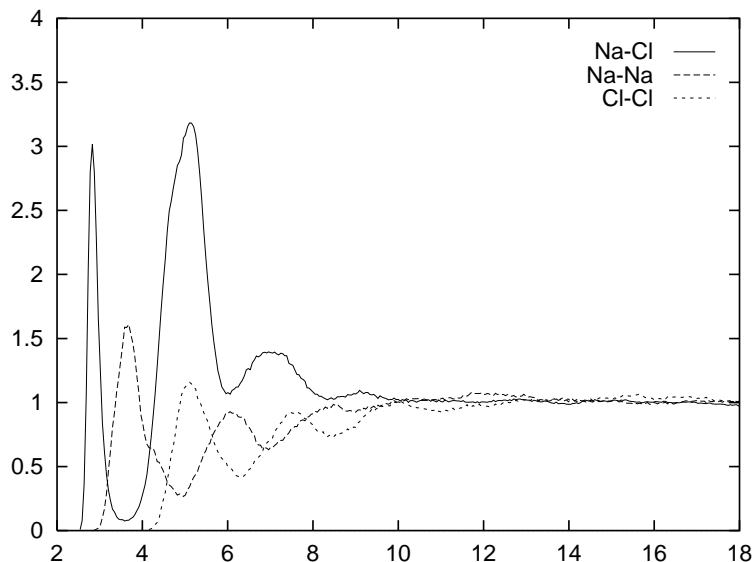
We have carried out simulation of system with 1960 water molecules (flexible SPC model) and 20 Na<sup>+</sup> and Cl<sup>-</sup> ions (that corresponds to 0.5M solution). The total number of atoms was 5920 and the simulation box size was about 39 Å. The constant temperature and constant pressure MD algorithm was used. The system was simulated during 1 ns after 200 ps of equilibration. Running on 8 nodes the program execute 1 ps of MD simulation (500 large time steps) in about 50 minutes. The main objective of this study was to calculate radial distribution functions (RDF) of ions and to compare with RDF obtained for smaller systems (256 and 512 water molecules) calculated before. The result is presented in Figure 8.2. Other structural and thermodynamical properties were obtained in this study.

*Studies of electrolyte solutions have a great practical interest both in technological and biological applications*

### *Perspective*

At present we are planning to use the program for molecular dynamics simulation of DNA in water solution in presence of ions. The available software makes it possible to use realistic flexible models of water and

**Figure 8.2.** Ion-ion radial distribution functions for 0.5 NaCl aqueous solution.



DNA molecules. This in conjunction with constant-pressure MD would allow us to study conformational properties of DNA at different salt concentrations. Obtaining of RDF in these simulations gives a way to construct effective potentials of effective ion-DNA interactions which could be used for further study in simplified (without water) models [Lyubartsev and Laaksonen, 1995]. The program can be used for study of interaction of DNA with other biologically important molecules.

#### 8.4 Molecular Dynamics Simulation of a Poly(Ethylene Oxide) Surface

*Alvo Aabloo, John O. Thomas*

Institute of Chemistry, Uppsala University

Potentials developed earlier for crystalline and amorphous bulk PEO systems have been used for the MD simulation of a PEO surface model. The surface comprises the outer region of a 122 Å thick sheet of PEO in which the PEO,  $-(\text{CH}_2-\text{CH}_2-\text{O})_n-$ , chains run obliquely across the cell, and are terminated by  $\text{C}_2\text{H}_5$  ethyl groups. The atoms on one side of the sheet are tethered to facilitate a satisfactory Ewald summation. The sheet expands from its "crystalline" width of 122 Å to 128 Å in the simulated model. Simulations were performed at three temperatures: 300 K, 400 K and 500 K. Different behavior in the surface layer was found compared to that in the bulk. The structural and dynamical properties of the surface were analyzed at each temperature. These calculations were performed using the IBM SP-2. For further details see [Aabloo and Thomas, 199Xa].

## 8.5 Molecular Dynamics Simulation of Ion Mobility in the Crystalline Poly(Ethylene Oxide) Surface

*Alvo Aabloo, John O. Thomas*

Institute of Chemistry, Uppsala University

Potentials developed earlier for crystalline and amorphous bulk PEO systems have been used subsequently to perform MD simulation of a PEO surface. This same model has then been extended to probe the behavior of ions in this surface compared to that in the bulk of the polymer. Neodymium ions have first been inserted to test the performance of the program, with chlorine as counter ions. The ions were found to concentrate in a 7 Å thick surface layer, and not penetrate further into the bulk. Evidence is found for a number of different ion association modes. Nd–Cl distances were between 1.5 and 1.7 Å, and Cl–Cl distances in the range 2.7 to 2.9 Å. The polymer structure was much like that of the ion-free system. Structural and dynamical properties of the ion-containing surface have been analyzed. These calculations were performed using the IBM SP-2. For further details see [Aabloo and Thomas, 199Xb].

*The ions were found to concentrate in a 7 Å thick surface layer*

## 8.6 An Integral Direct, Distributed-Data, Parallel MP2 Algorithm

*Martin Schütz, Roland Lindh*

Department of Theoretical Chemistry, Lund University

### *Introduction*

In recent years, advances in computer technology together with substantial improvements in quantum chemical algorithms have enabled *ab initio* electronic structure calculations on chemical systems of increasingly complexity. Common to all of these *ab initio* algorithms which aim at large scale problems is that they are *integral direct* in the sense that the electron repulsion integrals (ERIs) are reevaluated whenever needed, rather than computed once, stored on disk and read from disk when required. Hence, the bottleneck of storing the ERIs (formally  $N^4$ , where  $N$  denotes the number of basis functions), which precluded many applications, is avoided. Furthermore, the heavy input/output (I/O) load inflicted by conventional algorithms is also avoided. On the other hand, the CPU time required for a given problem, increases drastically. However, it was also recognized, that the number of ERIs one has to recompute can be reduced substantially using proper integral prescreening techniques, i.e. by estimating the maximal size of a batch of ERIs prior to evaluation, and eventually omitting the evaluation of the ERI batch.

Integral direct methods were first used in SCF theory (“direct SCF” approach by [Almlöf *et al.*, 1982], but have since been extended to methods which include electron correlation [Taylor, 1987, Sæbø and Almlöf,

1989, Head-Gordon *et al.*, 1988]. In contrast to the SCF method, where the ERIs over atomic orbitals (AOs), i.e. the basis functions) are immediately contracted to the Fock matrix in AO basis, and only AO integrals are needed, correlated methods are usually formulated in terms of ERIs over molecular orbitals (MOs). This means in practice, that an integral transformation of the ERIs in AO basis to the MO basis is required as an intermediate step. A full 4-index transformation, carried out as four quarter transformations has a flop count that scales as  $\mathcal{O}(N^5)$  and has  $\mathcal{O}(N^4)$  storage requirements. At a first sight these memory requirements seem to rule out any integral direct implementation of a correlated method. Fortunately enough, however, most correlated methods can be reformulated in terms of AO ERIs and a reasonably small subset of MO integrals. Such MO integral subsets typically have two indices restricted to the *occupied* orbital space of dimension  $O$ , which is usually much smaller than  $N$ . For example, the computation of the MBPT(2) energy only requires the exchange integrals ( $ia | jb$ ) (Mulliken notation with  $i, j$  denoting occupied, and  $a, b$  virtual orbitals). The memory necessary to hold such a subset of MO integrals then is  $\mathcal{O}(O^2N^2)$ . The memory requirements can further be reduced to  $\mathcal{O}(ION^2)$  by *paging* over the first transformation index and *multipassing* over the ERI list: here,  $I$  denotes the size of the segment of the first transformation index, while  $O/I$  is the corresponding number of integral passes.

Integral direct methods are especially powerful in combination with efficient parallelization strategies, moving problems of biochemical interest within reach of quantum chemical methods. Here we describe a scalable, distributed-data parallel implementation of direct integral transformation for a restricted set of MO indices. The code is capable of dealing with chemical systems beyond 1000 basis functions and 200 correlated electrons, including low-symmetry cases. Molecular symmetry is exploited by symmetry-adapting the AO ERIs prior to the transformation. Highly superlinear speedups were observed due to efficient use of both the compute power and the bulk memory of the MPP system. The algorithm is currently implemented in an MP2 code [Schütz and Lindh, 199Xb], yet it is easily adopted for other electron correlation methods, where only MO integrals with two indices in the virtual orbitals space are required: actually, distributed-data parallel implementations for MP2-R12 [Schütz and Klopper, 199X] and CASSCF, based on the same transformation code, are currently under development. In what follows, we will describe very superficially the computational problem and the parallel implementation of the MP2 code. For example, the handling of the molecular symmetry and ERI prescreening is omitted completely in this letter. For a more thorough discussion we refer to [Schütz and Lindh, 199Xb].

*Integral direct methods are especially powerful in combination with efficient parallelization strategies, moving problems of biochemical interest within reach of quantum chemical methods*

### Computational problem

The MBPT(2) contribution to the correlation energy for a closed shell system can be written in spin-free formalism as

$$E^{(2)} = \sum_{i,j,a,b} \frac{(ia | jb)^2 + \frac{1}{2}[(ia | jb) - (ib | ja)]^2}{\epsilon_i + \epsilon_j - \epsilon_a - \epsilon_b} \quad (8.4)$$

where  $i, j$  and  $a, b$  denote occupied and virtual, canonical MOs, respectively, and  $\epsilon_i, \epsilon_j, \epsilon_a, \epsilon_b$  the corresponding eigenvalues of the Fock matrix. The MO exchange integrals  $(ia | jb)$  are computed from a transformation of the AO or SO ERIs over restricted MO index ranges, i.e.

$$(ia | jb) = \sum_{\mu,\nu,\lambda,\sigma} C_{\mu i} C_{\nu a} C_{\lambda j} C_{\sigma b} (\mu\nu | \lambda\sigma) \quad (8.5)$$

where, in the present context,  $\mu, \nu, \lambda$  and  $\sigma$  denote SOs, and the MO coefficient matrix  $\mathbf{C}$  transforms from the SO to the MO basis. In order to keep the flop count as low as possible the integral transformation usually is carried out in four subsequent steps, with one index transformed after the other. In the following we will refer to the transformation of the 1st, 2nd, 3rd and 4th index as the Q1, Q2, Q3 and Q4 step, respectively. Accordingly, the Q1 block contains the integrals  $(i\nu | \lambda\sigma)$ , the Q2 block the integrals  $(ia | \lambda\sigma)$ , and so on, while the SO block comprises the untransformed SO integrals  $(\mu\nu | \lambda\sigma)$ . Using this notation the Q1 step, scaling as  $\mathcal{O}(ON^4)$  with the problem size, dominates the integral transformation. The evaluation of the SO ERIs requires  $\mathcal{O}(N^4)$  floating point operations. Antisymmetrization and summation according to equation (8.4) are all  $\mathcal{O}(O^2N^2)$  and not rate limiting.

The main obstacle in direct integral transformation schemes is the vast amount of memory, which is necessary to hold the partially transformed ERIs. For example, the Q1 block after full completion of the Q1 step requires  $\mathcal{O}(ON^3)$  memory. In direct transformations with two indices limited to the occupied orbital space as for MBPT(2) energy calculations, this can be reduced to  $\mathcal{O}(O^2N^2)$ , if the Q2 and Q3 steps already are carried out, *before* all SO integrals for the Q1 step are generated. [Head-Gordon *et al.*, 1988, Sæbø and Almlöf, 1989]. Furthermore, if the available memory still is exceeded, it is possible to segment the 1st MO index range with the limiting case of a single  $i$  and the corresponding memory requirement of  $\mathcal{O}(ON^2)$ . However, this implies *multiple passes through the integral list* (worst case:  $O$ ), thus it is desirable to have as large segments of  $i$  as possible.

### Parallel algorithm

The memory requirements are dominated by the Q3 and Q4 integral blocks (both  $\mathcal{O}(ION^2)$ ). These blocks therefore are distributed over

*The main obstacle in direct integral transformation schemes is the vast amount of memory, which is necessary to hold the partially transformed ERIs*

the aggregate memory of the MPP system using the concept of global arrays. The SO, Q1 and Q2 blocks on the other hand only contain the ERIs for a fixed quadruplet or doublet of symmetry-unique shells and hence are much smaller ( $\mathcal{O}(S^4)$  and  $\mathcal{O}(INS^2)$ , where  $S$  denote the size of a shell). These blocks thus are kept local and are private to each computational node, together with the MO coefficients, which are replicated. The underlying communication framework to access remote patches of global arrays is built on top of the Global Array (GA) toolkit of [Nieplocha *et al.*, 1994, Bernholdt *et al.*, 1995]. This toolkit provides a virtual “shared memory” programming model for two-dimensional arrays, yet nonuniform memory access is not hidden from the application program. *One-sided access* to remote patches without any need for cooperation between the computational threads on the data-requesting and the data-owning nodes is provided either by forking a shared-memory dataserver on each node, or by installing a data serving interrupt handler, as is the case on the IBM SP-2, which allows for interrupt driven message-passing. One-sided access of remote data eliminates unnecessary synchronization between nodes, implying enhanced performance relative to conventional message-passing schemes.

ERI generation and transformation up to the Q3 step are split up into individual *tasks*, which are distributed over the computational nodes and executed in parallel. If an ERI batch ( $\mu\nu \mid \lambda\sigma$ ) is defined by the symmetry-unique shell quadruplet  $\{M, N, \Lambda, \Sigma\}$ , then a single task corresponds to the shell doublet  $\Sigma, \Lambda \leq \Sigma$ , looping over all shells  $N, M \leq N$ . Hence, if the number of symmetry-unique shells  $\Sigma$  is denoted by  $n_\Sigma$ , then the number of individual tasks is equal to  $n_\Sigma(n_\Sigma + 1)/2$ , and grows quadratically with increasing size of the chemical system under study. Even for systems of only moderate size, the number of tasks is usually sufficient to ensure reasonable load balancing on a fair number of nodes.

Before the actual  $k^4$  loop for ERI evaluation and transformation is entered, each node creates a *private task list* by enumeration of all symmetry-unique shell doublets  $\Sigma, \Lambda \leq \Sigma$ . This task list is sorted afterwards with respect to a task criterion, which depends (i) on the assessed *task length* (i.e. long tasks have high priority, while short tasks are used for padding towards the end), and (ii) on the *locality* of each task.

The individual task length is estimated by the number of primitive pairs that belong to the corresponding  $\Sigma, \Lambda \leq \Sigma$  shell doublet. Since the prescreening of ERIs is based on primitive pair entities, and is already accomplished at that point (see [Schütz and Lindh, 199Xb] for further details), the estimate of the task length is actually based on the *genuine number* of primitive pairs that remain *after the prescreening*. The task locality on the other hand is defined as the ratio of the summed up sizes of the local Q3 patches, and the total Q3 patches, which will be accessed by a given task. The position of a given task in the list then reflects its priority for a given node. Before a node finally executes a task, it has to register it on a *global task list*. The mechanism of

*Even for systems of only moderate size, the number of tasks is usually sufficient to ensure reasonable load balancing on a fair number of nodes*

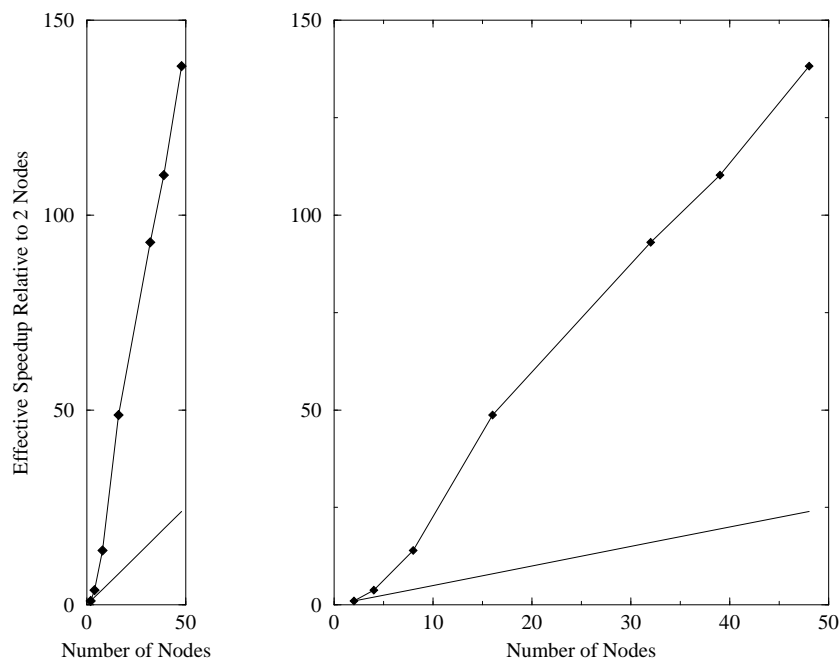


**Figure 8.3.** Observed and linear speedup relative to two nodes, in the range of 2 to 48 SP-2 nodes. The filled diamonds correspond to the timings, compiled in Table 8.1. The second graph displays the same data, but with a more appropriate scaling of the ordinate than the first one, which has the conventional scaling and yields the linear speedup line at 45°.

reserving individual tasks in a specific order on a global task list allows for dynamic load balancing in a “self-service” way, without any need for a special master or control process. Moreover, giving the tasks a priority relative to the locality of the data, which will be accessed, renders savings in interprocessor communications.

After all tasks are executed, the complete set of Q3 ERIs is available in global memory. Prior to the Q4 step the Q3 blocks are transposed and the Q4 step is performed completely local.

### *Performance*

The parallel efficiency of the algorithm is demonstrated by calculations on the phenantrene molecule ( $C_{2v}$  symmetry, with 762 primitive Gaussians, contracted to 412 basis functions). For molecular systems of this size, integral direct methods start to become the only possible route; hence this test case may have some practical significance, although it is still small enough to be well suited for scalability measurements. The number of symmetry-unique shells for this system is 31, forming 496 individual tasks.

The calculations were performed on the IBM SP-2 at PDC. Performance data is tabulated in Table 8.1 and Figure 8.3 displays this data graphically, comparing it with a linear speedup curve. The measured wall clock time on 48 nodes is less than 15 minutes for this calculation, and the speedup relative to single node execution is estimated to 527.

*For molecular systems of this size, integral direct methods start to become the only possible route*

**Table 8.1.** Wall clock times in seconds and speedup factors relative to 2 nodes as a function of nodes.

# nodes	$T_{\text{elapsed}}$	# passes	speedup
2	122238	8	1.00
4	32045	4	3.81
8	8730	2	14.00
16	2510	1	48.69
32	1315	1	92.97
39	1109	1	110.25
48	884	1	138.21

Speedup factors substantially above linear speedup are observed. On 48 nodes, the observed speedup is 5.8 times larger than linear speedup (with reference to 2 nodes). This superlinear speedup is a result of exploiting both the compute power and the aggregate memory of the parallel computer, reducing the number of necessary integral passes and hence saving not only wall clock but CPU time relative to single node execution. Outside of the superlinear regime, i.e. between 16 and 48 nodes when only a single pass is necessary, the algorithm still shows satisfying performance, with a parallel efficiency on 48 vs 16 nodes of 95%. Calculations in excess of 1000 basis functions with reasonable elapsed times are possible with our code. The largest calculations performed so far comprised 1266 primitives contracted to 702 basis functions, and 82 correlated electrons. On 64 SP-2 nodes, each with 128 Mbyte memory, this calculation took about 90 minutes in wall clock time, and two integral passes [Schütz and Lindh, 199Xa].

### *Applications*

Currently, two application projects based on the new integral direct, parallel MP2 code are in progress at PDC:

1. *Weakly bound van der Waals complexes between aromatic molecules and rare gas atoms*

Solvent clusters  $M-R_n$  between aromatic molecules (M) and rare-gas atoms (R) have become prototype systems for the investigation of solvation at the microscopic level. The combination of molecular beam techniques, laser and mass spectroscopy enables the synthesis of such clusters in collisionless environment, and their mass-specific detection and spectroscopy. Recently, the stimulated emission pumping/resonant two-photon ionization (SEP-R2PI) method was introduced, [Droz *et al.*, 1995], a novel spectroscopic technique, which allows for the mass-selective determination of vdW binding energies of such systems in the ground and 1st electronically excited state with very high accuracy. On the theoretical side, *ab initio* calculations on such system are very demanding, since in order to model the predominant dispersive interactions properly, large basis sets have to be used.

In the present PDC project the intermolecular potential energy surfaces (IPES) of the anthracene-Ar (cf. Figure 2.23 on page 24) and anthracene-Ar<sub>2</sub> vdW complexes are studied at the MP2 level, employing large ANO basis sets, i.e. 700 basis functions and more. Different bonding sites of the Ar atom on top of the catacondensed aromatic ring system are investigated. The computed *ab initio* IPES will be used later to construct an analytical model potential for the M-R solute-solvent interaction, which in turn can be employed in Monte Carlo and dynamics studies to investigate microsolvation effects, occurring in larger anthracene-Ar<sub>n</sub> ( $n = 10, \dots, 40$ ) and similar clusters.

## 2. *The significance of the trigger reaction of the calicheamicin anti cancer drug*

The new *enediynes* class of anti cancer drugs acts by cleaving the DNA strand after undergoing a Bergman like autoaromatization and forming a highly reactive biradical. This autoaromatization process is initiated by a so called *trigger reaction*. The calicheamicin (cf. Figure 2.23 on page 24) is a molecule of this class, which all have in common the enediyne moiety. Whereas the formation of the biradical is fully understood, the significance of the preceding trigger reaction still needs to be investigated. The favored hypothesis is that the effect of the trigger reaction is to alter the enediyne structure itself, leading to a decrease in the activation barrier of the biradical formation. Another theory is that the trigger reaction enables the biradical formation by saturating a double bond in the vicinity of the enediyne moiety. The presence of this double bond would make the biradical formation energetically unfavorable. i.e. the trigger reaction is reducing the reaction energy of the biradical formation. The present study investigates the latter hypothesis at the MP2 level of theory employing small to large ANO basis sets (400–800 basis functions). The calculations are extremely expensive since the molecules under study are large and do not have any symmetry.

## 8.7 The Structure of the Blue Copper Proteins

*Mats Olsson, Ulf Ryde, Björn Roos*

Department of Theoretical Chemistry, Lund University

*Jan der Kerpel, Kristin Pierloot*

Department of Chemistry, University of Leuven, Belgium

Blue copper proteins are a group of electron-transfer proteins that are characterized by an intense blue color, unusually high reduction potentials and unique electron spin resonance spectroscopic features [Adman, 1991, Sykes, 1990]. They all contain a copper ion that changes between the oxidation states +I and +II during electron transfer. A typical example is plastocyanin, a water-soluble protein with a key role in photosynthesis. The crystal structure of plastocyanin is known [Guss *et al.*,

1992, Adman, 1991] and shows an unusual ligand geometry around the copper atom: the copper atom is coordinated to three ligands at short distances, one thiolate group from a cysteine residue and two histidine nitrogen atoms. At a longer distance there is a fourth ligand, a methionine thioether sulphur atom. The ligands form a distorted tetrahedron, something which is rarely found in small inorganic Cu(II) complexes. Some blue copper proteins, e.g. azurin, have an additional fifth ligand, an amide oxygen from the protein backbone, coordinated at a long distance to the metal atom.

These unique chemical properties of the blue copper proteins early led to the suggestion that Cu(II) is forced by the protein into a strained conformation, namely to a geometry similar to the one preferred by Cu(I). In this way the protein would facilitate the electron transfer by minimizing the reorganization energy. This idea was later developed into more general hypotheses regarding protein function, the “induced rack” and “entatic state” theories [Malmström, 1994, Williams, 1995].

We have started a project on the blue copper proteins, where we intend to test the strain hypotheses and try to explain the extraordinary properties of the protein using theoretical methods. Naturally, the entire proteins are far too large for high-level quantum chemical calculations. Therefore smaller model systems are investigated, typically  $[\text{Cu}(\text{imidazole})_2\text{SCH}_3\text{S}(\text{CH}_3)_2]^+$ .

In order to test the strain hypotheses, the model systems are optimized in vacuum using a density functional method (B3LYP as implemented in the IBM quantum chemical software Mulliken [Rice *et al.*, 1995]). In this way, we can study the intrinsic coordination preferences of the metal ion and its ligands without the protein. If the optimized structure of the model system is similar to the structure found in the protein then the strain hypotheses probably have to be revised. In fact, this turns out to be the case, see Figure 2.24 on page 25; it seems that the unusual properties of the blue copper protein should rather be attributed to the chemical properties of the ligands [Ryde *et al.*, 1996].

Why is the copper ion quasi-tetrahedrally coordinated in the protein while most Cu(II) complexes assume a tetragonal (square-planar or octahedral) structure? We have tried to answer this question by optimizing a large number of small copper complexes with different ligands.

The geometry of a copper complex is governed by the ligand-ligand repulsion, the ligand-metal attraction and the ligand-field stabilization. The ligand-field theory provides simple rules that give a qualitative picture of the structure of metal complexes. For Cu(II) complexes, which have a  $d^9$  configuration (i.e. four filled and one half filled  $d$ -orbitals), it predicts a tetragonal structure with the ligands in the direction of the lobes of the energetically highest (singly) occupied  $d$ -orbital. This is in agreement with the optimized structure of  $[\text{Cu}(\text{NH}_3)_4]^{2+}$  which has a slightly distorted square-planar geometry, as can be seen in Figure 2.25 on page 25.

*We intend to test the strain hypotheses and try to explain the extraordinary properties of the protein using theoretical methods*

If an ammonia ligand is replaced by a thiolate ion ( $[\text{Cu}(\text{NH}_3)_3\text{SH}]^+$ ), the ground state is still tetragonal, but there is also a trigonal (see Figure 2.26 on page 25) state only 13 kJ/mole higher in energy. This is within the error limits of the method. In this state the thiolate ligand forms a three-electron S 3*p*-Cu 3*d*  $\pi$ -bond to the metal atom. This can be viewed as a special case of a square-planar structure, where the lobes of the sulphur 3*p*-orbital occupy two coordination positions, see Figure 2.26 on page 25.

It is interesting to note that for the best blue copper protein model,  $[\text{Cu}(\text{NH}_3)_2\text{SHSH}_2]^+$ , the trigonal state is in fact the ground state, in accordance with the protein structure, see Figure 2.27 on page 25. However, the energy difference is only 4 kJ/mole, i.e. so small that both structures may be populated at ambient temperature.

In conclusion, the unusual structure of the blue copper proteins seems to be an effect mainly of the cysteine thiolate ligand, which due to its size may form a strong  $\pi$ -bond to the copper ion. The role of the protein is probably to provide appropriate ligands and to exclude water from the active site.

*The unusual structure of the blue copper proteins seems to be an effect mainly of the cysteine thiolate ligand*

## 8.8 Ab Initio and DFT Investigations of Solution Tautomerism of DNA Bases

*Anders Broo, Anders Holmen*

Department of Physical Chemistry, CTH

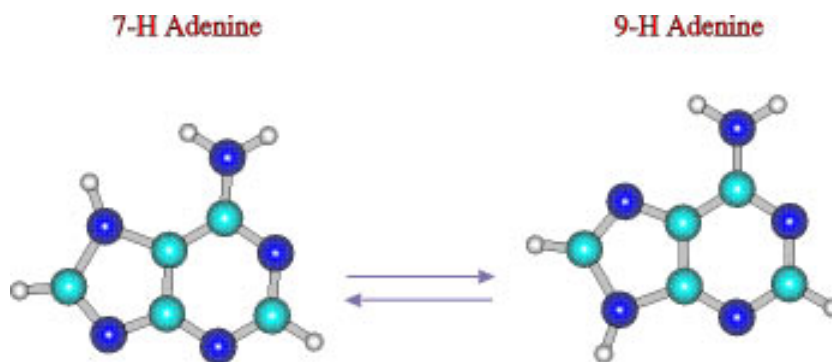
The structure and prototropic tautomeric equilibria of the nucleic acid bases have received much attention ever since the determination of the structure of the nucleic acids by Watson and Crick. Experimentally, structural data have been obtained from X-ray and neutron-diffraction studies of the individual nucleic acid bases. The tautomeric equilibria have been studied mainly by various spectroscopic techniques, both in fluid solution and in rigid rare-gas matrices.

The use of quantum chemical methods to calculate the equilibrium geometries and energies of molecules of the size of the DNA bases poses some problems due to the high cost of accurate calculations. Geometries obtained with semi-empirical or Hartree-Fock *ab initio* methods have been found to differ significantly from geometries obtained experimentally. Thus, there is a need for computational methods that include some of the electron correlation.

We have used the Gaussian94 set of programs to determine the geometry and relative energies of several purine and purine derivatives including the DNA base adenine. The 7,9 H tautomerism is exemplified in Figure 8.4. This type of calculations are very computer resource demanding, both on CPU power and I/O capacity. The IBM SP-2 computer have offered a suitable platform for the most expensive calculations in this study.

*The IBM SP-2 computer have offered a suitable platform for the most expensive calculations in this study*

**Figure 8.4.** An example of the 9-H/7-H tautomerism in adenine that have been studied in this project.



## 8.9 Basis Set and Correlation Effects on Geometry of Octahedral Second-Row Transition-Metal Complexes

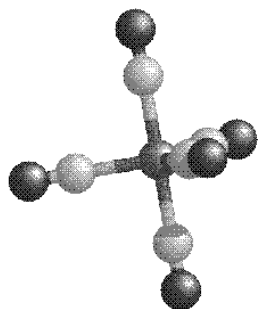
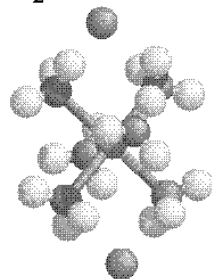
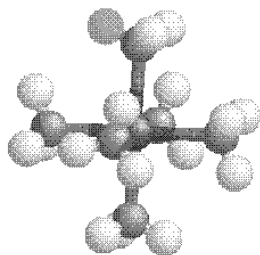
*Anders Broo*

Department of Physical Chemistry, CTH

Ruthenium complexes, especially  $[\text{Ru}(\text{bpy})_3]^{2+}$ , are among the most experimentally studied organometallic complexes, due to their unique combination of chemical stability, redox properties and electron-transfer properties, and excited-state reactivity. Despite of that, few quantum chemical investigations of ruthenium complexes have been published. Until just recently, only semi-empirical methods and density functional theory methods have been used. Part of the problem in applying *ab initio* quantum chemical methods to second-row transition metals is the relative large size, in terms of basis functions, of the metal complexes. Another aspect is the importance of relativistic effects on the electron structure of the metal. Yet, another important factor is the so far unclear role of electron correlation on the geometry and binding energy of second-row transition metals.

In this project several different basis sets, including so called relativistic effective core potential basis sets, were used to predict geometries, vibration spectrum, high-spin/low-spin energy separation of several ruthenium complexes. Electron correlation where treated at MP2, MP3, MP4(SDQ), CCSD, CCSD(T) and CASSCF levels of theory. Many of the heaviest calculations were performed on the IBM SP-2 computer at PDC, especially the CASSCF calculations were done in parallel mode. Examples of metal complexes in this study could be found in Figure 8.5. Absorption spectrum of  $[\text{Ru}(\text{NH}_3)_6]^{2+}$  was predicted with a novel computational scheme that uses CASSCF optimized orbitals in a truncated CISDT calculation. This scheme was proven surprisingly good in reproducing the lowest transition energies in the metal complex. This scheme is currently under further development to be suitable for calculations on absorptions spectrum of organic compounds.

*This scheme was proven surprisingly good in reproducing the lowest transition energies in the metal complex*



### Simple MO diagram

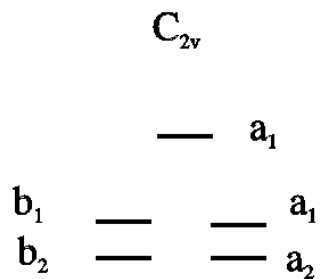
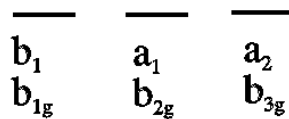
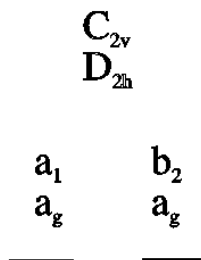


**Figure 8.5.** A picture of some of the studied metal complexes in this project, together with a schematic picture of the molecular orbital (MO) diagram of the metal centered MO's.

## 8.10 A First Principles Study of the Dehydroxylation of 2M<sub>1</sub>-Muscovite

*Michael Odelius*

Department of Physical Chemistry, Uppsala University

*Marco Bernasconi*

Max-Planck Institut für Festkörperforschung, Stuttgart, Germany

*Michele Parrinello*

Dipartimento di Fisica, Università di Milano, Italy

2M<sub>1</sub>-Muscovite, KAl<sub>2</sub>(Al,Si<sub>3</sub>)O<sub>10</sub>(OH)<sub>2</sub>, is a hydroxyl containing layered mineral (see Figure 8.6), which at elevated temperatures loses its hydroxyl groups, i.e. the hydroxyl groups react with each other to form water, and a phase transition to a metastable dehydroxylated form of 2M<sub>1</sub>-Muscovite occurs.

This work aims at determining the mechanism for the dehydroxylation of 2M<sub>1</sub>-Muscovite by means of first principle Car-Parrinello molecular dynamics (MD) simulations.

The dehydroxylation of 2M<sub>1</sub>-Muscovite and other micas have been carefully studied by many different experimental techniques, which have been successful in characterizing the difference between the 2M<sub>1</sub>-Muscovite crystal and its dehydroxylated form. However, the detailed mechanism for the reaction is still under debate. It is difficult to reach from the experimental information to a fully described mechanism.

It has been shown by X-ray diffraction and Mössbauer spectroscopy on dehydroxylated 2M<sub>1</sub>-Muscovite that the coordination in the “octahedral” layer is changed from six to five. The reaction occurs in a wide temperature range (800–1220 K), which has been interpreted as evidence both for the influence of the Al substitutions and for an inhibiting effect of the five coordinated Al<sup>3+</sup> on neighboring reaction sites.

In IR studies the OH line has been observed to shift with the temperature before disappearing, suggesting that an intermediate state exists for the hydroxyl group. Also shifts in the vibrational spectra of K<sup>+</sup> has been observed. Electrical conductivity indicates that the ions diffuse before forming water, and the activation energy for the proton diffusion is determined. Thus, a solid experimental ground exists for the study, and still valuable information on the mechanism of dehydroxylation is lacking, motivating the theoretical study.

Car-Parrinello [Car and Parrinello, 1985] has developed an *ab initio* method to perform MD simulations for classical nuclei, based on density functional theory. It enables us to calculate accurate quantum mechanical forces on the nuclei, as an alternative to the use of model potentials. The method is very suitable for studying crystals, since it is based on a plane wave description and periodic boundary conditions. This excludes an explicit treatment of the core electrons, but with *ab initio pseudo potentials* and *gradient corrections to the energy functional* we get a description comparable to MP2 calculations.

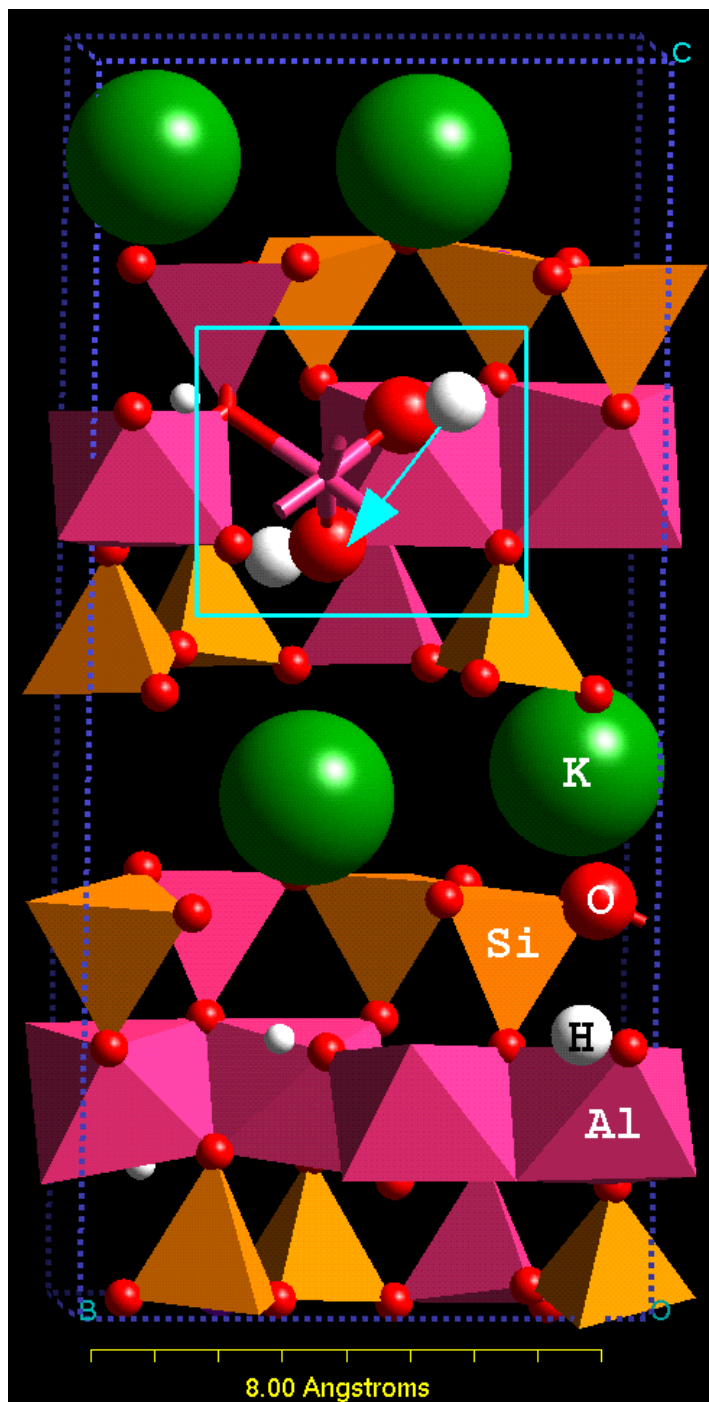


**Figure 8.6.** In the 2M<sub>1</sub>-Muscovite structure, a layer of octahedrally coordinated Al<sup>3+</sup> ions is sandwiched between two tetrahedral silicate layers, with vertices pointing towards the octahedral layer. The buckled basal plane of the tetrahedra forms distorted hexagonal rings of oxygens. Aluminum is randomly substituted for silicon with a ratio of 1:3, and for charge compensation potassium counterions are present at the center of all the hexagonal rings. The hydroxyl groups are located in the junction between the octahedral and tetrahedral layers, under the rings, and they form long hydrogen bonds to oxygens in the rings. The highlighted region contains a schematic picture of the dehydroxylation:  $2 \text{OH}^- \Rightarrow \text{H}_2\text{O} + \text{O}^{2-}$ .

It offers a large number of possibilities for analyzing the dehydroxylation process, since both the dynamics and the electron structure can be studied. We have seen in earlier structure calculations of 2M<sub>1</sub>-Muscovite [Odelius *et al.*, 199X] that the bond lengths and orientations of the hydroxyl groups depend strongly on the presence of the Al substitution sites, which will effect the reaction path way.

In the study we will perform MD simulations at increasing temperatures, in order to study the motion of the hydroxyl groups, the release of the protons and the transformation to the dehydroxylated form of 2M<sub>1</sub>-Muscovite.

## 9 Miscellaneous Projects

### 9.1 Multi-Disciplinary Parallel Optimization

*Dan Holm*

ALFGAM Optimering AB

The Swedish government has decided that a new Swedish marine vessel (YS2000) shall be developed. In the first round two ships are to be built. FMV, the Swedish Defense Material Administration, has given Karlskrona Varvet (KkrV) the task to construct and to manufacture the two vessels. At the request of, and in collaboration with, KkrV and FMV ALFGAM Optimering AB is responsible for the structural optimization of the hull of the vessel.

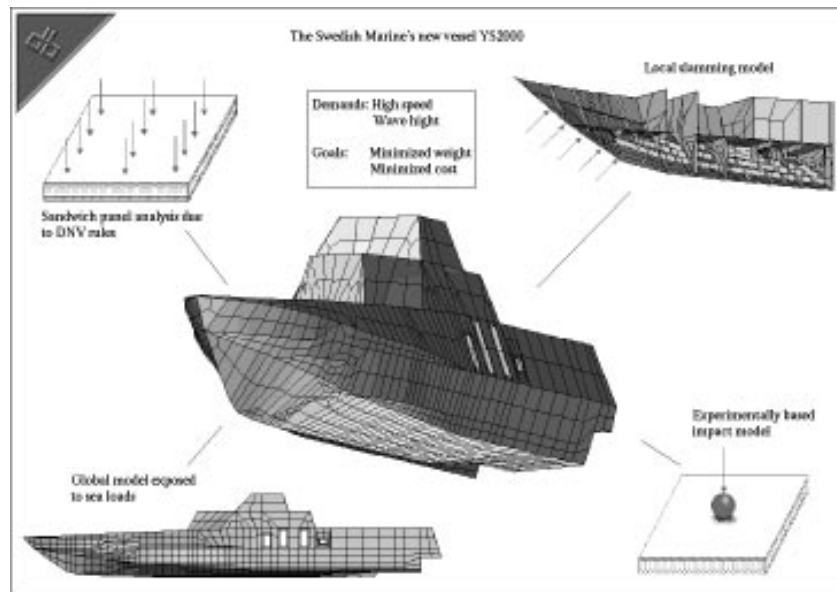
The vessel, which is 71 meters long, will be built using composite sandwich technique. Sandwich structures have the advantage, compared to traditional steel structures, that it is possible to build an as stiff and tough structure to a lesser weight. This weight reduction can either be used to lower the fuel consumption or to increase performance.

Demands exist on the performance of the vessel (such as speed and wave height etc. ) and it is necessary that the structure meets the stated demands to a minimum weight and/or cost. If the problem is reduced to an optimization problem, it can be formulated as follows: chose materials and dimensions of the core and face so the weight of the structure is minimized with constraints on stress, stiffness and cost. Accordingly, the primary goal with the structural analysis was to calculate and optimize the core and face materials as well as dimensions (i.e. chose thickness and quality of the foam core and thickness, material and lay up of the face composite laminates).

The constraints can be split into different parts: each sandwich panel must meet the regulations from DNV (Den Norske Veritas), local parts of the model must stand the pressure from local slamming loads, the whole model must be able to handle the global stress condition originated from global sea loads and the sandwich must stand declared impact criterions. Each of these mechanisms put demands on the core and face configuration.

OCTOPUS is an optimization program, developed at ALFGAM Optimering AB, that enables multi-disciplinary optimization. OCTOPUS uses MMA (Method of Moving Asymptotes) as optimization algorithm. OCTOPUS can handle criterions from different analyses and, based on them, perform a global optimization. The different analyses must not necessarily be structural. Every property that can be calculated can be used as a criterion in the analysis. The different analyses can also be

**Figure 9.1.** The Swedish Marine's new vessel YS2000.



run on different computers. OCTOPUS can handle analyses running on up to 100 different processors and is therefore very well suited to run on a parallel computer such as Strindberg.

In this particular case four “part analyses” models were developed. One panel analysis due to DNV rules, one FEM model analyzing local slamming, one FEM model analyzing the global stress conditions due to sea loads and one analysis controlling the impact. These analyses were run in parallel on different nodes on the Strindberg IBM SP-2 computer. For each iteration of the optimization process one analysis of the part analyses must be carried out. OCTOPUS administrates the collecting of criterions from the different part analyses and the distribution of variable values to the different part analyses. Using OCTOPUS and parallel optimization enables a solution which meet all the demands and criterions put on the structure to a minimum weight.

Parallel optimization problems like this are well suited to run on parallel computers like Strindberg. The total optimization problem can easily be split into different, independent part. The different part analyses can be run on different processors and OCTOPUS enables them to take part in the same global optimization. This cuts the total analysis time in the very time consuming optimization process. Figure 9.1 highlights some of the principles behind the construction of YS200.

## 9.2 Simulation and Prediction of Real and Artificial Financial Systems

*Erik Aurell, Per Öster*

Center for Parallel Computers, KTH

*Jesper Oettelstrup*

Department of Numerical Analysis and Computing Science, KTH

*Mats Nordahl*

Institute of Theoretical Physics, CTH

In the last ten years the word market (in Swedish “marknad”) has become one of the most frequently cited in the media, and the phenomenon it describes has risen to a dominating importance. Our interest stems from the fact that a market, as an object of scientific discourse, is still very poorly understood. The traditional viewpoint of economic theory is that market behavior can be understood in terms of equilibrium theory, but, as is evident from everyday life, real markets are dynamic and volatile, and speculation bubbles are not uncommon.

The objective of this project is to bring methods from modern theoretical physics, scientific computing and nonlinear dynamics to bear on the evolution, predictability and possibly prediction of markets. The senior members of the project are Erik Aurell and Per Öster at PDC, Jesper Oettelstrup at NADA and Mats Nordahl at the Institute of Theoretical Physics of Chalmers University of Technology in Göteborg. Several diploma students work in the project. The project is supported by a NUTEK grant.

### *Results*

1. A new theory of pricing of risky options, a generalization of the standard Black-Scholes theory, see [Aurell and Życzkowski, 1995].

A second paper on the same subject, in collaboration with Jean-Philippe Bouchaud of CEA-Saclay in France is in preparation.

2. An implementation of a genetic programming model to develop technical trading rules. Application has been made to one year of currency exchange data on the interbank market, purchased from Olsen & Associates in Zurich, Switzerland, see [Madjidi, 1996].

A second paper by Mats Nordahl, Håkan Jonsson and Payam Madjidi is in preparation.

3. Implementation of a model of an artificial market, originally proposed by Ken Steiglitz in Princeton. The study has so far not been pushed much further than in Steiglitz’ paper.

4. An analysis using wavelet techniques, looking for periodicities and cross-correlations in the high-frequency data of Olsen & Associates. A report by Denis Galyagin is in preparation.

### 9.3 Burgers' Equation with Noisy Initial Data

*Erik Aurell*

Center for Parallel Computers, KTH

*Sergey N. Gurbatov, Sergey I. Simdyankin*

University of Nizhny, Novgorod, Russia

This project is a collaboration between Erik Aurell, Uriel Frisch of Observatoire de Nice, France, and Sergey Gurbatov and Sergey Simdyankin, of the Radiophysics department at the University of Nizhny, Novgorod, Russia.

The problem studied is the statistical properties of solutions to Burgers' equation,  $v_t + vv_x = \nu v_{xx}$ , for large times, when the initial velocity and its potential are stationary Gaussian processes. The initial power spectral density at small wave numbers follows a steep power-law  $E_0(k) \sim |k|^n$  where the exponent  $n$  is greater than one. Burgers initially proposed his equation as a mathematical model of hydrodynamic turbulence. It has later turned out to be not quite adapted to this purpose, but the equation is anyhow simple and natural enough to crop up in many diverse physical systems.

The particular situation here, with these initial conditions, is relevant to the propagation and late decay of high-amplitude acoustic noise.

The great advantage of Burgers' equation from the numerical and theoretical point of view, is that it follows from a variational principle, and so can be integrated by a fast procedure, going directly from initial to final data.

Our first objective was to compare, in the special case of  $n$  greater than two, results of numerical simulations with dimensional predictions, and with asymptotic analytical theory. This theory, which has quite a long and distinguished history, predicts self-similarity of statistical characteristics of turbulence, and also leads to a logarithmic correction to the law of energy decay in comparison with dimensional analysis. We confirmed numerically the existence of self-similarity for the power spectral density, and the existence of a logarithmic correction to the dimensional predictions.

Our second objective was to extend the theory to the case when the exponent  $n$  is between one and two. In this case the spectrum for large times is no more self-similar, but exhibits several ranges. In particular, at sufficiently large spatial scales, the correlations present in the initial data are preserved, an instance of the general phenomena of the permanence of large eddies. We extended the theory by a sort of cluster expansion to get a hold of subleading terms, which give the correlation functions at large times.

We verified numerically the existence of several scaling ranges in the spectrum, and the locations of the breakpoints [Aurell and *et al.*, 1996].

## 9.4 PDC++ and Parade — C++ Class Library and Visualizer for Data Parallel Programming

*Erik Wallin*<sup>1</sup>

Center for Parallel Computers, KTH

*Mattias Sandström, Micael Bergerholm, Mattias Löfstedt, Patrik Nilsson*

*Fredrik Ruda, Jakob Sellgren, Ludvig Karlsson, Lars Persson*<sup>2</sup>

Department of Numerical Analysis and Computing Science, KTH

Object oriented programming is becoming more and more common in solving complex problems. The most important advantages are information hiding and abstraction. These two techniques together provide for reusability, portability and improved structure of programs.

So far, no object oriented tools have been available for the CM200 and only a few are available for data parallel programming in general. These all involve a modified compiler. We have developed a C++ class library and a visualization/debugging tool that runs on the CM200. The library is general enough to be possible to port to other architectures of both SIMD and MIMD type. It does not require any compiler modifications, and is thus easier to port. This also improves the stability, since stable C++ compilers and development tools are readily available.

Although portable, programs written using the library may not execute equally efficient on all architectures. This depends on what features of the library that are used, and on how the problem at hand has been parallelized. The important thing is that the program will work on any machine where the library has been ported. It may then be optimized for that particular machine by using different features of the library.

The new language called PDC++ is inspired by C\*, the parallel extension to C developed by TMC. It contains a number of classes for declaring and manipulating parallel arrays. These can be allocated in different dimensions, and with integer, real or complex types. Communication and arithmetic operations are implemented and overloaded on the regular mathematical operators.

The library also improves the language construction in several ways, by removing some of the restrictions of C\*. The most important one is that the programmer does not have to keep track of what the current shape is. This is handled automatically by the library. It is also possible to utilize the capability to use variable precision integers on the CM200. For example 5-bit integers.

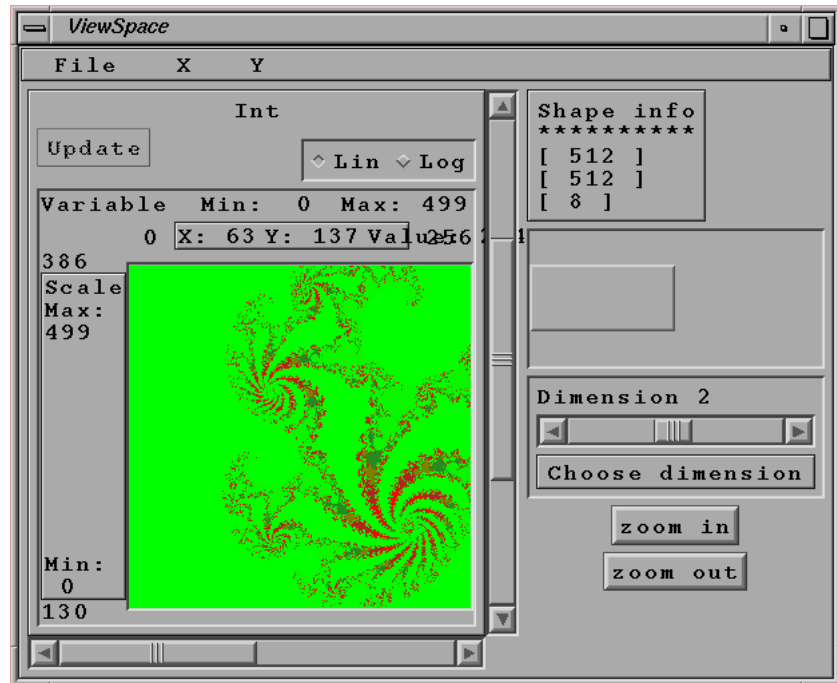
The current implementation on the CM200 is built as a class library wrapper around C/Paris. This makes it possible to utilize low-level CM200 functions, while maintaining a high level of abstraction. It is for example not necessary to keep track of how many bits are allocated for a particular integer array.

---

<sup>1</sup>Developed PDC++, initiated and supervised the development of Parade.

<sup>2</sup>Developed Parade as part of their M.Sc. program.

**Figure 9.2.** A prototype showing one part of the user interface.



Another improvement is a more standardized addressing of the arrays, by using the same syntax for parallel arrays as in serial arrays. It is also possible to create an array of parallel pointers. This enables common communication patterns to be stored once, and then reused.

All data parallel programming requires powerful debugging and visualization tools. Our approach to this problem is to develop a generic visualization tool. It can present array data with any number of dimensions. The data can be displaying in graphical form, as well as raw numbers. See Figure 9.2.

The visualizer is independent of the debugger used, and runs within the application being debugged. Thus it is possible to utilize other well tested and stable tools for the actual debugging. We considered it important for the visualizer (and the C++ library) to be independent of the choice of compiler and debugger. The visualizer could of course be integrated into the debugger for a particular implementation.

The code for the visualizer is independent both of the debugger and the implementation of the library. It should therefore run on any architecture without modification.

We hope to port the library to other MPP architectures in the future. It is of course also possible to port it to ordinary workstations for development and educational purposes. It could also prove to be an efficient tool for solving problems suited for data parallel programming even on a sequential computer.

# Bibliography

- [Aabloo and Thomas, 199Xa] AABLOO, A. AND THOMAS, J. O. (199Xa). Molecular Dynamics Simulation of a Poly(Ethylene Oxide) Surface. Submitted for publication in *Computational Polymer Science*. 126
- [Aabloo and Thomas, 199Xb] AABLOO, A. AND THOMAS, J. O. (199Xb). Molecular Dynamics Simulation of Ion Mobility in the Crystalline Poly(Ethylene Oxide) Surface. Submitted for publication in *J. Electrochim. Acta*. 127
- [Adman, 1991] ADMAN, E. T. (1991). Copper Protein Structures. *Adv. Prot. Chem.* **42**:145–197. 133, 134
- [Ågren *et al.*, 1993] ÅGREN, H., VAHTRAS, O., KOCH, H., JØRGENSEN, P., AND HELGAKER, T. (1993). Direct Atomic Orbital Based Self-Consistent Field Calculations of Non-linear Molecular Properties. Application to the Frequency Dependent Hyperpolarizability of Para-Nitroaniline. *Journal of Chemical Physics* **98**:64. 75
- [Almlöf *et al.*, 1982] ALMLÖF, J., K. FAEGRI, J., AND KORSELL, K. (1982). *J. Comput. Chem.* **3**:385. 127
- [Ålund *et al.*, 1994] ÅLUND, A., LÖTSTEDT, P., AND RYDÉN, R. (1994). Computational fluid dynamics on a workstation cluster in industrial environments. In: *PARA94*, number 879 in *Lect. Notes in Comp. Science*. Springer-Verlag, 1994. 51, 52
- [Ålund *et al.*, 1995] ÅLUND, A., LÖTSTEDT, P., AND SILLÉN, M. (1995). Solution of Compressible Flow Problems in Parallel with Static Load Balancing. Technical Report L-0-1 R159, Saab Military Aircraft, Linköping, Sweden. Also available as Technical Report 1995:2, ITM, Göteborg. 51
- [Ålund and Rydén, 1994] ÅLUND, A. AND RYDÉN, R. (1994). Solving the Navier-Stokes Equations with Combustion on a Cluster of Workstations in an Industrial Environment. Technical Report 1994:1, ITM, Chalmers Science Park, 412 88 Göteborg, Sweden. 52
- [Ålund and Sunderam, 1993] ÅLUND, S. W. A. AND SUNDERAM, V. S. (1993). The NAS Parallel Benchmarks on Virtual Parallel Machines. Technical Report 1993:7, ITM. 39
- [Andersson *et al.*, 1992] ANDERSSON, J.-O., MATTSSON, J., AND SVEDLINDH, P. (1992). *Phys. Rev. B* **46**:8297. 86

- [Andersson *et al.*, 1994] ANDERSSON, J.-O., MATTSSON, J., AND SVEDLINDH, P. (1994). *Phys. Rev. B* **49**:1120. 86
- [Andersson and Ledfelt, 1995] ANDERSSON, U. AND LEDFELT, G. (1995). Solving the Maxwell equations with a 2D Finite Volume Method on the CM200. To appear in Proceedings from workshop on approximations and numerical methods for the solution of the Maxwell equations, Oxford university computing laboratory. Also available at <http://www.nada.kth.se/na/publications>. 36
- [Aurell and *et al.*, 1996] AURELL, E. *et al.* (1996). TRITA-PDC Report 1996:2, submitted to Physics of Fluids. A more thorough report to be submitted to J Fluid Mech is in preparation. 144
- [Aurell and Życzkowski, 1995] AURELL, E. AND ŻYCZKOWSKI, K. (1995). Option Pricing and Partial Hedging: Theory of Polish Options. Technical report, PDC. TRITA-PDC Report 1995:1. 143
- [Bech *et al.*, 1995] BECH, K., TILLMARK, N., ALFREDSSON, P., AND ANDERSSON, H. (1995). An Investigation of Turbulent Couette Flow at Low Reynolds Numbers. *J Fluid Mech.* **286**:291–372. 47
- [Belonoshko, 1994] BELONOSHKO, A. (1994). Molecular Dynamics of MgSiO<sub>3</sub> Perovskite at High Pressures: Equation of State, Structure and Melting Transition. *Geochimica et Cosmochimica Acta* **58**:4039–4047. 113
- [Belonoshko and Ahuja, 199X] BELONOSHKO, A. AND AHUJA, R. (199X). Embedded-Atom Study of Iron Melting. Submitted to High Pressure Research. 113
- [Belonoshko and Dubrovinsky, 1995] BELONOSHKO, A. AND DUBROVINSKY, L. (1995). Molecular Dynamics of Stishovite Melting. *Geochimica et Cosmochimica Acta* **59**:1883–1889. 113
- [Belonoshko and Dubrovinsky, 1996] BELONOSHKO, A. AND DUBROVINSKY, L. (1996). Molecular Dynamics of NaCl (B1 and B2) and MgO (B2) Melting: Two Phase Simulation. *American Mineralogis* **81**:303–316. 113
- [Bergman and Sawley, 1993] BERGMAN, C. AND SAWLEY, M. (1993). The Use of the Message Passing Programming Model on Distributed Networks for Computational Fluid Dynamics. *EPFL Supercomputing Review* . 37, 38, 38
- [Bernholdt *et al.*, 1995] BERNHOLDT, D., APRÀ, E., FRÜCHTL, H., GUEST, M., HARRISON, R., KENDALL, R., KUTTEH, R., LONG, X., NICHOLAS, J., NICHOLS, J., TAYLOR, H., WONG, A., FANN, G., LITTLEFIELD, R., AND NIEPLOCHA, J. (1995). *Int. J. Quantum Chem.: Quantum Chem. Symp.* **29**:475. 130

- [Binder and Young, 1986] BINDER, K. AND YOUNG, A. P. (1986). *Rev. Mod. Phys.* **58**:801. 86
- [Boerlijst and Hogeweg, 1991] BOERLIJST, M. C. AND HOGEWEG, P. (1991). Spiral Wave Structure in Pre-Biotic Evolution: Hypercycles Stable Against Parasites. *Physica D* **48**:17–28. 81
- [Bölcs and Fransson, 1986] BÖLCS, A. AND FRANSSON, T. H. (1986). Aeroelasticity in Turbomachines, Comparison of Theoretical and Experimental Cascade Results. Communication de Laboratoire de Thermique Appliquée et de Turbomachines 1, EPFL, Switzerland. 64, 64, 64
- [Bott, 1989a] BOTT, A. (1989a). A Positive Definite Advection Scheme Obtained by Nonlinear Renormalization of the Advective Fluxes. *Mon. Wea. Rev.* **117**:1006–1015. 42
- [Bott, 1989b] BOTT, A. (1989b). Reply. Notes and Correspondance. *Mon. Wea. Rev.* **117**:2626–2633. 42
- [Bray and Moore, 1985] BRAY, A. AND MOORE, M. A. (1985). *Phys. Rev. B* **31**:631. 84
- [Brooks *et al.*, 1983] BROOKS, B. R., BRUCCOLERI, R. E., OLAFSON, B. D., STATES, D. J., SWAMINATHAN, S., AND KARPLUS, M. (1983). *J. Comp. Chem.* **4**:187–217. 119
- [Brower *et al.*, 1994] BROWER, R. C., TAMAYO, P., AND YORK, B. (1994). A Parallel Multigrid Algorithm for Percolating Clusters. Technical report. 88, 89
- [Cao *et al.*, 1996] CAO, G. X., WONG, A., AND ZHU, X. D. (1996). In: *Bulletin of the American Physical Society*, volume 41. NY: APS, p. 421. 93
- [Cao and He, 1996] CAO, J. AND HE, S. (1996). An Exact Absorbing Boundary Condition and its Application to Three-Dimensional Scattering from Thin Dispersive Structures. *J. Acoust. Soc. Am.* **99**:1854–1861. 80
- [Cao and He, 199X] CAO, J. AND HE, S. (199X). An Ill-Posed Problem of the Continuation of Transient Data for a Hyperbolic Equation in a Three-Dimensional Inhomogeneous Half-Space. *J. Math. Phys.*, In press. 80
- [Car and Parrinello, 1985] CAR, R. AND PARRINELLO, M. (1985). *Phys. Rev. Lett* **55**:2471. 138
- [Chakarova and Pázsit, 1995] CHAKAROVA, R. AND PÁZSIT, I. (1995). In: *Proceedings of International Conference on Mathematics and Computations, Reactor Physics and Environmental Analyses*, volume 2, 1995, p. 1195. 106

- [Childress, 1981] CHILDRESS, S. (1981). *Mechanics of Swimming and Flying*. University Press. 82
- [Corbett *et al.*, 1964] CORBETT, J. W., WATKINS, G. D., AND DONALD, R. S. M. (1964). New Oxygen Infrared Bands in Annealed Irradiated Silicon. *Phys. Rev. B* **135**:A1381. 98
- [Cronhjort, 1995] CRONHJORT, M. (1995). *Models and Computer Simulations of Origins of Life and Evolution*. PhD thesis, KTH, Stockholm. 81, 81
- [Cronhjort and Blomberg, 1994] CRONHJORT, M. AND BLOMBERG, C. (1994). Hypercycles versus Parasites in a Two-Dimensional Partial Differential Equations Model. *J. theor. Biol.* **169**:31–49. 81
- [Cronhjort and Nyberg, 1995] CRONHJORT, M. AND NYBERG, A. (1995). 3D Hypercycles have no Stable Spatial Structure. *Physica D* 88. 81
- [Drew, 1983] DREW, D. (1983). Mathematical Modeling of Two-phase Flow. *Ann. Rev. Fluid Mech.* **15**:261–291. 59
- [Droz *et al.*, 1995] DROZ, T., BÜRGI, T., AND LEUTWYLER, S. (1995). *J. Chem. Phys.* **103**:4035. 132
- [Dzugutov, 1995] DZUGUTOV, M. (1995). Phason Dynamics and Atomic Transport in an Equilibrium Dodecagonal Quasi-crystal. *Europhys. Lett.* **31**:95–100. 71
- [Dzugutov, 1996a] DZUGUTOV, M. (1996a). Atomic Kinetics and Dynamical Phason Disorder in a Quasicrystal. In: *MRS Proceedings*, volume 407, 1996, p. 319. 71
- [Dzugutov, 1996b] DZUGUTOV, M. (1996b). Entropy and Atomic Transport in Condensed Matter. Technical Report TRITA-PDC 1996:1, PDC, KTH, Stockholm, Sweden. 70
- [Dzugutov, 1996c] DZUGUTOV, M. (1996c). A Universal Scaling Law for Atomic Diffusion in Condensed Matter. *Nature* 381. 70
- [Dzugutov and Phillips, 1995] DZUGUTOV, M. AND PHILLIPS, J. C. (1995). Structural Relaxation in an Equilibrium Quasicrystal. *Journ. Non-Cryst. Solids* **192-193**:397–400. 71
- [Edwards and Anderson, 1975] EDWARDS, S. F. AND ANDERSON, P. W. (1975). *J. Phys. F* **5**:965. 83
- [Eigen *et al.*, 1981] EIGEN, M., GARDINER, W., SCHUSTER, P., AND WINKLER-OSWATITSCH, R. (1981). The Origin of Genetic Information. *Sci. Am.* 78–94. 81

- [Erdős *et al.*, 1977] ERDÖS, J., ALZNER, E., AND MCNALLY, W. (1977). Numerical Solution of Periodic Transonic Flow through a Fan Stage. *AIAA Journal* **15**:1559–1568. 63
- [Ewald, 1921] EWALD, P. (1921). *Ann. Phys.* **64**:253. 123
- [Ewels *et al.*, 1995] EWELS, C. P., JONES, R., AND ÖBERG, S. (1995). First Principles Investigation of Vacancy Oxygen Defects in Si. *Mat. Sci. Forum* **196-201**:1297–1302. 98
- [Ewels *et al.*, 1996a] EWELS, C. P., JONES, R., AND ÖBERG, S. (1996a). Oxygen-Carbon, Oxygen-Nitrogen and Oxygen-Dimer Defects in Silicon. *NATO ARW 'Oxygen '96', Exeter*, In press. 99
- [Ewels *et al.*, 1996b] EWELS, C. P., JONES, R., ÖBERG, S., *et al.* (1996b). Shallow Thermal Donor Defects in Silicon. *Phys. Rev. Lett.* **77**:865. 99
- [Fisher and Huse, 1988] FISHER, D. S. AND HUSE, D. A. (1988). *Phys. Rev. B* **38**:373 and 386. 84
- [Försching, 1974] FÖRSCHING, H. (1974). *Aeroelastizität*. Berlin-Heidelberg: Springer Verlag. 62
- [Fransson, 1993] FRANSSON, T., (1993). Aeroelasticity in Axial-Flow Turbomachines. Lecture Notes, KTH. 64
- [Frisch *et al.*, 1987] FRISCH, U., D'HUMIERES, D., HASSLACHER, B., P. LALLEMAND, Y. P., AND RIVET, J. (1987). *Complex Systems* **1**:649. 82
- [Frisch *et al.*, 1986] FRISCH, U., HASSLACHER, B., AND POMEAU, Y. (1986). *Phys. Rev. Lett.* **56**. 82
- [Fristedt and Bergman, 1994] FRISTEDT, E. AND BERGMAN, M. (1994). The Use of Workstation Farms for Industrial CFD Computations. Submitted to Journal of Distributed Computing. 37, 39, 40
- [Gould and Tobochnik, 1985] GOULD, H. AND TOBOCHNIK, J. (1985). *Introduction to Computer Simulations, Part 2*. Addison-Wesley Publishing Co. Inc. 89
- [Gradin and Ledfelt, 1995] GRADIN, U. AND LEDFELT, G. (1995). Computational Electromagnetics in 2D. Technical Report TRITA-NA-E9338, NADA, KTH, Stockholm, Sweden. 36
- [Guss *et al.*, 1992] GUSS, J. M., BARTUNIC, H. D., AND FREEMAN, H. C. (1992). Accuracy and Precision in Protein Crystal Structure Analysis: Restrained Least-Squares Refinement of the Crystal Structure of Poplar Plastocyanin at 1.33 Å Resolution. *Acta Cryst.* **B48**:790–807. 25, 134

- [Hallberg and Lindström, 1992] HALLBERG, T. AND LINDSTRÖM, J. L. (1992). Enhanced Oxygen Precipitation in Electron-Irradiated Silicon. *J. Appl. Phys.* **72**:5130. 98
- [Hammarlund and Ekeberg, 1996] HAMMARLUND, P. AND EKEBERG, Ö., (1996). Large Neural Network Simulations on Multiple Hardware Platforms. (Submitted.). 27
- [Hammer and Nørskov, 1995] HAMMER, B. AND NØRSKOV, J. (1995). Why Gold is the Noblest of All the Metals. *Nature* **376**:238. 91
- [Hammer *et al.*, 1994] HAMMER, B., SCHEFFLER, M., JACOBSEN, K., AND NØRSKOV, J. (1994). The Potential Energy Surface for H<sub>2</sub> Dissociation over Cu(111). *Phys. Rev. Lett.* **73**:1400. 91
- [Harlow and Amsden, 1975] HARLOW, H. AND AMSDEN, A. (1975). Numerical Calculation of Multiphase Flow. *J. Comp. Phys.* **17**:19–52. 60
- [Head-Gordon *et al.*, 1988] HEAD-GORDON, M., POPLÉ, J., AND FRISCH, M. (1988). *Chem. Phys. Letters* **153**:503. 128, 129
- [Helgaker *et al.*, 199X] HELGAKER, T., JENSEN, H., JØRGENSEN, P., H. KOCH, J. O., ÅGREN, H., BAK, K., BAKKEN, V., CHRISTIANSEN, O., DAHLE, P., DALSKOV, E., ENEVOLDSEN, T., HALKIER, A., HEIBERG, H., HETTEMA, H., JONSSON, D., KIRPEKAR, S., KOBAYASHI, R., DE MERAS, A., MIKKELSEN, K., NORMAN, P., PACKER, M., RUUD, K., TAYLOR, P., AND VAHTRAS, O. (199X). *DALTON, an ab initio Electronic Structure Program, 199X*. 73
- [Hemmingsson, 1995] HEMMINGSSON, J. (1995). *J. Phys. A: Math. Gen.* **28**:4245. 82
- [Jackson and Persson, 1995] JACKSON, B. AND PERSSON, M. (1995). Effects of Isotopic Substitution on Eley-Rideal Reactions and Adsorbate-Mediated Trapping. (*J. Chem. Phys. accepted*) . 95
- [Jonason *et al.*, 1996] JONASON, K., MATTSSON, J., AND NORDBLAD, P. (1996). *Phys. Rev. B* **53**:6507. 84, 87
- [Jonason *et al.*, 199X] JONASON, K., MATTSSON, J., AND NORDBLAD, P. (199X). Preprint. 84, 87
- [Jones, 1992] JONES, R. (1992). Ab initio Cluster Calculations of Defects in Solids. *Philosophical Transactions of the Royal Society, London, A* **341**:351. 97
- [Jones *et al.*, 1994a] JONES, R., ÖBERG, S., RASMUSSEN, F. B., *et al.* (1994a). Identification of the Dominant Nitrogen Defect in Silicon. *Phys. Rev. Lett.* **72**:1882. 99

- [Jones *et al.*, 1994b] JONES, R., EWELS, C., ÖBERG, S., *et al.* (1994b). Theoretical and Isotopic Infrared-Absorption Investigations of Nitrogen-Oxygen Defects in Silicon. *Semicond. Sci. Tech.* **9**:2145–2148. 99
- [Jonsson *et al.*, 1996] JONSSON, D., NORMAN, P., AND ÄGREN, H. (1996). Cubic Response Functions in the Multiconfiguration Self-Consistent Field Approximation. *The Journal of Chemical Physics* 105. 75
- [Juhlin, 1995] JUHLIN, C. (1995). Finite-Difference Elastic Wave Propagation in 2D Heterogeneous Transversely Isotropic Media. *Geophysical Prospecting* **43**:843–858. 115, 115
- [Kållberg, 1989] KÅLLBERG, P. (ed.). (1989). *HIRLAM Forecast Model Level 1 Documentation Manual*, S-601 76 Norrköping, Sweden, 1989. SMHI. 41
- [Karlsson, 1994] KARLSSON, H. O. (1994). Dynamics of Hydrogenic Wave Packets in Electric and Magnetic Fields. *Physical Review A* **50**:3787–3792. 121
- [Karlsson and Goscinski, 1993] KARLSSON, H. O. AND GOSCINSKI, O. (1993). *A Direct Recursive Residue Generation Method*, PDC Progress Report 1993. p. 66–67. 120, 121
- [Karlsson and Goscinski, 1994] KARLSSON, H. O. AND GOSCINSKI, O. (1994). A Direct Recursive Residue Generation Method. Application to Photoionization of Hydrogen in Static Electric Fields. *Journal of Physics B* **27**:1061–1072. 120, 121
- [Karlsson and Goscinski, 1995] KARLSSON, H. O. AND GOSCINSKI, O. (1995). Autocorrelation Functions in the Photoionization of Hydrogen in Electric and Magnetic Fields. *Physical Review A* **51**:1154–1158. 121
- [Klein and Batrouni, 1990] KLEIN, W. AND BATROUNI, G. G. (1990). Supersymmetry in Cahn-Hilliard Cook Theory. Technical report. 88
- [Koelbel *et al.*, 1994] KOELBEL, C., LOVEMAN, D., SCHREIBER, R., STEEL JR., G., AND ZOSEL, M. (1994). *The High Performance Fortran Handbook*. MIT Press. Cambridge MA. 88, 89
- [Komminaho, 1995] KOMMINAHO, J. (1995). Numerical Simulation of the Navier Stokes Equations on Massively Parallel Computers. TRITAMEK, KTH. 47
- [Komminaho *et al.*, 1995a] KOMMINAHO, J., LUNDBLADH, A., AND JOHANSSON, A. (1995a). Determination of the Transition Reynolds Number in Plane Couette Flow through Study of Relaminarization. *Submitted to Phys. Fluids* . 47

- [Komminaho *et al.*, 1995b] KOMMINAHO, J., LUNDBLADH, A., AND JOHANSSON, A. (1995b). Very Large Structures in Plane Turbulent Couette Flow. *J Fluid Mech.* **320**:259–285. 47
- [Koper and Hilhorst, 1988] KOPER, G. J. M. AND HILHORST, H. J. (1988). *J. Phys. France* **49**:429. 84
- [Lansner, 1991] LANSNER, A. (1991). A Recurrent Bayesian ANN capable of Extracting Prototypes from Unlabeled and Noisy Example. In: *Artificial Neural Networks (Proc. of ICANN-91)*, edited by T. Kohonen *et al.*, volume 1, 1991, p. 247–254. 29
- [Lansner and Ekeberg, 1989] LANSNER, A. AND EKEBERG, O. (1989). A One-Layer Feedback Artificial Neural Network with a Bayesian Learning Rule. *Int. J. of Neural Systems* **1**:77–87. 29
- [Levin, 1995] LEVIN, B. (1995). *On Extensions, Parallel Implementation and Applications of a Bayesian Neural Network*. PhD thesis, Royal Institute of Technology, Stockholm, Sweden. 30
- [Leyland *et al.*, 1995] LEYLAND, P., VOS, J. B., VAN KEMENADE, V., AND YTTERSTROM, A., (1995). NSMB: A Modular Navier Stokes multiblock code for CFD. AIAA Paper 95-0568. 48
- [Liljenström, 1991] LILJENSTRÖM, H. (1991). Modeling the Dynamics of Olfactory Cortex using Simplified Network Units and Realistic Architecture. *Int. J. Neural Systems* **2**:1–15. 33
- [Liljenström, 1995] LILJENSTRÖM, H. (1995). Autonomous Learning with Complex Dynamics. *Int. J. Neural Systems* **10**:119–153. 32
- [Lin and Gomer, 1991] LIN, T. S. AND GOMER, R. (1991). Diffusion of 1H and 2H on the Ni(111) and (100) Planes. *Surf. Sci.* **255**:41. 93, 94
- [Lindblad, 1995] LINDBLAD, M. (1995). VolMoP V1 User's Guide. Technical Report 9970-1221, Volvo Aero Corporation, 461 81 Trollhättan, Sweden. 52
- [Lindström and Hallberg, 1995] LINDSTRÖM, J. L. AND HALLBERG, T. (1995). Vibrational Infrared-Absorption Bands Related to the Thermal Donors in Silicon. *J. Appl. Phys.* **77**:2684. 101
- [Ljungquist *et al.*, 1993] LJUNGQUIST, J., RENULF, F., AND ÅKERMO, M. (1993). Lösning av Eulers Ekvationer på ett kluster av arbetstationer. Technical Report 1993:6, TDB, Uppsala University. 37
- [Lötstedt and Ålund, 1994] LÖTSTEDT, P. AND ÅLUND, A. (1994). Multigrid Solution of the Euler and Navier-Stokes Equations on a Workstation Cluster in an Industrial Environment. Technical Report L-0-1 R150, Saab Military Aircraft, Linköping, Sweden. Also available as Technical Report 1994:3, ITM, Göteborg. 51, 51

- [Lötstedt and Sillén, 1993] LÖTSTEDT, P. AND SILLÉN, M. (1993). Multigrid Multiblock Solver of the Stationary Euler and Navier-Stokes Equations. Technical Report L-0-1 R148, Saab Military Aircraft, Saab Military Aircraft, Linköping, Sweden. 50
- [Lyubartsev and Laaksonen, 1995] LYUBARTSEV, A. P. AND LAAKSONEN, A. (1995). *Phys. Rev. E*, (in press). 126
- [Madjidi, 1996] MADJIDI, P. (1996). Genetic Programming and Analysis of High-Frequency Financial data. Technical report, PDC. TRITA-PDC Report 1996:3. 143
- [Maletta *et al.*, 1982] MALETTA, H., AEPPLI, G., AND SHAPIRO, S. M. (1982). *Phys. Rev. Lett.* **21**:1490. 84
- [Malmström, 1994] MALMSTRÖM, B. G. (1994). Rack-Induced Bonding in Blue-Copper Proteins. *Eur. J. Biochem.* **223**:711–718. 25, 134
- [Mattsson *et al.*, 1993a] MATTSSON, J., JONSSON, T., NORDBLAD, P., KATORI, H. A., AND ITO, A. (1993a). *Phys. Rev. Lett.* **74**:4305. 86
- [Mattsson *et al.*, 1993b] MATTSSON, T. R., ENGBERG, U., AND WAHNSTRÖM, G. (1993b). H Diffusion on Ni(100): A Quantum Monte Carlo Simulation. *Phys. Rev. Lett.* **71**:2615. 93
- [Mattsson and Wahnström, 1995] MATTSSON, T. R. AND WAHNSTRÖM, G. (1995). Quantum Monte Carlo Study of Surface Diffusion. *Phys. Rev. B* **51**:1885. 93
- [Mattsson *et al.*, 1996] MATTSSON, T. R., WAHNSTRÖM, G., BENGTS-SON, L., AND HAMMER, B. (1996). Quantum Mechanical Calculation of H on Ni(001) Using a Model Potential Based on First Principles Calculations. *Applied Physics Report 96-39*, To be submitted to *Phys. Rev. B*. 93
- [McMillan, 1984] MCMILLAN, W. L. (1984). *J. Phys. C* **17**:3179. 84
- [Metropolis and *et al.*, 1953] METROPOLIS, N. *et al.* (1953). Equations of State Calculations by Fast Computing. *Journal of Chemical Physics* **21**:1087–1092. 89
- [Mirebeau *et al.*, 1990] MIREBEAU, I., ITOH, S., MITSUDA, S., WATANABE, T., ENDOH, Y., HENNION, M., , AND RAPOULAR, R. (1990). *Phys. Rev. B* **41**:405. 84
- [Mohammadi, 1994] MOHAMMADI, B. (1994). Fluid Dynamics Computation with NSC2KE. Technical Report RT-0164, INRIA, France. 57

- [Naimark and Ismail-Zadeh, 1995] NAIMARK, B. AND ISMAIL-ZADEH, A. (1995). Numerical Models of Subsidence Mechanism in Intracratonic Basin: Application to North American Basins. *Geophys. J. Int.* **123**:149–160. 111
- [Naimark *et al.*, 1996] NAIMARK, B., ISMAIL-ZADEH, A., AND JACOBY, W. (1996). Numerical Approach to Problems of Gravitational Instability of Geosstructures with Advected Material Boundaries. *Geophys. J. Int.*, in press. 111
- [NAT, 1996] NATO-ASL. (1996). *Quantum Diffusion Calculations of H on Ni(001) Using a Model Potential Based on First Principles Calculations*, New-York, 1996. Plenum. 94
- [Nielsen *et al.*, 1996] NEILSEN, B. B., LISBY, T., AND NIELSEN, K. B. (1996). Uniaxial Stress Measurements on Oxygen-Implanted Silicon: the 889 cm<sup>-1</sup> Local Mode. *NATO ARW 'Oxygen '96'*, In press. 98
- [Nieplocha *et al.*, 1994] NIEPLOCHA, J., HARRISON, R., AND LITTLEFIELD, R., (1994). Global Arrays: A Portable "Shared Memory" Programming Model for Distributed Memory Computers, page 330, IEEE. 130
- [Norberg and Nilsson, 1995a] NORBERG, J. AND NILSSON, L. (1995a). *J. Phys. Chem.* **7**:2550–2554. 119
- [Norberg and Nilsson, 1995b] NORBERG, J. AND NILSSON, L. (1995b). *J. Am. Chem. Soc.* **117**:10832–10840. 120
- [Norman *et al.*, 1996a] NORMAN, P., JONSSON, D., ÅGREN, H., DAHLE, P., RUUD, K., HELGAKER, T., AND KOCH., H. (1996a). Efficient Parallel Implementation of Response Theory: Calculation of the Second Hyperpolarizability of the Polyacenes. *Chemical Physics Letters* **253**:1. 75
- [Norman *et al.*, 1996b] NORMAN, P., JONSSON, D., VAHTRAS, O., AND ÅGREN, H. (1996b). Non-Linear Electric and Magnetic Properties Obtained from Cubic Response Functions in the Random Phase Approximation. *Chemical Physics* **203**:23. 75
- [Odelius *et al.*, 199X] ODELIUS, M., BERNASCONI, M., AND PARRINELLO, M. (199X). A First Principles Study of the Structure of 2M<sub>1</sub>-Muscovite. To be published. 140
- [Olowsom and Almstedt, 1990] OLOWSON, P. AND ALMSTEDT, A. (1990). Influence of Pressure and Fluidization Velocity on the Bubble Behaviour and Gas Flow Distribution in a Fluidized Bed. *Chem. Engin. Sci.* **45**:1733–1741. 60

- [Özen, 1993] ÖZEN, A. (1993). Data Mapping Algorithms For Distributed Memory MIMD Machines. Technical Report TRITA-NA-E9326, NADA, KTH. 37
- [Palm, 1995] PALM, T. (1995). Effects of Remote Impurity Scattering Including Donor Correlations in a Branching Electron Wave Guide. *Phys Rev B* **52**:11284. 108
- [Payne *et al.*, 1992] PAYNE, M. C., TETER, M. P., ALLAN, D. C., ARIAS, T. A., AND JOANNOPOULOS, J. D. (1992). Iterative Minimization Techniques for ab initio Total-Energy Calculations: Molecular Dynamics and Conjugate Gradients. *Rev. Mod. Phys.* **64**:1045. 91
- [Persson and Robertson, 1990] PERSSON, C. AND ROBERTSON, L. (1990). An Operational Eulerian Dispersion Model Applicable to Different Scales. In: *Proceedings of the 18th Technical Meeting of NATO-CCMS on Air Pollution Modelling and Its Applications*, Vancouver, Canada. 41
- [Persson, 1995] PERSSON, I. (1995). Performance Analysis of a CFD-code on the IBM-SP2. Technical Report T-95-16, IMHEF, EPFL, Switzerland. 56, 56
- [Persson and Ytterström, 1996] PERSSON, I. AND YTTERSTRÖM, A. (1996). Computations on an Inviscid Supersonic Flow Case with Structured and Unstructured Methods Using Serial and Parallel Computers. Technical Report TRITA-NA-96XX, C2M2, KTH, Sweden. 58
- [Persson and Jackson, 1995a] PERSSON, M. AND JACKSON, B. (1995a). A Flat Surface Model Study of Eley-Rideal Dynamics of Recombinative Desorption of Hydrogen on a Metal Surface. *J. Chem. Phys.* **102**:1078. 95
- [Persson and Jackson, 1995b] PERSSON, M. AND JACKSON, B. (1995b). Isotope Effects in the Eley-Rideal Dynamics of the Recombinative Desorption of Hydrogen on a Metal Surface. *Chem. Phys. Lett.* **237**:468. 95
- [Prins, 1995] PRINS, J. F. (1995). Ion-Implanted N-type Diamond—Electrical Evidence. *Diamond and Related Materials* **4**:580–585. 100
- [Pázsit and Chakarova, 1994] PÁZSIT, I. AND CHAKAROVA, R. (1994). *Phys. Rev. B* **50**:13953. 105
- [Pázsit and Chakarova, 1996] PÁZSIT, I. AND CHAKAROVA, R. (1996). Variance and Correlations in Sputtering and Defect Distributions. *Transport Theory and Statistical Physics*, In press. 101
- [Reger and Young, 1989] REGER, J. D. AND YOUNG, A. P. (1989). *J. Phys. Condens. Matter* **1**:915. 84

- [Rettner, 1992] RETTNER, C. (1992). Dynamics of the Direct Reaction of Hydrogen Atoms Adsorbed on Cu(111) with Hydrogen Atoms Incident from the Gas-Phase. *Phys. Rev. Lett.* **69**:383. 94
- [Rettner and Auerbach, 1995] RETTNER, C. AND AUERBACH, D. (1995). Dynamics of the Eley-Rideal Reaction of D Atoms with H Atoms Adsorbed on Cu(111): Vibrational and Rotational State Distribution of the HD Product. *Phys. Rev. Lett.* **74**:4551. 94, 95
- [Rev, 1991] (1991). Time-Dependent Methods for Quantum Dynamics. *Comp. Phys. Comm.* **63**. 94
- [Rice *et al.*, 1995] RICE, J. E., HORN, H., LENGSEI, B. H., MCLEAN, A. D., CARTER, J. T., REPLOGLE, E. S., BARNES, L. A., MALUENDES, S. A., LIE, G. C., GUTWSKI, M., RUDE, W. E., SAUER, S. P. A., LINDH, R., ANDERSSON, K., CHEVALIER, T. S., WIDMARK, P.-O., BOUZIDA, D., PACANSKY, G., SINGH, K., GILLAN, C. J., CARNEVALI, P., SWOPE, W. C., AND LIU, B. (1995). *Mulliken<sup>TM</sup> Version 2.25b, internal release*. IBM Corporation, Almaden, USA, 1995. 134
- [Rudgyard *et al.*, 1994] RUDGYARD, M., SCHONFELD, T., STRUIJS, R., AUDEMAR, G., AND LEYLAND, P. (1994). A Modular Approach for Computational Fluid Dynamics. In: *ECCOMAS 94, 1994*. 55
- [Ryde *et al.*, 1996] RYDE, U., OLSSON, M. H. M., AND ROOS, B. O. (1996). The Cupric Geometry of Blue Copper Proteins is not Strained. *J. Mol. Biol.* **261**:586–596. 134
- [Rydén, 1995] RYDÉN, R. (1995). VolSol V2 User's Manual. Technical Report 9970-1161, Volvo Aero Corporation, 461 81 Trollhättan, Sweden. 52
- [Sæbø and Almlöf, 1989] SÆBØ, S. AND ALMLÖF, J. (1989). *Chem. Phys. Letters* **154**:83. 128, 129
- [Saenger, 1988] SAENGER, W. (1988). *Principles of Nucleic Acid Structure*. New York: Springer-Verlag. 119
- [Safonov *et al.*, 1996] SAFONOV, A. N., LIGHTOWLERS, E. C., DAVIES, G., LEARY, P., JONES, R., AND ÖBERG, S. (1996). Interstitial-Carbon Hydrogen Interaction in Silicon. Submitted to *Phys. Rev. Letters*. 100
- [Sawley and Bergman, 1994] SAWLEY, M. AND BERGMAN, C. (1994). A Comparative Study of the Use of the Data-parallel Approach for Compressible Flow Calculations. *Journal of Parallel Computing*. 37
- [Sawley and Tegnér, 1994] SAWLEY, M. AND TEGNÉR, J. (1994). A Data-Parallel Approach to Multi-Block Flow Computations. *Int. J. Numer. Meth. in Fluids* **19**:707–721. 40

- [Sawley and Tegnér, 1995] SAWLEY, M. AND TEGNÉR, J. (1995). A Comparison of Parallel Programming Models for Multiblock Flow Computations. *J. Comp. Phys.* **122**:280–290. 41
- [Schütz and Klopper, 199X] SCHÜTZ, M. AND KLOPPER, W. (199X). An Integral-Direct, Distributed-Data Parallel MP2-R12 Algorithm. Manuscript in preparation. 128
- [Schütz and Lindh, 199Xa] SCHÜTZ, M. AND LINDH, R. (199Xa). To be published. 132
- [Schütz and Lindh, 199Xb] SCHÜTZ, M. AND LINDH, R. (199Xb). An Integral-Direct, Distributed-Data Parallel MP2 Algorithm. Accepted for publication in *Theor. Chim. Acta.* 128, 128, 130
- [Stavola *et al.*, 1983] STAVOLA, M., PATEL, J. R., *et al.* (1983). Diffusivity of Oxygen in Silicon at the Donor Formation Temperature. *Appl. Phys. Lett.* **42**:73. 99
- [Sundström, 1996] SUNDSTRÖM, A. (1996). FE-modellering av Akustisk Emission i kompositlaminat. Master's thesis, KTH, Department of Solid Mechanics. 78
- [Sykes, 1990] SYKES, A. G. (1990). Active-Site Properties of the Blue Copper Proteins. *Adv. Inorg. Chem.* **36**:377–408. 133
- [Taylor, 1987] TAYLOR, P. (1987). *Int. J. Quantum Chem.* **31**:521. 128
- [Thi, 1993] Thinking Machines Corporation, Cambridge, MA. (1993). *Using the CMAX Converter*, July 1993. 42
- [Thomas, 199X] THOMAS, L. V. (199X). Simulations for Supersymmetry in CHC Theory. In progress. 88, 89
- [Thomsen, 1986] THOMSEN, L. (1986). Weak Elastic Anisotropy. *Geophysics* **51**:1954–1966. 115, 116
- [TMC, 1994] TMC. (1994). *CM Fortran User's Guide Version 2.1*, January 1994. 89
- [Tukerman *et al.*, 1992] TUKERMAN, M., BERNE, B. J., AND MARTYNA, G. J. (1992). *J. Chem. Phys.* **97**:1990. 123
- [van Gunsteren and Berendsen, 199X] VAN GUNSTEREN, W. F. AND BERENDSEN, H. J. C. (199X). *Gromos Library Manual*. Biomos, Nijenborgh 16, Groningen, The Netherlands, 199X. 122
- [Vos *et al.*, 1995] VOS, J. B., LEYLAND, P., LINDBERG, P. A., KEMENADE, V. V., AND GACHERIEU, C., (1995). NSMB Handbook 3.3. ESPRIT Project 8421, Work Package WP6.1, RD21. 48

- [Wada and Liou, 1994] WADA, Y. AND LIOU, M. S., (1994). A Flux Splitting Scheme with High-Resolution and Robustness for Discontinuities. AIAA Paper 94-0083. 62
- [Weiner *et al.*, 1986] WEINER, S. J., KOLLMAN, P. A., NGYUEN, D. T., AND CASE, D. A. (1986). *J. Comput. Chem.* **7**:230. 122
- [White *et al.*, 1994] WHITE, J., BIRD, D., PAYNE, M., AND STICH, I. (1994). Surface Corrugation in the Dissociative Adsorption of H<sub>2</sub> on Cu(100). *Phys. Rev. Lett.* **73**:1404. 91
- [Wilhelmsson, 1995] WILHELMSSON, T. (1995). Simulating the Dynamics of Olfactory Cortex on a Connection Machine. Master's thesis, Linköping Institute of Technology, Linköping, Sweden. LiTH-ISY-EX-1336. 32
- [Williams, 1995] WILLIAMS, R. J. P. (1995). Energised (Entatic) States of Groups and of Secondary Structures in Proteins and Metalloproteins. *Eur. J. Biochem.* **234**:363–381. 25, 134
- [Worgan and Robinson, 1992] WORGAN, K. AND ROBINSON, P. (1992). Technical Report 91:13, SKI, Stockholm, Sweden. 109
- [Yström, 1993] YSTRÖM, J. (1993). On Convective Effects in Sedimentation of Concentrated Suspensions with High Effective Gravity. Technical Report TRITA-NA-931, NADA, KTH. 61
- [Yström, 1996] YSTRÖM, J. (1996). *On the Numerical Modeling of Concentrated Suspensions and of Viscoelastic Fluids*. PhD thesis, KTH. TRITA-NA-9603. 61
- [Zhu *et al.*, 1992] ZHU, X., LEE, A., WONG, A., AND LINKE, U. (1992). Surface Diffusion of Hydrogen on Ni(100): An Experimental Observation of Quantum Tunneling Diffusion. *Phys. Rev. Lett.* **68**:1862. 93

# Index

- Aabloo, Alvo, 126, 127  
ABB Corporate Research, 37, 52, 54  
Aerospaciale, 47, 49  
AFS, *see* Andrew File System  
Alfgam Optimering, 141  
Ålund, Anders, 8, 39  
Andersson, Jan-Olov, 83  
Andersson, Marlene, 108  
Andersson, Ulf, 35  
Andrew File System, 9  
ANN, *see* Artificial Neural Networks  
Arrhenius Laboratory, 121  
Artificial Neural Networks, 30  
Aurell, Erik, 8, 143, 144  
AVBP, 54–56
- Barth, Harald, 8  
Belgium, 133  
Belonoshko, Anatoly B., 113  
Bengtsson, Lennart, 91, 92  
Bergerholm, Micael, 145  
Bergman, Magnus, 37–39  
Bernasyyconi, Marco, 138  
Biology, 27–34  
    3D brain data, 34  
    airplane pilot dynamics, 30  
    hippocampus, 32  
    large neural networks, 27  
    neural network clustering for remote sensing, 29  
    olfactory cortex, 32  
Bodelsson, Berith, 8  
Broo, Anders, 135, 136
- C2M2, *see* Center for Computational Mathematics and Mechanics  
Cao, Jiasu, 79, 80  
Carlsson, Peter, 8  
CEM, *see* Computational Electromagnetics  
Center for Computational Mathematics and Mechanics, 35, 37–39, 54, 57, 60  
Center for Parallel Computers, 1, 2, 7–10, 27, 29, 37, 40, 41, 47, 50, 53, 67, 70, 91, 92, 96, 97, 103, 108, 109, 115, 125, 131–133, 136, 143–145  
Center for Structural Biochemistry, 119  
CERFACS, 47, 48, 54  
CFD, *see* Computational Fluid Dynamics  
Chakarova, Roumiana, 101, 103, 105  
Chalmers University of Technology, 10, 59, 91, 94, 101, 103, 105, 135, 136, 143  
    Department of Applied Physics, 91, 94  
    Department of Energy Conversion, 59  
    Department of Physical Chemistry, 135, 136  
    Department of Reactor Physics, 101, 103, 105  
    Department of Thermo and Fluid Dynamics, 59  
    Institute of Theoretical Physics, 143  
CHARMM, 119  
Chemistry, 119–140  
    2M<sub>1</sub>-Muscovite, 138  
    blue copper proteins, 133  
    conformational free energy landscape, 119  
    DNA systems, 121  
    hydrogen atoms in strong fields, 120  
    integral direct MP2 algorithm, 127

- poly(ethylene oxide) surface, 126, 127
- solution tautomerism of DNA bases, 135
- transition-metal complexes, 136
- CMAX, 42
- CMSSL, 95
- Computational Electromagnetics, 35, 36, 35–36
- Computational Fluid Dynamics, 35, 37, 38, 39, 50, 51, 52, 53, 54, 56, 37–64
  - adaptiva unstructured grids, 57
  - afterburner, 52
  - air pollution dispersion, 41
  - aircraft design, 47
  - compressible flow, 50
  - concentrated suspensions, 60
  - distributed CFD, 38
  - fluidized beds, 59
  - flutter analysis of turbomachines, 62
  - multi-block computations, 40
  - NAS parallel benchmarks, 39
  - parallel CFD at C2M2, 37
  - parallel CFD on SP-2, 54
  - supersonic inviscid flow, 57
  - turbulent Couette flow, 45
- Connection Machine, 35, 89
  - CM200, 7, 9, 29, 32–37, 40–43, 45, 47, 80, 84, 88, 89, 94, 96, 105, 106, 108, 115, 117, 120, 145, 148
  - CM5, 41, 96
- Convex, 48
- CRAY, 10, 27, 39, 50, 58
  - CRAY J90, 7, 9, 10, 48, 58
  - CRAY T3D, 41, 48, 97
  - CRAY Y-MP, 38, 39, 48, 51
- Cronhjort, Mikael, 81
- CSB, *see* Center for Structural Biochemistry
- CTH, *see* Chalmers University of Technology
- Danielsson, Johan, 8
- Data Migration Facility, 10
- DataVault, 9
- DEC, *see* Digital Equipment Denmark, 83
- Digital Equipment, 37–40, 45, 97
- DMF, *see* Data Migration Facility
- Dzugutov, Mikhail, 8, 67, 70
- Ecole Polytechnique Fédéral de Lausanne, 37, 38, 40, 47, 48
- Engquist, Björn, 2, 8
- Engström, Jonas, 8
- ESPRIT, 37, 48
- EUROPORT, 10, 48, 49
- Fast Fourier Transform, 34, 95
- FDDI, 9, 37
- FFT, *see* Fast Fourier Transform
- Fortran
  - CM Fortran, 88, 89, 95, 106
  - Fortran 77, 41, 42, 44, 45, 55
  - Fortran 90, 41, 42, 44, 45, 89
  - HPF, 88, 89
- France, 47, 143
- Fransson, Torsten, 62
- Frenje, Lena, 115
- Fristedt, Erland, 38, 39
- FRN, *see* Swedish Council for Planning and Coordination of Research
- Gaussian, 135
- Geophysics, 111–117
  - gravitational instability of geostuctures, 111
  - melting of Earth’s materials, 113
  - seismic wave propagation, 115
- Germany, 138
- Goscinski, Osvaldo, 120
- Gurbatov, Sergey N., 144
- Högskolan Gävle/Sandviken, 10
- Hammarlund, Per, 8, 27
- He, Sailing, 79, 80

Hedman, Fredrik, 8, 103  
 Hedström, P. G., 8  
 Hemmingsson, Jan, 82  
 Hewlett Packard, 38, 97  
 Hierarchial Storage Management, 10  
 HiPPI, 9  
 HIRLAM, 41, 44  
 Holm, Dan, 141  
 Holmen, Anders, 135  
 HP, *see* Hewlett Packard  
 HPDR, *see* Swedish Council for High Performance Computing  
 HPF, *see* Fortran  
 HSM, *see* Hierarchial Storage Management  
 Höhn, Wolfgang, 62  
  
 IBM, 10, 48, 88, 97, 134  
   SP-1, 48  
   SP-2, 1, 7–10, 27, 40, 41, 47, 48, 50, 51, 53–56, 60, 64, 78, 88, 89, 91, 97, 102, 109, 111, 113, 125–127, 130–132, 135, 136, 142  
 Ihrén, Johan, 8  
 IIEPTMG, *see* International Institute of Earthquake Prediction Theory and Mathematical Geophysics  
 IMHEF, *see* Institut de Machines Hydrauliques et de Mécanique des Fluides  
 Institut de Machines Hydrauliques et de Mécanique des Fluides, 38, 40, 47  
 Intel, 39  
   Paragon, 41, 48  
 International Institute of Earthquake Prediction Theory and Mathematical Geophysics, 111  
 Ismail-Zadeh, Ali T., 111  
 Italy, 138  
 ITM, *see* Swedish Institute of Applied Mathematics  
  
 Jönsson, Nils, 8  
 Jackson, Bret, 92, 94  
 Johansson, Arne, 45  
 Johnsson, S. Lennart, 8  
 Jonsson, Dan, 73  
 Jonsson, Tomas, 83  
 Juhlin, Christopher, 115  
  
 KALLSUP, 7, 9  
 Karlsson, Hans O, 120  
 Karlsson, Ludvig, 145  
 Karolinska Institutet, 34, 119  
   Center for Structural Biochemistry, 119  
   Department of Neuroscience, 34  
 Kemenade, Vincent van, 47  
 Kerpel, Jan der, 133  
 KI, *see* Karolinska Institutet  
 Komminaho, Jukka, 45  
 Kreiss, Heinz-Otto, 60  
 KTH, *see* Royal Institute of Technology  
  
 Laaksonen, Aatto, 121  
 Langner, Joakim, 41  
 Lansner, Anders, 30  
 Ledfelt, Gunnar, 35  
 Levin, Björn, 29  
 Liljenström, Hans, 32  
 Lindh, Roland, 127  
 Linköping University, 73, 82  
   Department of Physics, 73, 82  
 Löfstedt, Mattias, 145  
 Lofstrand, Hans, 59  
 Lötstedt, Per, 50  
 Luleå University, 96  
   Department of Mathematics, 96  
 Lund University, 127, 133  
   Department of Theoretical Chemistry, 127, 133  
 Lundbladh, Anders, 45  
 Lyubartsev, Alexander P., 121  
  
 Malinowsky, Lars, 8

MasPar, 42, 43, 45  
   MP-1, 40–43, 45  
   MP-2, 42, 43, 45  
 MATCH, 41, 42, 45  
 Mattsson, Johan, 83  
 Mattsson, Thomas, 91, 93  
 Max-Planck Institut für Festkörperforschung, 138  
 Meiko, 48  
 Mendes, Bruno, 108  
 Message Passing Interface, 27, 40, 60, 64, 102, 109  
 MIMD, 8, 37, 145  
 Miscellaneous, 141–146  
   Burgers' equation, 144  
   class library and visualizer, 145  
   financial systems, 143  
   parallel optimization, 141  
 Molecular dynamics simulation, 113, 119, 121, 126, 127  
 MPI, *see* Message Passing Interface  
  
 Naimark, Boris M., 111  
 NAS, *see* Numerical Aerospace Simulation Facility  
 National Science Foundation, 1  
 Neural Modelling, *see* Biology  
 NFR, *see* Swedish Natural Science Research Council  
 Nilsson, Lennart, 119  
 Nilsson, Patrik, 145  
 Norberg, Jan, 119  
 Nordahl, Mats, 143  
 Nordita, 83  
 Norman, Patrick, 73  
 NSF, *see* National Science Foundation  
 NSMB, 48, 49  
 Numerical Aerospace Simulation Facility, 39, 40  
 NUTEK, *see* Swedish National Board for Industrial and Technical Development  
  
 Öberg, Sven, 96  
  
 Odellius, Michael, 138  
 Office National d'Etudes et de Recherches Aéropetiale, 51, 54, 55, 64  
 Olsson, Mats, 133  
 ONERA, *see* Office National d'Etudes et de Recherches Aéropetiale  
 Opperstrup, Jesper, 143  
 Öster, Per, 8, 143  
  
 Palm, Thomas, 107  
 Parallel and Scientific Computing Institute, 1, 2  
 Parallel Virtual Machine, 27, 37, 39, 40, 48, 51, 52, 55, 91  
 PARMACS, 48  
 Parrinello, Michele, 138  
 Pázsit, Imre, 101, 103, 105  
 PDC, *see* Center for Parallel Computers  
 Peirano, Eric, 59  
 Pereira, Antonio, 108  
 Persson, Ingemar, 54, 57  
 Persson, Lars, 145  
 Persson, Magnus, 39  
 Persson, Mats, 91, 92, 94  
 PET, *see* Positron Emission Tomography  
 Physics, 67–110  
   3D thin structures, 79  
   acoustic emission, 78  
   atomic collision cascades, 101  
   atomic diffusion in condensed matter, 67  
   cluster-finding, 88  
   continuation of transient data, 80  
   defects in semiconductors, 96  
   elastic reflection of electrons, 103  
   electric and magnetic non-linear properties, 73  
   electronic structure of surfaces, 91  
   Ising spin glasses, 83  
   origin of life, 81

quantum wavepacket, 94  
 quasicrystal, 70  
 radiation transport benchmarks, 105  
 radionuclide transport, 108  
 self-propelling particles, 82  
 Smooth Particle Hydrodynamics, 106  
 Pierloot, Kristin, 133  
 Poinsot, Thierry, 47  
 Positron Emission Tomography, 34  
 PSCI, *see* Parallel and Scientific Computing Institute  
 PVM, *see* Parallel Virtual Machine  
  
 Rizzi, Arthur, 47  
 Robertson, Lennart, 41  
 Roos, Björn, 133  
 Rosenlund, Magnus, 30  
 Royal Institute of Technology, 1, 7–10, 27, 29, 30, 32, 35, 37–41, 45, 47, 48, 54, 57, 60, 62, 64, 67, 70, 78–81, 88, 103, 107, 143–145, 160  
 Department of Aeronautical Engineering, 47  
 Department of Electromagnetic Theory, 79, 80  
 Department of Electronics, 107  
 Department of Energy Technology, 62  
 Department of Mechanics, 45  
 Department of Numerical Analysis and Computing Science, 27, 41, 88, 143, 145  
 Department of Solid Mechanics, 78  
 Department of Theoretical Physics, 81  
 Ruda, Fredrik, 145  
 Russia, 111, 144  
 Russian Academy of Sciences, 111  
 Ryde, Ulf, 133  
 Rydén, Roland, 52  
  
 Saab, 47, 49  
 Saab Aerospace, 37  
 Saab Military Aircraft, 50, 52, 54  
 Sandström, Mattias, 145  
 SANS, *see* Studies of Artificial Neural Systems  
 Sawley, Mark, 38, 40  
 Schütz, Martin, 127  
 Selhammar, Magnus, 106  
 Sellgren, Jakob, 145  
 SGI, *see* Silicon Graphics Inc  
 Silicon Graphics Inc, 9, 38, 48, 97  
 Sillén, Mattias, 50  
 SIMD, 9, 29, 42, 123, 145  
 Simdyankin, Sergey I., 144  
 SMHI, *see* Swedish Meteorological and Hydrological Institute  
 SPARC, 91, 102, 105, 117  
 SPLIT, 27–29  
 Stockholm University, 108, 121  
 Arrhenius Laboratory, 121  
 Department of Physical Chemistry, 121  
 Department of Physics, 108  
 Strömqvist, Johan, 91, 92  
 Studies of Artificial Neural Systems, 29, 30, 32  
 Sun, 38, 102, 105, 117  
 Sundström, Anna, 78  
 SUNET, *see* Swedish University Network  
 Svensson, Britta, 8  
 Svensson, Gert, 8  
 Swedish Council for High Performance Computing, 1, 7–9  
 Swedish Council for Planning and Coordination of Research, 8, 9  
 Swedish Institute of Applied Mathematics, 39, 50, 52, 54  
 Swedish Meteorological and Hy-

drological Institute, 41, 42, 44  
 Swedish National Board for Industrial and Technical Development, 1, 8, 9, 37, 48, 52, 54, 94, 143  
 Swedish Natural Science Research Council, 70, 82, 94  
 Swedish University Network, 9  
 Switzerland, 38, 40, 47  
  
 Tegnér, Jon, 40  
 Thinking Machines Inc, 42, 145  
 Thomas, John O., 126, 127  
 Thomas, Lawrence V., 88  
 TMC, *see* Thinking Machines Inc  
  
 United States of America, 1, 60  
 Università di Milano, 138  
     Dipartimento di Fisica, 138  
 University of California, Los Angeles, 60  
 University of Leuven, 133  
     Department of Chemistry, 133  
 University of Massachusetts, 92, 94  
 University of Nizhny, 144  
 UNIX, 37  
 Uppsala University, 83, 106, 113, 115, 120, 126, 127, 138  
     Astronomical Observatory, 106  
     Centre of Technology, 83  
     Department of Geophysics, 115  
     Department of Physical Chemistry, 138  
     Department of Quantum Chemistry, 120  
     Institute of Chemistry, 126, 127  
     Institute of Earth Sciences, 113  
 USA, *see* United States of America  
  
 Vahtras, Olav, 73  
 VAST, 42, 45  
 Volvo Aero Corporation, 52, 54  
 Volvo Data, 37  
  
 Vos, Jan, 47  
  
 Wahnström, Göran, 91, 93  
 Wallin, Erik, 145  
 Wilhelmsson, Tomas, 27, 32, 41  
  
 Yström, Jacob, 60  
 Ytterström, Anders, 47